

Towards low-cost gigabit wireless systems at 60 GHz

Citation for published version (APA):

Yang, H. (2008). *Towards low-cost gigabit wireless systems at 60 GHz*. [Phd Thesis 1 (Research TU/e / Graduation TU/e), Electrical Engineering]. Technische Universiteit Eindhoven. <https://doi.org/10.6100/IR638026>

DOI:

[10.6100/IR638026](https://doi.org/10.6100/IR638026)

Document status and date:

Published: 01/01/2008

Document Version:

Publisher's PDF, also known as Version of Record (includes final page, issue and volume numbers)

Please check the document version of this publication:

- A submitted manuscript is the version of the article upon submission and before peer-review. There can be important differences between the submitted version and the official published version of record. People interested in the research are advised to contact the author for the final version of the publication, or visit the DOI to the publisher's website.
- The final author version and the galley proof are versions of the publication after peer review.
- The final published version features the final layout of the paper including the volume, issue and page numbers.

[Link to publication](#)

General rights

Copyright and moral rights for the publications made accessible in the public portal are retained by the authors and/or other copyright owners and it is a condition of accessing publications that users recognise and abide by the legal requirements associated with these rights.

- Users may download and print one copy of any publication from the public portal for the purpose of private study or research.
- You may not further distribute the material or use it for any profit-making activity or commercial gain
- You may freely distribute the URL identifying the publication in the public portal.

If the publication is distributed under the terms of Article 25fa of the Dutch Copyright Act, indicated by the "Taverne" license above, please follow below link for the End User Agreement:

www.tue.nl/taverne

Take down policy

If you believe that this document breaches copyright please contact us at:

openaccess@tue.nl

providing details and we will investigate your claim.

Towards Low-Cost Gigabit Wireless Systems at 60 GHz
Channel Modelling and Baseband Design

Towards Low-Cost Gigabit Wireless Systems at 60 GHz

Channel Modelling and Baseband Design

PROEFSCHRIFT

ter verkrijging van de graad van doctor aan de
Technische Universiteit Eindhoven, op gezag van de
Rector Magnificus, prof.dr.ir. C.J. van Duijn, voor een
commissie aangewezen door het College voor
Promoties in het openbaar te verdedigen
op dinsdag 18 november 2008 om 16.00 uur

door

Haibing Yang

geboren te Hebei, China

Dit proefschrift is goedgekeurd door de promotor:

prof.dr.ir. E.R. Fledderus

Copromotoren:

dr.ir. P.F.M. Smulders

en

dr.ir. M.H.A.J. Herben

CIP-DATA LIBRARY TECHNISCHE UNIVERSITEIT EINDHOVEN

Yang, Haibing

Towards Low-Cost Gigabit Wireless Systems at 60 GHz : Channel Modelling and Baseband Design / by Haibing Yang. – Eindhoven : Technische Universiteit Eindhoven, 2008.

Proefschrift. – ISBN 978-90-386-1425-0

NUR 959

Trefw.: draadloze communicatie / Mm-golfvoortplanting / breedbandige zend-ontvanger / RF imperfecties / signaalverwerking.

Subject headings: wireless communications / mm-wave propagation / wideband transceiver / RF impairments / signal processing.

Cover design by Haibing Yang

Typeset using L^AT_EX, printed by PPI in The Netherlands

Copyright© 2008 by Haibing Yang

All rights reserved. No part of this publication may be reproduced or transmitted in any form or by any means, electronic, mechanical, including photocopy, recording, or any information storage and retrieval system, without the prior written permission of the copyright owner.

*To my wife Jieheng,
and to our daughter Anjali*

Samenstelling van de promotiecommissie:

prof.dr.ir. A.C.P.M Backx, Technische Universiteit Eindhoven, voorzitter
prof.dr.ir. E.R. Fledderus, Technische Universiteit Eindhoven, promotor
dr.ir. P.F.M. Smulders, Technische Universiteit Eindhoven, eerste copromotor
dr.ir. M.H.A.J. Herben, Technische Universiteit Eindhoven, tweede copromotor
prof.dr.ir. L. van der Perre, Katholieke Universiteit Leuven
dr.ir. G.J.M. Janssen, Technische Universiteit Delft
prof.dr.ir. A.H.M. van Roermund, Technische Universiteit Eindhoven
prof.dr.ir. J.P.M.G. Linnartz, Technische Universiteit Eindhoven

Summary

Towards Low-Cost Gigabit Wireless Systems at 60 GHz Channel Modelling and Baseband Design

The world-wide availability of the huge amount of license-free spectral space in the 60 GHz band provides wide room for gigabit-per-second (Gb/s) wireless applications. A commercial (read: low-cost) 60-GHz transceiver will, however, provide limited system performance due to the stringent link budget and the substantial RF imperfections. The work presented in this thesis is intended to support the design of low-cost 60-GHz transceivers for Gb/s transmission over short distances (a few meters). Typical applications are the transfer of high-definition streaming video and high-speed download. The presented work comprises research into the characteristics of typical 60-GHz channels, the evaluation of the transmission quality as well as the development of suitable baseband algorithms. This can be summarized as follows.

In the first part, the characteristics of the wave propagation at 60 GHz are charted out by means of channel measurements and ray-tracing simulations for both narrow-beam and omni-directional configurations. Both line-of-sight (LOS) and non-line-of-sight (NLOS) are considered. This study reveals that antennas that produce a narrow beam can be used to boost the received power by tens of dBs when compared with omnidirectional configurations. Meanwhile, the time-domain dispersion of the channel is reduced to the order of nanoseconds, which facilitates Gb/s data transmission over 60-GHz channels considerably. Besides the execution of measurements and simulations, the influence of antenna radiation patterns is analyzed theoretically. It is indicated to what extent the signal-to-noise ratio, Rician- K factor and channel dispersion are improved by application of narrow-beam antennas and to what extent these parameters will be influenced by beam pointing errors. From both experimental and analytical work it can be concluded that the problem of the stringent link-budget can be solved effectively by application of beam-steering techniques.

The second part treats wideband transmission methods and relevant baseband algorithms. The considered schemes include orthogonal frequency division multiplexing (OFDM), multi-carrier code division multiple access (MC-CDMA) and single carrier with frequency-domain equalization (SC-FDE), which are promising candidates for Gb/s wireless transmission. In particular, the optimal linear equalization in the fre-

quency domain and associated implementation issues such as synchronization and channel estimation are examined. Bit error rate (BER) expressions are derived to evaluate the transmission performance. Besides the linear equalization techniques, a low-complexity inter-symbol interference cancellation technique is proposed to achieve much better performance of code-spreading systems such as MC-CDMA and SC-FDE. Both theoretical analysis and simulations demonstrate that the proposed scheme offers great advantages as regards both complexity and performance. This makes it particularly suitable for 60-GHz applications in multipath environments.

The third part treats the influence of quantization and RF imperfections on the considered transmission methods in the context of 60-GHz radios. First, expressions for the BER are derived and the influence of nonlinear distortions caused by the digital-to-analog converters, analog-to-digital converters and power amplifiers on the BER performance is examined. Next, the BER performance under the influence of phase noise and IQ imbalance is evaluated for the case that digital compensation techniques are applied in the receiver as well as for the case that such techniques are not applied.

Finally, a baseline design of a low-cost Gb/s 60-GHz transceiver is presented. It is shown that, by application of beam-steering in combination with SC-FDE without advanced channel coding, a data rate in the order of 2 Gb/s can be achieved over a distance of 10 meters in a typical NLOS indoor scenario.

Contents

Summary	vii
1 Introduction	1
1.1 Short-range gigabit radios at 60 GHz	1
1.2 Challenges in designing low-cost 60-GHz radios	3
1.3 Framework, objectives and related projects	7
1.4 Outline and contributions	8
2 Indoor radio propagation and channel modelling	11
2.1 Introduction	11
2.2 Wideband fading channel	13
2.2.1 Free space transmission model	13
2.2.2 Log-distance model	14
2.2.3 Channel impulse response	15
2.2.4 Frequency selectivity	19
2.2.5 Time selectivity	20
2.3 Channel measurement and analysis	20
2.3.1 Measurement setup and environment	20
2.3.2 Wideband received power	23
2.3.3 Channel impulse response and frequency response	25
2.3.4 Channel parameters	27
2.3.5 Modelling of power delay profile	32
2.3.6 Summary	33
2.4 Comparison of propagation in the frequency bands of 2 GHz and 60 GHz	33
2.4.1 Experimental setup and scenario	33
2.4.2 Normalized received power and shadowing effect	34
2.4.3 RMS delay spread	35
2.4.4 Effects of cool-shade curtain and antenna radiation pattern . .	36
2.4.5 Summary	37
2.5 Ray tracing simulations and analysis	37

2.5.1	RPS simulation setup	38
2.5.2	Prediction of the propagation simulator	38
2.5.3	Polarization effect	39
2.5.4	Multipath distribution in time and angular domain	44
2.6	Summary and conclusions	47
3	Impact of antenna pattern on radio transmission	49
3.1	Introduction	49
3.2	Channel characteristics and antenna effect	50
3.2.1	The received signal	50
3.2.2	Double-directional channel model without antenna effect	52
3.2.3	Impact of antenna radiation pattern on propagation channel	54
3.3	Extension to multi-antenna beamforming	57
3.3.1	MIMO channel model	57
3.3.2	Multi-antenna beamforming	58
3.4	Assumptions on the propagation channel	59
3.4.1	Separability of angular-delay spectrum in a single cluster model	60
3.4.2	Uniform power distribution in angular domain	61
3.4.3	Shape of power delay spectrum	62
3.5	Power patterns of antenna elements and beamformer	62
3.5.1	Cosine-shaped antenna pattern	63
3.5.2	Beam pattern of conventional beamformer	63
3.6	Impact analysis and illustrative examples	65
3.6.1	Impact analysis on the channel	65
3.6.2	Example one: a single directional element	66
3.6.3	Example two: conventional beamforming	68
3.6.4	Discussion	70
3.7	Conclusions	72
4	Wideband transmission and frequency-domain equalization	73
4.1	Introduction	73
4.2	Bandlimited transceiver system	74
4.3	Wideband transmission system model	78
4.4	Linear frequency-domain equalization and transmission performance	81
4.4.1	MMSE equalization and decision variables	81
4.4.2	Uncoded BER computation	84
4.4.3	Simulated BER performance	87
4.5	Synchronization and channel estimation	91
4.5.1	Training symbol design	91
4.5.2	Frequency offset	92
4.5.3	Symbol timing	96
4.5.4	Channel estimation error	99
4.6	Conclusions	102
5	Residual ISI cancellation for code-spreading systems	103
5.1	Introduction	103

5.2	Residual ISI cancellation	105
5.2.1	Receiver structure	106
5.2.2	Derivation of noise-predictive RISI canceller	108
5.2.3	Derivation of decision-directed RISI canceller	110
5.2.4	RISI cancellation with reduced-order filtering	111
5.2.5	Summary and discussion	113
5.3	Alternative implementation of the NP-HRC	114
5.3.1	RISI canceller in the FD	114
5.3.2	Derivation of the FD filter coefficients D_k	115
5.3.3	Significance of RISI filtering taps in the TD	117
5.4	Tentative detection and upper bound performance	118
5.4.1	Tentative detections	119
5.4.2	Ideal tentative decisions	120
5.4.3	Non-ideal tentative decisions	121
5.5	Simulation results	122
5.5.1	BER performance for ideal tentative decisions	122
5.5.2	BER performance for non-ideal tentative decisions	123
5.5.3	Comparison of implementation complexity	124
5.6	Conclusions	126
6	Quantization and RF impairments	127
6.1	Introduction	127
6.2	Influence of memoryless nonlinearity	129
6.2.1	Statistical model of nonlinearity	129
6.2.2	Influence on transmission performance	131
6.2.3	BER computation	134
6.3	D/A and A/D conversions	138
6.3.1	Modelling of the quantization process in DAC or ADC	139
6.3.2	BER performance	142
6.3.3	Summary and discussions	148
6.4	Nonlinear power amplification	149
6.4.1	Modelling of PA	150
6.4.2	BER performance	153
6.5	Phase noise	155
6.5.1	Modelling of phase noise	155
6.5.2	Influence on transmission performance	157
6.6	IQ imbalance	163
6.6.1	Amplitude and phase mismatch	163
6.6.2	Influence on transmission performance	165
6.7	Summary and conclusions	170
7	Baseline design of low-cost 60-GHz radios	173
7.1	Propagation channel and antenna effect	173
7.2	RF front-end and system architecture	175
7.2.1	Antennas and adaptive beamforming	176
7.2.2	RF architecture and impairments	177

7.2.3	Channelization	179
7.3	Transmission schemes and system design	180
7.4	Link budget design	182
7.5	Conclusions	184
8	Conclusions and future work	185
8.1	Summary and conclusions	185
8.2	Contributions of this thesis	188
8.3	Future work	188
A	Antennas and beamforming	191
A.1	Optimal antenna beamwidth	191
A.1.1	Uniform power angular spectrum in a sphere	191
A.1.2	Uniform PAS in the azimuth plane	191
A.2	Azimuth scan range and element beamwidth	193
B	Derivation of (4.49)	195
C	Differentiation involving complex vectors and matrices	197
D	Signal-to-distortion ratio at quantizer output	199
	Glossary	201
	References	205
	Author's publications	217
	Samenvatting	219
	Acknowledgements	221
	Curriculum vitae	223
	Index	224

Chapter 1

Introduction

1.1 Short-range gigabit radios at 60 GHz

After the first transatlantic wireless experiment in 1901, wireless communication systems are nowadays evolving at a fast pace, enabled by the underlying advances in the semiconductor and radio connectivity technologies. Today's wireless service and applications are widely available and accessible in large and small geographical areas. Specifically, wireless wide-area networks (WWAN) provide connectivity for regional-wide and city-wide access; wireless metropolitan area networks (WMAN) operate in the range of about 5 km; and wireless local-area networks (WLAN) are used for building-wide access. In the past decade, fast growing internet services and wide spread usage of electronic devices call for personalized wireless access and information exchange between devices, which drive the emergence of wireless personal-area networks (WPAN). Typical operational ranges and data rates for these wireless networks are illustrated in Fig. 1.1. WPAN technologies target at low-cost low-power applications within a short range up to tens of meters, while WLAN covers greater distances up to hundreds of meters, but requires more expensive hardware and higher power consumption.

Depending on the applications, the required data rates in WPANs vary significantly. Currently available WPAN technologies such as ZigBee and Bluetooth are mainly designed for low power and low data rate applications, such as wireless control and information exchange between devices. These technologies operate in the license-free industrial, scientific and medical (ISM) radio band, which is rather crowded and not suitable for high data throughput. For multimedia applications, especially video applications, broadband spectrum is required to support high data throughput, as high as several gigabit per second (Gb/s) [1]. One possible way is to use wireless USB based on ultra-wideband (UWB) technology, which operates in the 3.1 to 10.6

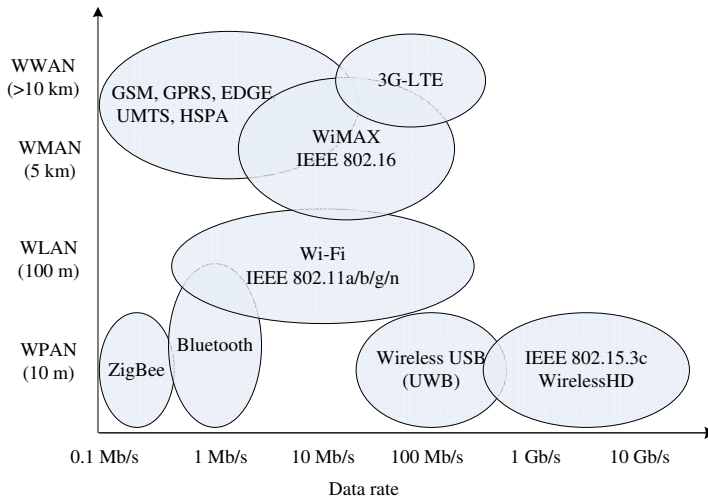


Fig. 1.1: Typical operational range and data rate for WLAN and WPAN standards and applications. Millimeter wave technologies at 60 GHz aim at multi-Gb/s in a short range.

GHz frequency range. However, wireless USB is only capable of sending 0.5 Gb/s, which can only support compressed video, and the required improvement will not be seen in a short future, due to restrictions on the transmitter power levels imposed by regulatory bodies.

The availability of broadband spectrum in the frequency band of 60 GHz provides a great opportunity for ultra-high data rate short-range wireless communications [2]. In addition, it is promising to provide the last mile in-building broadband connectivity by using radio-over-fiber (RoF) technologies [3], since the broadband spectrum at 60 GHz narrows down the bandwidth gap between the radio access and the fiber backbone. The 60 GHz spectrum has been or is being allocated worldwide for unlicensed use, as summarized in Table 1.1 for different regions and countries around the world. The spectral space of the allocated frequency band is up to 7 GHz with a common bandwidth of approximately 3.5 GHz. The main reason for this allocation is the occurrence of a severe absorption attenuation of the waves by oxygen molecules in the atmosphere (10 – 15 dB/km). Also listed in Table 1.1 are the effective isotropic radiated powers (EIRP) allowed in different countries and regions. The allowed EIRP is within the range of 40 and 50 dBm in most countries. In Australia, China and Japan, the allowed total peak transmitter power into the antenna is 10 dBm. Particularly in Japan, the maximum allowed antenna gain is 47 dBi and the maximum transmission bandwidth must not exceed 2.5 GHz. Compared with other WLAN and WPAN standards in the lower frequency bands, e.g. the maximum permitted EIRP is 20 dBm at 2 GHz in Europe, 60-GHz regulation allows much higher transmit power, which is necessary to overcome the higher path loss at 60 GHz.

Besides the local regulatory requirements on the 60-GHz radios, several industrial standardization bodies are making efforts to develop standards for the 60-GHz WPAN.

Table 1.1: Spectrum allocation and emission power requirements of 60-GHz radios around the world [4–6].

Region	Frequency	EIRP
Australia	59.4 – 62.9 GHz	51.8 dBm
Canada/USA	57 – 64 GHz	40 – 43 dBm
China	59 – 64 GHz	44 – 47 dBm
Europe	59 – 66 GHz	40 dBm
Japan	59 – 66 GHz	10 dBm/47 dBi
Korea	57 – 64 GHz	40 – 43 dBm

The IEEE 802.15.3 Task Group 3c (TG3c) was formed in March 2005 to develop a millimeter-wave-based alternative physical layer (PHY) for the existing 802.15.3 WPAN standard 802.15.3-2003 [4]. The proposed standard will allow a mandatory data rate of 2 Gb/s and an optional data rate of 3 Gb/s. In addition, many industrial partners have joined together to form WirelessHD or WiHDTM, an industry-led effort to define a specification for the next generation wireless digital network interface for consumer electronics products [1]. Specifically, WirelessHD has set a goal of enabling wireless connectivity operating at 60 GHz for streaming high-definition contents between source devices and high-definition displays, where the target data rates for the first generation products are 2 to 5 Gb/s. Besides TG3c and WirelessHD, the industry association ECMA International also started recently to develop a 60 GHz PHY and media access control (MAC) for short-range wireless applications [7], which will support a data rate up to 5 Gb/s as well.

The 60-GHz gigabit WPAN systems are suitable for numerous short-range applications in residential areas, conference rooms, offices, etc. Typical applications include wireless gigabit Ethernet, wireless high-speed download, wireless streaming of high definition video, etc [8]. In particular, wireless video streaming is one of the most attractive applications and the required data rates vary from 0.5 Gb/s to 5 Gb/s, depending on the video format and whether it is compressed or not compressed.

1.2 Challenges in designing low-cost 60-GHz radios

Despite the great opportunity of deploying gigabit wireless devices at 60 GHz, the huge data throughput and the ultra-high carrier frequency give rise to serious challenges for the low-cost radio design. The challenges involve the aspects of channel propagation issues, baseband modulation schemes, antennas and integrated circuit technologies. These aspects are strongly related when aiming at a low-cost system design. In the following, we address the general concerns and issues regarding these aspects.

Channel propagation and antenna effect

The propagation path loss at 60 GHz is significantly higher than those at lower frequencies and results in a stringent link budget. For instance, the free space loss at 60 GHz is about 20 and 30 dB higher than those at 5 and 2 GHz, respectively. Besides the severe propagation loss, there is a high penetration loss, as high as tens of dBs, through construction materials, which limits the typical 60-GHz radios to be within the range of 10 meters in a single room [2]. Additionally, a large amount of scattered waves propagating in a room can result in a highly dispersive channel in time.

Concerning the limited link budget and severe multipath dispersion, a high gain antenna is preferred to support reliable transmission at 60 GHz. Due to the short wavelength at 60 GHz, antenna gain can be conveniently achieved by using multiple antennas in combination with adaptive beamforming techniques. By this narrow-beam antenna configuration, the Doppler effect at 60 GHz, which is a priori 30 times severe than at 2 GHz, can be significantly suppressed as well. On the other hand, the narrow-beam configuration makes the gigabit communication link in the air very sensitive to beam obstructions and beam pointing errors, because of the poor diffraction feature. When the beams are blocked by a human body, for instance, the signal could be completely lost. In such a case, measures need to be taken, e.g. adapting the beam pointing directions at a sufficiently fast speed, in order to avoid a serious disruption of the communication link. The beam pointing errors can be caused by, for instance, limited bit resolutions of RF phase shifters and tend to worsen the channel condition.

Regarding the poor diffraction properties of the 60-GHz waves, broad-beam or omnidirectional antennas might be used in some applications where a full coverage is required, by taking advantage of rich reflections in indoor environments. By these configurations, the system becomes less vulnerable to obstructions of objects. However, the resulting multipath time dispersion will cause severe inter-symbol interference (ISI), especially for multi-Gb/s transmission. In such a case, advanced baseband signal processing techniques, such as ISI cancellation techniques or multiple-input and multiple-output (MIMO) techniques, may be used to fully explore the power contributed by multiple propagation paths.

For low-cost gigabit 60-GHz radios, antenna configurations and the corresponding radio channel properties have significant impacts on the selection of modulation schemes and the optimization of baseband processing. Therefore, characterization of the channel propagation and antenna effect is an important step prior to the system design.

Antennas and RF beamforming

As mentioned earlier, antenna arrays can be used to achieve a sufficient link budget, by performing adaptive beamforming, at both transmitter (TX) and receiver (RX) side. Because the wavelengths are so short, it is possible to implement many antennas on a small area of printed circuit board (PCB). For the purpose of low-cost applications,

such an antenna array should be low cost and power efficient, and should have a sufficient bandwidth and directivity. The challenge of designing such an antenna array is to have a good match and integration between the antennas and RF front-end circuits, including power amplifier (PA) and low noise amplifier (LNA), such that the reflection loss, caused by the balanced antenna feed, is as small as possible. In addition, implementing a larger phase array is also challenging because of the more complex phase control network, the higher feed network loss and stronger coupling between antennas as well as feed lines, etc.

With multiple antennas in combination with RF phase shifters, RF beamforming can be carried out in the RF stage. The control signals for the beamforming, including variable gains and phase shifts, are calculated in the baseband and fed back to the RF stage. It is obvious that the RF beamforming only requires one mixer and one digital-to-analog (D/A) or analog-to-digital (A/D) converter (DAC or ADC) for each in-phase/quadrature branch. This is quite advantageous over digital beamforming, in which a number of the conversion devices are necessary and a significant amount of data throughput introduces a heavy burden to the baseband processor. Therefore, RF beamforming is a particularly effective way to reduce the power consumption and fabrication costs of the whole system, since DAC/ADC and baseband processor are among the most power consuming units in a transceiver [9]. Another advantage of applying RF beamforming is that analog signals have a wider dynamic range, compared with digital signals as in digital beamforming which suffer from quantization errors, though more elaborate algorithms can be used in digital beamforming.

Device and circuitry technologies

The 60-GHz RF technologies have been traditionally based on III-V compound materials, such as gallium arsenide (GaAs) and indium phosphide (InP). Despite their outstanding performance, these technologies are expensive and have a limited capability for low-cost chip-scale packaging. The recent progress in semiconductor technologies based on silicon, such as silicon germanium (SiGe) and baseline complementary metal-oxide semiconductor (CMOS) technologies, has provided new options for the low-cost 60-GHz RF front-end with considerable RF performance and remarkable integration levels [10, 11]. CMOS is particularly more attractive for its potential of integration with analog devices and baseband digital signal processing (DSP) functions, enabling true systems-on-chip [12]. Successful CMOS implementation of the key RF building blocks operational at 60 GHz, such as PA, LNA, mixers, local oscillators (LO), frequency synthesizers, etc. has been reported, e.g. in [12–15]. The high level of integration for CMOS 60-GHz RF front-ends was demonstrated in [15–18]. In particular, the direct-conversion architecture is a promising solution for the low-cost and low-power implementation of 60-GHz RF front-ends [16, 17]. As CMOS circuitry continues to scale down, the analog and RF blocks suffer from large variations over process, voltage and temperature, and the resulting “dirty effects”, such as nonlinear distortion, phase noise and I-Q imbalance, give rise to a serious performance loss [19].

Besides the RF front-ends, wireless digital communications at 60 GHz requires DAC

and ADC devices to convert the signal with a sufficient bit resolution and to operate at over twice the Nyquist rate of the signal. With the speed of several Gb/s, the DAC and ADC devices become difficult to realize and are some of the most power consuming components. In spite of the steady progress in sampling rate and power reduction in the past decade, the bit resolution falls off by about 1 bit for every doubling of the sampling rate [20–23]. With the reduced resolution, however, the signal distortion at the DAC/ADC output will become serious and eventually limit the system performance.

The severe signal distortion and impairments caused by both the dirty RF and the limited bit resolution of DAC and ADC may be largely absorbed by the baseband section, e.g. by applying appropriate baseband modulation schemes and digital compensation techniques [19]. Combating the dirty RF by the baseband optimization is a paradigm shift of the conventional design approach that keeps the analog problem domain largely separated from the digital processing domain. The new paradigm allows a low-cost implementation of wireless devices, such as low-cost 60-GHz radios, which operate at high carrier frequencies with large transmission bandwidths.

Transmission schemes

Although the high path loss and severe multipath dispersion of 60-GHz wave propagation can be largely resolved by using narrow-beam antenna configurations, the wideband transmission of gigabit radios calls for a reliable demodulation and signal detection at receiver. In addition, it is expected that a low-cost 60-GHz RF front-end based on e.g. CMOS technologies will cause severe impairments, such as phase noise, nonlinearity, I-Q imbalance, etc. Therefore, baseband modulation schemes have to be carefully designed and baseband algorithms might be needed to compensate the signal attenuation caused by the channel dispersion and the severe RF impairments.

With the several GHz bandwidth available at 60 GHz, it is possible to use constant envelope modulations to minimize the requirements on the RF front-end at the data throughput of several Gb/s. However, the low spectrum efficiency of these modulations would not allow multiple devices operational at the same time, for instance for the personal usage of video systems and downloading devices at home. Besides, these modulation options are not a long term solution for 60-GHz radios with the ever increasing demand on data speed. Other options are to use linear modulations in combination with wideband transmission schemes such as orthogonal frequency division multiplexing (OFDM). Although linear modulations suffer from performance loss under the effect of nonlinearities, they are necessary for achieving high spectrum efficiency. In these wideband transmission schemes, low-complexity frequency domain equalization (FDE) can be conveniently performed at receiver using the fast Fourier transform (FFT). In addition, wideband transmission systems are more scalable for different scenarios and compatible with the currently used WLAN systems.

In general, wideband transmission schemes are divided into two categories: multi-carrier transmission, such as OFDM and multi-carrier code division multiple access

(MC-CDMA), and single-carrier transmission schemes, such as single-carrier transmission with FDE (SC-FDE). It is well known that OFDM suffers larger impairments from RF nonlinearities than single-carrier transmissions, due to higher peak-to-average ratios (PAPRs) of multi-carrier signals. MC-CDMA is based on OFDM and has the same high PAPR, but is essentially different from OFDM in that frequency diversity is inherently utilized. In comparison, it is generally needed for OFDM to use coding schemes to achieve the frequency diversity gain. The frequency diversity is inherently utilized in SC-FDE as well, but single-carrier signals have a much lower PAPR compared with multi-carrier signals. Therefore, the three schemes will have different performance under the influences of RF impairments. For low-cost 60-GHz radios, a comprehensive comparison of these schemes is needed with respect to the particular channel properties and RF impairments at 60 GHz.

1.3 Framework, objectives and related projects

The work presented in this thesis was mainly carried out within the framework of the “*Foundations of Wireless Communication*” (WiComm) project, which is part of the Dutch national research programme Freeband Communications in the period of 2004 - 2008 [24]. The Freeband Communication programme is managed by the Telematica Instituut and has the goal of creating a leading knowledge position for the Netherlands in the area of ambient and intelligent communication. The WiComm project brought together a consortium of industrial and academic partners, i.e., TNO Defense Security and Safety (TNO-D&V), Philips, Delft University of Technology, Eindhoven University of Technology and Twente University, and is aimed at integrating wireless systems on silicon for low-power and broadband applications. The project consists of three work packages WP1, WP2 and WP3. In WP1, antenna designs and RF front-end interface for both low and high radio frequencies are the main concerns. WP2 covers the design of baseband modulation and RF building blocks for short-range applications at 60 GHz. WP3 focuses on ultra low-power radio designs regarding different scenarios, including highly integrated single-chip radios, flexible software-defined radios and single-chip IC design in different frequency bands.

As part of WP2, the work presented in this thesis is intended to contribute to the *low-cost system design* of 60-GHz digital radios and mainly focuses on channel characterization and baseband optimization. Multiple standardization activities grow rapidly worldwide for the 60-GHz gigabit multimedia applications. Therefore, the presented work in this thesis is not particularly oriented to a specific standard and we are supposed to contribute with our research work to the ongoing standardizations.

To allow mass market production of low-cost and high-performance gigabit 60-GHz transceivers, the system design needs to take into account the particular properties of the 60-GHz channel, antennas and RF front-end. To support the ultra-high data throughput, wideband transmission schemes, e.g. OFDM, MC-CDMA and SC-FDE, are promising candidates due to the beneficial feature of efficient equalization and detection at receiver. Therefore, the main objectives of this thesis are:

- characterization of antenna effect and channel propagation in the frequency band of 60-GHz,
- performance evaluation of quantization and RF impairments on potential wideband transmission schemes, applicable in the context of 60-GHz radios,
- development of high performance baseband algorithms suitable for low-cost and low-power 60-GHz radio designs.

In addition to WiComm, there have been two other national projects related to the work presented in this thesis. The first one is the “*B4 Broadband Radio@Hand*” (BR@H) project (2001-2005), which focused on joint research on broadband telecommunication technology, especially on MIMO-OFDM algorithms and 3G mobile systems. Part of the 60-GHz channel measurements in Chapter 2 was conducted within the BR@H project. The second one is the project of “*60 GHz radio technology for high-capacity wireless in-home communication networks*” (SiGi-Spot) supported by SenterNovem through its IOP GenCom programme for the period of 2005-2009. As a complementary project to WiComm, SiGi-Spot mainly focuses on low-cost antenna array solutions, CMOS design of analog beam steering and the direct-conversion transceiver architecture, modulation and coding suitable for adaptive beamforming and MAC layer protocol design. Since some partners in SiGi-Spot are also involved in WiComm, there are close liaisons and cooperations between the two projects.

1.4 Outline and contributions

The structure of the thesis is schematically depicted in Fig. 1.2. Different aspects of system design for 60-GHz radios are individually treated in Chapter 2, 3, 4, 5 and 6. Based on the overall consideration of these aspects, a baseline system design is addressed in Chapter 7. Each one of these chapters, except Chapter 7, stands for a relatively independent topic and can be read on its own. The background information of each topic is given in the introduction of each chapter. In the following, we provide a short summary of individual chapters and their contributions.

At first, *channel characteristics and antenna effects* will be considered in Chapter 2 and 3, respectively. Based on extensive measurements and simulations, Chapter 2 presents the wave characteristics and propagation models for 60-GHz channels with various antenna configurations. In Chapter 3, the influences of directional antennas and multi-antenna beamformers on radio transmission are analytically formulated. Specific scenarios are considered to support the formulation and part of the results obtained in Chapter 2.

Next, potential *wideband transmission schemes* for 60-GHz radios are treated in Chapter 4 and 5, describing signal detection and relevant baseband algorithms development in linear Rician fading channels. In detail, Chapter 4 presents the system models of OFDM, SC-FDE and MC-CDMA, and deals with linear channel equalization and performance evaluation in linear Rician fading channels. Also concerned in this chap-

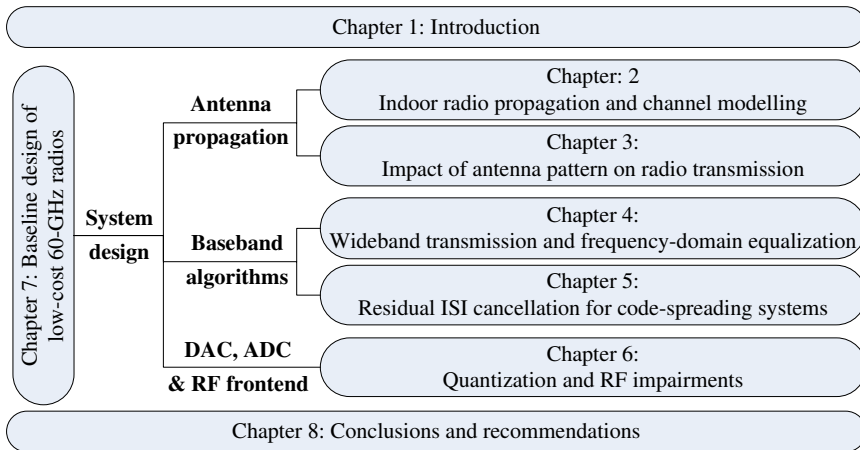


Fig. 1.2: Structure of the thesis.

ter are some implementation issues, such as synchronization and channel estimation. In Chapter 5, a low-complexity ISI cancellation technique is proposed to achieve a much better performance than by using linear equalization techniques for a class of code-spreading schemes, such as SC-FDE and MC-CDMA.

The influences of *DAC*, *ADC* and *RF impairments* on the considered transmission schemes and possible *digital compensation* in baseband are investigated in Chapter 6. Both LOS and NLOS channel conditions are concerned for the performance evaluation. This chapter consists of two parts. In the first part of the chapter, the signal distortions caused by DAC, ADC and nonlinear amplification are deterministically and statistically modelled. Based on the models, optimal linear channel equalization and signal detection are studied, and BER expressions are derived to evaluate the performance of the considered wideband systems under the influence of nonlinear distortions. The second part treats the influences of phase noise and IQ imbalance, occurring in the RF front-ends at both the TX and RX side, on wideband transmission. Computer simulations are conducted to evaluate the BER performance with and without applying digital compensation techniques in the baseband.

Based on the overall considerations of channel propagation, baseband modulations, antennas and RF front-ends, a *baseline design* of low-cost multi-Gb/s 60-GHz radios is addressed in Chapter 7. Link budget calculations are performed to evaluate the feasibility of single- and multi-carrier transmission schemes as regards the considered baseline system configuration.

Finally, Chapter 8 summarizes the results and main conclusions of the work and provides a perspective for the future work.

The main contributions of the work presented in this thesis are listed as follows:

- *Characteristics and modelling of 60-GHz radio channels* in the considered LOS

and *NLOS* environments are derived from measured results in Chapter 2 for both *narrow-beam* and *omnidirectional* antenna configurations. In addition, the channel properties in the frequency bands of 2 and 60 GHz are compared to reveal some particular features of 60-GHz channels in room environments, as regards *shadowing path loss* and *time dispersion*.

- Simulations of various antenna polarization schemes in Chapter 2 reveal that *circularly-polarized schemes provide little benefit on the wideband transmission* of 60-GHz radios, as regards path loss and channel fading levels. Also, 3D ray tracing results confirm the significance of time dispersion reduction by using directional antennas.
- The *influences of antenna directivity* on wireless transmission in double-directional channels are systematically formulated and analyzed in Chapter 3. The influences on both multipath time dispersion and the received power level are included in the formulation. The theoretical analysis of the influence on time dispersion is the first time considered in literature. Also considered in the formulation is the *influence of beam pointing errors*. The obtained results are applicable not only to 60-GHz radios, but also to wireless transmission in other frequency bands.
- Explicit *BER expressions* of OFDM, MC-CDMA and SC-FDE under *Rician fading channel conditions* are derived in Chapter 4 within the same framework. Later in Chapter 6, BER expressions are also derived for systems affected by *nonlinear distortions*, including quantization and clipping caused by DAC and ADC. The computed BERs have good agreement with the simulated BERs.
- A signal processing technique is proposed in Chapter 5 to cancel the *residual ISI* occurring in a class of code-spreading schemes (e.g. SC-FDE), such that a better detection performance is achieved. Explicit derivation of filter coefficients in the scheme allows a linear channel equalizer and an interference canceller fully implemented in the frequency domain, resulting in a low complexity for channel equalization. Both theoretical analysis and simulations demonstrate that the proposed scheme has great advantages, as regards both complexity and performance, over the existing decision-feedback equalization schemes and reduced-order cancellation schemes.
- In Chapter 4 and 6, comprehensive *comparisons of single- and multi-carrier transmissions* are performed and supported by extensive theoretical and simulation results, with and without taking into account *DAC/ADC, nonlinear amplification, phase noise* and *I-Q imbalance*, with and without applying *digital compensation* techniques at receiver. The comprehensive comparisons are insightful for the overall considerations on the selection of transmission schemes.
- The *baseline design* of low-cost 60-GHz radios in Chapter 7 leads to the conclusion that by using *narrow-beam antennas* in combination with *RF beamforming*, a data rate in the order of 2 Gb/s can be achieved over a distance of 10 meters in a typical NLOS indoor scenario.

Indoor radio propagation and channel modelling

2.1 Introduction

Understanding and modelling of radio wave propagation are fundamental issues for designing wireless transceiver systems. For low-cost 60-GHz radios, a significant challenge is to achieve a sufficient signal strength, when compared with conventional systems deployed at lower frequency bands, e.g. 2 GHz. The main reasons for this are the much lower performance of the low-cost RF front-end and the much higher channel propagation loss. Fortunately, antenna gains can be achieved by applying multi-antenna beam steering at both transmitter (TX) and receiver (RX) sides to compensate the lower RF performance and the higher propagation loss. Therefore, prior to the design of low-cost 60-GHz radios, it is of utmost importance to study the characteristics of wave propagation at 60 GHz and the influence of directional antenna configurations on the propagation.

In order to separate the influence of antennas and the wave propagation itself, we distinguish between the *propagation channel* and the *radio channel* [25], as schematically illustrated in Fig. 2.1. The former is described by the double-directional channel response, which is characterized by the direction of departure (DOD), direction of arrival (DOA) and channel delay, excluding both the TX and RX antennas. The latter is described by the non-directional channel response with the antenna effect included. In general, it is difficult to have a reliable modelling of the pure propagation channels based on channel sounding techniques, since the antenna effect can not be clearly separated from the wave propagation. In comparison, deterministic channel simulations based on three-dimensional (3D) ray tracing tools are convenient for the modelling of propagation channels.

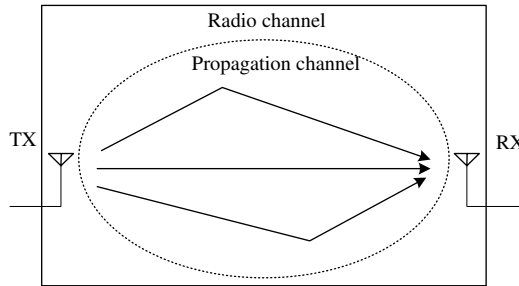


Fig. 2.1: The distinction between the radio channel and the propagation channel.

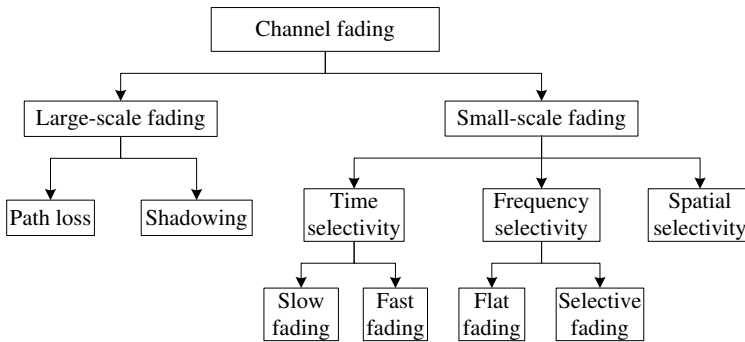


Fig. 2.2: Types of channel fading.

Channel models are divided into two groups: *narrowband* and *wideband* channel models, which are defined in connection with the narrowband and wideband communication systems, respectively [26]. A system is said to be narrowband, when the inverse of the system bandwidth is larger than the time span of the channel impulse response, and narrowband models apply. Otherwise, it is said to be a wideband system and wideband models apply. In narrowband channel models, multipath components are combined into one signal with random amplitude and phase, since no multipath components can be distinguished by the receiver. In wideband models, multipath components are grouped into bins and the time resolution of the bin is determined by the receiver bandwidth.

In a typical radio environment, the field strength of the received signal fluctuates due to the multipath propagation of the transmit signal. The fluctuations are called *channel fading* and characterized in various aspects, which are schematically listed in Fig. 2.2. On a very-short-distance scale in the order of a wavelength, the fluctuations are called *small-scale fading*. The mean of the field strength over the distance of a number of wavelengths shows fluctuations as well. But these fluctuations occur on a large scale, typically over hundreds of wavelengths, and are referred to as *large-scale fading*. Large-scale fading is caused by the shadowing of main objects in the propaga-

tion environment, and can be characterized by path loss and shadowing loss [26, 27]. Small-scale fading is characterized by three aspects of a channel: *time selectivity*, *frequency selectivity* and *spatial selectivity*. Time selectivity of the channel is caused by the Doppler effect and in this respect, the channel is classified either as a *fast fading channel* or *slow fading channel*, depending on how rapidly the channel changes compared with the data rate. Frequency selectivity is due to the multipath time dispersion of the transmit signal within the channel, and the channel is classified either as *flat fading* or *frequency selective fading*, depending on how large is the channel coherence bandwidth compared with the applied signal bandwidth. Spatial selectivity of the channel is caused by multipaths arriving from many different directions in space and is often characterized by the power angular spectrum [28].

The purpose of this chapter is to investigate the 60-GHz channel characteristics based on extensive channel measurements and simulations. The influence of directional antennas and multi-antenna beamformers on wave propagation will be analytically formulated and studied in Chapter 3. The outline of this chapter is as follows. In Section 2.2, an overview of the generic theory of wideband channel propagation is presented as the basics for the other sections and as well as the rest of the thesis. In Section 2.3, radio channel measurements and the obtained results at 60 GHz will be reported in indoor environments for various antenna configurations. Next in Section 2.4, the effects of multipath propagation on the received power and the time dispersion property are compared in the frequency bands of 2 and 60 GHz. In Section 2.5, multipath propagation channels in both time and angular domains are studied based on three-dimensional ray tracing simulations. In addition, various antenna polarization schemes will be studied as regards large- and small-scale fading. Lastly the results and conclusions will be summarized in Section 2.6.

2.2 Wideband fading channel

2.2.1 Free space transmission model

The free space path loss model is used to predict the received signal strength when the transmitter and receiver have only one unobstructed line-of-sight (LOS) path between them. If d represents the TX-RX separation distance and f represents the carrier frequency of the propagating wave, the free space power received by a receiving antenna is given by the Friss transmission equation [29]

$$P_R(d) = \frac{G_T G_R P_T}{(4\pi f d / c)^2}, \quad (2.1)$$

where $c = 3 \times 10^8$ m/s is the speed of light, P_T is the transmitted power at the input of the TX antenna, G_T and G_R represent the TX and RX antenna gains, respectively. For fixed antenna gains, the equation (2.1) means that the received signal level reduces with frequency and distance. The path loss in free space is defined

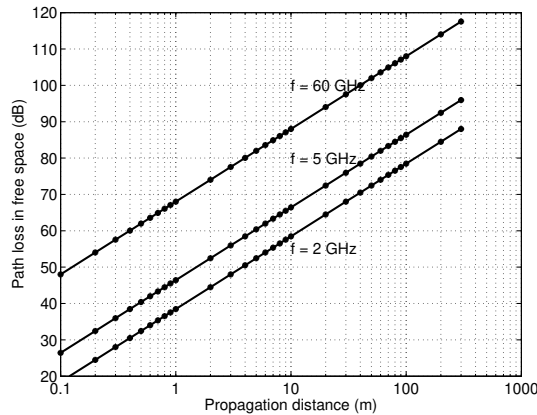


Fig. 2.3: Path loss in free space versus propagation distance for carrier frequencies at $f = 2, 5$ and 60 GHz.

as the ratio between the TX antenna output power and the RX antenna input power at the antenna outputs, i.e. $PL = P_T G_T G_R / P_R$, which can be described by

$$PL_{\text{fs[dB]}}(d) = 20 \log_{10} \left(\frac{4\pi f d}{c} \right) \quad (2.2)$$

in dB. The free space path loss depends on the carrier frequency and the antenna separation. For instance, Fig. 2.3 depicts the path loss versus the propagation distance in free space at carrier frequency $f = 2, 5$ and 60 GHz. It is clear from the figure that the path loss at 60 GHz is 29.5 and 21.6 dB higher than at 2 and 5 GHz, respectively. Such a high path loss is often seen as one of the limiting factors for the 60-GHz radio design because of the tight link budget. Fortunately, the high path loss at 60 GHz can be compensated by increasing the antenna gains. The antenna gain G of an antenna is related to its aperture size S and frequency f by

$$G = \frac{4\pi S f^2}{c^2}. \quad (2.3)$$

From (2.3) and (2.1), we see that for the same aperture size, the received power is improved actually at the higher frequency because of the large antenna gain. For 60-GHz applications, for instance, the antenna gain can be achieved by using antenna arrays at both TX and RX sides.

2.2.2 Log-distance model

In a typical radio environment, multiple propagation paths exist and will contribute to the total received power. For example in an indoor environment, propagation is often affected by reflections and attenuations caused by walls, floors, furniture, people, etc. For purpose of link budget calculations, a log-distance model is widely used to

characterize the path loss [26]. At a separation distance d from a transmitter, the received power in dBm is given by

$$P_R(d)_{[\text{dBm}]} = P_T[\text{dBm}] + G_T[\text{dB}] + G_R[\text{dB}] - PL_{[\text{dB}]}(d). \quad (2.4)$$

Here the path loss is commonly modelled over the logarithm of the distance [30] and given by

$$PL(d)_{[\text{dB}]} = PL_{d_0[\text{dB}]} + 10 \cdot n \cdot \log_{10} \left(\frac{d}{d_0} \right) + X_{\Omega[\text{dB}]} \quad (d \geq d_0), \quad (2.5)$$

where PL_{d_0} gives the reference path loss at d_0 m, n is the loss exponent and X_{Ω} denotes a zero mean random variable with a standard deviation $\Omega[\text{dB}]$. As will be seen later in this chapter, the loss exponent varies significantly depending on the antenna configurations and the channel environments. The standard deviation statistically describes the variation of the path loss with respect to the mean path loss. Particularly, in a non-line-of-sight (NLOS) propagation environment, the deviation is referred to as the *shadowing* caused by obstacles with values depending on the severity of shadow fading. Mostly, the model parameters in (2.5) are empirically derived by linearly fitting the measured path loss in dB over log-distance.

2.2.3 Channel impulse response

Consider a wireless channel $h(t, \tau)$ which relates the input signal $u(t)$ and output signal $r(t)$ of the channel by [31]

$$r(t) = \int_0^{\infty} u(t - \tau)h(t, \tau)d\tau. \quad (2.6)$$

The impulse response $h(t, \tau)$ characterizes the amplitude and phase attenuation of the transmit signal caused by the channel at the time $(t - \tau)$. For a wideband transmission system, the impulse response of the channel is modelled as a direct or strong specular path plus L independent channel paths and can be expressed by

$$h(t, \tau) = h_0(t)\delta(\tau - \tau_0) + \sum_{l=1}^L h_l(t)\delta(\tau - \tau_l), \quad (2.7)$$

where $h_0(t)$ is the complex amplitude of the direct or dominant specular path, the parameters $L, h_l(t)$ and τ_l represent the number of multiple paths, the complex amplitude and arrival-time of the l th path, respectively. The time dependency of the channel is introduced by arbitrary movements of the transmitter, the receiver or other objects in the environment. For such a channel, the received signal (2.6) becomes

$$r(t) = h_0(t)u(t - \tau_0) + \sum_{l=1}^L h_l(t)u(t - \tau_l). \quad (2.8)$$

For a Rician fading channel, the direct path $h_0 \neq 0$ and does not change over time, other paths $\{h_l\}$ with $l = 1, \dots, L$ follow complex Gaussian distributions with zero mean and are independent from each other¹. Therefore, both the in-phase and quadrature components of the received signal $r(t)$ can be interpreted as the sum of many independent signals. According to the central-limit theorem, both the in-phase and quadrature components follow non-zero Gaussian distributions with the same variance. As a result, the magnitude $|r(t)|$ follows a Rician distribution. The Rician fading channel can be characterized by the Rician K -factor, which describes the dominance of the direct/specular path as compared with all the other paths. The Rician K -factor is defined as the ratio between the powers contributed by the direct/specular path and the scattered paths, i.e.

$$K = \frac{\mathbb{E}\{|h_0|^2\}}{\mathbb{E}\left\{\sum_{l=1}^L |h_l(t)|^2\right\}}, \quad (2.9)$$

where $\mathbb{E}\{\cdot\}$ denotes the mathematical expectation over time. In case that the Rician factor $K = 0$, i.e. the specular path disappears, the signal magnitude $|r(t)|$ becomes Rayleigh distributed and the channel is called Rayleigh fading channel.

The channel statistics are assumed to be *wide-sense stationary* (WSS) within the time duration of one transmitted symbol or one data packet. In addition, signals coming via different paths will experience uncorrelated attenuations, phase shifts and time delays, which is referred to as *uncorrelated scattering* (US). The assumption of WSS and US (WSSUS) for physical channels has been experimentally confirmed and widely accepted in literature [28, 31, 32, 34–36]. In particular, the WSSUS assumption for millimeter-wave propagation was confirmed in [35, 36]. Under the WSSUS assumption, the autocorrelation of the complex impulse response $h(t, \tau)$ will satisfy

$$\begin{aligned} \mathcal{R}_h(\Delta t; \tau_1, \tau_2) &= \frac{\mathbb{E}\{h^*(t, \tau_1)h(t + \Delta t, \tau_2)\}}{\sqrt{\mathbb{E}\{|h^*(t, \tau_1)|^2\} \mathbb{E}\{|h(t + \Delta t, \tau_2)|^2\}}} \\ &= \mathcal{R}_h(\Delta t, \tau_1)\delta(\tau_2 - \tau_1), \end{aligned} \quad (2.10)$$

where $*$ stands for conjugate. Furthermore, the average power delay profile (PDP) of the channel is defined as the autocorrelation function when $\Delta t = 0$

$$P(\tau) = \mathbb{E}\{|h(t, \tau)|^2\} = \mathbb{E}\left\{\sum_{l=0}^L |h_l(t)|^2 \delta(\tau - \tau_l)\right\}, \quad (2.11)$$

which is the average of impulse responses in a local area. From the average PDP, the root-mean-squared (RMS) delay spread σ_τ can be defined by

$$\sigma_\tau = \sqrt{\sum_{l=0}^L P(\tau_l)(\tau_l - \bar{\tau})^2} \quad (2.12)$$

¹In other words, the magnitude $|h_l|$ for $l = 1, \dots, L$ follows a Rayleigh distribution. The assumption of Rayleigh fading for the non-specular paths is supported by the indoor channel measurements given in [32, 33].

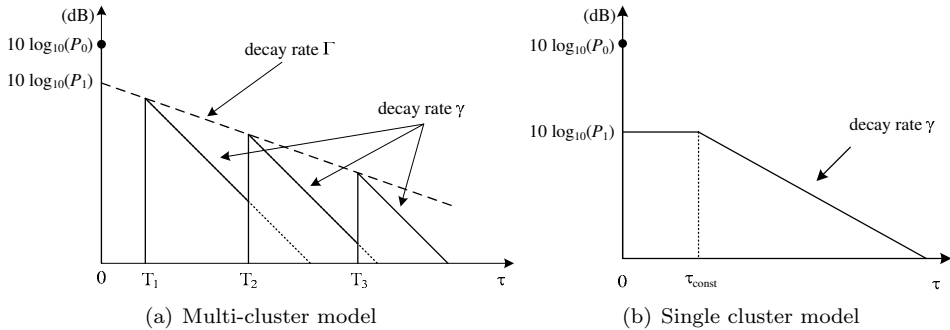


Fig. 2.4: single- and multi-cluster models of power delay profile.

with the mean excess delay $\bar{\tau} = \sum_{l=0}^L \tau_l P(\tau_l)$, where it is assumed that the channel power is normalized, i.e. $\mathbb{E} \left\{ \sum_{l=0}^L |h_l(t)|^2 \right\} = 1$. RMS delay spread is generally used to characterize the multipath time dispersion of the channel.

2.2.3.1 Shape of power delay profiles

The influence of the environment on the channel can be noticed in the PDP as defined in (2.11), which describes the span of the received signal over arriving time when a Dirac-delta impulse is transmitted. In a local area within a range of tens of wavelengths, cluster-wise arrival behavior of scattered waves has been observed from measurements and the average PDP is formulated by multi-cluster models [37–39]. The clusters are attenuated in amplitude along time and the waves in each cluster decays along time as well. The often used multi-cluster model is based on the Saleh-Valenzuela (SV) model in [37] and follows a double exponential decaying law (see a sketch in Fig. 2.4(a)). For such a model, the average PDP is expressed by

$$P(\tau) = P_0 \delta(\tau) + \sum_{k=1}^{\mathcal{K}} \sum_{l=1}^{L_k} P_1 e^{-\Gamma T_k} e^{-\gamma \tau_{k,l}} \delta(\tau - T_k - \tau_{k,l}), \quad (2.13)$$

where $P_0 = \mathbb{E}\{|h_0|^2\}$ is the average power of the LOS path with zero delay, $P_1 e^{-\Gamma T_1}$ is the average power of the first arrival of the first cluster, \mathcal{K} is the number of clusters, L_k is the number of scattered waves in the k th cluster associated with the cluster arrival time T_k , and $\tau_{k,l}$ is the time delay of the l th scattered wave in the k th cluster. The parameters Γ and γ characterize the signal decay rates of inter-clusters and each cluster, respectively. Note that the SV cluster model (2.13) is generally used to describe a channel without any antenna effect. This model can be extended by including the angular information of the channel into the model as well [38, 39].

In a global area such as a room environment, the average PDP is very likely to show a single cluster, which is exponentially decaying over delay, in addition to the LOS path [40, 41]. If the antenna effect is taken into account in this single cluster model, a more

Table 2.1: Relation between model and channel parameters when the shape parameter s is known for the single cluster model (2.14) (from [42]).

model \rightarrow channel		channel \rightarrow model	
$s = \tau_{\text{const}}\gamma \in [0, \infty)$	$s = 0$	$s = \tau_{\text{const}}\gamma$	$s = 0$
$P = P_0 + \frac{P_1}{\gamma}s_1$	$P = P_0 + \frac{P_1}{\gamma}$	$P_0 = \frac{KP}{K+1}$	$P_0 = \frac{KP}{K+1}$
$K = \frac{P_0\gamma}{P_1s_1}$	$K = \frac{P_0\gamma}{P_1}$	$\gamma = \frac{1}{\sigma_\tau} \sqrt{\frac{1}{K+1} \frac{s_3}{s_1} - \frac{1}{(K+1)^2} \frac{s_2^2}{s_1^2}}$	$\gamma = \frac{1}{\sigma_\tau} \frac{\sqrt{2K+1}}{K+1}$
$\sigma_\tau = \frac{1}{\gamma} \sqrt{\frac{1}{K+1} \frac{s_3}{s_1} - \frac{1}{(K+1)^2} \frac{s_2^2}{s_1^2}}$	$\sigma_\tau = \frac{1}{\gamma} \frac{\sqrt{2K+1}}{K+1}$	$P_1 = \frac{P}{K+1} \frac{\gamma}{s_1}$	$P_1 = \frac{P}{K+1} \gamma$

or less constant-level part might appear before the decaying part, which is caused by the elevation dependence of antenna radiation patterns and the antenna beam misalignment between the TX antenna and the RX antenna [41] (see Fig. 2.4(b)). The single cluster model with a constant part was first proposed in [41] and further developed in [42]. Mathematically, the PDP shape of a Rician channel is modelled by

$$P(\tau) = \begin{cases} 0 & \tau < 0 \\ P_0\delta(\tau) & \tau = 0 \\ P_1 & 0 < \tau \leq \tau_{\text{const}} \\ P_1 \cdot e^{-\gamma(\tau - \tau_{\text{const}})} & \tau > \tau_{\text{const}} \end{cases} \quad (2.14)$$

where $\sqrt{P_1}$ is the amplitude of the constant part with duration τ_{const} and γ is the decay exponent. When the constant part disappears, i.e. $\tau_{\text{const}} = 0$, it becomes the commonly applied exponentially decaying channel model. Letting $P_0 = 0$, Rayleigh fading channels are described.

It is pointed out in [41] that the duration τ_{const} in the model (2.14) is strongly related to the decay rate γ via the return loss of the most dominant wall partitions in indoor environments. A high return loss intends to result in a relatively small duration τ_{const} and a relatively large decay rate γ . Therefore, it is reasonable to assume that the product $\tau_{\text{const}}\gamma$ is fixed for a specific antenna configuration in an environment. Based on this assumption, a new parameter $s = \tau_{\text{const}} \cdot \gamma$ is introduced to describe the shape of a profile [42]. When the shape parameter is known, the channel parameters $\{P, K, \sigma_\tau\}$, where P is the average channel power, can be related to the model parameters $\{P_0, P_1, \gamma, \tau_{\text{const}}\}$, as listed in Table 2.1. In the table, we have $s_1 = s + 1$, $s_2 = s^2/2 + s + 1$ and $s_3 = s^3/3 + s^2 + 2s + 2$.

The single cluster model (2.14) will be used later in this chapter to model PDPs obtained from channel measurements, since the antenna effect can not be separated from the measured PDPs there.

2.2.4 Frequency selectivity

The equivalent complex channel frequency response $H(t, f)$ is written as

$$H(t, f) = \sum_{l=0}^L h_l(t) e^{-i2\pi\tau_l f}, \quad (2.15)$$

which is the Fourier transform of (2.7) over τ . Here $i = \sqrt{-1}$ denotes the imaginary unit. Under the WSSUS assumption, it can be shown that the frequency autocorrelation function of $H(t, f)$ does not depend on the specific frequency and can be written as

$$\mathcal{R}_H(\Delta t; f_1, f_2) = \frac{\mathbb{E}\{H^*(t, f_1)H(t + \Delta t, f_2)\}}{\sqrt{\mathbb{E}\{|H^*(t, f_1)|^2\}\mathbb{E}\{|H(t + \Delta t, f_2)|^2\}}} = \mathcal{R}_H(\Delta t, \Delta f) \quad (2.16)$$

with $\Delta f = f_2 - f_1$, where $\mathcal{R}_H(\Delta t, f)$ is the Fourier transform of $\mathcal{R}_h(\Delta t, \tau)$ in (2.10). For $\Delta t = 0$, the resulting $\mathcal{R}_H(\Delta f) \triangleq \mathcal{R}_H(0, \Delta f)$ represents the channel coherence level over the frequency separation Δf . The coherence bandwidth B_{c_x} is defined as the largest frequency separation over which the correlation $|\mathcal{R}_H(\Delta f)|$ is not smaller than a pre-determined level x , e.g. 0.5 or 0.9, and given by

$$B_{c_x} = \Delta f \Big|_{|\mathcal{R}_H(\Delta f)| \geq x}. \quad (2.17)$$

The coherence bandwidth is a statistical measure in characterizing the frequency selectivity of a channel. When the bandwidth of the transmitted signal is much larger than the coherence bandwidth, the signal will fade in different levels at different frequencies and the channel is said to be *frequency selective*. On the other hand, when the signal bandwidth is much smaller than the coherence bandwidth, the channel is said to be *frequency nonselective*.

Channel frequency selectivity is due to the impact of multipath propagation and related to the dispersive property in time domain. For a WSSUS channel, the frequency autocorrelation function and the PDP are related through the Fourier transform [41, 43, 44]. A smaller RMS delay spread generally implies a reduced frequency selectivity and a larger coherence bandwidth. In addition, the RMS delay spread of a Rician channel PDP is strongly related to the Rician K -factor. Generally speaking, the larger is the Rician K -factor, the smaller is the RMS delay spread and thus the larger is the coherence bandwidth. In literature, coherence bandwidth is approximately modelled to be inversely proportional to RMS delay spread with a proportionality constant, which is related to the shape of the PDP [43, 45].

For the special case of an exponentially decaying PDP (2.14) with $\tau_{\text{const}} = 0$, the frequency autocorrelation function can be written as [46]

$$\mathcal{R}_H(\Delta f) = \frac{1}{K+1} \left(K + \frac{1}{1 + \frac{i2\pi\Delta f}{\gamma}} \right), \quad (2.18)$$

where the decay exponent is related to the RMS delay spread and the Rician K -factor by $\gamma = \frac{\sqrt{2K+1}}{\sigma_\tau(K+1)}$. Therefore, the frequency autocorrelation function can be uniquely determined by the RMS delay spread for a specific decay exponent.

2.2.5 Time selectivity

Propagation channels can vary over time due to the movements of the surrounding objects or the movements of TX/RX antennas. As a result, *Doppler effects* occur and result in a spectrum broadening of the received signal. Proportional to the carrier frequency, the Doppler effects at 60 GHz are relatively severe. For instance, a moving object at a speed of 3 m/s can lead to a Doppler spread of the 60-GHz carrier signal as large as 1.2 kHz, which is 30 times of the spread at 2 GHz. For a fixed point-to-point application, Doppler effects caused by moving objects can be significantly reduced by employing directive antennas or smart antenna technologies.

As compared to the dramatic phase change caused by the Doppler effect, the amplitudes and the incident angles of multipath waves stay quasi-stationary in a local area. When the receiver is moving at speed v , the phase of the l th path $h_l(t)$ changes over time and can be modelled by [47, 48]

$$\phi_l(t) = \bar{\phi}_l + 2\pi f_D t \cos \theta_l, \quad (2.19)$$

where $\bar{\phi}_l$ is the phase when the channel is static, $f_D = \frac{f_c v}{c}$ represents the Doppler spread and θ_l the angle between the moving direction and the incident direction. When the angles of arrival of the multipath components are uniformly distributed in all the directions in a horizontal plane, a “U”-shape Doppler spectrum, that is well known as the classic 2-D Clarke’s model, will appear [47, 48]. When a specular path exists in the channel, a spike will appear in the Doppler spectrum.

For most applications of indoor 60 GHz radio systems, the transmitter and receiver are stationary and the time variations of the channel are actually caused by moving objects. Then, the phase of the l th path reflected at a moving object with the speed v becomes [49]

$$\phi_l(t) = \bar{\phi}_l + 4\pi f_D t \cos \vartheta_l \cos \varphi_l, \quad (2.20)$$

where ϑ_l is the reflection angle of the path at the moving object, and φ_l the angle between the direction of movement and the direction orthogonal to the reflecting surface. In a similar way, the Doppler shift caused by multiple moving objects can be expressed. The resulting Doppler spectrum will show a “bell” shape, which has been observed from measurements [35, 36, 50].

2.3 Channel measurement and analysis

2.3.1 Measurement setup and environment

An HP 8510C vector network analyzer was employed to measure complex channel frequency responses. During the measurement, the frequency step mode was used and each measurement of each frequency response took about 20 seconds. Channel impulse responses were obtained by Fourier transforming the frequency responses to

Table 2.2: Antenna parameters

Type of antennas	Half power beamwidth (°)		Gain (dBi)
	E-plane	H-plane	
Fan-beam	12.0	70.0	16.5
Pencil-beam	8.3	8.3	24.4
Omnidirectional	9.0	omnidirectional	9

the time domain after a Kaiser window² was applied with a sidelobe level of -44 dB. With the Kaiser window function applied, a time-domain resolution of 1 ns is achieved, for instance, for the bandwidth $B = 2$ GHz. Three types of vertically polarized antennas with different radiative patterns, i.e. omnidirectional, fan-beam and pencil-beam antennas, were applied in our measurements. Parameters of these antennas, half power beamwidth (HPBW) and antenna gain, are listed in Table 2.2.

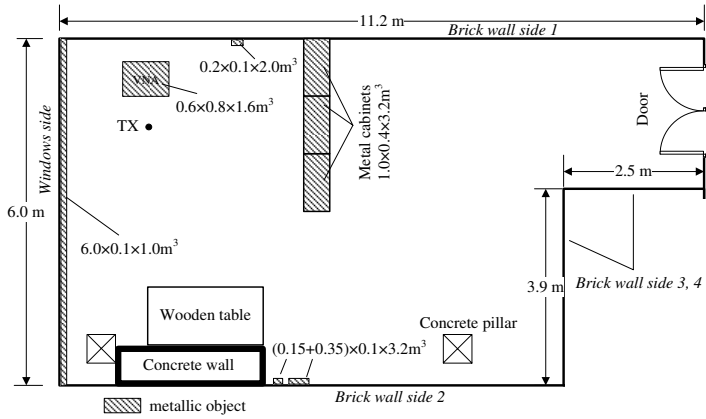
Two groups of measurements were conducted in two rooms, which we denote Room A and Room B, on the 11th floor of the PT-building at Eindhoven University of Technology. The plan view of both rooms are given in Fig. 2.5. The dimensions of the rooms are $11.2 \times 6.0 \times 3.2$ m³ and $7.2 \times 6.0 \times 3.2$ m³, respectively. Both rooms have a similar structure. The windows side consists of window glasses with a metallic frame one meter above the floor and a metallic heating radiator below the window. The concrete walls are smoothly plastered and the concrete floor is covered with linoleum. The ceiling consists of aluminium plates and light holders. Some large metallic objects, such as cabinets, were standing on the ground. Note that in Room A, three aligned metallic cabinets are standing in the middle of the room and two metallic cable boxes with a height of 3.2 m are attached to the brick wall side 2. The space between cabinets and ceiling has been blocked by aluminum foil for the ease of the measurement analysis.

Table 2.3 lists the antenna configurations and scenarios. In Room A, at both the TX and RX side, we use the omnidirectional antennas. Three height differences of TX-RX antennas were considered, viz. 0.0, 0.5 and 1.0 m (denoted by OO_{0.0}, OO_{0.5} and OO_{1.0} for three cases, respectively). Both LOS and NLOS channels were measured in Room A. In Room B, a sectoral horn antenna with fan-beam pattern was applied at the TX side and located in a corner of the room at the height of 2.4 m. At the RX side, we used three types of antennas with omnidirectional, fan-beam and pencil-beam patterns at the height of 1.4 m. The three TX-RX combinations are denoted by FO, FF and FP, respectively, in which of the latter two cases the TX-RX beams are

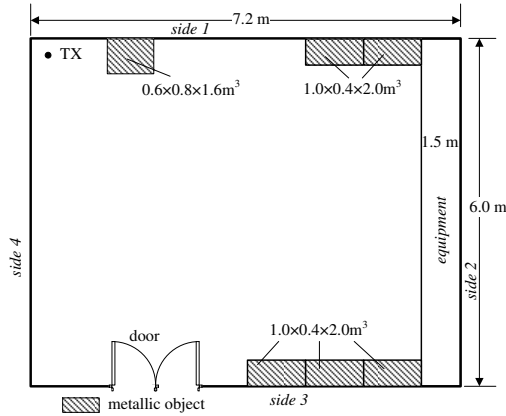
²The Kaiser window is a window function defined by [51]

$$W_{\text{Kaiser}}(\tau) = \begin{cases} \frac{I_0\left(\beta\sqrt{1-\left(\frac{2n}{N}-1\right)^2}\right)}{I_0(\beta)} & 0 \leq n \leq N \\ 0 & \text{otherwise} \end{cases}$$

where $I_0(\cdot)$ is the zero order modified Bessel function and β determines the shape of the window. During our measurement, we set $\beta = 6$ so that the highest side-lobe level is about -44 dB. This side-lobe level is consistent with the 40 dB signal-to-noise ratio of the measurement system.



(a) Room A



(b) Room B

Fig. 2.5: Plan view of the measured rooms.

Table 2.3: Antenna configurations

Room	Freq. range (GHz)	Antenna (TX – RX)			Denoted
		TX	RX	Height (m)	
A	57 ~ 59	Omni-directional	Omni-directional	1.4 – 1.4	OO _{0.0}
				1.9 – 1.4	OO _{0.5}
				2.4 – 1.4	OO _{1.0}
B	58 ~ 59	Fan-beam	Omni-directional	2.4 – 1.4	FO
			Fan-beam		
			Pencil-beam		
					FF, FF _{±35°}
					FP, FP _{±35°}

directed towards each other. In addition, we measured the channels for the cases of FF and FP with TX-RX beams misaligned by $\pm 35^\circ$ (denoted by $\text{FF}_{\pm 35^\circ}$ and $\text{FP}_{\pm 35^\circ}$). In Room B, only LOS channels were measured.

During measurement, the transmitter and receiver were kept stationary and there were no movement of persons in the rooms.

2.3.2 Wideband received power

Fig. 2.6 depicts the measured wideband power level at the receiver for various antenna configurations when a unit power (0 dBm) is transmitted. The wideband received power is simply the sum of the powers received in each multipath component [41]. The solid line shows the calculated received power of the direct path in free space, where the peak gains of the TX and RX antennas are taken into account during the calculation³.

For the omnidirectional configurations in the LOS environment, in case of TX-RX antennas at the same height (Omn-Omn 1.4–1.4m in Fig. 2.6(a)), most of the received power values are several dBs higher than the power of the LOS component, because of multiple paths existed in such a highly reflective environment. In such a case, the scattered path and the LOS path have a comparable contribution to the received power. In case the TX-RX antennas are not located at the same height, the received power is much lower and mainly contributed by the scattered paths, since the misaligned beams cause a significant drop of the power of the LOS component.

In the NLOS environment, see Fig. 2.6(b), the main contribution of the received power is due to reflections from the brick wall (side 2 in Fig. 2.5(b)). With increasing the TX-RX separation distance, the strongest reflected path becomes less dominant in the received power. Also, the received power level becomes less sensitive to the TX-RX height difference in the NLOS environment. In addition, for the receiver positions located in a deep shadow region, which is just behind the cabinets (the TX-RX distance in the range of 3.5 ~ 4.2 meters in Fig. 2.6(b)), the channels suffer from severe shadowing effect, due to the lack of first-order reflections. The power levels in this deep shadow region are about 9.3, 12.4 and 16.6 dB lower on average than in free space, for the three TX heights at 1.4, 1.9 and 2.4 m, respectively. For the other region, the levels are about 5.0, 9.3 and 11.4 dB lower on average, respectively.

In comparison, for the directive antenna configurations in Fig. 2.6(c), the power levels are much higher (due to antenna gains) and the received power levels strongly follow the power level of the LOS component, except those points close to the transmitter that are very sensitive to the (unintentional) beam pointing errors (see also figures in Section 2.3.3)⁴. When the RX beams are misaligned intentionally by $\pm 35^\circ$ over the boresight, the received power by the Fan-Pen configuration will drop about 25 dB

³In other words, the antenna effect is not ideally included in the calculation, when TX-RX beams are not perfectly pointing to each other.

⁴Note that for the Fan-Omn case, when the TX and RX are close to each other, the lower signal level is caused by the narrow beamwidth of the omnidirectional antenna in the vertical plane.

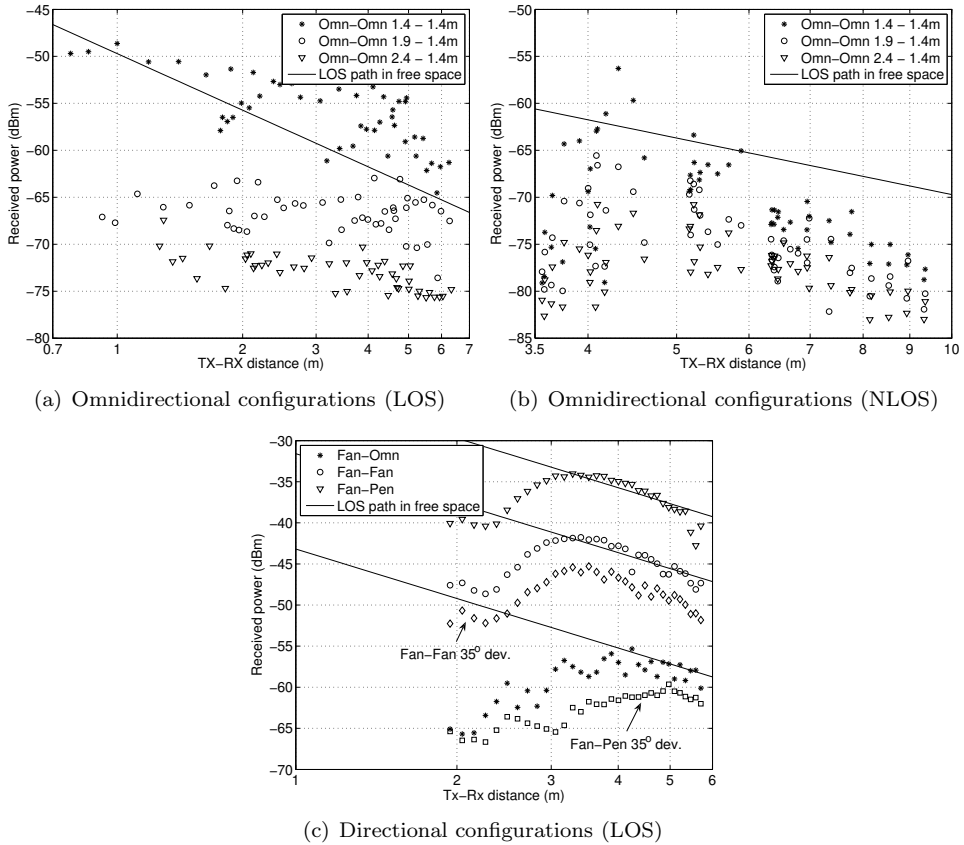


Fig. 2.6: Measured wideband received powers for various antenna configurations (the transmit power is 0 dBm).

due to narrower antenna beam, compared to the 4 dB drop by the Fan-Fan one. Note that the 35° -misalignment is about half the beamwidth of the fan-beam antenna and thus the direct path is still within the sight, which is apparently not the case for the pencil-beam antenna.

By fitting the measured data in Fig. 2.6 to the equation (2.4), we get the log-distance model parameters, which are listed in Table 2.4. Note that for the NLOS channels, the scattered points in the deep shadow region, in the range of $3.5 \sim 4.2$ meters, are not taken into account in the fittings. In addition, for the case of directive configurations in Fig. 2.6(c), the scattered points within the distance of 2 to 3 meters are also not taken into account, because of the relatively large errors of unintentional beam mispointing. It appears that in LOS channel environments, the loss exponents are much smaller than the free-space exponent, i.e. $n < 2$, for the Omn-Omn configurations, but approximately equal to 2 for the directive ones. In NLOS environments configured with omnidirectional antennas, the loss exponents are about 4.3, 3.7 and 3.0 for

the cases of $OO_{0.0}$, $OO_{0.5}$ and $OO_{1.0}$, respectively, without considering the deep shadowing positions.

2.3.3 Channel impulse response and frequency response

To have an immediate impression of the property of multipath fading and frequency selectivity, we show the measured channel impulse and frequency responses. Fig. 2.7-2.10 plot the measured responses in Room B along distance, where the fan beam antennas are used at TX side. The measured results in Room A, where omnidirectional antennas are used at TX and RX sides in both LOS and NLOS areas, are not given here, since their multipath properties are similar to the case of Fan-Omn

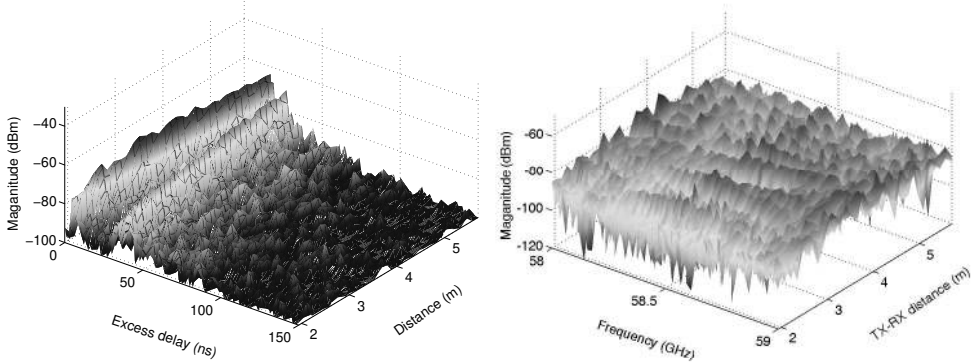


Fig. 2.7: Channel time impulse (left) and frequency response (right) along distance for the Fan-Omn configuration.

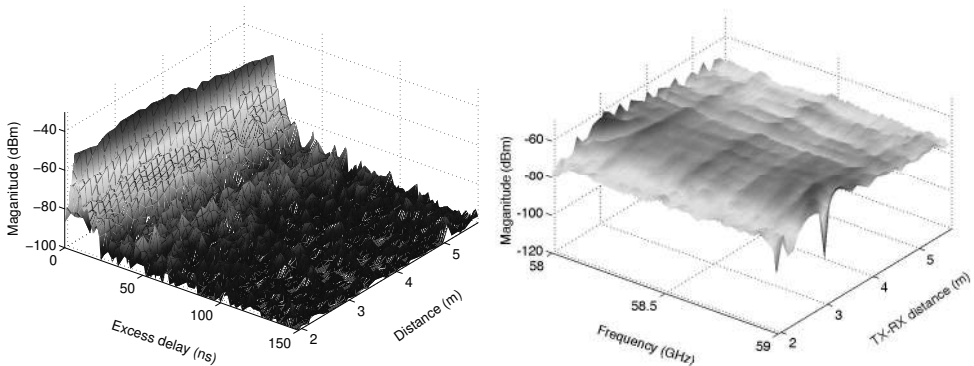


Fig. 2.8: Channel time impulse (left) and frequency response (right) along distance for the Fan-Fan configuration without beam misalignment.

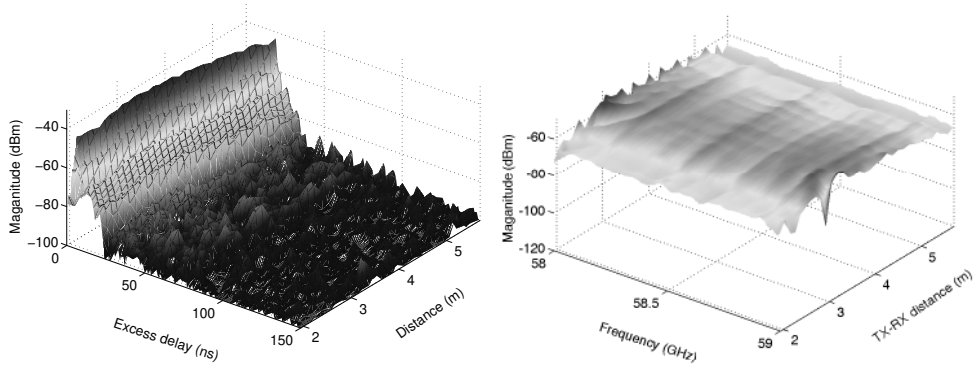


Fig. 2.9: Channel time impulse (left) and frequency response (right) along distance for the Fan-Pen configuration without beam misalignment.

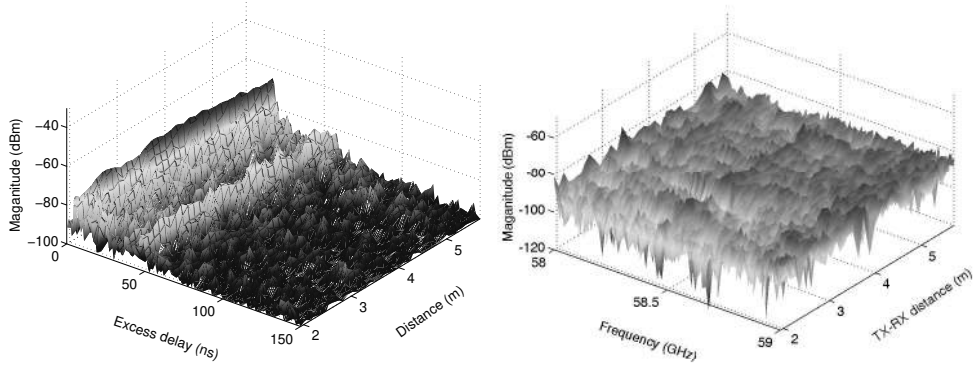


Fig. 2.10: Channel time impulse (left) and frequency response (right) along distance for the Fan-Pen configuration with 35° deviation off the boresight.

configuration. When the omnidirectional antenna is applied in the receiver, from Fig. 2.7(left), one can see two strong paths from the impulse responses, the LOS wave and the reflected wave, in addition to the other paths. Because of the multipath effect, many dips can be observed from the frequency responses, which indicate strong channel frequency selectivity. When narrow-beam antennas (fan-beam and pencil-beam antennas) were used, multiple paths are significantly suppressed by the narrow antenna beams. As a result, only the LOS wave is visible in the impulse responses and the frequency selectivity is significantly reduced.

However, the misalignment of the RX beam from the boresight leads to different impacts on the channels for the fan-beam and pencil-beam antennas at RX side. For the fan-beam antenna, the deviation of 35° doesn't cause a noticeable change on the impulse response and frequency response (not given here). Notice that the 35° -deviation is about half the beamwidth of the fan-beam antenna, which means that

the direct path is still within the sight. For the pencil-beam antenna, on the contrary, the deviation causes a significant power drop in the LOS wave and some paths arise in the impulse responses, which can be seen from Fig. 2.10. This leads to a fast fluctuation in the frequency response.

2.3.4 Channel parameters

2.3.4.1 Rician K -factor, RMS delay spread and coherence bandwidth

Based on the data sets of channel measurements with different antenna configurations, we investigate the frequency selectivity of 60-GHz channels, concerning Rician K -factor, RMS delay spread and coherence bandwidth as follows. When calculating the Rician K -factor, the power contributed by the dominant path is derived by adding up the powers within the resolution bin. The RMS delay spread is calculated from the PDP with a dynamic range fixed at 30 dB, which is well above the noise level.

Fig. 2.11 and 2.12 depict Rician K -factors and RMS delay spreads derived from the measured PDPs. Fig. 2.12(d) shows a magnified version of Fig. 2.12(c) so that the results can be well distinguished for narrow-beam configurations. In addition, we also estimated the coherence bandwidth $B_{c_{0.5}}$ and $B_{c_{0.9}}$ at the correlation level 0.5 and 0.9, respectively, as shown in Fig. 2.13 for $B_{c_{0.5}}$. The mean values of them are listed in Table 2.4 for each configuration.

From Fig. 2.11-2.13, we observe that when an omnidirectional antenna is used either at the TX side or at the RX side, most of the channel parameters are in the range of $K < 3$, $\sigma_\tau > 5$ ns, $B_{c_{0.5}} < 200$ MHz and $B_{c_{0.9}} < 20$ MHz. The Rician K -factors in the LOS case are generally small because of the highly reflective environment. Under the NLOS condition, channel parameters are strongly variant depending on the position of the receiver, due to the absence of the direct path. In some NLOS channels, a strong wave reflected from walls appears and leads to desirable values of channel parameters. In particular, the Rician K -factors at some NLOS positions are larger than 4, since the strongest wave reflects at the metallic cable boxes attached to the wall and is much stronger than other reflected waves.

For the narrow-beam configurations of Fan-Fan and Fan-Pen, as the result of the significant suppression of multipath waves, it is observed that most of the channel parameters are in the range of $K > 10$, $\sigma_\tau < 1.5$ ns, $B_{c_{0.5}} > 400$ MHz and $B_{c_{0.9}} > 40$ MHz, respectively. When the TX-RX beams are not pointing to each other, the beam-pointing errors, e.g. the 35° -misalignment for the Fan-Pen configuration, can seriously worsen the channel condition in terms of increased RMS delay spreads and the largely reduced received powers, Rician K -factors and coherence bandwidths. This implies that channel configurations with wider beams are less sensitive to beam-pointing errors. Therefore, the width of the beam has to be properly designed to prevent an enormous drop of channel quality caused by beam-pointing errors.

The coherence bandwidth is strongly related to the Rician K -factor and the RMS delay spread, which reflects the Fourier transform relationship between the frequency

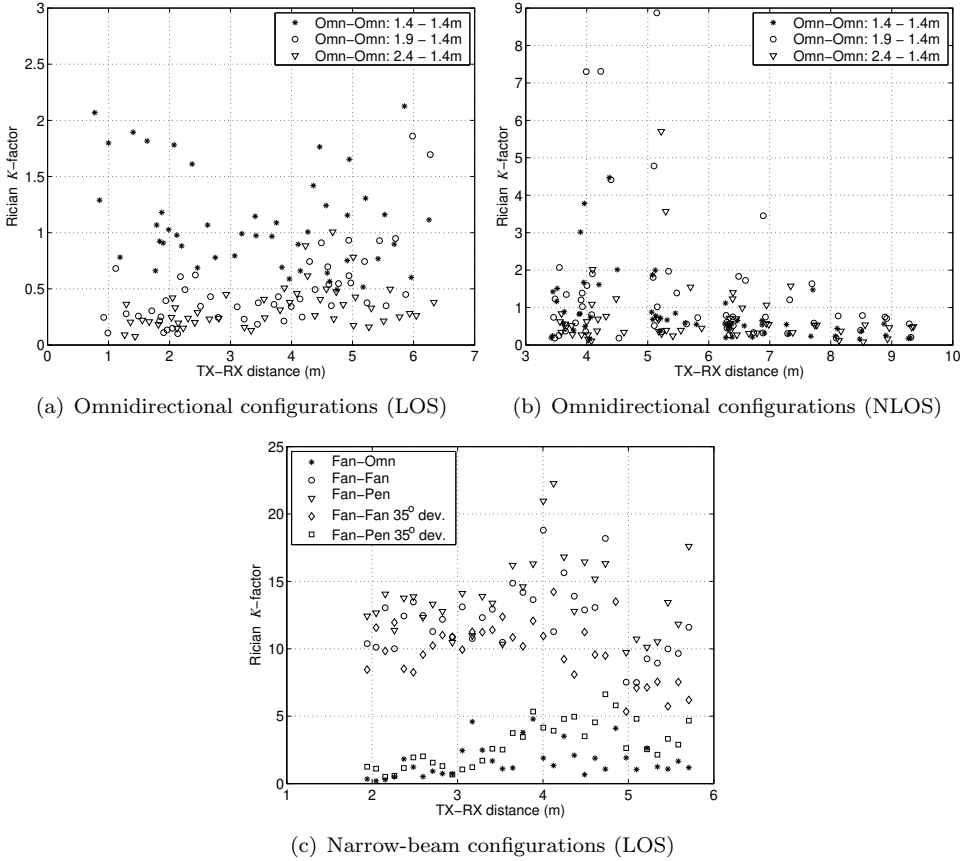


Fig. 2.11: Measured Rician K -factors for various antenna configurations.

autocorrelation function and the PDP described in Section 2.2. Generally speaking, the larger the Rician K -factor, the smaller is the RMS delay spread and thus the larger is the coherence bandwidth. For a specific shape of the PDP, one would expect a fixed relationship between coherence bandwidth and RMS delay spread [43]. For a Rayleigh fading channel (i.e. Rician factor $K = 0$) with delay profile exponentially decaying, for instance, one can obtain $\sigma_\tau \cdot B_{c_{0.9}} = 0.077$ and $\sigma_\tau \cdot B_{c_{0.5}} = 0.276$, respectively, from (2.17) and (2.18).

From the measured data for all the antenna configurations, the coherence bandwidths at level 0.9 can be empirically related to the RMS delay spreads given by

$$\sigma_\tau \cdot B_{c_{0.9}} = 0.063 \quad (2.21)$$

based on data fitting, where σ_τ and $B_{c_{0.9}}$ are in nanosecond and GHz, respectively. But the product of $\sigma_\tau \cdot B_{c_{0.5}}$ are highly variant for different configurations and have

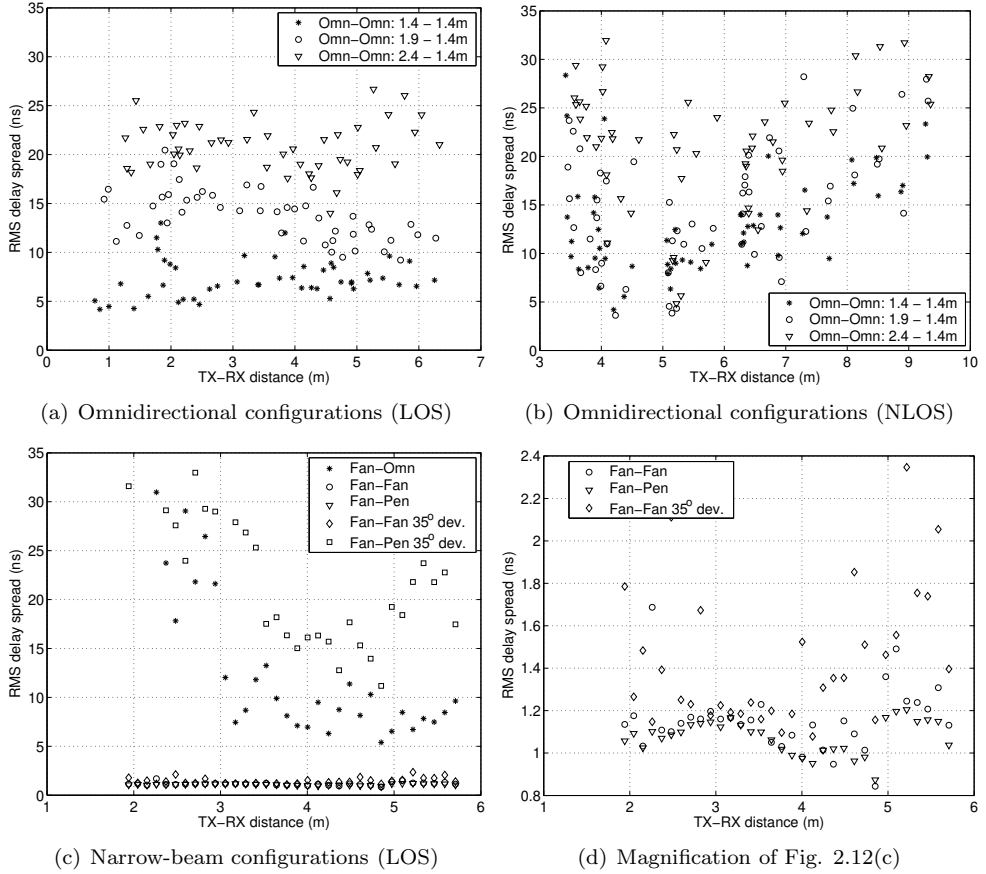


Fig. 2.12: Measured RMS delay spreads for various antenna configurations.

a mean value given by

$$\mathbb{E} \{ \sigma_{\tau} \cdot B_{c_{0.5}} \} = 0.951. \quad (2.22)$$

These empirical relationships can be used in practice to quantify the frequency selectivity of a channel based on its known RMS delay spread. For instance, the coherence bandwidth of the channel with a RMS delay spread $\sigma_{\tau} = 1$ ns can be estimated to be 63 MHz and 951 MHz at the correlation level of 0.9 and 0.5, respectively.

2.3.4.2 Maximum excess delay and number of multipath components

Within the dynamic range of 30 dB of PDPs, the maximum excess delay τ_{\max} and the number of multipath components L are investigated for various measurement configurations. Multipath components are recognized from the local peaks in a profile.

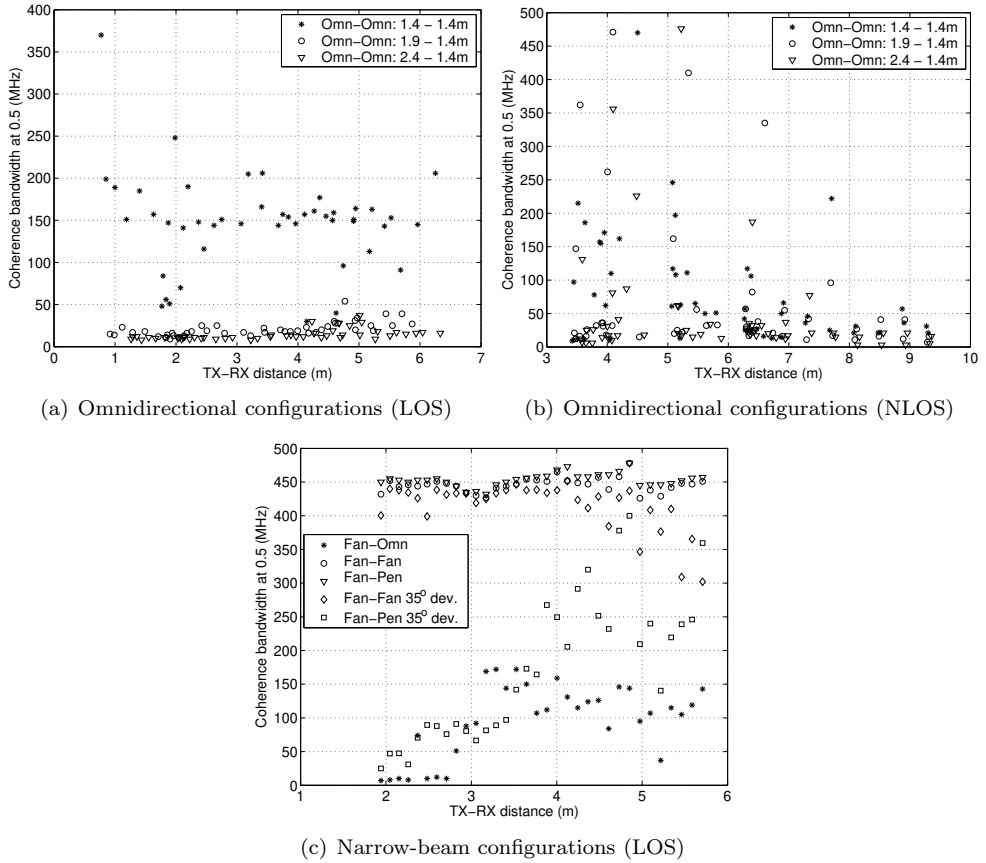


Fig. 2.13: Measured coherence bandwidth at level 0.5 for various antenna configurations.

According to the data analysis, the values of τ_{\max} are wildly distributed within 10 to 170 ns and so is the case for the values of L within 3 to 100, depending on the channel configurations. The mean values are summarized in Table 2.4. Also, the values of L are strongly related to the values of τ_{\max} , that is, the number of multipath components will increase with the maximum excess delay. For all the measured profiles, the number of paths per ns, $\frac{L}{\tau_{\max}}$, has a mean value of 0.30 with a small standard deviation of 0.06. This leads to an empirical relationship

$$L = \lceil 0.30 \cdot \tau_{\max[\text{ns}]} \rceil, \quad (2.23)$$

where the ceiling function $\lceil x \rceil$ returns the smallest integer not less than x .

Table 2.4: The log-distance model parameters $\{PL_0, n, \Omega\}$, the mean values of K , σ_r , B_c , τ_{\max} and L for various configurations, and the PDP shape parameters $\{s, \tau_{\text{const}}, \gamma\}$.

Cases	LOS			NLOS			LOS					
	OO _{0,0}	OO _{0,5}	OO _{1,0}	OO _{0,0}	OO _{0,5}	OO _{1,0}	FO	FF	FP	FF _{±35°}	FP _{±35°}	
PL_0 (dB)	68.3	83.8	87.8	51.5	64.3	72.5	79.7	67.0	67.4	72.2	115	
n	1.2	0.2	0.6	4.3	3.7	3.0	0.4	2.1	2.0	1.9	-1.5	
Ω (dB)	2.7	2.0	1.3	2.1	2.2	1.8	1.0	0.8	0.6	0.9	0.8	
$\mathbb{E}\{K\}$	1.1	0.5	0.3	0.9	1.6	0.7	1.7	12.5	14.5	9.8	2.9	
$\mathbb{E}\{\sigma_r\}$ (ns)	7.3	13.8	20.8	12.9	14.8	21.0	14.6	1.2	1.1	1.4	23.3	
$\mathbb{E}\{B_{c_{0.5}}\}$ (MHz)	155.1	37.6	14.0	108.4	148.2	55.9	95.3	445.9	453.4	414.1	173.0	
$\mathbb{E}\{B_{c_{0.9}}\}$ (MHz)	15.4	5.6	3.0	6.4	6.5	2.6	6.3	51.8	55.6	44.7	3.2	
$\mathbb{E}\{\tau_{\max}\}$ (ns)	67.8	116.6	144.8	120.6	133.4	146.1	113.2	15.7	15.4	21.5	141.7	
$\mathbb{E}\{L\}$	20.0	34.0	47.2	35.5	38.6	47.5	28.7	5.0	4.8	5.8	38.3	
s (dB)	0	3.3	2.7	0	0	0	3.1	0	0	0	3.3	
$\mathbb{E}\{\tau_{\text{const}}\}$ (ns)	0	29.5	39.0	0	0	0	27.6	0	0	0	66.7	
$\mathbb{E}\{\gamma\}$ (dB/ns)	0.2	0.11	0.07	0.07	0.06	0.04	0.14	0.48	0.48	0.42	0.05	

2.3.5 Modelling of power delay profile

To investigate the shapes of power delay profiles for various channel configurations, we take the average over all the measured profiles for each configuration. Here each individual measured profile is normalized by its total received power. As an example, Fig. 2.14 depicts the average profiles for the configurations of Omn-Omn and Fan-Pen. From these average profiles, we observe the following:

- when the TX-RX beams are aligned to each other under the LOS condition, e.g. the cases of Omn-Omn 1.4/1.4m, Fan-Fan and Fan-Pen, the average PDP consists of a direct ray and an exponentially decaying part.
- In other LOS cases when the TX-RX beams are strongly misaligned and out sight of each other, a constant level part will appear before an exponentially decaying part. The duration of the constant part depends on the severity of the misalignment and the sharpness of the antenna beam pattern.
- In addition, under the NLOS condition, the average delay profile will be exponentially decaying without a constant part, due to the lower dependency of antenna pattern and beam misalignment.

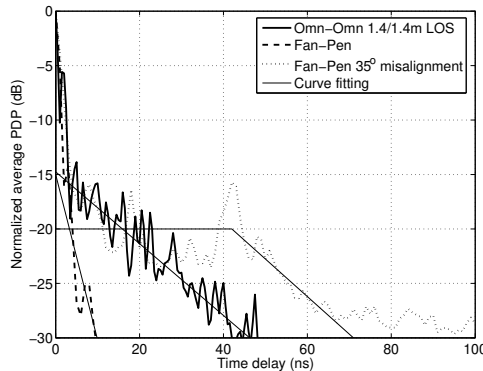


Fig. 2.14: Average power delay profiles and curve fittings for the Omn-Omn and Fan-Pen configurations.

According to the observation, the average PDP can be modelled as a function of excess delay that consists of a direct ray, a constant part and a linear decaying part, as shown in Fig. 2.14, which is just the model given in (2.14). From the measured results, the shape parameter $s = \tau_{\text{const}} \cdot \gamma$ can be achieved by fitting the average PDP with (2.14) for each configuration. Then for each individual measured profile, the model parameters $\{P_0, P_1, \gamma, \tau_{\text{const}}\}$ can be retrieved by taking the channel parameters $\{P, K, \sigma_\tau\}$ into the channel-to-model formulas in Table 2.1. With these model parameters, the channel can be simulated and used for the performance evaluation of a system. Table 2.4 lists the shape parameters s and the mean values of the model parameters γ and τ_{const} for various configurations.

2.3.6 Summary

In this section, the multipath properties of 60-GHz channels in LOS and NLOS channel environments were analyzed for omnidirectional and narrow-beam antenna configurations based on extensive channel measurements. Statistical channel parameters were retrieved from measurements and compared. In addition, the measured power delay profiles were modelled by a simple single-cluster model.

First of all, it is seen that antenna radiation patterns have significant impacts on channel properties. Omnidirectional configurations generally result in a lower received power and much severe multipath dispersion, while narrow-beam configurations not only boost the power level, in the order of tens of dBs, but also lower the multipath dispersion significantly. But on the other hand, wider-beam antennas, such as the considered fan-beam antenna, is more resistant to beam pointing errors, than narrower beam antennas, such as the considered pencil-beam antenna. The analysis on the results suggest that a high gain antenna is preferred for a 60-GHz channel, but the antenna beamwidth has to be properly selected to optimize the impact of the beam's pointing error on the channel. A theoretical analysis of beam pointing errors will be conducted in Chapter 3.

In addition to the influence of radiation patterns, the shadowing effect in the NLOS channel environment is severe, especially in a deep shadow region where first-order reflections can not reach the receiver.

2.4 Comparison of propagation in the frequency bands of 2 GHz and 60 GHz

Due to the high penetration loss through walls and ceilings, the typical range of the indoor wireless communication at 60 GHz is actually confined to a single room [41]. Therefore, this section will closely look at the propagation in a single room and investigate the channel properties in the frequency bands of 60 and 2 GHz based on channel measurements.

2.4.1 Experimental setup and scenario

The 60-GHz channel sounding system used here is the same as the one described in Section 2.3.1. A vertically polarized biconical antenna has been used at both the TX and RX side. The antenna pattern is omnidirectional in the horizontal plane and the 3-dB beam width in the vertical plane is 9° . As for channel measurements at 2 GHz, a sliding correlator channel sounder was used with the central frequency at 2.25 GHz and the bandwidth of 100 MHz. During the measurements, the complex channel impulse responses are recorded with a resolution of 20 ns and a dynamic range of 40 dB. Dipole antennas are used at the TX and RX sides. Both antennas are vertically polarized and omnidirectional in the horizontal plane.

The measurements have been conducted in the Room A as described in Section 2.3.1. During measurement, the transmitter is fixed at a position as shown in Fig. 2.5 and the height of the antenna is 1.4 meters. The receivers are at the height of 1.4 meters too and located in the LOS and NLOS areas.

2.4.2 Normalized received power and shadowing effect

According to the propagation model (2.2) in free space, the path loss of a radio signal is related to the frequency and TX-RX separation. At the same TX-RX separation, the free space propagation loss at 58.0 GHz is about 28.2 dB higher than at 2.25 GHz. In a multipath environment, the reflected, diffracted and scattered waves with different magnitudes and phases will also contribute to the received signal. Since the permittivities of building materials are related to the carrier frequency of radio waves, the propagation of multiple waves at 2.25 GHz and 58.0 GHz is different in terms of their magnitudes and relative phases. As a result, the PDPs of the radio channels at the two frequencies are different. Consequently, the wideband received powers, even with the 28.2 dB difference in free space removed, will be different at the two frequencies, as well as the RMS delay spreads as will be discussed in Section 2.4.3.

In order to compare the influence of the room environment on the received signal level at the two frequencies, the normalized received power is defined according to

$$\text{NRP}_{[\text{dBm}]} = P_{\text{R}[\text{dBm}]} - P_{\text{T}[\text{dBm}]} - G_{\text{T}[\text{dB}]} - G_{\text{R}[\text{dB}]} + 20 \log_{10}(f_{[\text{GHz}]}) \quad (2.24)$$

with the frequency dependency in free space removed. Here G_{T} and G_{R} represent the peak values of the antenna gains at the TX and RX sides, respectively.

Fig. 2.15(a) and (b) depict the measured NRPs in the LOS and NLOS regions, respectively. It shows that the NRP levels of the LOS channels are comparable at the two frequencies. This indicates that the differences in penetration and reflection loss between them do not have a significant impact on the level.

In the NLOS region, the NRP levels at 58.0 GHz are mostly lower than that at 2.25 GHz except the region near the shadow boundary, where they are at a comparable level. In the deep shadow regions behind the cabinets and near the door, as marked in Fig. 2.16, where the first-order reflections can not reach the receiver, the mean NRP level at 58.0 GHz is about 5.3 dB lower than at 2.25 GHz. These observations can be explained by the phenomena of radio wave diffractions. Diffracted waves appear to bend into shadow regions when the radio waves encounter the edges of objects, such as the rectangular cabinets and walls in our case [52]. The contribution of the diffracted waves to the NRP is negligible in the deep shadowed region at frequency 58.0 GHz, as observed in [41] and [52], but not at 2.25 GHz. While in the region close to the shadow boundary, the diffracted waves at 58.0 GHz are not negligible.

The path losses at the two frequencies are also fitted by using the log-distance model (2.5) and the fitted parameters are listed in Table 2.5. During data fitting, the deep shadow region in the range of 3.5 ~ 4.2 m in Fig. 2.15(b) is not taken into account.

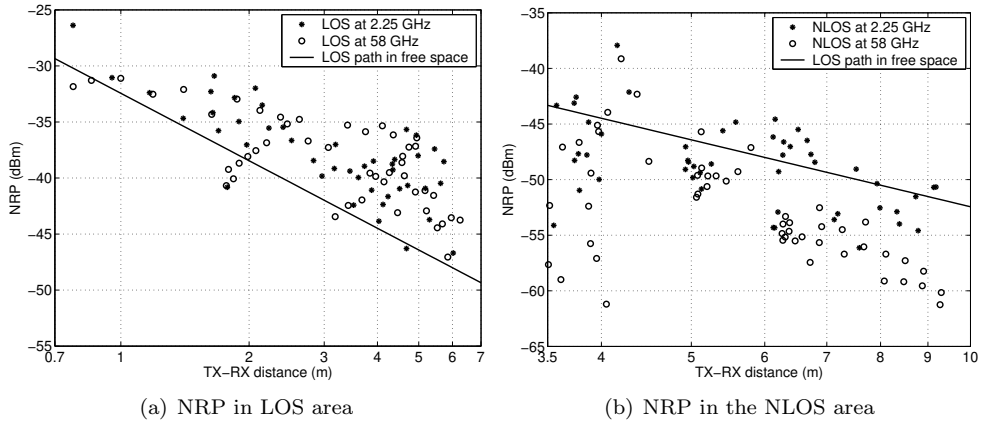


Fig. 2.15: Normalized received power at 2.25 GHz and 58.0 GHz.

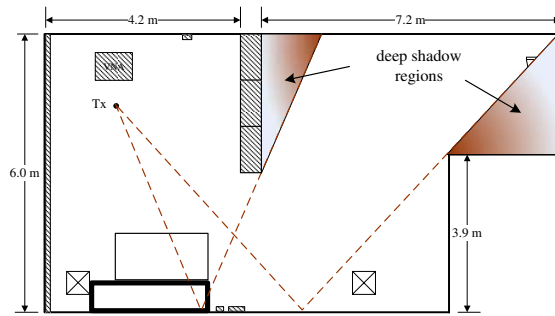


Fig. 2.16: Deep shadow regions where the first-order reflections can not reach the receivers.

It is seen that in the LOS area, the loss exponent at 58.0 GHz is about the same as that at 2.25 GHz, while in the NLOS area it is much higher due to lower diffraction levels in the shadow region.

2.4.3 RMS delay spread

RMS delay spread is used to quantify the time dispersion of an indoor channel and can be derived from the measured PDP. The resolution of the PDP in time domain is limited by the bandwidth of the channel sounding equipment. In our case, the bandwidths configured for the measurements at 2.25 and 58.0 GHz are 100 MHz and 2 GHz, which correspond to the resolutions of 20 ns and 0.5 ns, respectively. In order to have a fair comparison of RMS delay spread, the effect of the difference in bandwidth can be removed by using the formula given in [53] and the estimated RMS

Table 2.5: Fitted path loss models over the log-distance.

Experiment	LOS region			NLOS region		
	PL ₀ (dB)	<i>n</i>	Ω (dB)	PL ₀ (dB)	<i>n</i>	Ω (dB)
$f_c = 2.25$ GHz	37.6	1.5	2.5	40.6	2.0	2.7
$f_c = 58.0$ GHz	68.3	1.2	2.7	51.5	4.6	2.1

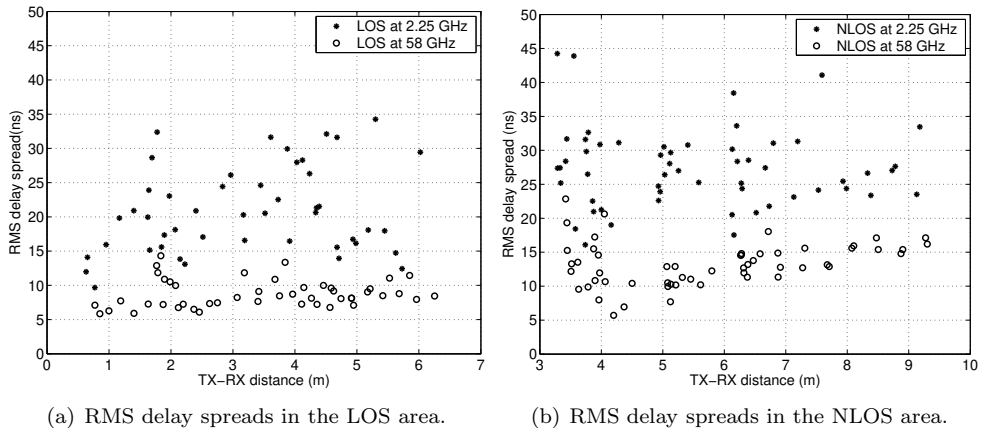


Fig. 2.17: RMS delay spreads of the channels at frequency 2.25 GHz and 58.0 GHz.

delay spread is given by

$$\sigma_{\tau} = \sqrt{\sigma_{\tau_{\text{meas}}}^2 - \sigma_{\tau_{\text{sys}}}^2}, \quad (2.25)$$

where $\sigma_{\tau_{\text{meas}}}$ is the measured RMS delay spread and $\sigma_{\tau_{\text{sys}}}$ is the RMS delay spread of the system impulse response of the equipment itself.

Fig. 2.17(a) and (b) depict the RMS delay spreads at 2.25 and 58.0 GHz with the effect of bandwidth difference removed. The RMS delay spreads at 58.0 GHz are about half of those at 2.25 GHz, which is consistent with the observation in [54]. The main reason for lower delay spreads is that, due to the high penetration loss of walls, multipath components at 58.0 GHz are mostly the reflected waves confined to the room [41], while the reflected waves from neighboring rooms at 2.25 GHz have longer delays and are still significant.

2.4.4 Effects of cool-shade curtain and antenna radiation pattern

The previous section analyzed the measured NRPs and RMS delay spreads at 2.25 GHz and 58.0 GHz. Here we analyze the effects of the cool-shade curtain and antenna pattern on the measured results.

The cool-shade curtain outside the windows is actually a grid of rectangular copper wires. Since the antenna is vertically polarized, the penetration of the waves through the curtain is related to the width of the space between the wires in the horizontal direction, which is about 13 mm, and the thickness of the curtain, which is about 2 mm. By using the calculation in [55, pp. 469], we have the power transmission coefficients < 0.1 and > 0.9 for the radio penetration at 2.25 GHz and 58 GHz, respectively. In other words, most of the radio waves at 58.0 GHz can penetrate the curtain, while most of the waves at 2.25 GHz are reflected. As a result, the curtain will enlarge the NRP at 2.25 GHz but not at 58.0 GHz. This can partly explain, for instance, the mean NRP difference of 1.5 dB in the LOS region.

Radiation patterns of antennas used at the two frequencies are different in the elevation plane. Since larger number of multipath components can be received, the pattern of the dipole antenna at 2.25 GHz might cause a higher NRP and a higher RMS delay spread compared to the pattern of the biconical antenna at 58.0 GHz. But note that the antennas at both TX and RX side are always at the same height, the radiation pattern will not have noticeable effect on the LOS results, since the dominant waves propagate in the horizontal plane. In the case of NLOS, most of the reflected waves from the ceiling and the floor have been blocked by the aluminium foil.

2.4.5 Summary

Normalized received power and RMS delay spread were examined in this section and used to compare the characteristics of the radio wave propagation at 2 and 60 GHz. In summary, the differences in penetration and reflection loss do not have a significant impact on the received signal strength at both frequencies. In case of NLOS, the shadowing effect caused by obstacles is generally higher at 60 GHz, especially in the deep shadow regions, where the NRP level is on average 5.3 dB lower than at 2 GHz, due to the poor diffraction level. But meanwhile the reflected waves from walls have a strong contribution to the NLOS received signal. Moreover, RMS delay spreads at 60 GHz are about half of those at 2 GHz on average. The decisive factor of the large difference between them is that the reflected waves from neighboring rooms with longer delays have been well blocked by walls at 60 GHz.

2.5 Ray tracing simulations and analysis

The studies of channel fading characteristics at 60 GHz in Section 2.3 and 2.4, as well as in many references, are based on channel sounding techniques [41, 56, 57]. However, the reported results are affected by the impact of the measurement system. For instance, the impact of antenna patterns on wave propagation can not be removed via calibration. In addition to channel sounding techniques, ray-tracing approaches are computer based and can be used for accurate prediction of wave propagation in micro- and pico-cellular environments [58]. Compared to field measurements using sounding techniques, ray-tracing simulators can provide additional channel information that is

difficult to obtain from measurements directly, such as the angular information of multipath radio waves, but that information is essential for the design and performance evaluation of 60-GHz systems with smart antennas [59].

In this section, the 3D ray-tracing tool Radiowave Propagation Simulator (RPS) developed by Actix Inc. is used to predict the signal propagation at 60 GHz in an indoor environment. Simulations are performed to investigate the multipath fading in time and angular domain and study the polarization effect as well.

2.5.1 RPS simulation setup

The measured environment described in Fig. 2.5(a) has been built in the RPS ray tracing simulator, including walls, windows, ceiling, floor, corridors, neighboring rooms, etc. Among these, the metallic cabinets appear to have the most significant effect on the channels. Small objects and several chairs in the corner behind a pillar are not included in the simulation.

The complex permittivity for dielectric materials, depending on the radio frequencies, is essential for the simulation of reflection and penetration of radio waves in ray tracing methods. Permittivity of many materials can be found from handbooks or open literature. A relatively complete collection of permittivity figures at 60 GHz can be found in [60] and [61] for all kinds of building materials retrieved from published articles. Table 2.6 lists the thicknesses and permittivities of the simulated objects in this section. In addition, according to the contribution and significance on wave transmission, the orders of reflection, penetration and diffraction are set to be 9, 6 and 2, respectively. Considering the dimension of the environment in Fig. 2.5(a), we limit the maximum propagation delay to 300 ns. The bandwidth is 2 GHz centered around the carrier frequency 58.0 GHz.

Table 2.6: The thicknesses and the complex permittivities of major objects modelled in the simulator.

Objects	Thickness (m)	Complex permittivity
glass window	0.015	$7.78 + j0.1167$
glass door	0.005	$7.78 + j0.1167$
concrete ceiling/floor	0.5	$6.14 + j0.3015$
metallic objects	-	$1 + j1000000$
brick wall	0.12	$3.0 + j0.1047$
pillar	0.25	$6.14 + j0.3015$

2.5.2 Prediction of the propagation simulator

To obtain reliable results from the RPS simulator, first the predictions of RPS are validated based on comparisons between measured and predicted results for a small

data set. The measured results have already been presented in Section 2.3. Here only the case of the omnidirectional configuration (Omn-Omn) is considered and the TX-RX antennas are at the same height 1.4 m. The TX-RX positions and some of the dominant waves are shown in Fig. 2.18.

First we have a look at the measured and predicted sample PDPs in Fig. 2.19(a) and (c), which are normalized to the strongest path in the LOS and NLOS channels, respectively. Besides the delay profiles, the predicted power distributions of waves in the angle-of-departure (AOD) and angle-of-arrival (AOA) domain in the horizontal plane are also shown in Fig. 2.19(b) and (d).

Comparing the measured and predicted delay profiles, we observe that: 1) the dominant components are well predicted; 2) there are fewer waves predicted than measured, but the missing waves are typically small in magnitude. The second observation can be explained by the fact that small objects and the roughness of object surfaces are not included in the simulations, which results in fewer number of the scattered waves.

Next, we compared the predicted wideband received power and RMS delay spread with the measured ones, as shown in Fig. 2.20(a)-(d), respectively. It is observed from the comparisons that the received power generally can be well predicted by the ray tracing tool, except for those RX positions located in the deep shadow region and the border region between LOS and NLOS. The average predicted signal levels are about 0.8 dB and 2.7 dB lower than those measured in LOS and NLOS regions, respectively. As for RMS delay spread, predictions for the LOS channels perform better than those for the NLOS channels. The average predicted RMS delay spreads are about 0.9 ns and 2.3 ns lower than those measured. The deviation of the predicted results from the measured results arises mainly because of the following factors: absence of small objects in the simulations; the inaccuracy of material permittivities and imperfect modelling of object layers, e.g. paint on the walls; the imperfect alignment of TX-RX antennas during measurements. Also note from Fig. 2.20(d) that RMS delay spreads of the NLOS channels, especially those in deep shadow region, are very sensitive to the above factors.

2.5.3 Polarization effect

By using the configured RPS simulator as described in Section 2.5.1, the multipath wave propagation is simulated for various polarization schemes. The transmitter is fixed and the receivers are positioned along trajectories with a step size of half a wavelength in the LOS and NLOS areas, see Fig. 2.21. The simulated signal bandwidth is 2 GHz around the central frequency 58.0 GHz, which indicates a time resolution of 0.5 ns. Isotropic antennas are used at both the TX and RX side during simulations, such that the propagation channels will not be affected by the antenna radiation pattern.

Starting from the instantaneous received signal level at distance d , $P_{\text{inst}}(d)$, we investigate the effect of polarization on the large- and small-scale fading. On average, the instantaneous received signal level is decreasing with increasing distance between

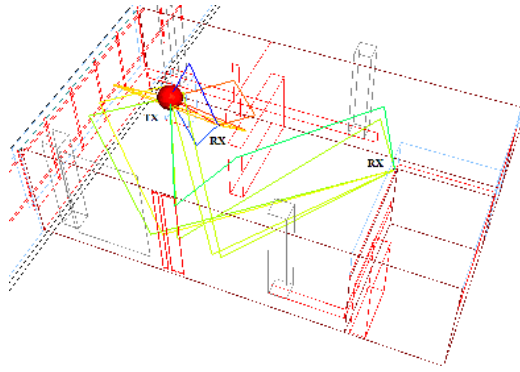


Fig. 2.18: TX-RX positions of the considered channels in Fig. 2.19. Dominated waves are also given in the figure.

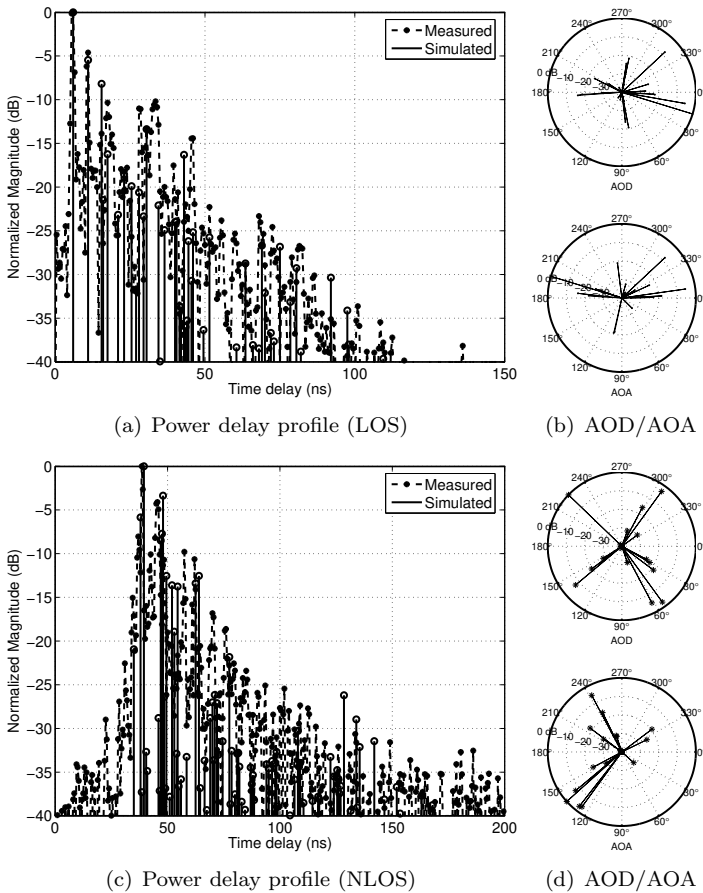


Fig. 2.19: Sample measured and predicted PDPs for the LOS and NLOS channels with the corresponding predicted power distributions in AOD and AOA domain.

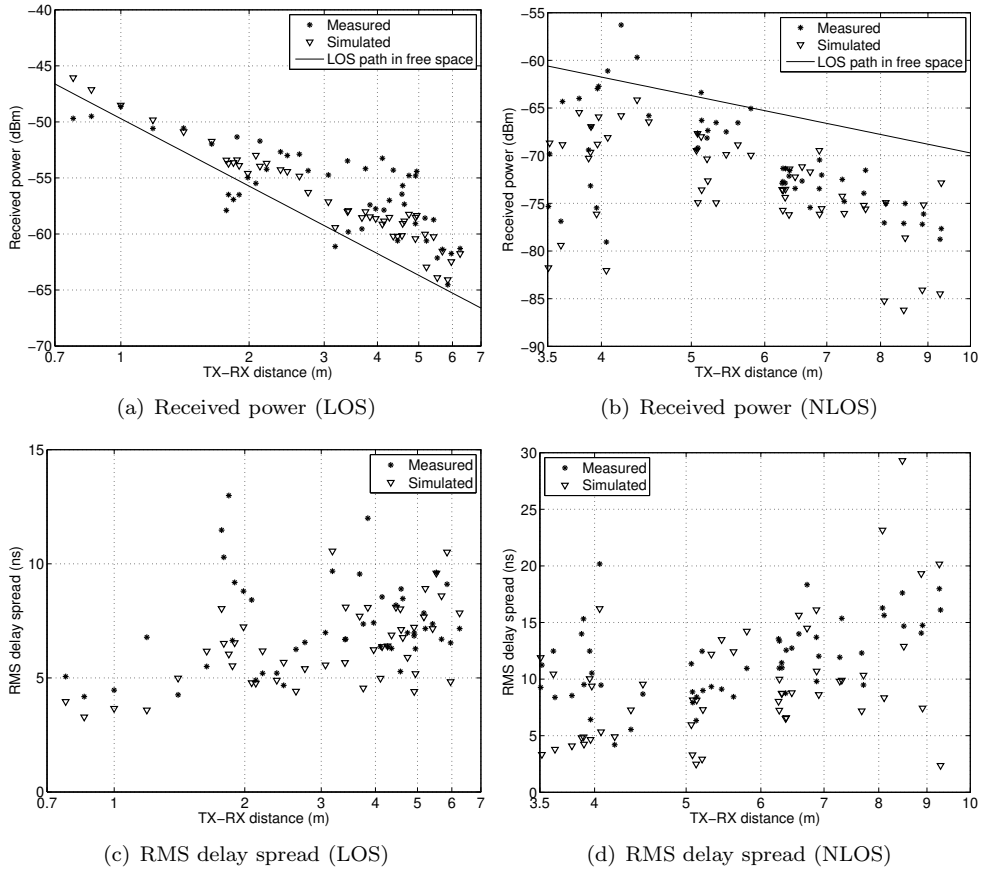


Fig. 2.20: The measured and predicted power levels (the transmitted power is 0 dBm) and RMS delay spreads.

TX and RX. However, in a local area, the signal fading can be in the order of 10 dB within a very short distance interval of several wavelengths. For the purpose of modelling, the signal fading can be decomposed into two parts: large-scale fading and small-scale fading, and given by

$$P_{\text{inst[dB]}}(d) = P_{\text{large[dB]}}(d) + P_{\text{small[dB]}}(d). \quad (2.26)$$

Here the large-scale fading, $P_{\text{large}}(d)$, describes the average behavior of the channel, mainly caused by the free space path loss and the blocking effect of large objects, while the small-scale fading $P_{\text{small}}(d)$ characterizes the signal change in a local area within a range of tens of wavelengths. The small-scale fading is obtained merely by subtracting the large-scale fading in dB from the instantaneous signal strength in dB.

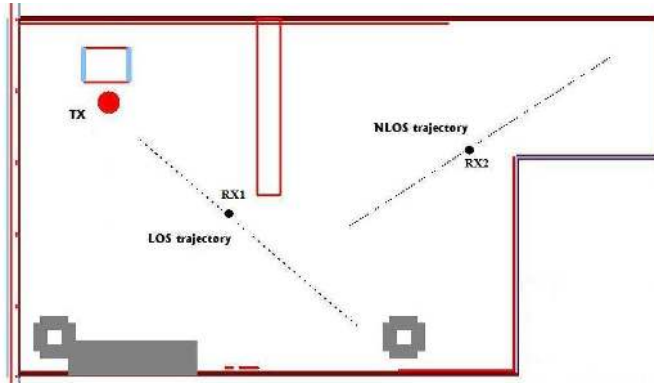


Fig. 2.21: The plan view of receiver positions along trajectories in the LOS and NLOS regions.

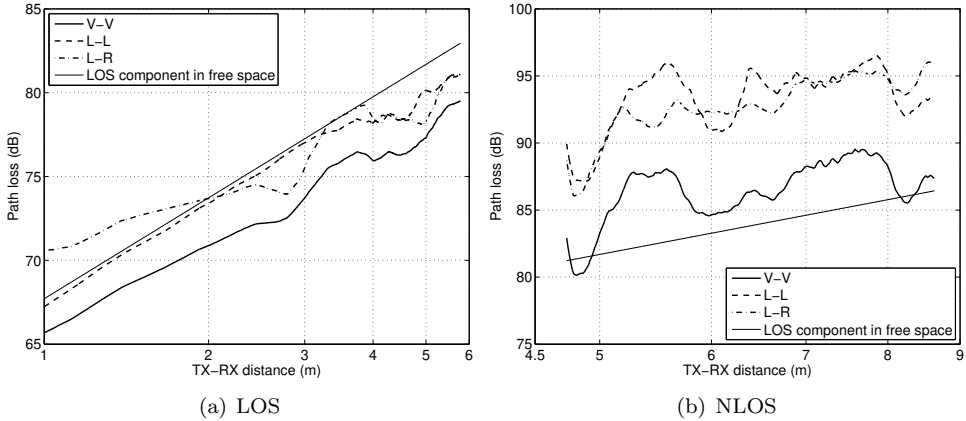


Fig. 2.22: Large-scale path loss of the V-V, L-L and L-R polarization schemes.

2.5.3.1 Large-scale path loss

In order to get an impression of large-scale fading, we took simulations over a straight trajectory under LOS conditions, as well as over a straight trajectory under NLOS conditions. To obtain the large-scale fading signal $P_{\text{large}}[\text{dB}](d)$, we take a moving average of the field strength over a distance of 100 points in a local area, which corresponds to fifty wavelengths [28]. Note that here the field strength at a position is the power addition of all the resolvable channel taps by the receiver, which is a wideband approach and different from the narrowband approach in [56]. The wideband approach is used here, since wideband transceivers will be definitely used for 60 GHz radios, as is the case for many of nowadays wireless systems.

Fig. 2.22(a) and (b) depict the large-scale path loss, which is given by $PL_{[\text{dB}]}(d) =$

$-P_{\text{large[dB]}}(d)$ for the transmit power of 0 dBm, of LOS and NLOS channels, respectively. Three TX-RX antenna polarization schemes, V-V, L-L and L-R, are considered, where “V”, “L” and “R” stand for linear vertical polarization, left-hand and right-hand circular polarization, respectively. The solid thin lines in the figures represent the path loss as a function of distance for free-space propagation of the direct wave.

From Fig. 2.22(a) and (b), we observe that the large-scale path loss is quite smooth over distance, in particular for LOS channels, while the fading obtained by the narrow-band approach is quite fluctuating [56]. The fluctuation observed in NLOS channels are due to the shadowing effect by the cabinets between the TX and RX antennas. In addition, applying circular polarization schemes does not have advantages over applying linearly polarized schemes on reducing the fluctuation of the large-scale path loss, but eventually lead to higher path losses, as seen from Fig. 2.22. The average path losses of the L-L and L-R schemes are about 2.3 and 2.5 dB higher than the V-V scheme for LOS channels, and about 6.9 and 6.3 dB higher for the NLOS channels, respectively. For the LOS channels, the difference originates from the fact that only one half of the reflected waves are received by circularly-polarized schemes, namely all even times reflected waves in case of L-L or all odd times reflected waves in case of L-R. As for the NLOS channels, such high path losses in circularly polarized schemes are caused by not only the cancellation of one half waves, but also by the reduced signal strength of diffracted waves, compared with the linearly polarized scheme.

Table 2.7 lists the log-distance model parameters according to (2.5) as the result of fitting the large-scale path loss in Fig. 2.22(a) and (b). The L-R scheme is worse than the L-L scheme under LOS conditions in terms of high path loss PL_0 and deviation Ω . This is because the dominant LOS path is effectively cancelled by the receiver because of the opposite polarizations of TX and RX antennas. Under NLOS conditions, however, it is the L-L scheme that performs worst because dominant single reflected waves are suppressed effectively leading to relatively high values of PL_0 and Ω and a low exponent of n .

Table 2.7: Log-distance model parameters of various polarization schemes fitted from Fig. 2.22 according to (2.5).

Schemes		PL_0 (dB)	n	Ω (dB)
LOS	V-V	65.8	1.7	0.52
	L-L	68.1	1.8	0.47
	L-R	70.2	1.3	0.91
NLOS	V-V	71.7	1.8	1.74
	L-L	80.2	1.6	2.00
	L-R	72.2	2.5	1.14

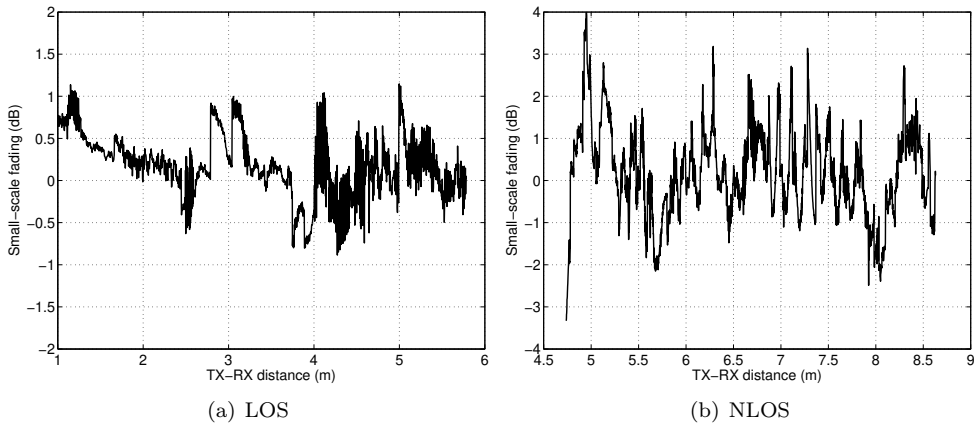


Fig. 2.23: Small-scale fading in LOS and NLOS environments.

2.5.3.2 Small-scale fading

Fig. 2.23 shows only the small-scale fading, $P_{\text{small}}[\text{dB}](d)$, of the V-V scheme in both LOS and NLOS environments, whereas the circularly-polarized schemes have similar fading levels as the V-V scheme. One can see that the small-scale fluctuation of the wideband received signal level in a local area is only about 1 and 3 dB in the LOS and NLOS channel environments, respectively, whereas narrowband received signals can fluctuate in the order of tens of dB within a range of several wavelengths. This is because a receiver with a sufficiently wide bandwidth, e.g. the bandwidth $B = 2$ GHz here, can resolve a large amount of paths with a small resolution bin in time, where the resolution bin is the inverse of the receiver bandwidth.

2.5.4 Multipath distribution in time and angular domain

Knowing both the time and angular distributions of the multipath waves is useful for designing smart antennas and transmission techniques. For instance, the beamwidth of the RX antenna or beamformer can be properly designed and the beam can be steered to the incident direction of the strongest wave, which will significantly improve the channel quality with increased SNR and meanwhile reduced multipath effects.

Fig. 2.24 and Fig. 2.25 depict the normalized power distribution of received multipath waves over time delay τ , azimuth AOD ϕ_T and azimuth AOA ϕ_R , i.e. $P(\tau, \phi_T, \phi_R)$, for the receiver RX1 in the LOS area and RX2 in the NLOS area (see Fig. 2.21), respectively. Here the elevation information is not considered because most of the waves are concentrated in the horizontal plane. Vertically polarized antennas are used here at both TX and RX side. The distribution $P(\tau, \phi_T, \phi_R)$ is obtained by taking the average over all the channels in the local area, of which the strongest wave of each channel departs from $(\phi_{T,0} = 0$ and arrives at $\phi_{R,0} = 0)$. For clarity, the

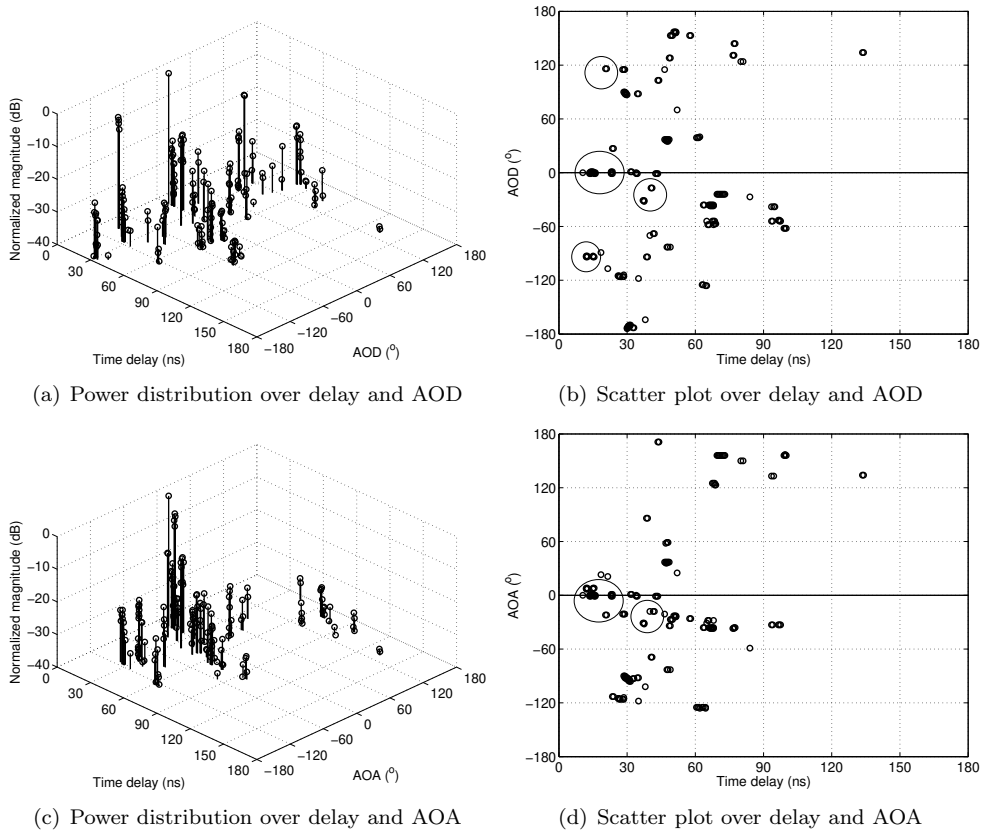


Fig. 2.24: In a LOS local area, the power distribution and scatter plot of multipath waves over time delay, AOD and AOA.

waves within the dynamic range of 20 dB, which have the most significant impact on the channel, are marked by circles. From these figures, one can see that around the direction of the direct wave in the LOS case or the strongest specular wave in the NLOS case, there are multipath waves that arrive at the receiver at different moments. In addition, there exist strong waves departing from or arriving at other directions. These multipath waves will introduce time and spatial dispersion into the channel.

If directive beams are formed at the TX and RX side, then by pointing the antenna beam to the direction of the strongest path, the multipath effect can be reduced besides the increase of the received signal level. To examine to what extent the multipath effect will be reduced with a directional antenna, the RMS delay spreads are calculated as a function of antenna beamwidths at both ends of the link.

Fig. 2.26 depicts the RMS delay spread values over the TX antenna beamwidth, when the RX antenna beamwidth is fixed, for the LOS and NLOS channels shown in

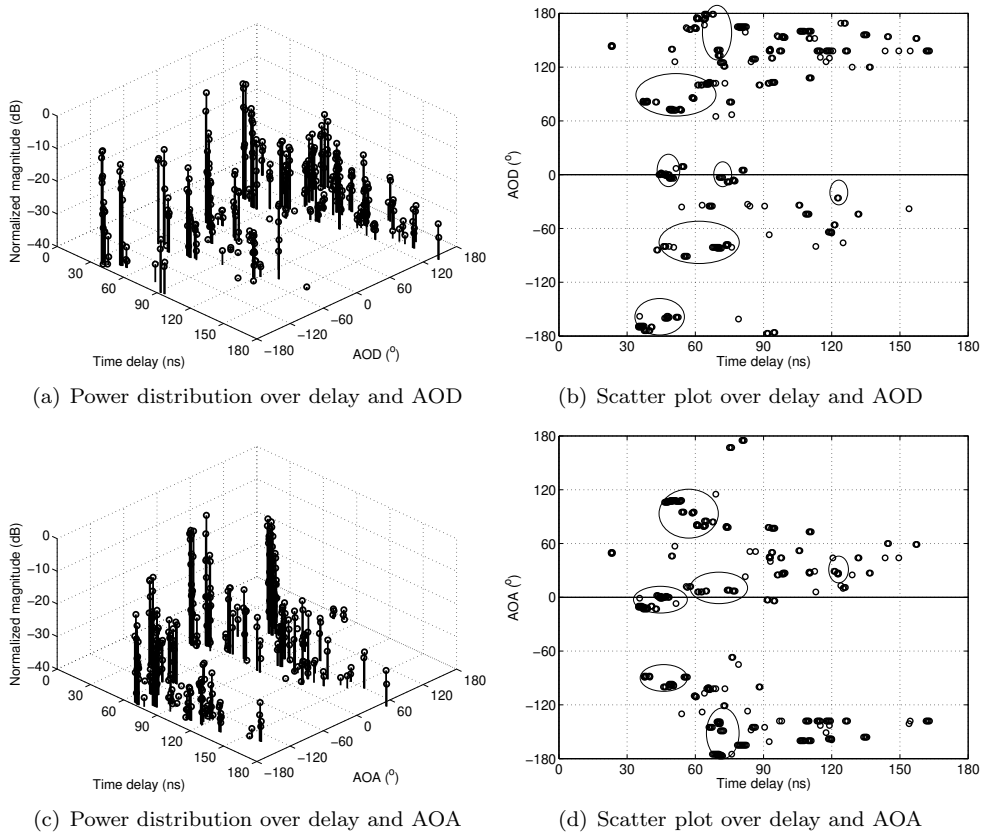


Fig. 2.25: In a NLOS local area, the power distribution and scatter plot of multipath waves over time delay, AOD and AOA.

Fig. 2.24 and 2.25, respectively. When the TX and RX antennas are isotropic, i.e. TX, RX beamwidth = 360° in Fig. 2.26(a) and (b), the RMS delay spread values are 10.9 and 13.8 ns for the LOS and NLOS channels, respectively. Reducing the beamwidth of the antenna beam that is aligned with the direction of the direct path or the specular reflected wave generally leads to reduced RMS delay spread values depending on the distribution of waves in time and angular domain. Also, different combination of TX-RX beamwidths can achieve the same RMS delay spread values. For instance, in the LOS channel, the beamwidths of $\{\text{TX}, \text{RX}\} = \{110^{\circ}, 60^{\circ}\}$ and $\{60^{\circ}, 90^{\circ}\}$ will lead to RMS delay spread values below 1 ns; in the NLOS channel, the beamwidth of $\{15^{\circ}, 15^{\circ}\}$ will achieve RMS delay spread values below 1 ns. Here the NLOS channel requires a narrower beamwidth, since more waves travel around the direction of the strongest specular reflected wave. This analysis is somewhat optimistic since, in practice, the multipath waves will be also received via side lobes of the antenna beam pattern, which were not taken into account here.

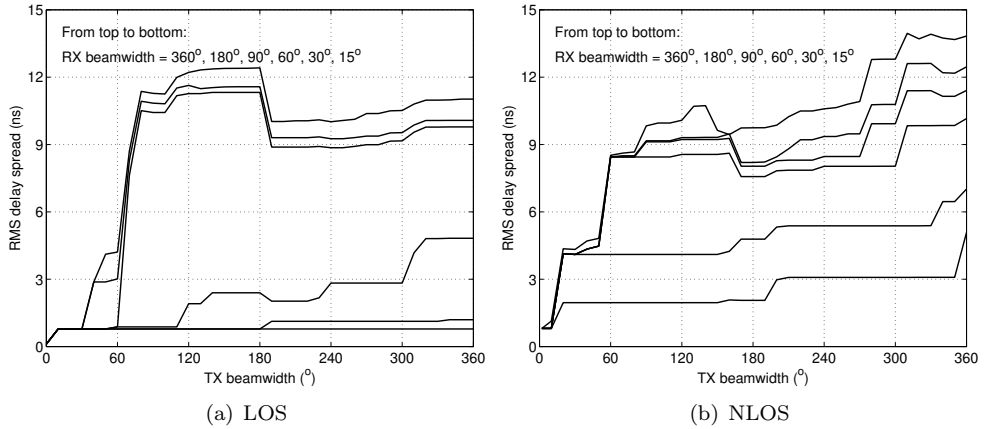


Fig. 2.26: The RMS delay spread values as the function of TX antenna beamwidths, when the RX beamwidth is fixed.

2.6 Summary and conclusions

Channel characteristics in the frequency band of 60 GHz were investigated and analyzed based on channel measurements and 3D ray tracing simulations in this chapter. Statistical channel parameters were retrieved from measurements to study the multipath effect and frequency selectivity of the radio channels configured with omnidirectional and narrow-beam antennas. By doing ray tracing simulations, linear and circular polarization schemes were examined. In addition, the multipath dispersion behavior was also investigated both in time and angular domains. The main conclusions are summarized as follows.

- The penetration and reflection losses in LOS circumstances have no significant impact on the received power level at 2 and 60 GHz, while the diffraction loss is significant for the 60-GHz signal in the NLOS area. In addition, the RMS delay spreads at 60 GHz are about half of those at 2 GHz because of blocked reflections from the neighboring rooms.
- Shadowing effects at 60 GHz result in 5 - 9 dB loss of wideband received power on average, compared with the propagation of a LOS path in free space.
- Antenna radiation patterns have a significant impact on channel properties. With omnidirectional antennas, the measured radio channel parameters are distributed in the range of $K < 3$, $\sigma_\tau > 5$ ns, $B_{c_{0.5}} < 200$ MHz and $B_{c_{0.9}} < 20$ MHz. Narrow-beam antenna configurations not only can offer the extra dBs of received signal strength to meet the link budget, but can also significantly suppress the multipath effects. With narrow-beam antennas, the channel parameters are in the range of $K > 10$, $\sigma_\tau < 1.5$ ns, $B_{c_{0.5}} > 400$ MHz and $B_{c_{0.9}} > 40$ MHz.

- Antenna beam pointing errors result in a significant drop in the received power and an increase in the RMS delay spread, in case that the beam errors are significantly larger than half of the antenna HPBW.
- The measured power delay profiles of radio channels were statistically modelled by a single cluster model, which can be simply described by a Rician K -factor, a RMS delay spread and a shape parameter.
- The RMS delay spread and the coherence bandwidth were empirically related by $\sigma_\tau \cdot B_{c_{0.9}} = 0.063$ and $\sigma_\tau \cdot B_{c_{0.5}} = 0.951$ according to the measurements. For all the measured delay profiles, number of multipath waves and the maximum excess delay can be empirically related by $L = \lceil 0.30 \cdot \tau_{\max[\text{ns}]} \rceil$.
- For the simulated wideband channels, circularly-polarized antennas schemes give no improvement on reducing both large-scale and small-scale fading, compared with the linearly-polarized scheme. The circularly-polarized schemes result in more than 2 dB in LOS conditions and more than 6 dB in NLOS conditions lower signal level on average than the linearly-polarized one.
- According to the 3D ray tracing simulations, multipath dispersion in time can be significantly reduced by using narrow-beam antennas. In the NLOS environment, it generally requires an even narrower antenna beamwidth to achieve the same RMS delay spread as in the LOS environment, because the specular wave is often comparable to other multipath waves in strength. For the considered channels here, setting the $\{\text{TX}, \text{RX}\}$ beamwidth = $\{110^\circ, 60^\circ\}, \{60^\circ, 90^\circ\}$ for the LOS channel and $\{15^\circ, 15^\circ\}$ for the NLOS channel will lead to RMS delay spread values below 1 ns.

Impact of antenna pattern on radio transmission

3.1 Introduction

As seen from channel measurements and simulations in Chapter 2, applying narrow-beam antennas in wireless communication systems increases the power level of the received signal and meanwhile reduces the multipath dispersive effect. In multi-user or multi-device environments, narrow-beam antennas can be also used to reduce co-channel interferences from other users or devices, as reported in literature [48, 62–64]. An alternative but more flexible way is to use multiple antennas for adaptive beamforming. Especially for wideband radio systems, such as the multi-gigabit-per-second system deployed at the frequency band around 60 GHz, multi-antenna beamforming is advantageous to high data rate transmission, which is generally limited by a stringent link budget requirement and multipath channel dispersions. Such a narrow-beam configuration would allow a low-complexity and low-cost design of transceiver systems [2, 59]. To design such a system, it is essential to have some quantitative knowledge about the impact of directional antennas and multi-antenna beamformers on radio transmission, so that the antenna patterns and array configurations can be properly designed.

Measurements and ray-tracing simulations have been reported in literature, including the work of Chapter 2 in this thesis, to investigate the influences of antenna directivity on radio propagation and systems [10, 59, 62, 64–67]. These studies concern specific indoor or outdoor environments at different frequency bands. In detail, the reduction of root-mean-squared (RMS) delay spread caused by antenna directivity in urban line-of-sight (LOS) street environments was experimentally studied in [64], in which the effect of main beam misalignment was observed as well. In [67], it is found that

the reduction of RMS delay spread is in the range of 35 – 55% for the directional antenna configurations in comparison with the omnidirectional one in indoor LOS environments. Extensive measurements and simulations were conducted in [66] and [10, 59, 65] for indoor LOS communication at 19.37 and 60 GHz, respectively. Their results indicated that the use of fairly narrow antenna beamwidths could be accepted for high data rate transmission in indoor LOS and some non-LOS (NLOS) scenarios.

In [48], the effect of directional antennas on signal level and level crossing rate was analyzed. In [69], a general expression was derived to compute the mean effective signal gain of mobile antennas for Rayleigh fading channels with both the vertical- and horizontal-polarizations taken into account. A theoretical analysis of the mean effective gain of antennas in Rician channels was performed in [70] and [71].

Clearly, the signal gain analysis only involves the mutual effect between the antenna power gain pattern and the power angular distribution of the multipath waves. Besides the angular information, additional information attached to the multipath wave propagation is the propagation time delay, which is the source of time dispersion. By pointing the main beam of a directional transmitter (TX) or receiver (RX) antenna to the departing or arriving direction of the strongest wave, the received signal level can be usually increased and meanwhile, the time dispersion level will be very likely reduced, as observed in Chapter 2. In case that beam pointing errors occur, optimal beamforming performance is likely not to be achieved. To our best knowledge, the theoretical analysis concerning the change of multipath time dispersion caused by directional antennas has not been reported in literature. This chapter is aimed to introduce a theoretical analysis on the impact of directional antennas at both the TX and RX sides on signal-to-noise ratio (SNR) gain at receiver, Rician channel K -factor gain and RMS delay spread reduction, in double-directional Rician channels. The influence of antenna beam pointing errors will be also included in the analysis.

The outline of this chapter is as follows. Section 3.2 describes the signal and channel models applied in this work and formulates the antenna effect on radio transmission. The applied approach in Section 3.2 will be extended to multi-antenna beamforming in Section 3.3. Based on channel and antenna assumptions introduced in Section 3.4 and the radiation patterns given in Section 3.5, examples are illustrated in Section 3.6. Finally, conclusions are discussed in Section 3.7.

3.2 Channel characteristics and antenna effect

3.2.1 The received signal

Consider a radio transmission system, where the signal propagation paths and the antennas at the TX and RX sides are positioned in the spherical coordinate system shown in Fig. 3.1. A coordinate point on a spherical surface is given by $\Omega = (\theta, \phi)$, where $\theta \in [0, \pi]$ and $\phi \in [-\pi, \pi]$ represent the elevation and azimuth angles, respectively. The notation $\Omega_x = (\theta_x, \phi_x)$ with $x \in \{T, R\}$ stands for the direction of the

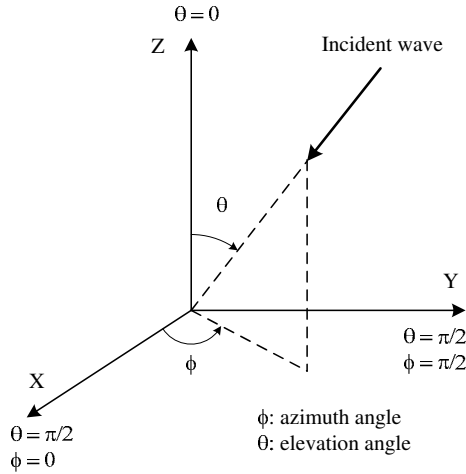


Fig. 3.1: Spherical coordinate system at the transmitter or receiver sides.

departed path at the TX side or the incident path at the RX side, respectively. Here, we assume that identical single-polarized antennas are used at the TX and RX sides. For a wideband transmission system, the baseband received signal is expressed by

$$r(t) = \sum_{l=0}^L h_l \sqrt{A_T(\Omega_{T,l}, \Psi_T) A_R(\Omega_{R,l}, \Psi_R)} \cdot u(t - \tau_l) + v(t), \quad (3.1)$$

where $A_x(\Omega_x, \Psi_x)$ is the antenna power pattern with $\Psi_x = (\theta_{x,\text{ANT}}, \phi_{x,\text{ANT}})$ the direction of the antenna main lobe, $u(t)$ is the baseband transmitted signal with $\mathbb{E}\{|u(t)|^2\} = E_s$ and $v(t)$ is the zero-mean additive white Gaussian noise (AWGN) with $\mathbb{E}\{|v(t)|^2\} = N_0$. Here $\mathbb{E}\{\cdot\}$ denotes an expectation operation. Antenna power pattern is a three-dimensional (3D) representation of the power radiation properties of an antenna and is generally described by a complicated function depending on the type of the antenna [72, 73]. The channel parameters $\{L, h_l, \tau_l, \Omega_{T,l}, \Omega_{R,l}\}$ describe the number of scattered paths, the complex amplitude, the time of arrival (TOA), the direction of departure (DOD) and the direction of arrival (DOA) of the l th multipath wave, respectively. The channel parameters of the LOS wave are $\{h_0, \tau_0, \Omega_{T,0}, \Omega_{R,0}\}$, where $\Omega_{x,0} = (\theta_{x,0}, \phi_{x,0})$.

It should be pointed out that for physical channels, the channel parameters $L, h_l, \tau_l, \Omega_{T,l}, \Omega_{R,l}$ in (3.1) are in general randomly time varying variables, because of the arbitrary movements of the transmitter, the receiver or surrounding objects. In practice, it is reasonable to assume that the channel statistic is stationary or quasi-static, i.e. *wide-sense stationary* (WSS), within the time duration of one transmitted symbol or one data packet. For this reason, the time dependency of the channel parameters has been omitted in (3.1). Moreover, signals coming via different paths will experience uncorrelated attenuations and time delays, which is referred to as *uncorrelated scattering* (US). In the rest of the chapter, time-invariant channels in a

local area will be considered under the WSSUS assumption.

Moreover, the TX and RX filters are not explicitly included in the signal model (3.1). But any linearly filtering effect occurring in the signal transmission chain can be incorporated into the channel response h_l , as will be pointed out in Chapter 4.

3.2.2 Double-directional channel model without antenna effect

The concept of *double-directional channels* was proposed earlier and applied to take into account the angular information of wave propagation at both the TX and RX sides for channel characterization [25, 74], in addition to the propagation delay information. The description of double-directional channels is particularly important for systems with multiple antennas at both the TX and RX sides. A schematic illustration of the double-directional channel is given in Fig. 3.2. From the received signal

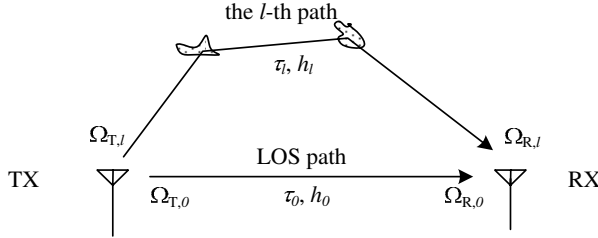


Fig. 3.2: A double-directional channel.

model (3.1), the instantaneous delay-DOD-DOA channel function and the instantaneous power delay-DOD-DOA spectrum of the channel with isotropic antennas can be retrieved as

$$h(\tau, \Omega_T, \Omega_R) = \sum_{l=0}^L h_l \delta(\tau - \tau_l) \delta(\Omega_T - \Omega_{T,l}) \delta(\Omega_R - \Omega_{R,l}) \quad (3.2)$$

$$P_I(\tau, \Omega_T, \Omega_R) = \sum_{l=0}^L |h_l|^2 \delta(\tau - \tau_l) \delta(\Omega_T - \Omega_{T,l}) \delta(\Omega_R - \Omega_{R,l}), \quad (3.3)$$

respectively. Under the WSSUS assumption, the local-mean power delay-DOD-DOA spectrum can be obtained by taking the average over instantaneous spectra in a local area and can be expressed by [25, 75]

$$\begin{aligned} P(\tau, \Omega_T, \Omega_R) &= \mathbb{E}\{P_I(\tau, \Omega_T, \Omega_R)\} \\ &= \mathbb{E}\{|h_0|^2\} \delta(\tau) \delta(\Omega_T - \Omega_{T,0}) \delta(\Omega_R - \Omega_{R,0}) + P_S(\tau, \Omega_T, \Omega_R), \end{aligned} \quad (3.4)$$

where

$$P_S(\tau, \Omega_T, \Omega_R) = \mathbb{E}\left\{ \sum_{l=1}^L |h_l|^2 \delta(\tau - \tau_l) \delta(\Omega_T - \Omega_{T,l}) \delta(\Omega_R - \Omega_{R,l}) \right\} \quad (3.5)$$

is the spectrum caused by scattered multipath waves. For convenience, the time of arrival of the LOS path was set to be $\tau_0 = 0$ in (3.4). Moreover, the directions of departure and arrival belong to certain angular regions, $\Omega_T \in U_T$ and $\Omega_R \in U_R$, respectively, which are not necessarily continuous in space.

Notice that $P(\cdot)$ and $P_S(\cdot)$ denote the channel power spectra with and without the LOS path, respectively, for isotropic radiation patterns. The joint and separate spectra should be distinguished according to the parameters within (\cdot) . Later, similar notations $P'(\cdot)$ and $P'_S(\cdot)$ will be introduced to represent the channel spectra for non-isotropic antenna radiation patterns.

Next, the power delay spectrum (PDS, or power delay profile) and power DOD-DOA spectrum can be obtained by

$$\begin{aligned} P(\tau) &= \iint P(\tau, \Omega_T, \Omega_R) d\Omega_T d\Omega_R \\ &= \mathbb{E}\{|h_0|^2\} \delta(\tau) + \underbrace{\iint P_S(\tau, \Omega_T, \Omega_R) d\Omega_T d\Omega_R}_{P_S(\tau)}, \end{aligned} \quad (3.6)$$

$$\begin{aligned} P(\Omega_T, \Omega_R) &= \int P(\tau, \Omega_T, \Omega_R) d\tau \\ &= \mathbb{E}\{|h_0|^2\} \delta(\Omega_T - \Omega_{T,0}) \delta(\Omega_R - \Omega_{R,0}) + \underbrace{\int P_S(\tau, \Omega_T, \Omega_R) d\tau}_{P_S(\Omega_T, \Omega_R)}, \end{aligned} \quad (3.7)$$

where $d\Omega = \sin(\theta)d\theta d\phi$ is a solid angle, and $P_S(\tau)$ and $P_S(\Omega_T, \Omega_R)$ are the delay spectrum and DOD-DOA spectrum of the scattered waves, respectively. In addition, the separate DOD and DOA spectra can be defined by

$$P_S(\Omega_T) = \oint P_S(\Omega_T, \Omega_R) d\Omega_R \quad (3.8)$$

$$P_S(\Omega_R) = \oint P_S(\Omega_T, \Omega_R) d\Omega_T, \quad (3.9)$$

respectively.

When a stationary LOS path wave appears during data transmission, the propagation channel is characterized as a Rician fading channel and the L scattered paths are Rayleigh faded independently with zero mean. Here we define the Rician K -factor to characterize Rician fading channels. Rician K -factor is the ratio between the average powers contributed by the LOS path and the scattered paths, as defined in (2.9). For convenience, we repeat the definition here

$$K = \frac{\mathbb{E}\{|h_0|^2\}}{\mathbb{E}\left\{\sum_{l=1}^L |h_l|^2\right\}}. \quad (3.10)$$

For a wireless channel with a larger Rician K -factor, the received signal level over time intends to be less fluctuated. In addition to Rician K -factor, RMS delay spread

of the channel is defined in (2.12), which is repeated here

$$\sigma_\tau = \sqrt{\frac{\int \tau^2 P(\tau) d\tau}{\int P(\tau) d\tau} - \left(\frac{\int \tau P(\tau) d\tau}{\int P(\tau) d\tau} \right)^2} = \sqrt{\overline{\tau^2} - \bar{\tau}^2}, \quad (3.11)$$

where $\bar{\tau} = \frac{\int \tau P(\tau) d\tau}{\int P(\tau) d\tau}$ is the mean excess delay and $\overline{\tau^2} = \frac{\int \tau^2 P(\tau) d\tau}{\int P(\tau) d\tau}$ is the second moment of the delay spectrum $P(\tau)$. The RMS delay spread σ_τ is generally used to characterize the time dispersion of the channel.

If the channel power is normalized in a local area, i.e. $\mathbb{E} \left\{ \sum_{l=0}^L |h_l|^2 \right\} = 1$, then the average SNR at receiver is

$$\rho = \frac{\mathbb{E} \left\{ \sum_{l=0}^L \sum_{l'=0}^L h_l h_{l'}^* u(t - \tau_l) u^*(t - \tau_{l'}) \right\}}{\mathbb{E} \{|v(t)|^2\}} = \frac{E_s}{N_0} \quad (3.12)$$

when isotropic antennas are applied, where the scattered waves are assumed to be uncorrelated with each other and independent of the transmit signal. Here the superscript * denotes complex conjugate. Also, the following equations are valid

$$\begin{aligned} \iiint P(\tau, \Omega_T, \Omega_R) d\tau d\Omega_T d\Omega_R &= \int P(\tau) d\tau \\ &= \iint P(\Omega_T, \Omega_R) d\Omega_T d\Omega_R = \oint P(\Omega_x) d\Omega_x = 1, \end{aligned} \quad (3.13)$$

$$\begin{aligned} \iiint P_S(\tau, \Omega_T, \Omega_R) d\tau d\Omega_T d\Omega_R &= \int P_S(\tau) d\tau \\ &= \iint P_S(\Omega_T, \Omega_R) d\Omega_T d\Omega_R = \oint P_S(\Omega_x) d\Omega_x = \frac{1}{K+1}, \end{aligned} \quad (3.14)$$

where the first and second equations represent the total channel power and the power of the scattered waves, respectively.

3.2.3 Impact of antenna radiation pattern on propagation channel

When non-isotropic antennas are applied in the channel, the joint power delay-DOD-DOA spectrum becomes

$$P'(\tau, \Omega_T, \Omega_R) = P(\tau, \Omega_T, \Omega_R) A_T(\Omega_T, \Psi_T) A_R(\Omega_R, \Psi_R) \quad (3.15)$$

and the separate spectra can be obtained accordingly. In particular, the power delay spectrum becomes

$$\begin{aligned} P'(\tau) &= \iint P'(\tau, \Omega_T, \Omega_R) d\Omega_T d\Omega_R \\ &= \mathbb{E} \{|h_0|^2\} A_T(\Omega_{T,0}, \Psi_T) A_R(\Omega_{R,0}, \Psi_R) \delta(\tau) + P'_S(\tau), \end{aligned} \quad (3.16)$$

where the delay spectrum of scattered waves is

$$P'_S(\tau) = \iiint P_S(\tau, \Omega_T, \Omega_R) A_T(\Omega_T, \Psi_T) A_R(\Omega_R, \Psi_R) d\Omega_T d\Omega_R. \quad (3.17)$$

An explicit expression of $P'_S(\tau)$ can be derived when the antenna radiation patterns and the power-delay-angular spectrum $P_S(\tau, \Omega_T, \Omega_R)$ are given. Power delay profiles obtained from measurements, for instance those given in Fig. 2.7-2.10, are already the result of integrating joint power-delay-angular distribution affected by TX and RX antenna radiation patterns over the angular variables.

To investigate the impact of antenna radiation patterns on the transmission system and channel, we consider the change of the Rician K -factor, the RMS delay spread and the change of the SNR caused by non-isotropic radiation patterns. First, the gain of the Rician K -factor is defined as

$$G_K = \frac{K'}{K} \quad (3.18)$$

which describes how the dominance of the LOS wave is relatively changed due to the antenna power pattern. Second, the gain of the SNR

$$G_\rho = \frac{\rho'}{\rho} \quad (3.19)$$

quantifies the SNR change at receiver. Third, the relative change of RMS delay spread

$$R_{\sigma_\tau} = \frac{\sigma_\tau - \sigma'_\tau}{\sigma_\tau} \cdot 100\% \quad (3.20)$$

characterizes the relative change of multipath dispersion. Here the two parameter sets $\{K, \rho, \sigma_\tau\}$ and $\{K', \rho', \sigma'_\tau\}$ are for the channels configured with isotropic and non-isotropic antennas, respectively. These parameters are defined to formulate the impact of antenna radiation patterns on propagation channels and thus useful for the purpose of system design. The larger the values of $\{G_K, G_\rho, R_{\sigma_\tau}\}$, the larger is the channel quality improvement.

Here we first have a look at the effect of antenna radiation patterns on the channel power contributed by scattered waves. When non-isotropic antenna radiation patterns are used in the channel, the power angular spectrum of the scattered waves becomes

$$P'_S(\Omega_T, \Omega_R) = P_S(\Omega_T, \Omega_R) A_T(\Omega_T, \Psi_T) A_R(\Omega_R, \Psi_R), \quad (3.21)$$

which is integrated to obtain the power of the scattered waves. Therefore, the channel power gain of the scattered waves, E_A , due to TX-RX antenna radiation patterns can be readily obtained by

$$\begin{aligned} E_A &= \frac{\iint P'_S(\Omega_T, \Omega_R) d\Omega_R}{\iint P_S(\Omega_T, \Omega_R) d\Omega_T d\Omega_R} \\ &= (K + 1) \iiint P_S(\Omega_T, \Omega_R) A_T(\Omega_T, \Psi_T) A_R(\Omega_R, \Psi_R) d\Omega_T d\Omega_R, \end{aligned} \quad (3.22)$$

where $\iint P_S(\Omega_T, \Omega_R) d\Omega_T d\Omega_R = \frac{1}{K+1}$. The parameter E_A characterizes how the total channel power contributed by the scattered waves will change when non-isotropic antenna radiation patterns are used in the channel.

Now we derive explicit expressions of the impact parameters (3.18)-(3.20). Note that the channel power of the LOS path, $\mathbb{E}\{|h_0|^2\} = \frac{K}{K+1}$, is scaled by the TX and RX antenna gains, $A_T(\Omega_{T,0}, \Psi_T)$ and $A_R(\Omega_{R,0}, \Psi_R)$, along the LOS direction $\Omega_{x,0} = (\theta_{x,0}, \phi_{x,0})$. In addition, the power of scattered waves, $\mathbb{E}\left\{\sum_{l=1}^L |h_l|^2\right\} = \frac{1}{K+1}$, is scaled by the gain E_A . Therefore, the received SNR in the non-isotropic channel becomes

$$\rho' = \frac{E_s}{N_0} \left(\frac{K}{K+1} A_T(\Omega_{T,0}, \Psi_T) A_R(\Omega_{R,0}, \Psi_R) + \frac{1}{K+1} E_A \right) \quad (3.23)$$

and the Rician K -factor of the non-isotropic channel is

$$K' = \frac{K}{E_A} A_T(\Omega_{T,0}, \Psi_T) A_R(\Omega_{R,0}, \Psi_R). \quad (3.24)$$

Following the definition (3.18) and (3.19), the Rician K -factor gain and SNR gain can be readily obtained as follows

$$G_K = \frac{A_T(\Omega_{T,0}, \Psi_T) A_R(\Omega_{R,0}, \Psi_R)}{E_A}, \quad (K \neq 0) \quad (3.25)$$

$$G_\rho = \beta E_A, \quad (3.26)$$

where $\beta = \frac{K G_K + 1}{K + 1}$. In case that an isotropic channel is Rayleigh faded, i.e. $K = 0$, the resulting non-isotropic channel is still a Rayleigh fading channel because of $K' = 0$. Besides the Rician K -factor gain and SNR gain, the reduction of RMS delay spread is derived as

$$R_{\sigma_\tau} = 1 - \sqrt{\frac{\overline{\tau'^2} - \overline{\tau}^2}{\overline{\tau^2} - \overline{\tau}^2}} \quad (3.27)$$

according to (3.11) and (3.19), where the mean excess delay $\overline{\tau}' = \frac{\int \tau P'(\tau) d\tau}{\int P'(\tau) d\tau}$ and the second moment of the power delay spectrum $P'(\tau)$ is $\overline{\tau'^2} = \frac{\int \tau^2 P'(\tau) d\tau}{\int P'(\tau) d\tau}$ for the non-isotropic channel.

Clearly, for a certain power delay-DOD-DOA spectrum and antenna patterns, the impact of non-isotropic antennas on the channel can be analytically studied. Note that the Rician K -factor gain and the SNR gain are independent of the power delay spectrum. For a fixed orientation of the antennas, the SNR gain G_ρ depends only on the Rician K -factor and the gain of the scattered waves. In addition, the RMS delay spread reduction is determined by the first and second moments of the delay spectra before and after non-isotropic antennas are applied. These moments are related to the Rician K -factor and the parameter E_A .

3.3 Extension to multi-antenna beamforming

The purpose of applying directional antennas in many applications is to satisfy the link budget requirement at receiver and meanwhile to reduce the multipath effect on data transmission. However, besides the involvement of adjusting the main beam to a certain direction, the antenna beamwidth can not be designed as narrow as we like due to the finite size of the antenna, which results in a reduced directivity. In comparison, multiple antennas can be applied to adaptively form a desired beam pattern having its maximum gain along the desired direction. In this regard, adaptive multi-antenna beamforming becomes a better solution to increase the mobility of a transceiver system, to further increase the directivity and to reduce the multipath effect. To this end, this section will focus on the impact of multi-antenna beamforming on radio transmission.

3.3.1 MIMO channel model

Without losing generality, here we consider uniform linear arrays (ULA) used at the TX and RX sides. The first element in the array is positioned at the origin. The array direction is represented by $\Upsilon_x = (\theta_{x, \text{ULA}}, \phi_{x, \text{ULA}})$ with $x \in \{\text{T}, \text{R}\}$ as illustrated in Fig. 3.3. Assuming locally plane waves at both the TX and RX, the l th multipath wave propagation between any pair of transmitting and receiving elements can be modelled to experience the same amplitude attenuation but different phases due to path length differences.

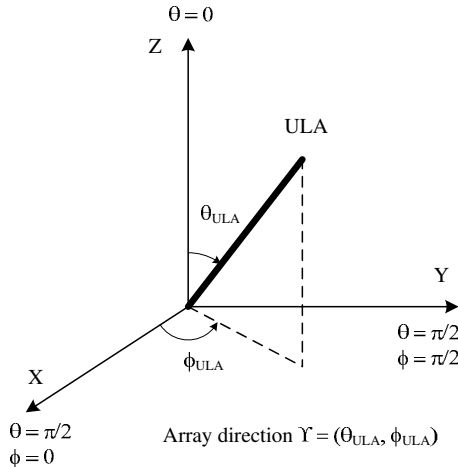


Fig. 3.3: A ULA antenna array in the coordinate system. Each element has the same orientation and main lobes are perpendicular to the array direction.

For the antenna arrays composed of P antenna elements and Q antenna elements at the TX and RX sides, respectively, the multipath MIMO channel response matrix can

be described by

$$\mathbf{H}(\tau, \Omega_T, \Omega_R) = \sum_{l=0}^L \mathbf{H}_l \delta(\tau - \tau_l) \delta(\Omega_T - \Omega_{T,l}) \delta(\Omega_R - \Omega_{R,l}), \quad (3.28)$$

where

$$\mathbf{H}_l = h_l \mathbf{a}_R(\Omega_{R,l}, \Upsilon_R) \mathbf{a}_T^H(\Omega_{T,l}, \Upsilon_T), \quad (3.29)$$

is the channel matrix of the l th path, the superscript \mathcal{H} represents the Hermitian operation and $\mathbf{a}_x = \mathbf{a}_x(\Omega_x, \Upsilon_x)$ is the array response vector of the direction Ω_x, l for the array direction Υ_x . The array response either at the TX or RX side can be expressed by

$$\mathbf{a}_x(\Omega_x, \Upsilon_x) = \left[1 e^{j\varepsilon_x} \dots e^{j(M-1)\varepsilon_x} \right]^T, \quad (3.30)$$

where the superscript T denotes the transpose operation, the relative phase difference between elements

$$\varepsilon_x = \frac{2\pi d}{\lambda} (\sin \theta_x \sin \theta_{x, \text{ULA}} \cos[\phi_x - \phi_{x, \text{ULA}}] + \cos \theta_x \cos \theta_{x, \text{ULA}}), \quad (3.31)$$

λ is the wavelength, d is the antenna element spacing and $M \in \{P, Q\}$ is the number of elements.

3.3.2 Multi-antenna beamforming

Suppose that ULA arrays with non-isotropic elements are applied and a narrowband beamforming is performed at both the TX and RX sides. All the elements are assumed to have the same power pattern with the same orientation, i.e., Ψ_x is the same for all the elements either at the TX or RX side. Therefore, the weighted output of the beamformer at receiver is written as

$$r'(t) = \sum_{l=0}^L h_l \underbrace{\sqrt{A_R(\Omega_{R,l}, \Psi_R)} \mathbf{w}_R^T \mathbf{a}_R}_{\sqrt{C_R(\Omega_{R,l}, \Psi_R, \Upsilon_R)}} \underbrace{\sqrt{A_T(\Omega_{T,l}, \Psi_T)} \mathbf{a}_T^H \mathbf{w}_T}_{\sqrt{C_T(\Omega_{T,l}, \Psi_T, \Upsilon_T)}} u(t - \tau_l) + \mathbf{w}_R^T \mathbf{v}, \quad (3.32)$$

where the total transmit power is equally allocated to each element, i.e. $\mathbb{E}\{|u(t)|^2\} = \frac{E_s}{P}$, the weights satisfy $\mathbf{w}_T^H \mathbf{w}_T = P$ and $\mathbf{w}_R^H \mathbf{w}_R = Q$, and the elements of the noise vector $\mathbf{v} = [v_1(t) v_2(t) \dots v_Q(t)]^T$ at receiver are independently and identically distributed (i.i.d.) AWGN with the variance N_0 . The phase information of $\mathbf{w}_R^T \mathbf{a}_R$ and $\mathbf{a}_T^H \mathbf{w}_T$ has been included in the channel impulse response h_l , which will not affect the following derivations. The synthesized power pattern C_x is composed of the antenna pattern A_x and the array pattern B_x , according to

$$C(\Omega_x, \Psi_x, \Upsilon_x) = A(\Omega_x, \Psi_x) B(\Omega_x, \Upsilon_x), \quad (3.33)$$

where the array pattern

$$B_x(\Omega_x, \Upsilon_x) = |\mathbf{a}_x^H \mathbf{w}_x|^2. \quad (3.34)$$

Note that the signal model (3.32) has the same form as the model (3.1) of the single antenna case if replacing the antenna pattern A_x by the synthesized pattern C_x . Therefore, the joint impact of the element pattern and the multi-antenna beamforming on the channel can be analyzed by the same approach as in Section 3.2.3. Keep in mind that *the computation of impact factors here is always relative to the case of the single-input-single-output channel configured with isotropic antennas*. Particularly, the Rician K -factor gain G_K and RMS delay spread reduction G_{σ_τ} are obtained by simply replacing the antenna pattern $A_x(\Omega_{x,n}, \Psi_x)$ by the synthesized pattern $C_x(\Omega_{x,n}, \Psi_x, \Upsilon_x)$ into (3.25) and (3.27), respectively. But the expression of the SNR gain here is somewhat different. Bearing in mind that the transmit power in each element is $\frac{1}{P}$ times the total transmit power and the total receiver noise is Q times the noise power at each element, the SNR gain $G_\rho = \frac{\rho'}{\rho}$ is calculated as

$$G_\rho = \frac{\frac{E_s}{P} \cdot \left(\frac{K}{K+1} C_T(\Omega_{T,0}, \Psi_T, \Upsilon_T) C_R(\Omega_{R,0}, \Psi_R, \Upsilon_R) + \frac{1}{K+1} E_C \right)}{Q N_0 \cdot \rho} = \frac{\beta E_C}{PQ}, \quad (3.35)$$

where $\rho = \frac{E_s}{N_0}$ and $\beta = \frac{K G_K + 1}{K+1}$. The Rician K -factor gain is given by

$$G_K = \frac{C_T(\Omega_{T,0}, \Psi_T, \Upsilon_T) C_R(\Omega_{R,0}, \Psi_R, \Upsilon_R)}{E_C}, \quad (K \neq 0) \quad (3.36)$$

and the power gain of the scattered waves, E_C , is given by

$$E_C = (K+1) \iiint P_S(\Omega_T, \Omega_R) C_T(\Omega_T, \Psi_T, \Upsilon_T) C_R(\Omega_R, \Psi_R, \Upsilon_R) d\Omega_T d\Omega_R \quad (3.37)$$

for the synthesized pattern. Note that the results in Section 3.2.3 for single TX and RX elements are merely a special case in this section.

3.4 Assumptions on the propagation channel

As seen in Section 3.2, by knowing the power distributions of the radio waves in time and angular domain, the impact of directional antennas and multi-antenna beamformers on the channel can be analyzed. When isotropic antennas are used, the power distributions of radio waves will be very dependent on the environment. Many researchers have performed channel measurements to study the joint delay-angular spectra in certain environments [38, 76–79]. The measured delay-angular spectra can be applied to study the impact of antennas on channels. Moreover, statistical models for the joint channel spectrum $P(\tau, \Omega_T, \Omega_R)$ can be applied as an input to study the impact of antennas and beamformers. However, it is arduous to find a general

form or an explicit function for describing the joint multi-dimensional information of propagation channels. In this regard, the integration in (3.17) is not a trivial task for the purpose of analytical formulation. To solve this limitation, a general approach is to assume that the joint delay-angular spectrum can be decomposed into separate spectra in time and angular domain [38, 77]. Based on the decomposition, the integration in (3.17) could be relaxed as will be shown in Section 3.6, since statistical models for separate delay spectra and angular spectra have been widely studied and are available in literature.

3.4.1 Separability of angular-delay spectrum in a single cluster model

Assume the joint power spectrum, $P_S(\tau, \Omega_T, \Omega_R)$, of scattered waves is densely distributed in delay and angles and the joint spectrum is proportional to the power angular spectrum at a specific time delay and proportional to the power delay spectrum at a specific direction, i.e.

$$P_S(\tau, \Omega_T, \Omega_R)|_\tau \propto P_S(\Omega_T, \Omega_R) \text{ and } P_S(\tau, \Omega_T, \Omega_R)|_{(\Omega_T, \Omega_R)} \propto P_S(\tau), \quad (3.38)$$

then the spectrum can be decomposed as the product of delay spectrum and angular spectrum given by [77]

$$\text{Decomposition 1: } P_S(\tau, \Omega_T, \Omega_R) = c_1 P_S(\tau) P_S(\Omega_T, \Omega_R), \quad (3.39)$$

where the constant $c_1 = K + 1$ can be determined from (3.6)-(3.14). The decomposition has been experimentally validated for typical outdoor urban channel environments in [77]. In indoor environments, scattered waves become even denser in the directions of departure and arrival. In addition, it is reasonable to assume that the angular spectra of DOD and DOA of scattered waves are independent of each other. This leads to the following decomposition

$$\text{Decomposition 2: } P_S(\Omega_T, \Omega_R) = c_2 P_S(\Omega_T) P_S(\Omega_R), \quad (3.40)$$

where the constant $c_2 = K + 1$. Combining (3.39) and (3.40) leads to the decomposition

$$P_S(\tau, \Omega_T, \Omega_R) = (K + 1)^2 P_S(\tau) P_S(\Omega_T) P_S(\Omega_R). \quad (3.41)$$

With the decomposition in (3.41), the power delay spectrum of scattered waves in (3.17) becomes

$$P'_S(\tau) = F_{T,C} F_{R,C} P_S(\tau) \quad (3.42)$$

due to the synthesized pattern (3.33). Here the total channel power gain of scattered waves

$$E_C = F_{T,C} F_{R,C} \quad (3.43)$$

are the product of the gains contributed by the synthesized patterns at the TX and RX sides separately, where

$$F_{x,C} = (K + 1) \oint P_S(\Omega_x) C_x(\Omega_x, \Psi_x, \Upsilon_x) d\Omega_x. \quad (3.44)$$

Taking the separate spectra into (3.36), (3.35) and (3.27), the impact of antennas and beamformer on channels can be analytically obtained.

3.4.2 Uniform power distribution in angular domain

If the channel power of scattered waves are uniformly distributed in the angular region

$$U_x = (\theta_x \in [\theta_x^L, \theta_x^H], \phi_x \in [\phi_x^L, \phi_x^H]) \quad (3.45)$$

with $x \in \{T, R\}$ for the DOD and DOA, respectively, then the power angular spectra (PAS) of the scattered waves can be expressed by

$$P_S(\Omega_x) = \begin{cases} \frac{1}{(K+1)(\phi_x^H - \phi_x^L)(\cos \theta_x^L - \cos \theta_x^H)} & \Omega_x \in U_x \\ 0 & \text{otherwise.} \end{cases} \quad (3.46)$$

Now the channel power gain of the scattered waves becomes

$$F_{x,C} = \frac{\oint_{U_x} C_x(\Omega_x, \Psi_x, \Upsilon_x) d\Omega_x}{(\phi_x^H - \phi_x^L)(\cos \theta_x^L - \cos \theta_x^H)}, \quad (3.47)$$

which is a constant for the waves distributed in a certain region. In the following, two special cases are presented for the uniform power angular spectra.

3.4.2.1 Uniform power angular spectrum in a sphere

The channel power of the scattered waves is uniformly distributed in a sphere for DOD and DOA, i.e. $U_x = (\theta_x \in [0, \pi], \phi_x \in [-\pi, \pi])$. Then the gain of the scattered waves caused by the synthesized pattern (3.33) becomes

$$F_{x,C} = \frac{1}{4\pi} \oint C_x(\Omega_x, \Psi_x, \Upsilon_x) d\Omega_x. \quad (3.48)$$

In particular, the gain caused by a single antenna is given by $F_{x,A} = 1$ independent of the orientation and the type of antennas, since the antenna pattern always satisfies $\oint A_x(\Omega_x, \Psi_x) d\Omega_x = 4\pi$ [73].

3.4.2.2 Uniform power angular spectrum in the azimuth plane

The power of the scattered waves is uniformly distributed in the azimuth plane, i.e. $U_x = (\theta_x \rightarrow \frac{\pi}{2}, \phi_x \in [-\pi, \pi])$. The gain of the scattered waves caused by the

synthesized pattern (3.33) can be obtained by

$$\begin{aligned} F_{x,C} &= \lim_{\theta_x^L, \theta_x^H \rightarrow \frac{\pi}{2}} \frac{\int_{-\pi}^{\pi} \int_{\theta_x^L}^{\theta_x^H} C_x(\Omega_x, \Psi_x, \Upsilon_x) \sin(\theta_x) d\theta_x d\phi_x}{2\pi (\cos \theta_x^L - \cos \theta_x^H)} \\ &= \frac{1}{2\pi} \int_{-\pi}^{\pi} C_x(\phi_x, \psi_x, \varphi_x) d\phi_x, \end{aligned} \quad (3.49)$$

where $C_x(\phi_x, \psi_x, \varphi_x)$ is the pattern in the azimuth plane. In particular, for an isotropic antenna pattern, the gain of scattered waves is $F_{x,A} = 1$. In addition, for a cosine-shaped antenna power pattern A , that will be introduced in (3.52), the gain is equal to

$$F_{x,A} = \frac{1}{2\pi} \int_{-\frac{\pi}{2}}^{\frac{\pi}{2}} 2(2q+1) \cos^{2q} \phi_x d\phi_x = \frac{(2q+1)\Gamma[\frac{1}{2}+q]}{\sqrt{\pi}\Gamma[1+q]} \quad (3.50)$$

in case the main lobe direction is in the azimuth plane, where $\Gamma[z] = \int_0^{\infty} t^{z-1} e^{-t} dt$ is the Gamma function.

3.4.3 Shape of power delay spectrum

It can be seen from (3.27) that the reduction of RMS delay spread caused by non-isotropic antennas depends on the first and the second moments of the power delay spectra before and after introducing non-isotropic antennas. Under the decomposition of (3.41), the delay spectrum shape of scattered waves will not be changed by the use of non-isotropic antennas. Therefore, if the spectrum shape is known, the reduction of RMS delay spread can be readily computed. For an exponentially decaying shape, the power delay spectrum can be expressed by

$$P(\tau) = \begin{cases} 0 & \tau < 0 \\ \frac{K}{K+1} \delta(\tau) & \tau = 0 \\ P_S(\tau) & \tau > 0, \end{cases} \quad (3.51)$$

where $P_S(\tau) = \frac{\gamma}{K+1} e^{-\gamma\tau}$ is the PDS of scattered waves and γ is the decay exponent.

3.5 Power patterns of antenna elements and beamformer

Directivity and *half-power beamwidth* (HPBW) are two important parameters among others to describe an antenna pattern. Here we introduce the cosine-shaped power pattern of antenna elements that will be used in Section 3.6. Throughout this chapter, the applied antennas are considered to be single polarized.

3.5.1 Cosine-shaped antenna pattern

For a cosine-shaped antenna pattern positioned in the spherical coordinate system (see Fig. 3.1) with the main lobe direction aligned with the X -axis, i.e. $\Psi_x = (\frac{\pi}{2}, 0)$, the 3D power pattern is expressed by

$$A_x(\theta_x, \phi_x) = 2(2q_x + 1)(\sin \theta_x \cos \phi_x)^{2q_x} \quad (3.52)$$

with $\theta_x \in [0, \pi]$ and $\phi_x \in [-\frac{\pi}{2}, \frac{\pi}{2}]$, where $x \in \{T, R\}$ stands for TX or RX antennas, respectively. The parameter $q_x \geq 0$ is used to adjust the pattern shape and can be related to the HPBW of the pattern. For such an antenna pattern, the HPBWs on the principal azimuth and elevation planes are the same and expressed by

$$\sigma_{A_x} = 2 \arccos \left(2^{-\frac{1}{2q_x}} \right). \quad (3.53)$$

The larger the value of q_x , the narrower the antenna beamwidth σ_{A_x} . The cosine-shaped pattern has no side lobes but is a good approximation of the power patterns for many types of elementary antennas, such as horn, patch and dipole antennas [73].

3.5.2 Beam pattern of conventional beamformer

In Section 3.3.2, a general approach has been described for a multi-antenna beamforming of ULA arrays. For a conventional beamformer applied in the multipath MIMO channel (3.28), the main beams at the TX and RX sides are steered to the direction of the direct path by adjusting the phase of the weight at each antenna element. In such a case, the weight ideally equals the conjugate of the array vector at the direction of the LOS path $\Omega_{x,0} = (\theta_{x,0}, \phi_{x,0})$, i.e.

$$\mathbf{w}_x = \mathbf{a}_x^*(\Omega_{x,0}, \Upsilon_x) \quad (3.54)$$

for $x \in \{T, R\}$. For the non-ideal weight

$$\mathbf{w}_x = \mathbf{a}_x^*(\Omega'_{x,0}, \Upsilon_x), \quad (3.55)$$

the formed main beam is pointing at the direction $\Omega'_{x,0} = (\theta'_{x,0}, \phi'_{x,0})$, instead of the direction of the LOS wave $\Omega_{x,0}$. This non-ideal beamforming could happen in practical situations, where the direction of the LOS wave cannot be perfectly estimated.

Without losing generality, we consider ULA arrays at the TX and RX sides positioned along the Y -axis (see Fig. 3.3), i.e., $\Upsilon_x = (\theta_{x, \text{ULA}}, \phi_{x, \text{ULA}}) = (\frac{\pi}{2}, \frac{\pi}{2})$, and each element has the cosine-shaped power pattern with the same beamwidth and orientation. The main lobe direction of each element is in the X - Y plane, i.e. $\Psi_x = (\theta_{x, \text{ANT}}, \phi_{x, \text{ANT}}) = (\frac{\pi}{2}, \phi_{x, \text{ANT}})$, and then the synthesized pattern of a non-ideal beamformer (3.55) is readily obtained,

$$C_x(\Omega_x, \Omega'_{x,0}, \Psi_x) = A_x(\theta_x, \phi_x - \phi_{x, \text{ANT}}) B_x(\theta_x, \phi_x, \theta'_{x,0}, \phi'_{x,0}) \quad (3.56)$$

thanks to the symmetric feature of the antenna pattern in (3.52), where the azimuth angle is now in the range of $|\phi_x - \phi_{x,\text{ANT}}| \leq \frac{\pi}{2}$. The synthesized pattern in case of an ideal beamformer can be obtained by merely replacing $(\theta'_{x,0}, \phi'_{x,0}) = (\theta_{x,0}, \phi_{x,0})$. The antenna pattern A_x is defined in (3.52) and the array pattern is given by

$$B_x(\theta_x, \phi_x, \theta'_{x,0}, \phi'_{x,0}) = \left| \sum_{m=0}^{M-1} e^{jm\varepsilon'_x} \right|^2 = \frac{\sin^2 \frac{M\varepsilon'_x}{2}}{\sin^2 \frac{\varepsilon'_x}{2}} \quad (3.57)$$

using (3.34) and (3.55), where $M \in \{P, Q\}$ is the number of antenna elements and the parameter

$$\varepsilon'_x = \frac{2\pi d}{\lambda} (\sin \theta_x \sin \phi_x - \sin \theta'_{x,0} \sin \phi'_{x,0}). \quad (3.58)$$

As an example, Fig. 3.4(a), (b) and (c) show the element antenna pattern A_x , six-elements ULA pattern B_x and the synthesized beam pattern C_x , respectively. Here the element antenna is directed at $\Psi_x = (\theta_{x,\text{ANT}}, \phi_{x,\text{ANT}}) = (\frac{\pi}{2}, 0)$ and the formed beam is directed at $\Omega'_{x,0} = (\theta'_{x,0}, \phi'_{x,0}) = (\frac{\pi}{2}, 0)$.

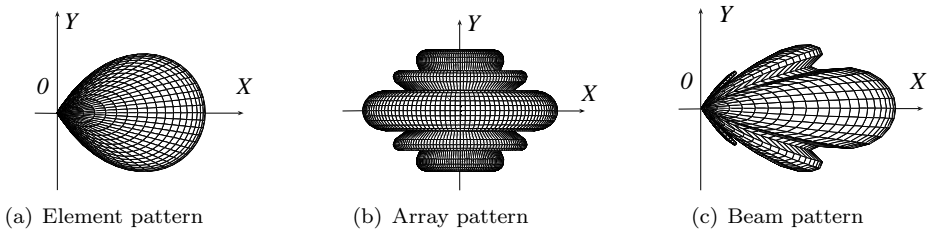


Fig. 3.4: A cosine-shaped element antenna power pattern (a), array pattern of a ULA with six elements (b) and the synthesized beam pattern (c).

For the synthesized pattern, the directivity at the main beam direction $\Omega'_{x,0}$ equals

$$\text{Beam directivity: } 2M^2(2q_x + 1) (\sin \theta'_{x,0} \cos(\phi'_{x,0} - \phi_{x,\text{ANT}}))^{2q_x}. \quad (3.59)$$

When the formed beam direction is aligned with the element lobe direction, i.e. $\Omega'_{x,0} = \Psi_x$, the largest directivity is achieved and given by $2M^2(2q_x + 1)$. In addition, it is seen from (3.56) that the beamwidth of the synthesized pattern σ_{C_x} depends not only on the antenna pattern, but also on the array pattern that is related to the number of elements and the positioning of the array. In practice, to have a sufficient radio coverage, the antenna pattern generally has a much wider beam than the array pattern, and in this case the beamwidth of the synthesized pattern can be approximated by $\sigma_{C_x} \approx \sigma_{B_x}$ [80], where σ_{B_x} denotes the HBPW of the array pattern B_x .

3.6 Impact analysis and illustrative examples

Directivity and beamwidth are two important parameters to characterize a directional antenna and have a significant effect on a channel. Therefore, it is interesting to quantitatively relate the antenna pattern parameters with their impact on the channel. Based on the channel and antenna models in the previous sections, the impact of a single antenna and multi-antenna beamformer on the channels is analytically formulated and illustrated by examples in this section.

3.6.1 Impact analysis on the channel

Suppose that the joint channel spectrum is decomposable as in (3.41) and the angular spectra are uniformly distributed either in a sphere or in the azimuth plane. Consider the conventional beamforming of a ULA array with the orientation $\Upsilon_x = (\frac{\pi}{2}, \frac{\pi}{2})$ and the beam is steered to the direction $\Omega'_{x,0} = (\theta'_{x,0}, \phi'_{x,0})$. In addition, each element antenna has the same main lobe direction in the $X - Y$ plane, i.e. $\Psi_x = (\frac{\pi}{2}, \phi_{x,\text{ANT}})$. Applying the synthesized pattern $C_x(\Omega_x, \Psi_x, \Omega'_{x,0})$ of (3.56) into (3.36), (3.35) and (3.27) results in the Rician K -factor gain, SNR gain and RMS delay spread reduction of the channel due to the conventional beamforming

$$G_K = \frac{C_T(\Omega_{T,0}, \Omega'_{T,0}, \Psi_T)C_R(\Omega_{R,0}, \Omega'_{R,0}, \Psi_R)}{F_{T,C}F_{R,C}}, \quad (K \neq 0) \quad (3.60)$$

$$G_\rho = \frac{\beta F_{T,C}F_{R,C}}{PQ} \quad (3.61)$$

$$R_{\sigma_\tau} = 1 - \frac{1}{\beta} \sqrt{\frac{\beta\eta - 1}{\eta - 1}}, \quad (3.62)$$

respectively, where $\beta = \frac{KG_{K+1}}{K+1}$. The channel power gain of the scattered waves is given by

$$F_{x,C} = \frac{1}{4\pi} \int_{\phi_{x,\text{ANT}} - \frac{\pi}{2}}^{\phi_{x,\text{ANT}} + \frac{\pi}{2}} \int_0^\pi C_x(\theta_x, \phi_x, \theta'_{x,0}, \phi'_{x,0}, \phi_{x,\text{ANT}}) \sin \theta_x d\theta_x d\phi_x \quad (3.63)$$

or

$$F_{x,C} = \frac{1}{2\pi} \int_{\phi_{x,\text{ANT}} - \frac{\pi}{2}}^{\phi_{x,\text{ANT}} + \frac{\pi}{2}} C_x\left(\frac{\pi}{2}, \phi_x, \theta'_{x,0}, \phi'_{x,0}, \phi_{x,\text{ANT}}\right) d\phi_x \quad (3.64)$$

when the scattered waves are uniformly distributed in a sphere or in the azimuth plane, respectively. Here the integral regions are $|\theta_x - \frac{\pi}{2}| \leq \frac{\pi}{2}$ and $|\phi_x - \phi_{x,\text{ANT}}| \leq \frac{\pi}{2}$.

In addition, the parameter

$$\eta = \overline{\tau^2} / \overline{\tau}^2 \quad (3.65)$$

is the ratio between the second moment and the first moment square of the power delay spectrum for channels with isotropic antennas. For the exponentially decaying delay spectrum in (3.51), the ratio $\eta = 2(K + 1)$.

In case of ideal-beamforming where the beam is steered to the direction of the LOS wave, $\Omega'_{x,0}$ in (3.60), (3.61) and (3.62) can be replaced by $\Omega_{x,0}$.

3.6.2 Example one: a single directional element

Given the Rician channel K -factor, the antenna pattern and the number of elements, in the following, the change of channel statistics, K -factors, SNR and RMS delay spreads, will be predicted by using (3.60)-(3.62) for the exponentially decaying power delay spectrum.

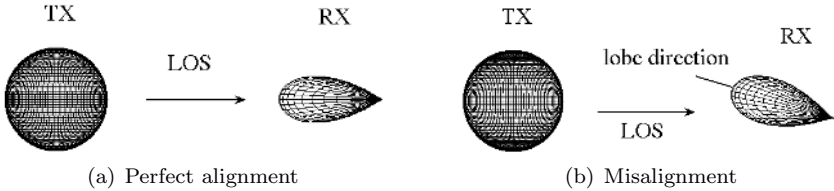


Fig. 3.5: The antenna lobe is aligned and misaligned with the LOS wave.

Consider a scenario that an isotropic antenna is applied at the TX side and a directional antenna is applied at the RX side, as illustrated in Fig. 3.5(a) and (b) for perfect and imperfect beam alignment, respectively. The Rician K -factor gain, the SNR gain and the reduction of RMS delay spread can be computed by

$$G_K = \frac{1}{F_{R,A}} 2(2q_R + 1) (\cos \phi_{R,ANT})^{2q_R} \quad (K \neq 0) \quad (3.66)$$

$$G_\rho = \frac{KG_K + 1}{K + 1} \cdot F_{R,A} \quad (3.67)$$

$$R_{\sigma_\tau} = 1 - \frac{K + 1}{KG_K + 1} \sqrt{\frac{2KG_K + 1}{2K + 1}}, \quad (3.68)$$

where $q_R = \frac{-\ln 2}{2 \ln \cos \frac{\phi_{AR}}{2}}$, $F_{R,A} = 1$ or $F_{R,A} = \frac{(2q_R + 1)\Gamma[\frac{1}{2} + q_R]}{\sqrt{\pi}\Gamma[1 + q_R]}$ for the uniform waves distributed in a sphere or in the azimuth plane, respectively.

Fig. 3.6 depicts the impact parameters versus the RX beamwidths. Here the thick and thin lines are the results for the uniform waves distributed in a sphere or in the azimuth plane, respectively. From these figures, we have the following observations.

- When the main lobe direction is perfectly aligned with the arrival direction of the LOS path at $\Psi_R = \Omega_{R,0} = (90^\circ, 0^\circ)$, which can be seen from the solid line curves in Fig. 3.6(a)-(c), the Rician K -factor gain, SNR gain and RMS delay spread reduction decrease with the HPBW. This means that it is preferable

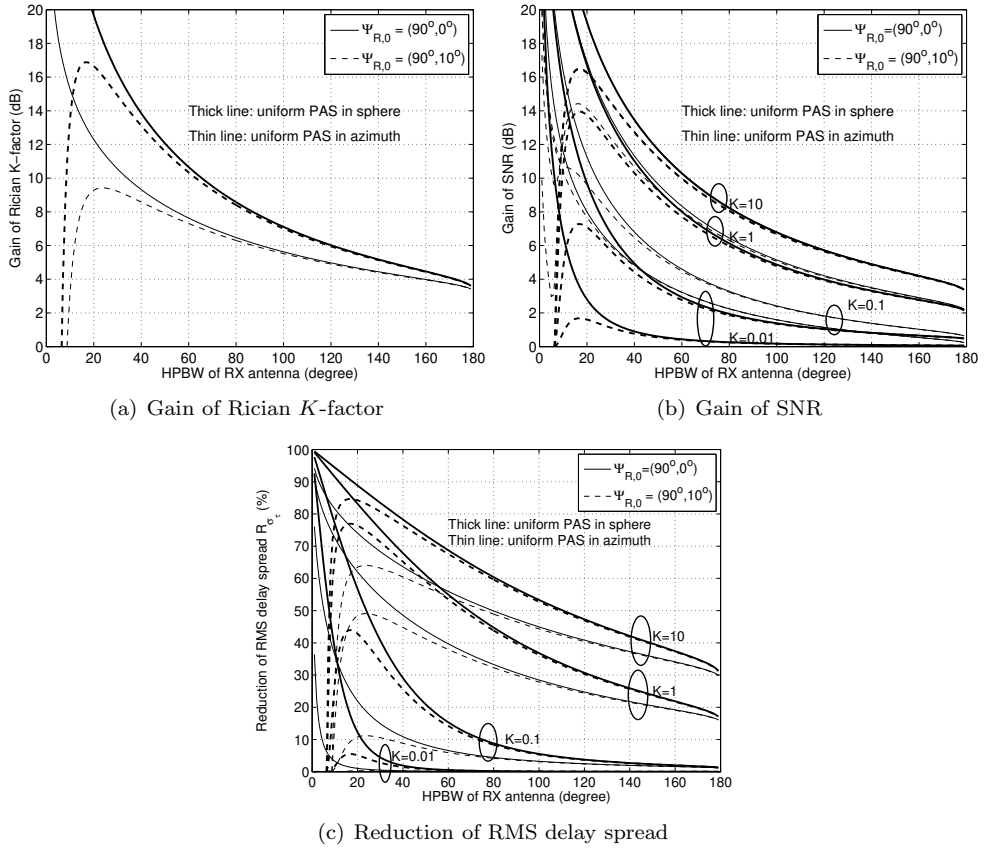


Fig. 3.6: With isotropic antenna at the TX side, the Rician K -factor gain (a), the SNR gain (b) and the reduction of RMS delay spread (c) versus RX antenna beamwidth. The arriving direction of the LOS wave is $\phi_{R,0} = 0^\circ$, the main lobe directions are $\phi_{R,ANT} = 0^\circ$ and 10° .

to have the HPBW as small as possible. In addition, the SNR gain and the reduction of RMS delay spreads are more significant for the channels with a larger Rician K -factor (Fig. 3.6(b) and (c)).

- When the main lobe has a 10° misalignment with the LOS path (dash lines), e.g. $\Psi_R = (90^\circ, 10^\circ)$, the received power contributed by the LOS wave can significantly drop, especially for a narrow beam antenna, and at a certain point the scattered waves become dominant in the received power. Consequently, the Rician K -factor gain and RMS delay spread reduction can not monotonically increase when reducing antenna beamwidth, as observed from the dash line curves in Fig. 3.6. It is also observed that the optimal K -factor gain and RMS delay spread can be achieved at a certain beamwidth, as will be given in the later paragraph. In general, the Rician K -factor gain and the RMS delay spread reduction drop rapidly for beamwidths smaller than the optimal beamwidth, as

observed from the figures.

- When the waves are concentrated in the azimuth plane (thin dash line in Fig. 3.6(b)), in case of beam misalignment, the SNR gain as a function of HPBW has a local minimum and a local maximum for large K -factors. A better view of the curves can be found in Fig. A.2 in Appendix A.1.2. As explained in Appendix A.1.2, the signal power is dominated by the contribution from the scattered waves or the LOS wave, when the antenna beamwidth is smaller or larger than the beamwidth where the local minimum appears, respectively. In comparison, the SNR gain has a unique maximum at a certain beamwidth, when the scattered waves are distributed in a sphere. This is different from the case of wave distribution in the azimuth plane, since the power gain of scattered waves is a constant instead of a decreasing function along antenna beamwidth (see Appendix A.1.2).
- For the scattered waves distributed in a sphere, the Rician K -factor gain and RMS delay spread reduction are larger than those in the azimuth plane, while the SNR gain is slightly lower. But as $K > 1$ the SNR gain becomes less sensitive to the wave distribution. The impact difference is due to the fact that the waves distributed in a sphere are suppressed in a larger extent than those in the azimuth plane.

Theoretically, the largest Rician K -factor gain and RMS delay spread reduction can be achieved at a certain beamwidth for the misalignment $\phi_{R,ANT} \neq 0$ between the main lobe and the LOS path. By computing $\frac{\partial G_K}{\partial \sigma_{AR}} = 0$ and $\frac{\partial R_{\sigma\tau}}{\partial \sigma_{AR}} = 0$, the optimum HPBW for a small misalignment $\phi_{R,ANT}$ can be approximated by

$$\sigma_{AR[opt]} \approx 1.67\phi_{R,ANT} \quad (3.69)$$

$$\sigma_{AR[opt]} \approx 2.35\phi_{R,ANT} \quad (3.70)$$

for the scattered waves in a sphere and in the azimuth plane, respectively (see Appendix A.1). As for the SNR gain, the optimum SNR gain G_ρ is achieved at $\sigma_{AR[opt]} \approx 1.67\phi_{R,ANT}$ for the case of scattered waves in a sphere. For the case of scattered waves distributed in the azimuth plane, the local maximum of G_ρ is achieved approximately at $\sigma_{AR[opt]} \approx 1.67\phi_{R,ANT}$ for a large Rician K -factor.

3.6.3 Example two: conventional beamforming

When designing a multi-antenna beamforming system, the requirements about radio coverage and SNR gain are important issues to take into account. The radio coverage is related to the individual antenna pattern beamwidth and the SNR gain depends not only on the directivity of elements, but also on the array configuration, e.g. the number of elements. The impact factors in (3.60)-(3.62) can be taken as the criteria for selecting the antenna pattern and the number of elements.

By way of illustration, we consider TX-RX arrays with isotropic elements at the TX side and cosine-shaped directional elements at the RX side, as illustrated in Fig. 3.7.

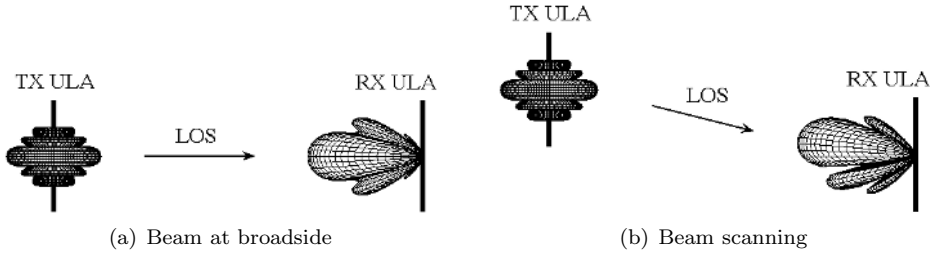


Fig. 3.7: TX-RX beamforming with isotropic elements at the TX side and cosine-shaped elements at the RX side.

The numbers of elements are $(P, Q) = (1, 1), (2, 2), (3, 3), (4, 4), (5, 5)$ and $(6, 6)$, and the element spacing in each array is half wavelength. We further assume that the TX and RX arrays are parallel to each other in a plane, the directions of TX-RX element lobes are also in the plane and in each array the antenna lobe directions are perpendicular to the array direction.

First we have a look at the special case when the departure and arrival directions of the LOS wave are at the broadside of the TX and RX arrays, i.e. the directions that are perpendicular to the arrays (see Fig. 3.7(a)). In such a case, the Rician K -factor gain, the SNR gain and RMS delay spread reduction versus the RX antenna beamwidth are depicted in Fig. 3.8. Here the Rician channel with $K = 1$ is considered for the computation of SNR gain and RMS delay spread reduction. It is observed that the SNR gain due to multi-antenna beamforming is not sensitive to whether the waves are distributed in a sphere or the azimuth plane, which is the same as observed in the single element case. However, it is only true that the waves distributed in a sphere are more suppressed than those distributed in the azimuth plane when the element antenna beamwidth is smaller than a certain value, depending on the configurations. This is reflected in the gain of Rician K -factor and the reduction of RMS delay spread.

For the same TX-RX array configurations, Fig. 3.9 depicts the impact factors over the scanning angle $\phi_{R,0} \in [-90^\circ, 90^\circ]$ for the RX element beamwidth $\sigma_{A_R} = 95^\circ$.

For a specific design requirement, the number of elements and antenna beamwidth can be determined and the impact of this configuration on the channel can be checked from these figures. For instance, the link budget requirement of 20 dB gain in the channel with $K = 1$ can be satisfied by using an antenna array with $(P, Q) = (6, 6)$ with the RX element beamwidth $\sigma_A = 95^\circ$ (see Fig. 3.8(b)). This configuration leads to a 3-dB scan range that is about the same as the RX element beamwidth (see Fig. 3.9(b)). This observation confirms the analysis in Appendix A.2 that a 3-dB RX azimuth scan range can be approximated by the RX element beamwidth, i.e.

$$\phi_{\text{scan}} \approx \sigma_{A_R}, \quad (3.71)$$

for a fairly large Rician K -factor and a large number of elements. It is further observed that within the 3-dB scan range, the Rician K -factor gain is about 22.5 dB and the reduction of RMS delay spread is about 87.5%.

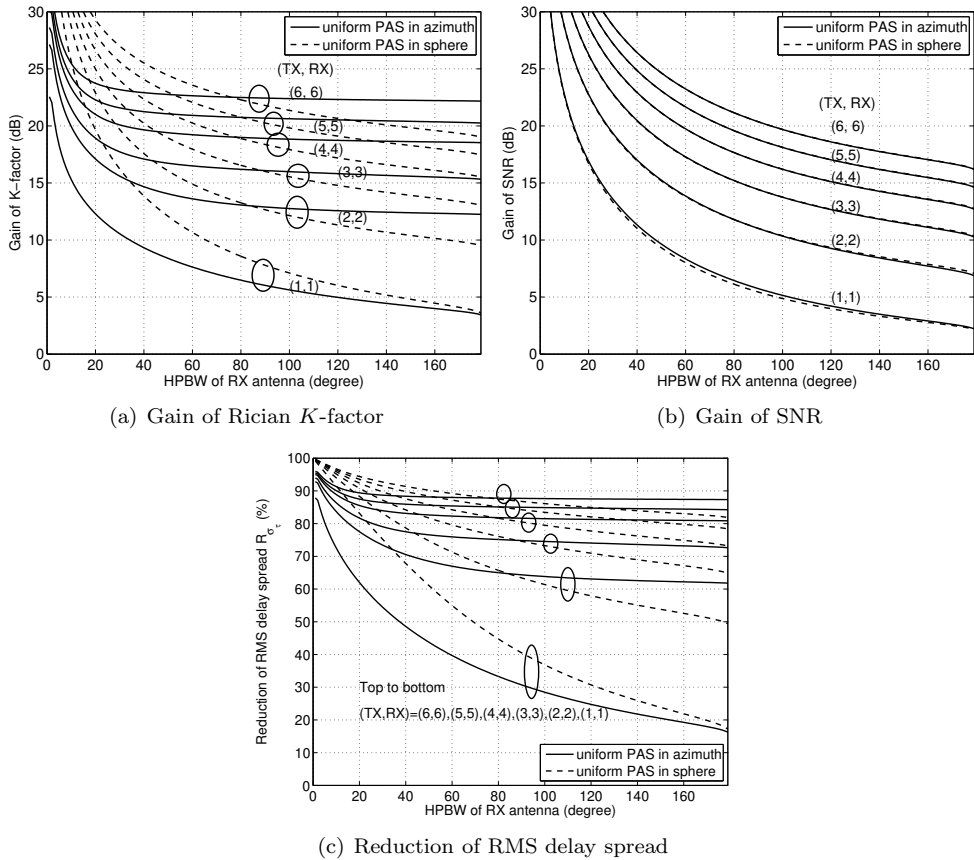


Fig. 3.8: For isotropic and directional antenna elements at the TX and RX sides, the Rician K -factor gain (a), the SNR gain (b) and the RMS delay spread reduction (c) caused by conventional beamforming over RX element beamwidth for various (TX, RX)=(P , Q) configurations.

3.6.4 Discussion

The impact of radiation pattern on the considered channels are predicted here without taking into account some practical issues, such as antenna cross polarizations and side lobes. When both the vertical and horizontal polarized field components exist in the wave transmission, a similar approach as in Section 3.2 can be used to predict the impact of antennas on the channel, but the antenna radiation patterns and the channel power spectra for each polarization have to be considered separately [69, 81]. Existence of side lobes in a radiation pattern will lead to a reduced directivity and as a result, the Rician K -factor gain and RMS delay spread reduction become less pronounced.

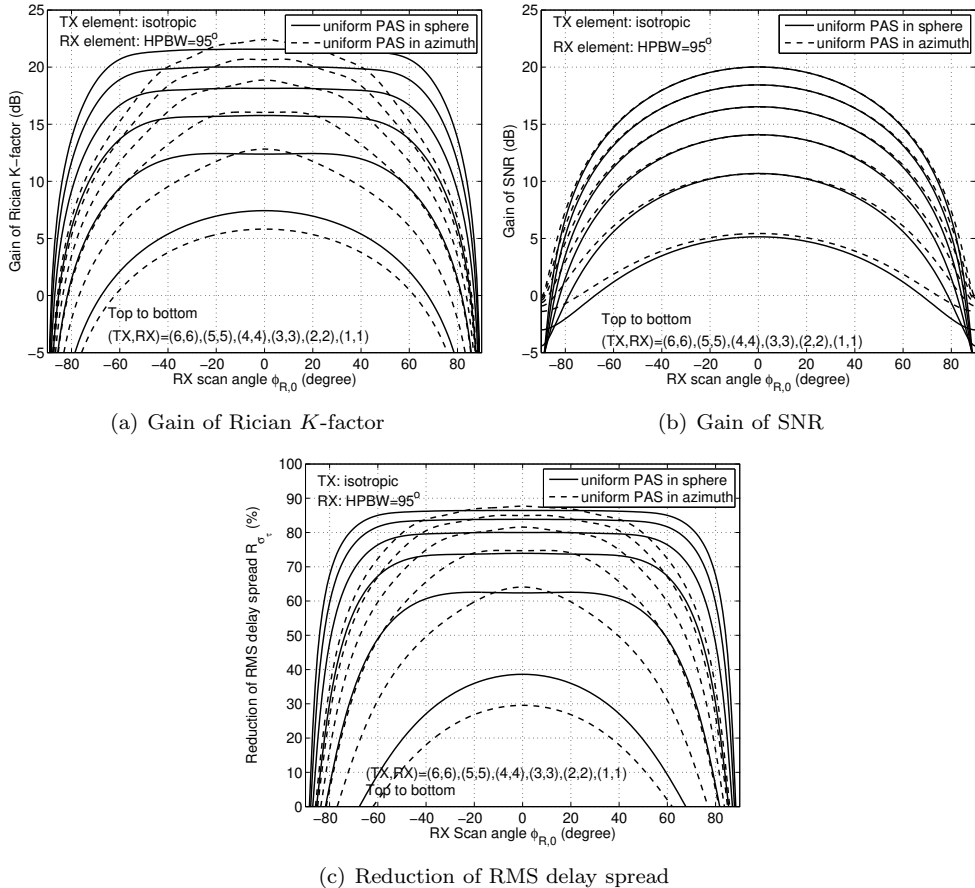


Fig. 3.9: For isotropic elements at the TX side and directional elements ($\sigma_{A_R} = 95^\circ$) at the RX side, the Rician K -factor gain (a), the SNR gain (b) and the RMS delay spread reduction (c) over RX scan angles $\phi_{R,0}$ for various configurations (TX, RX) = (P, Q).

It is seen from Section 3.4 that the assumption about a decomposable channel spectrum leads to an easier analysis in this section. For further study, it is interesting to model the joint distribution of channel power in time delay and angular domain, as conducted in [82] for urban environments, and to investigate the decomposability of realistic indoor channels. In addition, in practical propagation channels, the scattered waves are often cluster-wise distributed in time and space, and the departing and arriving directions are typically not uniformly distributed. It is yet not known how much the impact on realistic channels is different from those obtained in this section, and which one of the assumptions about the exponentially decaying PDS and uniform power angular spectrum will give the most significant effect on the differences. This analysis needs to be conducted in the future.

3.7 Conclusions

In this chapter, the impact of directional antennas and multi-antenna beamformers on radio transmission were analytically formulated for multipath Rician channel environments. By way of illustration, a hypothetical antenna with the cosine-shaped power pattern was applied to show the impact on the channel with an exponential delay spectrum and uniform angle spectra. It was found, for instance, that in case of misalignment between the antenna main lobe and the LOS wave, the optimal HPBW of the antenna equals about twice the misaligned angle. For the waves distributed in sphere, with the misaligned angle larger than one half the antenna beamwidth, the SNR gain, the Rician K -factor gain and RMS delay spread reduction drop rapidly. These are consistent with the observation based on measured results in Chapter 2 that the misaligned angle should not be larger than half of the antenna beamwidth, in order to maintain the channel quality. By using a narrow-beam antenna at one side of the radio link, the Rician K -factor and SNR gain can range up to 16 dB and the RMS delay spread reduction may be more than 80%. If multi-antenna beamformers are used at both sides of the radio link, the Rician K -factor gain, SNR gain and RMS delay spread reduction will be even higher. Further, it was found that for conventional beamforming, the 3-dB scan range can be approximated by the antenna element HPBW.

Chapter 4

Wideband transmission and frequency-domain equalization

4.1 Introduction

A significant system design consideration is the choice of the modulation scheme and values of the associated parameters, because this determines important figures of merit, such as spectral efficiency, power efficiency, required level of transmit power, required coding overhead, and system complexity. There are several modulation options applicable for 60-GHz radio applications, such as continuous phase modulations (CPM) and linear modulations among others. CPM covers a large class of nonlinear modulation schemes, which only carry information in the phase or frequency of the signal. Having a constant envelope, CPM is resistant to the effect of nonlinearities at RF front-ends and allows low requirements on the power amplifier (PA), digital-to-analog converter (DAC) and analog-to-digital converter (ADC). Among the class of CPM, Gaussian minimum shift keying (GMSK) is one of the most power and spectrum efficient schemes, and may be used for the first generation of 60-GHz radios with data rates up to 2 gigabit per second (Gb/s). However, concerning the theoretical spectrum efficiency of 1.33 bits/s/Hz and given the bandwidth of 1.7 GHz, GMSK is not suitable for the data rate of 3 Gb/s, let alone the data rate of 3 – 5 Gb/s for the uncompressed transmission of high definition content [1]. Although higher data rates are possible by increasing the Gaussian filter bandwidth, the unwanted out-of-band power emission will result in serious adjacent band interferences. Another disadvantage of GMSK is that the signal detection at receiver can be quite involved, e.g. using a Viterbi algorithm at a data rate of a few Gb/s, in order to combat the inter-symbol interference (ISI) caused by both the multipath channels and the long tails of the Gaussian filters.

Compared with the CPM, linear modulations, such as quadrature amplitude modulations (QAM), can provide higher spectrum efficiency by carrying information in both phase and amplitude. Linear modulations suffer from performance loss under the effect of nonlinearities, but are necessary for high data throughput systems, especially when the spectrum becomes a scarce resource in the future. The combination of linear modulations with wideband transmission schemes, such as orthogonal frequency division multiplexing (OFDM), by inserting guard intervals between data blocks, low-complexity frequency-domain equalizations (FDE) can be conveniently performed at receiver using the fast Fourier transform (FFT). Moreover, wideband transmission systems are more scalable for different environments, bandwidths and data rates. Also, they are compatible with the FFT processing core embedded in the current wireless local area network (WLAN) systems and allow a convenient integration of various radio functions in the future software-defined radio systems.

In general, wideband transmission schemes can be divided into two categories: multi-carrier transmission, such as OFDM and multi-carrier code division multiple access (MC-CDMA), and single-carrier transmission schemes, such as single-carrier block transmission with FDE (SC-FDE). It is well known that OFDM suffers larger impairments from nonlinear components than single-carrier transmissions, due to the higher peak-to-average power ratios (PAPRs). MC-CDMA is based on the OFDM technique and suitable for multi-user applications, but essentially different from OFDM in that frequency diversity is inherently utilized in MC-CDMA. SC-FDE utilizes frequency diversity as well, but the signals have lower PAPRs than multi-carrier signals.

The purpose of this chapter is to study the channel equalization and the transmission performance of the wideband schemes in Rician fading channels, and address relevant implementation issues, such as synchronization and channel estimation. The transmission performance under the influence of quantization and RF impairments will be considered in Chapter 6. The outline of this chapter is as follows. First, a general bandlimited transceiver system is described in Section 4.2. Wideband transmission systems of OFDM, SC-FDE and MC-CDMA are described in Section 4.3. Then in Section 4.4 we study the optimal linear channel equalization of the considered systems in the baseband and derive bit error rate (BER) expressions under Rician fading channel conditions. Section 4.5 treats practical issues, such as synchronization and channel estimation, and investigates their influence on BER performance. Lastly conclusions will be drawn in Section 4.6.

4.2 Bandlimited transceiver system

Wireless signals are normally transmitted and received over a limited bandwidth, in order to prevent signal interference in the radio spectrum. Here we describe a digital baseband equivalent transmission system with a limited bandwidth, as illustrated in Fig. 4.1, without considering its modulation format. Also, a multipath propagation channel is included in the description.

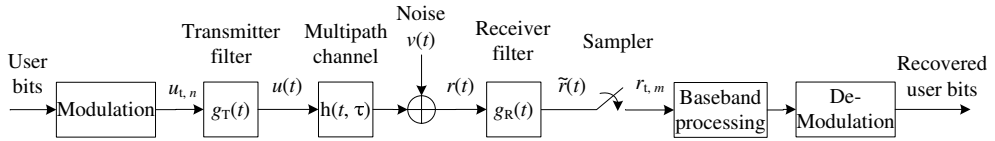


Fig. 4.1: Baseband equivalent bandlimited transceiver system.

Let $\{u_{t,n}\}$ with the index $n \in [0, \infty)$ be the signal sequence after baseband modulation in the time domain. Here the subscript “ t ” is used to distinguish the time domain sequence $\{u_{t,n}\}$ from its frequency sequence $\{u_k\}$ used in later sections. At the transmitter (TX) side, the baseband equivalent complex signal before up-conversion to RF frequency is given by

$$u(t) = \sum_{n=0}^{\infty} u_{t,n} g_T(t - nT_s), \quad (4.1)$$

where T_s is the sampling period and $g_T(t)$ is a low pass filter (LPF) used for shaping the signal spectrum. After up-conversion to a carrier frequency f_{tx} , the RF signal, $\text{Re}\{u(t)e^{i2\pi f_{tx}t}\}$ with the imaginary unit $i = \sqrt{-1}$, undergoes a multipath propagation channel $h(t, \tau)$. The channel impulse response has been described in (2.7) and is repeated here

$$h(t, \tau) = \sum_{l=0}^L h_l(t) \delta(\tau - \tau_l), \quad (4.2)$$

where $h_l(t)$ is the complex amplitude of the l th channel path at the delay τ_l . In the following, we assume that the channel is invariant over time during the transmission of one data packet and the time dependency (t) will be omitted. After the receiver (RX) has down-converted the signal with a carrier frequency f_{rx} , the received complex baseband signal, contaminated by the receiver noise, is given by

$$r(t) = e^{i2\pi f_{\Delta}t} \sum_{l=0}^L h_l u(t - \tau_l) + v(t), \quad (4.3)$$

where $f_{\Delta} = f_{tx} - f_{rx}$ is the frequency mismatch, which is called frequency offset for the rest of the chapter, between the TX and RX carrier frequencies and $v(t)$ is zero-mean additive white Gaussian noise (AWGN). Here we have assumed that no other RF impairments occur at the front-end. RF impairments will be elaborated in Chapter 6. Subsequently, the received signal passes through a RX LPF $g_R(t)$ that is matched to $g_T(t)$ and the filtering output yields

$$\tilde{r}(t) = e^{i2\pi f_{\Delta}t} \sum_{n=0}^{\infty} u_{t,n} \sum_{l=0}^L h_l \tilde{g}_{TR}(t - \tau_l - nT_s) + \tilde{v}(t), \quad (4.4)$$

where $\tilde{v}(t)$ is the filtered AWGN noise with $\mathbb{E}\{|\tilde{v}(t)|^2\} = N_0$. The composite response

$$\begin{aligned}\tilde{g}_{\text{TR}}(t) &= \left(\left(g_{\text{T}}(t) e^{i2\pi f_{\Delta} t} \right) * g_{\text{R}}(t) \right) \cdot e^{-i2\pi f_{\Delta} t}, \\ &= \int_{-\infty}^{\infty} g_{\text{R}}(\tau) g_{\text{T}}(t - \tau) e^{-i2\pi f_{\Delta} \tau} d\tau\end{aligned}\quad (4.5)$$

is due to the frequency offset and transceiver filters [83], where “*” denotes linear convolution. In case of zero frequency offset, $\tilde{g}_{\text{TR}}(t) = g_{\text{TR}}(t) = g_{\text{T}}(t) * g_{\text{R}}(t)$ is the time impulse response of the Nyquist filter. The matched-filter output is sampled at the rate $1/T_s$ at a certain time offset t_0 , yielding the sampled sequence, $r_{t,m} = \tilde{r}(t_0 + mT_s)$, given by

$$r_{t,m} = e^{i2\pi f_{\Delta}(t_0 + mT_s)} \sum_{l=0}^L \sum_{n=0}^{\infty} u_{t,n} h_l \tilde{g}_{\text{TR}}(t_0 - \tau_l - (n - m)T_s) + v_{t,m}, \quad (4.6)$$

where $v_{t,m} = \tilde{v}(t_0 + mT_s)$ is the m th noise sample.

1) *Nyquist filter:* The often used Nyquist filter is the raised-cosine filter, whose time response and frequency response are given by

$$g_{\text{TR}}(t) = \text{sinc}\left(\frac{t}{T_s}\right) \cdot \frac{\cos\left(\frac{\pi\alpha t}{T_s}\right)}{1 - \frac{4\alpha^2 t^2}{T_s^2}}, \quad (4.7)$$

$$G_{\text{TR}}(f) = \begin{cases} T_s & |f| \leq \frac{1-\alpha}{2T_s} \\ \frac{T_s}{2} \left\{ 1 + \cos\left(\frac{\pi T_s}{\alpha} \left[|f| - \frac{1-\alpha}{2T_s} \right] \right) \right\} & \frac{1-\alpha}{2T_s} < |f| \leq \frac{1+\alpha}{2T_s} \\ 0 & |f| > \frac{1+\alpha}{2T_s} \end{cases}, \quad (4.8)$$

respectively, where $\text{sinc}(x) = \frac{\sin \pi x}{\pi x}$ is the normalized sinc function and $\alpha \in [0, 1]$ is the roll-off factor. From (4.7) we see that the raised-cosine filter response follows the *Nyquist criterion*, i.e. the response is zero at $t = n'T_s$ for all integers $n' \neq 0$, which prevent the ISI in a channel with frequency flat response [84]. The matched TX and RX filters $g_{\text{T}}(t)$ and $g_{\text{R}}(t)$ are generally square-root Nyquist filters, having the same frequency response of $\sqrt{G_{\text{TR}}(f)}$, in order to minimize the interference and noise outside the frequency band. The roll-off factor is related to the excess bandwidth by $\text{BW}_e = \frac{\alpha}{2T_s}$ and to the whole bandwidth of the raised-cosine filter $\text{BW} = \frac{1+\alpha}{2T_s}$. Therefore, the frequency spectrum can be shaped by adjusting the roll-off factor α to limit the out-of-band emission. As the roll-off factor approaches 0, the raised-cosine filter becomes an ideal brick wall filter having a rectangular function $G_{\text{TR}}(f) = \text{rect}(fT_s)$ and the time response $g_{\text{TR}}(t) = \text{sinc}\left(\frac{t}{T_s}\right)$, which will be used for the rest of the thesis.

A non-zero frequency offset gives rise to both ISI and inter-carrier interference (ICI) of the received signal. The ISI occurs even in a single path propagation channel [83], because the matched filter output $\tilde{g}_{\text{TR}}(t)$ in (4.5) is a distortion of the Nyquist response $g_{\text{TR}}(t)$. The ICI occurs, since the resulting phase rotation $2\pi f_{\Delta}(t_0 + mT_s)$

changes over the signal samples, as seen from (4.6). A frequency offset can be corrected before or after the matched filter $g_R(t)$ in the analog or digital domain, respectively. In the former case, the effects of frequency offset can be completely removed. Nowadays, many receivers correct the frequency offset after the matched filter, by compensating $e^{j2\pi f_\Delta(t_0+mT_s)}$ in (4.6), to enjoy the flexibility and the low cost of digital hardware. After the compensation in this case, the ISI remains, but can be cancelled by the subsequent equalization procedure.

2) *Overall response of the transmission system:* The cascade of the transmitter filter, the multipath channel and the receiver filter leads to the overall system response

$$\tilde{h}(t) = \sum_{l=0}^L h_l \tilde{g}_{\text{TR}}(t - \tau_l). \quad (4.9)$$

It is evident from (4.9) that the overall system response is a weighted addition of all the multipath components and has a wider span over time than the channel response $h(t)$. Strictly speaking, the system response $\tilde{h}(t)$ has an infinite span over time, because of the bandlimited Nyquist filter. Since most energy of $\tilde{h}(t)$ is concentrated over a rather small range, we assume that the system response has a limited span over time for the rest of the thesis. Now we rewrite the sampled signal sequence (4.6) as follows

$$r_{t,m} = e^{j2\pi f_\Delta(t_0+mT_s)} \sum_{l=0}^{\tilde{L}} \tilde{h}_l u_{t,m-l} + v_{t,m}. \quad (4.10)$$

where $\tilde{h}_l = \tilde{h}(t_0 + lT_s)$ for $0 \leq l \leq \tilde{L}$ are sampled taps of the overall system response $\tilde{h}(t)$ that has a limited time span over $t \in [t_0, t_0 + \tilde{L}T_s]$. The sampled taps $\{\tilde{h}_l\}$ for $0 \leq l \leq \tilde{L}$ are merely the convolution between the channel taps $\{h_l\}$ and the sampled sequence of $\tilde{g}_{\text{TR}}(t)$, i.e.

$$\tilde{h}_l = \sum_{l'=0}^L h_{l'} \tilde{g}_{\text{TR}}(t_0 + lT_s - \tau_{l'}). \quad (4.11)$$

3) *Sampling offset:* Due to a time shift between transmitter and receiver clocks, a sampling offset t_0 is required to synchronize the two clocks, as seen in (4.6). In addition, multiple copies of the transmitted signal with different amplitudes and time delays, caused by the multipath propagation, lead to a certain ambiguity of the time shift. To determine the timing offset, the best we can do is to choose the sampling offset t_0 such that the captured signal power is maximized according to

$$\hat{t}_0 = \arg \max_{t_0} \mathbb{E} \{ |r_{t,m}|^2 \}, \quad (4.12)$$

where the expectation is with respect to the transmit sequence $\{u_{t,n}\}$ only. Since the channel response is assumed to be time invariant, we have the received signal power

$$\mathbb{E} \{ |r_{t,m}|^2 \} = \sum_{l=0}^{\tilde{L}} \sum_{l'=0}^{\tilde{L}} \tilde{h}_l \tilde{h}_{l'}^* \mathbb{E} \{ u_{t,m-l} u_{t,m-l'}^* \} + N_0 \quad (4.13)$$

from (4.10), where the superscript $*$ denotes conjugate and the l th tap of the overall system response $\tilde{h}_l = \tilde{h}(t_0 + lT_s)$. When the data sequence $\{u_{t,m}\}$ follows a certain random distribution, which is for example the case for linearly modulated data sequences, we have the expectation $\mathbb{E}\{u_{t,m-l}u_{t,m-l'}^*\} = E_s\delta(l-l')$ that is independent of the time offset t_0 . As a result, the received signal power

$$\mathbb{E}\{|r_{t,m}|^2\} = E_s \sum_{l=0}^{\tilde{L}} |\tilde{h}_l|^2 + N_0 \quad (4.14)$$

varies over t_0 , since \tilde{h}_l is the function of t_0 . It is now evident to see that \hat{t}_0 in (4.12) is a deterministic quantity. There are various approaches to track the sampling offset in practical systems and they can be found in [83] among others.

4.3 Wideband transmission system model

As seen from (4.4) in the last section, the transmission of a data sequence in multipath dispersive channels suffers from ISI. The data sequence may be transmitted block by block with guard intervals inserted between them, such that ISI is limited inside each block. Note that the block-based transmission is merely a special case of the bandlimited transmission. For such a transmission scheme, the ISI inside each block can be efficiently compensated in the frequency domain by taking advantage of FFT. OFDM, MC-CDMA and SC-FDE are typical block-based wideband transmission systems and their baseband equivalent transmission can be described by a general structure illustrated in Fig. 4.2.

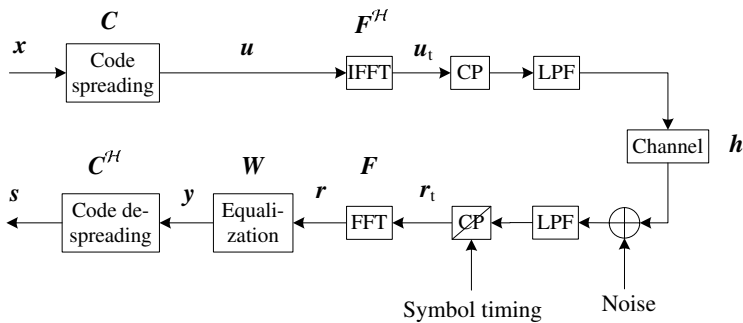


Fig. 4.2: Block diagram of baseband equivalent wideband transmission systems with cyclic prefix.

In the transmitter, user symbols are grouped into data blocks with the block size N . For convenience, we only consider one block denoted as $\mathbf{x} = [x_0, x_1, \dots, x_{N-1}]^T$, where T denote transpose, the data symbols have a zero mean and are independent

and identically distributed (i.i.d.) with variance E_s , i.e.

$$\mathbb{E} \{ \mathbf{x} \mathbf{x}^{\mathcal{H}} \} = E_s \mathbf{I}, \quad (4.15)$$

where \mathbf{I} is an $N \times N$ identity matrix and \mathcal{H} denotes conjugate transpose. Each block is linearly transformed by a code spreading matrix \mathbf{C} and the spread data signals, given by $\mathbf{u} = \mathbf{C} \mathbf{x}$ with $\mathbf{u} = [u_0, \dots, u_{N-1}]^T$, are used to modulate N narrowband subcarriers in the frequency domain. This modulation is performed by applying the inverse FFT on \mathbf{u} , yielding the transmit signal vector $\mathbf{u}_t = [u_{t,0}, \dots, u_{t,N-1}]^T$ in the time domain given by

$$\mathbf{u}_t = \mathbf{F}^{\mathcal{H}} \mathbf{u}, \quad (4.16)$$

where \mathbf{F} represents the Fourier matrix with the entries $F_{m,n} = \frac{1}{\sqrt{N}} e^{-i2\pi mn/N}$. The signal samples $\{u_{t,n}\}$ in the time domain are related to the subcarrier components $\{u_k\}$ by

$$u_{t,n} = \frac{1}{\sqrt{N}} \sum_{k=0}^{N-1} u_k e^{i2\pi kn/N}, \quad (4.17)$$

where $\{u_k\}$ are related to the user symbols $\{x_{k'}\}$ by

$$u_k = \sum_{k'=0}^{N-1} x_{k'} C_{kk'} \quad (4.18)$$

with $C_{kk'}$ the (k, k') th entry of the code spreading matrix \mathbf{C} . Choosing an appropriate code spreading matrix leads to the transmission schemes of OFDM, SC-FDE and MC-CDMA, respectively, according to

- OFDM: \mathbf{C} is an identity matrix, i.e. $\mathbf{C} = \mathbf{I}$ (This is a special case, since the symbols are not spread over frequency);
- SC-FDE: \mathbf{C} is a Fourier matrix, i.e. $\mathbf{C} = \mathbf{F}$;
- MC-CDMA: \mathbf{C} is a Walsh-Hadamard (WH) matrix¹.

Basically, any unitary matrix satisfying $\mathbf{C}^{\mathcal{H}} \mathbf{C} = \mathbf{I}$ and $\mathbf{C} \neq \mathbf{I}$ can be used for the purpose of code spreading. In order to equally spread the energy of individual symbols over all the subcarriers, which maximizes the frequency diversity gain [85], the entries of the unitary matrix are constrained to have the same amplitude, i.e.

$$|C_{mn}| = \frac{1}{\sqrt{N}} \quad (4.20)$$

¹A WH matrix \mathbf{C} has the entries

$$C_{m,n} = \frac{1}{\sqrt{N}} \prod_{i=0}^{N-1} (-1)^{m_i n_i} \quad (4.19)$$

with $m = \sum_{i=0}^{N-1} m_i 2^i$, $n = \sum_{i=0}^{N-1} n_i 2^i$, where $m_i, n_i \in \{0, 1\}$ are the i th bit of the binary representations of m and n , respectively.

for $m, n \in \{0, 1, \dots, N-1\}$.

After the inverse FFT (IFFT), a guard interval with a length N_g is inserted in front of the data block yielding a serial data sequence before transmission. The guard interval can be a cyclic extension (prefix) or merely a zero sequence. In this thesis, we have chosen the cyclic prefix (CP), and then the transmitted baseband signal can be written as follows

$$u(t) = \sum_{n=0}^{N+N_g-1} u_{t, \text{mod}(n-N_g, N)} g_T(t - nT_s), \quad (4.21)$$

where “mod” denotes the modulo operation.

Similar to the bandlimited transmission described in the last section, the wideband transmitted signal undergoes the multipath channel and the matched filter at receiver. Sampling at $t_0 + mT_s$ yields the sequence

$$r_{t,m} = e^{j2\pi f_\Delta(t_0+mT_s)} \sum_{l=0}^{\tilde{L}} \tilde{h}_l u_{t, \text{mod}(m-N_g-l, N)} + v_{t,m} \quad (4.22)$$

with the index $m \geq 0$, where the channel paths $\{\tilde{h}_l\}$ are defined in (4.11). The zero-mean AWGN $v_{t,m}$ has the variance $\mathbb{E}\{|v_{t,m}|^2\} = N_0$. From now on, the notations h_l and L will be used for convenience in the rest of the thesis in replacing \tilde{h}_l and \tilde{L} , respectively, without giving further notice. For the rest of the thesis, the channel length is assumed to be always not longer than the guard interval, i.e. $L+1 \leq N_g$, such that the current data block causes no interference to the next data block. Also, the channel power is normalized for convenience, i.e.,

$$\mathbb{E} \left\{ \sum_{l=0}^L |h_l|^2 \right\} = 1. \quad (4.23)$$

For the time being, it is also assumed that there is no frequency offset, i.e. $f_\Delta = 0$, and the symbol timing is perfect. After removal of the cyclic prefix, the remaining samples, $\{r_{t,m}\}_{N_g \leq m < N_g+N}$, form a length- N vector \mathbf{r}_t . The vector \mathbf{r}_t can be expressed by

$$\mathbf{r}_t = \text{cir}\{\mathbf{h}\} \mathbf{u}_t + \mathbf{v}_t, \quad (4.24)$$

where the noise vector \mathbf{v}_t is formed by the noise samples $\{v_{t,m}\}_{N_g \leq m < N_g+N}$ and the channel matrix $\text{cir}\{\mathbf{h}\}$ is an $N \times N$ circulant matrix with the first column $\mathbf{h} = [h_0, \dots, h_L, 0, \dots, 0]^T$. The N -point FFT of \mathbf{r}_t results in a vector $\mathbf{r} = \mathbf{F} \mathbf{r}_t$ with $\mathbf{r} = [r_0, r_1, \dots, r_{N-1}]^T$, which is given by

$$\mathbf{r} = \mathbf{H} \mathbf{u} + \mathbf{v}, \quad (4.25)$$

where \mathbf{v} is the noise vector after the FFT, $\mathbf{H} = \mathbf{F} \text{cir}\{\mathbf{h}\} \mathbf{F}^H$ is the channel matrix in the frequency domain. For the considered time-invariant channel, the matrix \mathbf{H} is

diagonal and the k th diagonal element H_k , given by

$$H_k = \sum_{l=0}^L h_l e^{-j2\pi kl/N}, \quad (4.26)$$

represents the complex attenuation of the channel at the k th subcarrier.

The received signal (4.25) is first equalized by a weight matrix \mathbf{W} in the frequency domain, yielding the equalized signal $\mathbf{y} = \mathbf{W}\mathbf{r}$. For OFDM, the equalized signal can be directly used for detection. But for SC-FDE and MC-CDMA, the equalized signal is transformed into the time domain by applying the code despreading operation before detection. For all three systems, the vector of decision variables can be expressed in the common form given by

$$\mathbf{s} = \mathbf{C}^H \mathbf{W} \mathbf{H} \mathbf{u} + \mathbf{C}^H \mathbf{W} \mathbf{v}, \quad (4.27)$$

which are fed into a detection device for the recovery of the user data symbols.

4.4 Linear frequency-domain equalization and transmission performance

4.4.1 MMSE equalization and decision variables

After the FD equalization by the weight matrix \mathbf{W} , the vector of decision variables in (4.27) has the disturbance, $\mathbf{e} = \mathbf{s} - \mathbf{x}$, given by

$$\mathbf{e} = \mathbf{C}^H (\mathbf{W} \mathbf{H} - \mathbf{I}) \mathbf{C} \mathbf{x} + \mathbf{C}^H \mathbf{W} \mathbf{v}, \quad (4.28)$$

which has the autocorrelation matrix of

$$\mathbb{E} \{ \mathbf{e} \mathbf{e}^H \} = E_s \mathbf{C}^H (\mathbf{W} \mathbf{H} - \mathbf{I}) (\mathbf{W} \mathbf{H} - \mathbf{I})^H \mathbf{C} + N_0 \mathbf{C}^H \mathbf{W} \mathbf{W}^H \mathbf{C}. \quad (4.29)$$

By choosing the weight matrix appropriately, we can minimize the mean-square error (MSE), i.e. the trace of the matrix $\mathbb{E} \{ \mathbf{e} \mathbf{e}^H \}$, yielding the linear minimum MSE (MMSE) weight matrix

$$\mathbf{W} = \mathbf{H}^H \left(\mathbf{H} \mathbf{H}^H + \frac{1}{\bar{\gamma}} \mathbf{I} \right)^{-1}. \quad (4.30)$$

where $\bar{\gamma} = \frac{E_s}{N_0}$ is the average SNR of the received signal. The weight matrix is a diagonal matrix with the k th diagonal entry given by

$$W_k = \frac{\bar{\gamma} H_k^*}{\bar{\gamma} |H_k|^2 + 1}. \quad (4.31)$$

For OFDM, the code matrix $\mathbf{C} = \mathbf{I}$ and the decision variables are therefore in the frequency domain. Given the channel H_k , the k th decision variable within one data block and the corresponding SNR can be expressed by

$$s_k = \frac{\bar{\gamma} H_k^*}{\bar{\gamma} |H_k|^2 + 1} (H_k x_k + v_k), \quad (4.32)$$

$$\gamma_k = \bar{\gamma} |H_k|^2, \quad (4.33)$$

respectively.

For both SC-FDE and MC-CDMA, the expression of the n th decision variable within one data block is more involved than the one for OFDM in (4.32). Note that we use n as the index of decision variables, instead of k , to distinguish the fact that the detection of SC-FDE and MC-CDMA occurs in the time domain, instead of in the frequency domain as in OFDM. The n th decision variable can be expressed as

$$s_n = \beta x_n + \tilde{e}_n, \quad (4.34)$$

where the scaling factor of the desired signal β and the disturbance \tilde{e}_n are given by

$$\beta = \frac{1}{N} \sum_{k=0}^{N-1} \frac{\bar{\gamma} |H_k|^2}{\bar{\gamma} |H_k|^2 + 1} \quad (4.35)$$

$$\tilde{e}_n = \sum_{\substack{m=0 \\ m \neq n}}^{N-1} x_m \sum_{k=0}^{N-1} \frac{C_{kn}^* C_{km} |H_k|^2}{|H_k|^2 + 1/\bar{\gamma}} + \sum_{m=0}^{N-1} \frac{C_{nm} H_m^*}{|H_m|^2 + 1/\bar{\gamma}} \cdot v_m, \quad (4.36)$$

respectively. The disturbance (4.36) consists of residual ISI in the first term and noise in the second term. The residual ISI occurs since after the MMSE equalization, the signal components at individual subcarriers have different signal strength and are combined into the decision variable either by the IFFT operation in SC-FDE or the WH code despreading operation in MC-CDMA. The cancellation of the residual ISI improves the SNR of the decision variables and results in a better performance in the code-spreading schemes, as will be considered in Chapter 5.

Note that the disturbance \tilde{e}_n has a zero mean and after some manipulations the variance of the disturbance is found to be $\mathbb{E}\{|\tilde{e}_n|^2\} = \beta(1 - \beta)$. From (4.34), one can check that given the channel $\{H_k\}$ for $k = 0, \dots, N - 1$, the SNRs of the decision variables in SC-FDE and MC-CDMA are exactly the same for all n and given by

$$\eta = \frac{\beta}{1 - \beta} = \frac{1}{\frac{1}{N} \sum_{k=0}^{N-1} \frac{1}{\gamma_k + 1}} - 1 \leq \frac{1}{N} \sum_{k=0}^{N-1} \gamma_k, \quad (4.37)$$

where $\gamma_k = \bar{\gamma} |H_k|^2$ is the SNR of the k th subcarrier. According to (4.37), both SC-FDE and MC-CDMA should achieve the same uncoded detection performance, based on the symbol-by-symbol detection rule. Therefore, we conclude that the two schemes are essentially the same, though it is more convenient to apply MC-CDMA into multi-user applications. The inequality in (4.37) is verified using Jensen's inequality and

indicates that the SNR of each decision variable is never larger than the average SNR of all the subcarriers. The equality is only valid in case of a frequency flat channel, i.e. $|H_k|^2 = 1$ for $k = 0, \dots, N - 1$.

Biased and unbiased detection: From (4.32) and (4.34), one can see that the direct detection based on the decision variables is biased in the sense that the scaling factors, $\frac{\sqrt{\gamma}|H_n|^2}{\sqrt{\gamma}|H_n|^2+1}$ and β , of the desired signals are slightly smaller than 1. The bias in the decision variables is caused by the MMSE equalization, which makes a tradeoff between the noise enhancement and the signal distortion for each subcarrier signal. After removing the bias, we have the unbiased decision variables

$$s_k = x_k + \frac{v_k}{H_k} \quad (4.38)$$

$$s_n = x_n + \frac{\tilde{e}_n}{\beta} \quad (4.39)$$

for OFDM and code-spreading schemes, respectively. The unbiased decision variables have the same SNR as those biased.

For the purpose of illustration, Fig. 4.3 depicts the clouds of biased and unbiased decision variables². The center of the biased signal cloud is off the constellation point. In comparison, the unbiased signal cloud has the center positioned overlapped with the constellation point, and meanwhile the noise around the center is enhanced. The unbiased detection is optimal in the sense of the symbol-by-symbol decision rule

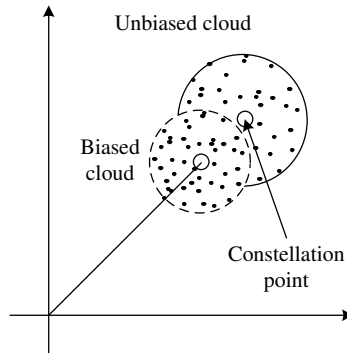


Fig. 4.3: The clouds of biased and unbiased decision variables. The small circles represent the centers of the clouds.

[86]. However, this does not necessarily mean that the unbiased detection always leads to the optimal BER performance, since the noise enhancement in the unbiased detection could result in a worse performance, in case that a lot of noise samples are outside the decision boundary. For a sufficiently large channel SNR, both the biased and unbiased detections in the three systems yield the same performance [86].

²Note that the scale in this figure is exaggerated only for the purpose of illustration.

4.4.2 Uncoded BER computation

In this section, the BER performance is analytically formulated for the detection in the transmission systems after MMSE equalization. Without further notice, the following BER computation concerns only the unbiased detection to follow the symbol-by-symbol decision rule.

In an AWGN channel with the SNR γ , the uncoded BER for constellations with Gray bit-mapping can be well approximated by [84]

$$\text{BER}(\gamma) \approx A \cdot \text{erfc}[B\sqrt{\gamma}] \quad (4.40)$$

where $A = 2(1 - 1/\sqrt{\mathcal{M}})/\log_2 \mathcal{M}$, $B = \sqrt{\frac{3}{2(\mathcal{M}-1)}}$ for a square \mathcal{M} -QAM and $A = 1/\log_2 \mathcal{M}$, $B = \sin \frac{\pi}{\mathcal{M}}$ for \mathcal{M} -PSK, respectively, for the constellation size \mathcal{M} of the data symbols. Here the complementary error function is defined as $\text{erfc}[x] = \frac{2}{\sqrt{\pi}} \int_x^\infty e^{-t^2} dt$.

As discussed in Chapter 2, a specular path, e.g. the line-of-sight (LOS) path, is present in a typical indoor channel at 60 GHz and thus the channel is Rician fading. In a Rician fading channel, the magnitude of each subcarrier channel, $|H_k|$, follows a Rician distribution [87]. Given the average channel SNR $\bar{\gamma} = E_s/N_0$, the SNR of each subcarrier $\gamma_k = \bar{\gamma}|H_k|^2$ has the probability density function (pdf) given by

$$p_\gamma(\gamma) = \frac{1+K}{\bar{\gamma}} e^{-(K+\frac{(1+K)\gamma}{\bar{\gamma}})} I_0 \left[2\sqrt{\frac{K(K+1)}{\bar{\gamma}}}\gamma \right], \quad (4.41)$$

where K is the Rician factor and $I_0[x] = \frac{1}{\pi} \int_0^\pi e^{x \cos \theta} d\theta$ is the zero-order modified Bessel function of the first kind. The subscript of γ_k is dropped in (4.41) for convenience, since the pdf is the same for all the subcarriers. For the special case of the Rayleigh fading channel, we have the Rician factor $K = 0$ and the pdf of γ_k becomes

$$p_\gamma(\gamma) = \frac{1}{\bar{\gamma}} e^{-\frac{\gamma}{\bar{\gamma}}}. \quad (4.42)$$

In the following we calculate the BER performance of the considered systems individually in Rician fading channels.

1) *OFDM*: Note from (4.32) that each decision variable in OFDM is contaminated by AWGN and has the SNR $\gamma_k = \bar{\gamma}|H_k|^2$ for a channel realization H_k . The average BER of OFDM transmission can be obtained by averaging the BER over all the possible channel realizations, i.e.,

$$\overline{\text{BER}}(K, \bar{\gamma}) = \frac{1}{N} \sum_{k=0}^{N-1} \int_0^\infty \text{BER}(\gamma_k) p_\gamma(\gamma_k) d\gamma_k. \quad (4.43)$$

By using an alternative expression of $\text{erfc}[x] = \frac{2}{\pi} \int_0^{\frac{\pi}{2}} \exp\left(-\frac{x^2}{\sin^2 \theta}\right) d\theta$ for $x \geq 0$ [88] and using $\int_0^\infty e^{-px} I_0[\sqrt{qx}] dx = \frac{1}{p} e^{\frac{q}{4p}}$ for $p > 0$ [89], the average BER can be simplified

into

$$\begin{aligned}\overline{\text{BER}}(K, \bar{\gamma}) &= \frac{2A(1+K)}{\pi\bar{\gamma}e^K} \int_0^{\frac{\pi}{2}} \int_0^{\infty} e^{-\left(\frac{B^2}{\sin^2\theta} + \frac{1+K}{\bar{\gamma}}\right)\gamma} \gamma d\gamma d\theta \\ &= \frac{2A(1+K)}{\pi} \int_0^{\frac{\pi}{2}} \frac{\sin^2\theta}{f(\theta)} e^{-\frac{KB^2\bar{\gamma}}{f(\theta)}} d\theta,\end{aligned}\quad (4.44)$$

where the function $f(\theta) = B^2\bar{\gamma} + (1+K)\sin^2\theta$. In case of a Rayleigh fading channel, i.e. when $K = 0$, the average BER equals

$$\overline{\text{BER}}(0, \bar{\gamma}) = A - AB\sqrt{\frac{\bar{\gamma}}{1+B^2\bar{\gamma}}}.\quad (4.45)$$

2) *SC-FDE and MC-CDMA*: Assuming that the transmitted symbol sequence $\{x_m\}$ has a zero mean and is Gaussian distributed [84]. It is observed from (4.36) that the additive disturbance \tilde{e}_n in each decision variable has a zero mean and is Gaussian distributed as well, independent of the spreading matrix \mathbf{C} . Since the decision variables in both SC-FDE and MC-CDMA have the same SNR η , as given in (4.37), both schemes eventually can achieve the same BER. Similar as in OFDM, the average BER of SC-FDE and MC-CDMA in Rician channels can be calculated according to

$$\overline{\text{BER}}(K, \bar{\gamma}) = \int_0^{\infty} \text{BER}(\eta) p_{\eta}(\eta) d\eta,\quad (4.46)$$

where $p_{\eta}(\eta)$ is the pdf of the SNR η of each decision variable. Note from (4.37) that each realization of η is the function of $\gamma_0, \dots, \gamma_{N-1}$, which are SNRs of N subcarriers for a particular channel realization $\{H_k\}$. Obtaining the pdf $p_{\eta}(\eta)$ needs to compute the joint pdf of the N variables $\{\gamma_k\}$ with $0 \leq k \leq N-1$, which is hard to obtain. For this reason, it is not feasible to compute the BER by using (4.46).

It is further noted from (4.37) that the SNR η of each decision variable involves the discrete averaging of $1/(\gamma_k + 1)$ over all the subcarriers. For a limited number of subcarriers N , the SNR η randomly changes over the channel realization $\{H_k\}$. When the number of subcarriers is infinitely large, the discrete averaging of $\frac{1}{\gamma_k + 1}$ approaches a continuous averaging, i.e.

$$\lim_{N \rightarrow \infty} \frac{1}{N} \sum_{k=0}^{N-1} \frac{1}{\gamma_k + 1} = \mathbb{E} \left\{ \frac{1}{\gamma_k + 1} \right\} = \int_0^{\infty} \frac{1}{\gamma_k + 1} p_{\gamma}(\gamma_k) d\gamma_k.\quad (4.47)$$

Consequently, the SNR η approaches a constant value for a certain pdf of γ_k , i.e.

$$\eta_{\infty} = \frac{1}{\varepsilon} - 1,\quad (4.48)$$

where the term $\varepsilon = \mathbb{E} \left\{ \frac{1}{\gamma_k + 1} \right\}$. For a Rician fading channel, the SNR of each subcarrier γ_k has the pdf of (4.41). As a result, the term ε is the function of K and $\bar{\gamma}$ and

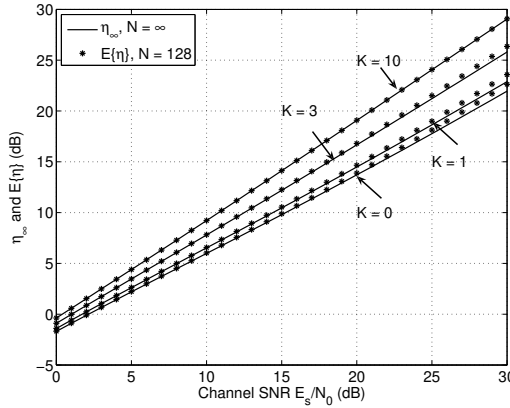


Fig. 4.4: The SNR η for $N \rightarrow \infty$ versus the channel SNR $\bar{\gamma}$ and the Rician K -factor. The stars represent $\mathbb{E}\{\eta\}$ for $N = 128$ obtained from simulation.

is found to be

$$\varepsilon[K, \bar{\gamma}] = \frac{1+K}{\bar{\gamma}} e^{-K+\frac{1+K}{\bar{\gamma}}} \sum_{m=0}^{\infty} \frac{K^m}{m!} E_{m+1} \left[\frac{1+K}{\bar{\gamma}} \right], \quad (4.49)$$

as derived in Appendix B, where $E_m[x] = \int_1^{\infty} \frac{e^{-xt}}{t^m} dt$ is the exponential integral function [90]. For the special case of Rayleigh fading channel, i.e. when the Rician factor $K = 0$, we have

$$\varepsilon[K, \bar{\gamma}] = \frac{1}{\bar{\gamma}} e^{\frac{1}{\bar{\gamma}}} E_1 \left[\frac{1}{\bar{\gamma}} \right]. \quad (4.50)$$

The values η_{∞} in (4.48), as a function of K and $\bar{\gamma}$, are depicted in Fig. 4.4 (solid lines). Also shown in the figure are the mean values of η for $N = 128$ obtained from simulations (stars) for Rician fading channels. From the figure, we have the following observations and discussions.

- For $N \rightarrow \infty$, the value η_{∞} in dB is approximately linearly increasing over the channel SNR $\bar{\gamma}$ in dB.
- For $N \rightarrow \infty$, the SNR value of each decision variable η_{∞} is smaller than the average channel SNR $\bar{\gamma} = E_s/N_0$, due to the residual ISI occurring in the decision variable, as seen in (4.34). The larger is the Rician K -factor, which implies less frequency selectivity, the smaller is the discrepancy between η_{∞} and $\bar{\gamma}$.
- For a large number of subcarriers ($N \geq 128$), the mean value of η can be well approximated by η_{∞} given in (4.48), especially for a relatively large Rician K -factor.

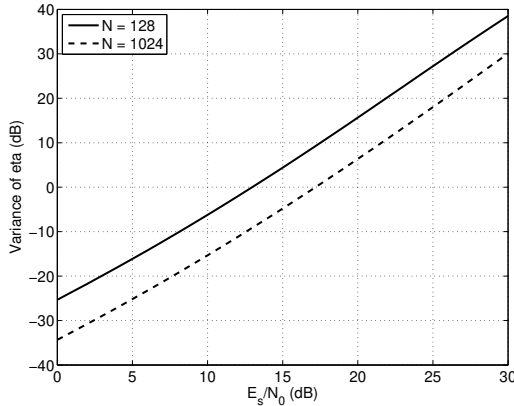


Fig. 4.5: The variance of η versus the channel SNR $\bar{\gamma} = E_s/N_0$ in simulated Rician fading channels with the Rician factor $K = 1$. The considered subcarrier numbers are $N = 128$ and 1024.

For the subcarrier number $N \rightarrow \infty$, by using (4.48) and (4.46), we have the BER of SC-FDE and MC-CDMA given by

$$\overline{\text{BER}}(K, \bar{\gamma}) = A \cdot \text{erfc} \left[B \sqrt{\eta_\infty[K, \bar{\gamma}]} \right], \quad (N \rightarrow \infty) \quad (4.51)$$

in Rician fading channels, where $\eta_\infty[K, \bar{\gamma}] = \frac{1}{\varepsilon[K, \bar{\gamma}]} - 1$. Obviously, the BER performance of SC-FDE and MC-CDMA behaves just like in AWGN channels, due to the exploited frequency diversity.

For a limited number of subcarriers N , the BER can still be computed approximately by using (4.51). The accuracy of the approximation is related to the variance of η , which is related to the channel SNR $\bar{\gamma}$ and the Rician K -factor. With the variance of η decreasing, the pdf of η tends to be a Dirac's delta function and the individual realization of η better approaches the expectation of η , i.e. $\eta \rightarrow \mathbb{E}\{\eta\} \approx \eta_\infty$, which implies a better BER approximation by using (4.51). To study the change of the variance of η , we simulated a Rician fading channel with $K = 1$ to obtain the variance of η . Fig. 4.5 depicts the obtained variance of η versus the channel SNR $\bar{\gamma}$ for two cases when the subcarrier numbers are $N = 128$ and 1024. It is observed from the figure that the variance of η increases with the increasing channel SNR $\bar{\gamma}$, resulting in a less accurate BER computation by using (4.51), as will be observed in Section 4.4.3. In addition, the larger the number of subcarrier, the smaller is the variance, indicating a more accurate BER computation by (4.51).

4.4.3 Simulated BER performance

In this section, baseband equivalent simulations are performed to evaluate the BER performance in Rician fading channels. For the simulated channels, the first tap

is fixed and the other taps follow zero-mean complex Gaussian distributions with variances exponentially decaying. In addition, the fading process is assumed to be stationary during the transmission of the block of data sequence. Two sets of channel parameters are used, consisting of Rician K -factors, tap numbers, root-mean-squared (RMS) delay spread and maximum excess delay: $\{1, 25, 7.5 \text{ ns}, 75 \text{ ns}\}$ and $\{10, 7, 1.5 \text{ ns}, 15 \text{ ns}\}$, which represent a relatively high and low level frequency selectivity of the channels. These channel parameters are taken from the measured indoor channels at 60 GHz configured with omnidirectional and narrow-beam antennas, respectively, as presented in Chapter 2. The simulated signal bandwidth is 1.75 GHz and the data block length is $N = 1024$, which could be a typical configuration parameters for 60-GHz radios, as will be elaborated in Chapter 7. The cyclic prefix is chosen to be 1/8 of the block length so that the inter-block interference is completely resolved. For all the simulations, the system is perfectly synchronized and the channel information is perfectly known at receiver.

4.4.3.1 Uncoded BER

The average uncoded BER performance versus the channel SNR per bit is shown in Fig. 4.6(a) and (b) for QPSK and 16-QAM with Gray bit-mapping, respectively. Also shown in the figures are the analytical BER in (4.44) for OFDM and the approximate computed BER in (4.51) for SC-FDE and MC-CDMA, respectively. As a reference, the BER performance under AWGN channel conditions is also depicted and is the same for the three schemes. Here the channel SNR per bit E_b/N_0 is related to the channel SNR per symbol E_s/N_0 by

$$\frac{E_b}{N_0} = \frac{\frac{E_s}{N_0}}{\log_2 \mathcal{M}}. \quad (4.52)$$

Although code spreading matrices \mathbf{C} are different in SC-FDE and MC-CDMA, the BER performance is the same, which has been explained in the previous section. Therefore, we only show the BER performance of SC-FDE.

From Fig. 4.6, we see that there is a good agreement between the analytically derived BER and the simulated BER for OFDM, especially for the QPSK modulation format. As for SC-FDE, a good agreement between the approximately computed BER and the simulated BER can be observed as well at low channel SNRs. With the SNR increasing, the computed BER tends to deviate from the simulated BER, because the approximation accuracy of the BER (4.46) by using (4.51) is reduced, as explained in the previous section. It is also observed from Fig. 4.6 that as expected, SC-FDE indeed significantly outperforms OFDM in Rician fading channels, especially for a low Rician K -factor channel. This can be explained by the fact that in OFDM, user symbols are carried directly by subcarrier channels and some subcarrier signals might be in deep fades below the noise level due to the channel frequency selectivity, resulting in a significant information loss in these subcarriers. In contrast, in SC-FDE, the deep faded subcarrier signals does not have such a big impact on signal detection, since each user symbol is spread over all the spectrum within the signal bandwidth.

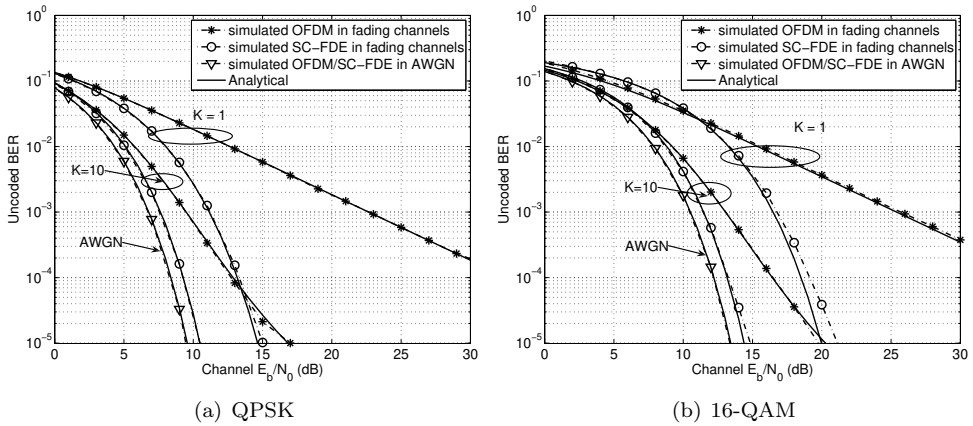


Fig. 4.6: Average uncoded BER performance versus average SNR per bit in the AWGN channel and Rician fading channels with $K = 1$ and 10 .

Table 4.1: The required E_b/N_0 (dB) at the target BER 1×10^{-3} for QPSK and 16-QAM modulated signals in OFDM and SC-FDE under AWGN and Rician fading channel conditions (from simulations). MC-CDMA has the same performance as SC-FDE.

Cases		AWGN		$K = 10$		$K = 1$	
		QPSK	16-QAM	QPSK	16-QAM	QPSK	16-QAM
Uncoded	OFDM	6.8	10.5	9.5 dB	13.1 dB	22.6 dB	25.7 dB
	SC-FDE			7.6 dB	11.4 dB	11.2 dB	16.8 dB
Coded	OFDM	4.5	7.8	5.6 dB	8.7 dB	9.9 dB	12.5 dB
	SC-FDE			5.2 dB	8.6 dB	8.1 dB	13.1 dB

In other words, an inherent frequency diversity gain is achieved in SC-FDE, because of the extra code-spreading and despreading operations.

The required channel SNRs at the target BER 1×10^{-3} are listed in Table 4.1 for OFDM and SC-FDE. It is seen from the table that for QPSK modulated signals, the uncoded SC-FDE has the advantages of about 11.4 and 1.9 dBs over the uncoded OFDM in Rician fading channels with $K = 1$ and 10 , respectively. For 16-QAM, the advantages are about 8.9 and 1.7 dBs. It is also observed that for SC-FDE, frequency selectivity of the Rician fading channel with $K = 10$ causes only about 1 dB loss compared in the AWGN channel.

4.4.3.2 Coded BER

Besides the uncoded BER, we also simulated the coded performance. A $3/4$ convolutional punctured encoder and a random bit-interleaver are combined in the transmitter for the three considered schemes. The code has the constraint length of 7 and the

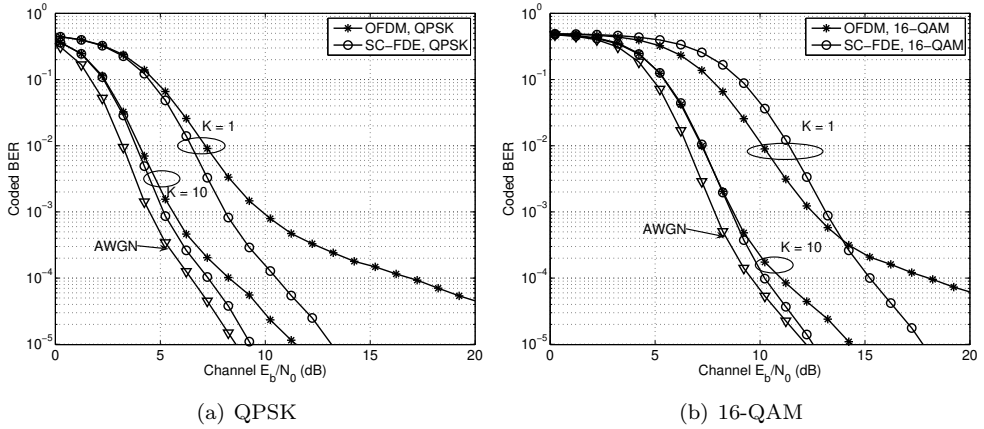


Fig. 4.7: Average coded BER versus average SNR per user bit in AWGN and Rician fading channels with $K = 1$ and 10 (convolutional code with 3/4 code rate and random bit interleaving).

minimum distance of 5 [87]. In the receiver, the sequence is recovered by using a soft Viterbi decoder. In doing so, the frequency diversity is exploited by both OFDM and SC-FDE, which results in a relatively fair comparison. Fig. 4.7(a) and (b) depict the coded BER over the channel SNR per user bit. Here the SNR per user bit for the code rate R_c is defined as

$$\frac{E_b}{N_0} = \frac{\frac{E_s}{N_0}}{R_c \log_2 \mathcal{M}}, \quad (4.53)$$

which is different from uncoded systems.

From Fig. 4.7, one can see that the performance gap between coded OFDM and coded SC-FDE has been remarkably narrowed down under Rician channel conditions. The required channel SNRs at the BER 1×10^{-3} are listed in Table 4.1. It is seen from the table that for the channel with a high Rician K -factor ($K = 10$), OFDM and SC-FDE achieve about the same coded performance. In case of low Rician K -factor ($K = 1$), QPSK-modulated OFDM requires about 1.8 dB more than SC-FDE to achieve the same BER at 1×10^{-3} . In comparison, for 16-QAM in the $K = 1$ channel, OFDM outperforms SC-FDE when the SNR is below a certain value ($\frac{E_b}{N_0} < 13.9$ dB), but not at higher SNR, which is consistent with the observations in [91]. Recall that under frequency selective channel conditions, decision SNRs are the same for all the decision variables in SC-FDE, while the decision SNRs in OFDM are frequency selective. Therefore, the probability of wrong detection for the higher constellations in coded SC-FDE becomes higher than that in coded OFDM at lower SNRs, but vice versa at higher SNRs. In other words, coded OFDM achieves more frequency diversity gain than coded SC-FDE at lower SNR but not at higher SNR. The still existing gap between OFDM and SC-FDE at high SNR indicates that in severe frequency selective

channels, a large constraint length or a strong code is needed for coded OFDM to achieve the same performance as coded SC-FDE.

4.5 Synchronization and channel estimation

So far, we have assumed perfect synchronization and channel estimation for the reception of the considered systems. However, synchronization and channel estimation are critical tasks before the steps of equalization and detection in digital transmission systems. A more realistic receiver diagram of transmission systems is illustrated in Fig. 4.8, where the operations of channel estimation and synchronization are included. In this diagram, the ADC unit consists of a sampler and a quantizer, which will be elaborated in Chapter 6. The sample timing issue is already addressed in Section 4.2. In this section, we address practical issues relevant to synchronization and channel estimation and their influences on BER performance.

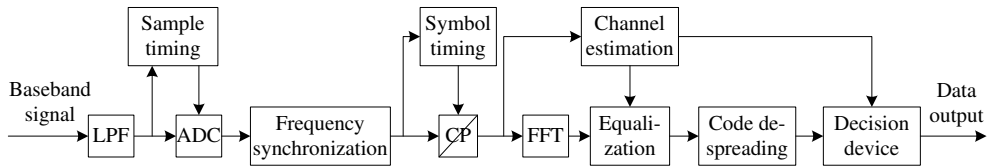


Fig. 4.8: Receiver structure with channel estimation, time and frequency synchronization included.

4.5.1 Training symbol design

For the purpose of synchronization and channel estimation, a sequence of known training symbols are generally transmitted before the user data sequences. For OFDM and MC-CDMA, the training sequences are carried by individual subcarrier channels, while in SC-FDE the training sequences are carried in the time domain. For a training sequence $\mathbf{c} = [c_0, \dots, c_{N-1}]^T$, the following two properties are desirable [91–94]

- The periodic autocorrelation function of the sequence is zero, except at the origin. In other words, the periodic autocorrelation of the sequence $\{c_n\}$ satisfies

$$\mathcal{R}_{\mathbf{c}}(j) = \sum_{n=0}^{N-1} c_n c_{\text{mod}(n+j, N)}^* = a\delta(j) \quad (4.54)$$

for $j = 0, \dots, N - 1$, where a is a constant. Sequences satisfying the condition (4.54) are called *perfect sequences* in literature and have been widely used in synchronization, fast-startup equalizations, etc.

- The training sequence has a constant amplitude in both the time domain and frequency domain. In other words, the elements of both the training sequence vector \mathbf{c} and its FFT $\mathbf{F}\mathbf{c}$ have constant amplitudes.

With the first property of the training sequence, the optimal starting position of an FFT window can be determined with a high resolution. The second property ensures that each frequency component of the channel is probed uniformly and meanwhile it avoids the nonlinear distortion at RF front-end.

Frank-Zadoff sequences and Chu sequences are two types of sequences that satisfy both the properties. The lengths of Frank-Zadoff sequences are restricted to perfect squares, i.e. \sqrt{N} is an integer for the sequence length of N [95]. The Frank-Zadoff sequences with a length N can be constructed according to

$$\mathbf{c} = \sqrt{E_s} \exp \left\{ \frac{i2\pi m}{\sqrt{N}} [0, \dots, \sqrt{N} - 1]^T \otimes [0, \dots, \sqrt{N} - 1]^T \right\}, \quad (4.55)$$

where m is relatively prime to \sqrt{N} and \otimes denotes Kronecker product. In comparison, the Chu sequences can be constructed for any length [96]. A length- N Chu sequence is given by

$$\mathbf{c} = \begin{cases} \sqrt{E_s} \exp \left\{ \frac{i\pi m}{N} [0, \dots, N - 1]^T \odot [0, \dots, N - 1]^T \right\} & \text{for even } N \\ \sqrt{E_s} \exp \left\{ \frac{i\pi m}{N} [0, \dots, N - 1]^T \odot [1, \dots, N]^T \right\} & \text{for odd } N \end{cases}, \quad (4.56)$$

where m is relatively prime to N and \odot denotes element-wise product. The two types of sequences have the same periodic autocorrelation function given by

$$\mathcal{R}_{\mathbf{c}}(j) = NE_s \delta(j) \quad (4.57)$$

for $j = 0, \dots, N - 1$. It is interesting to point out that after Fourier transformation, the resulting sequence $\mathbf{F}\mathbf{c}$ has the same property as \mathbf{c} in (4.57), i.e.

$$\mathcal{R}_{\mathbf{F}\mathbf{c}}(j) = NE_s \delta(j) \quad (4.58)$$

for $j = 0, \dots, N - 1$. Because of the properties in (4.57) and (4.58), the training sequence \mathbf{c} can conveniently be carried either in the frequency domain or in the time domain in the considered transmission systems.

4.5.2 Frequency offset

Frequency offsets in wireless transceiver systems are caused by the mismatch between the local oscillators of TX and RX. For the considered transmission systems in this chapter, the frequency offsets result in cross leakage among subcarrier signals, which destroys the orthogonality among the parallel transmission in multiple narrowband subcarrier channels. Therefore, accurate frequency synchronization is needed to recover the subcarrier orthogonality. Many data-aided and nondata-aided algorithms

have been proposed to estimate and correct the frequency offset, see [97–101]. Instead of developing new synchronization algorithms in this section, we investigate the influence of the residual frequency offset on different transmission systems after the compensation of the frequency offset.

Recall the sampled sequence (4.22) of the received signal with a non-zero frequency offset f_Δ . The offset is either the frequency mismatch between TX/RX local oscillators or the residual frequency error after the correction of frequency offset. Since the phase rotation caused by the frequency offset increases over time, multiple data blocks have to be taken into account. Consider the i th block of user symbol vector $\mathbf{x}(i) = [x_0(i), \dots, x_{N-1}(i)]^T$ for the index $i \geq 0$ and the corresponding transmit signal vector $\mathbf{u}_t(i) = \mathbf{F}^H \mathbf{C} \mathbf{x}(i)$. After removal of the cyclic prefix at receiver, the i th received signal vector in the time domain is given by

$$\mathbf{r}_t(i) = \mathbf{E}(i) \text{cir}\{\mathbf{h}\} \mathbf{u}_t(i) + \mathbf{v}_t(i) \quad (4.59)$$

where $\mathbf{v}_t(i)$ is the i th noise vector in the time domain. The diagonal matrix $\mathbf{E}(i)$ is the phase rotation matrix for the i th data block, due to the frequency offset, with the n th diagonal element $\exp\{j2\pi(n + N_g + i(N + N_g))f_\Delta T_s\}$. The N -size FFT leads to the signal vector in the frequency domain given by

$$\mathbf{r}(i) = \mathbf{\Xi}(i) \mathbf{H} \mathbf{u}(i) + \mathbf{v}(i), \quad (4.60)$$

where $\mathbf{u}(i) = \mathbf{C} \mathbf{x}(i)$ is the i th transmit signal vector in the frequency domain and the matrix $\mathbf{\Xi}(i) = \mathbf{F} \mathbf{E}(i) \mathbf{F}^H$. The matrix $\mathbf{\Xi}$ models the influence of the frequency offset in the frequency domain and is given by

$$\mathbf{\Xi}(i) = \begin{pmatrix} \xi_0(i) & \xi_{-1}(i) & \cdots & \xi_{-N+1}(i) \\ \xi_1(i) & \xi_0(i) & \cdots & \xi_{-N+2}(i) \\ \vdots & \vdots & \ddots & \vdots \\ \xi_{N-1}(i) & \xi_{N-2}(i) & \cdots & \xi_0(i) \end{pmatrix}, \quad (4.61)$$

where the element

$$\xi_k(i) = \frac{\sin(\pi(\delta - k))}{N \sin\left(\frac{\pi}{N}(\delta - k)\right)} e^{j\frac{\pi(N-1)}{N}(\delta - k)} e^{j\frac{2\pi\delta(i(N+N_g)+N_g)}{N}} \quad (4.62)$$

for $k \in (-N, N)$, where δ is the normalized frequency offset over the subcarrier spacing and given by $\delta = N f_\Delta T_s$.

To study the influence of the frequency offset, we re-arrange the received signal at the k th subcarrier into

$$r_k(i) = \xi_0(i) H_k u_k(i) + \underbrace{\sum_{\substack{k'=0 \\ k' \neq k}}^{N-1} \xi_{k-k'}(i) H_{k'} u_{k'}(i)}_{v_{\text{ICI},k}} + v_k(i), \quad (4.63)$$

where the transmit signal component at the k th subcarrier $u_k(i) = \sum_{n=0}^{N-1} C_{kn} x_n(i)$.

It is observed from (4.63) that the frequency offset gives rise to not only a complex attenuation ξ_0 , but also the ICI term $v_{\text{ICI},k}$. The attenuation is common to all the subcarrier signals within the same data block and given by

$$\xi_0(i) = \frac{\sin(\pi\delta)}{N \sin\left(\frac{\pi}{N}\delta\right)} e^{i\frac{\pi(N-1)}{N}\delta} e^{i\frac{2\pi\delta(i(N+N_g)+N_g)}{N}}, \quad (4.64)$$

which has the same influence on the performance of OFDM, SC-FDE and MC-CDMA. From (4.64), we see that the attenuation magnitudes are independent of the data block index, but the phase rotation increases over the data blocks and tends to shift decision variables out of the decision boundary. As a result, the BER performance is particularly sensitive to the phase rotation, especially for high-order constellations. For instance, consider the transmission of block data with block size $N = 1024$ and guard interval $N_g = 128$, the phase rotation versus data blocks is depicted in Fig. 4.9 for the normalized frequency offset $\delta = 0.001, 0.01, 0.03$ and 0.05 . From this figure, it is evident that the increasing phase rotation is very harmful to the detection performance, even for very small frequency offset.

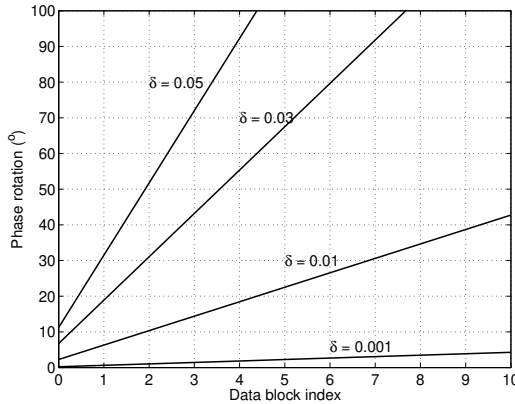


Fig. 4.9: Phase rotation increases over data blocks.

Besides the attenuation and phase rotation, the ICI also has a significant influence on the performance. The ICI is a weighted sum of the signals carried on all other subcarriers, as seen from (4.63), where the weight $|\xi_k|^2$ decreases with increasing subcarrier distance. The ICI destroys the orthogonality among subcarriers and will deteriorate the detection performance. For the k th subcarrier, the average ICI level, defined as $\sigma_{\text{ICI},k}^2 = \mathbb{E}\{|v_{\text{ICI},k}|^2\}$, is given by

$$\sigma_{\text{ICI},k}^2 = E_s \sum_{k'=0}^{N-1} |\xi_{k-k'}|^2 \mathbb{E}\{|H_{k'}|^2\} - E_s |\xi_0|^2 \mathbb{E}\{|H_k|^2\} \approx E_s (1 - |\xi_0|^2), \quad (4.65)$$

where $\mathbb{E}\{|H_{k'}|^2\} = 1$ and the approximation $\sum_{k'=0}^{N-1} |\xi_{k-k'}|^2 \approx 1$ [98]. Taking the ICI

as noise, frequency offset results in a reduced SNR of the k th subcarrier given by

$$\hat{\gamma}_k \approx \frac{|\xi_0|^2 \bar{\gamma} |H_k|^2}{\bar{\gamma}(1 - |\xi_0|^2) + 1}, \quad (4.66)$$

where $\bar{\gamma} = E_s/N_0$ is the average channel SNR. Here we define the average SNR loss caused by the frequency offset as $\bar{\gamma}|H_k|^2/\hat{\gamma}_k$, which is given by [98]

$$\mathcal{L}_{\text{FO}} = \frac{\bar{\gamma}(1 - |\xi_0|^2) + 1}{|\xi_0|^2} \approx \frac{\pi^2 \delta^2 \bar{\gamma} + 3}{3 - \pi^2 \delta^2}, \quad (4.67)$$

where the approximation is applied using $|\xi_0|^2 \approx 1 - \frac{(\pi\delta)^2}{3}$ for a small offset δ [98]. The expression (4.67) suggests that the SNR loss increases with the channel SNR $\bar{\gamma}$. At the required SNR listed in Table 4.1 under AWGN and Rician channel conditions for achieving the target BER 1×10^{-3} , the SNR losses caused by various frequency offsets are depicted in Fig. 4.10 for uncoded OFDM and SC-FDE. From this figure, we see that the SNR loss increases with the frequency offset and as well the channel frequency selectivity. The constellation with fewer points can tolerate larger frequency offsets. In addition, uncoded OFDM is more sensitive to the frequency offset than uncoded SC-FDE.

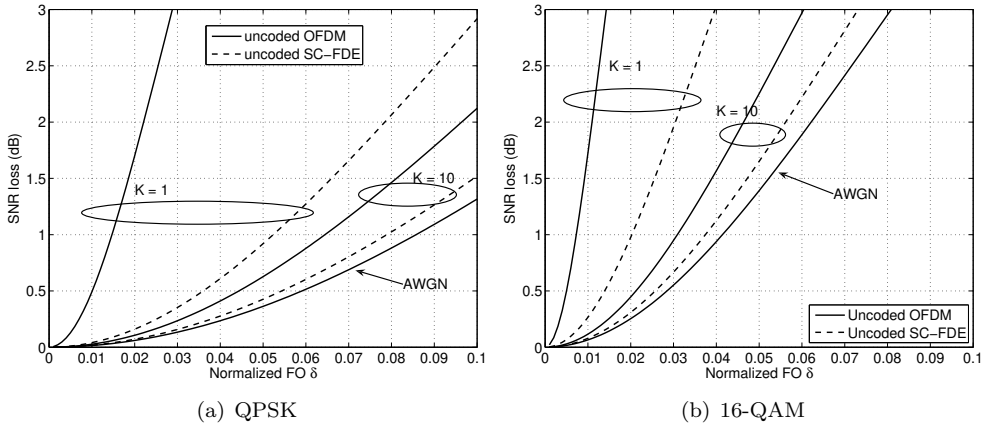


Fig. 4.10: SNR losses caused by frequency offset in QPSK and 16-QAM modulated OFDM and SC-FDE under AWGN and Rician channel conditions.

Frequency offset can be estimated by using training symbols to synchronize the transmit and received signal. Since frequency synchronization is not a perfect process, so there is always a residual frequency error. The resulting ICI should not be a problem, if the frequency error can be reduced to a level such that the SNR loss is negligible, whereas the resulting phase rotation is the main problem. For instance, for the residual frequency error $\delta = 0.01$, the SNR loss $L_{\text{FO}} < 0.5$ dB for QPSK modulation (see Fig. 4.10(a)), but the phase rotation is larger than 40° after only 10 data symbols (see Fig. 4.9), which makes it impossible for correct demodulation. Therefore, the phase

rotation has to be tracked while data symbols are received. This can be realized by inserting pilot symbols in the data symbol sequence, as used in wireless LAN systems [102].

4.5.3 Symbol timing

In the described transmission systems, guard intervals are inserted between data blocks to prevent ISI between data blocks. Symbol timing (ST) is to determine the best starting moment of each data block at receiver. With the starting position determined, the FFT window is defined. Ideally, the optimal symbol timing is positioned at the first sample of each data block, as shown in Fig. 4.11 for the ideal FFT window. In this case, the cyclic prefix is completely eliminated and thus no ISI from the previous data block is introduced in the current block, as long as the channel length is not longer than the CP length. In practical situations, however, it is hard to fix the symbol timing at the perfect position. As shown in Fig. 4.11, the actual symbol timing estimate could be before or after the ideal position. In case of after the ideal position (the FFT window B in Fig. 4.11), a significant ISI is caused by the CP part of the next data block.

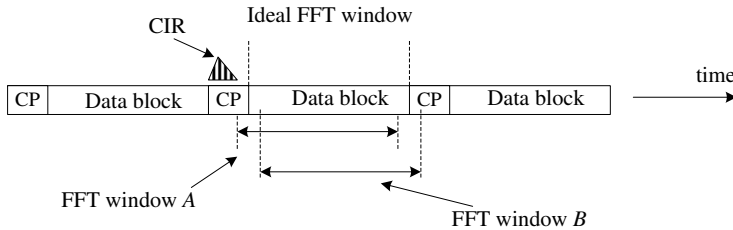


Fig. 4.11: Symbol timing estimation and FFT windowing.

In case of before the ideal position (the FFT window A in Fig. 4.11), the orthogonality among subcarriers is preserved, as long as the samples within the FFT window is not affected by the previous data block. The only effect suffered by each subcarrier signal is the phase rotation which increases with the subcarrier index. The phase rotation can not be distinguished from the channel and thus is compensated during channel equalization in the frequency domain. When the samples within the FFT window A are affected by the previous data block, however, the orthogonality among subcarriers is disturbed [103, 104]. Consequently, the k th subcarrier signal of the received signal (4.25) is phase rotated and contaminated by the disturbance. Then, the k th subcarrier signal becomes

$$r_k = \hat{H}_k u_k + v_k + d_k, \quad (4.68)$$

where u_k is the frequency component of the transmit signal at the k th subcarrier, \hat{H}_k is the phase rotated channel at the k th subcarrier, and d_k is the disturbance due to the interference from the previous data block. The phase rotated channel can be

conveniently compensated during channel equalization, but the disturbance d_k can have a significant influence on the BER for a bad symbol timing.

Symbol timing estimation can be performed with the aid of training sequences, which are generally available in the preamble part. Without losing generality, we consider that the Frank-Zadoff or Chu sequences are carried in the time domain in the considered transmission systems and are known at the receiver. For the purpose of symbol timing, it is important to acquire the cross correlation between the received signal with the known training sequence $\{c_n\}_{n \in [0, N-1]}$. Assuming that the training sequence is periodically transmitted in the time domain, the correlation is given by

$$\mathcal{X}(j) = \sum_{n=0}^{N-1} c_n^* r_{t, n+j} \quad (4.69)$$

for the index $j \geq 0$, where the received signal is given by

$$r_{t, m} = \sum_{l=0}^L h_l c_{\text{mod}(m-N_g-l, N)} + v_{t, m} \quad (4.70)$$

for $m \geq 0$. The correlation sequence can be further simplified as

$$\mathcal{X}(j) = \begin{cases} NE_s h_{\text{mod}(j, N+N_g)-N_g} + \sum_{n=0}^{N-1} c_n^* v_{t, n+j} & j \geq N_g \\ \sum_{n=0}^{N-1} c_n^* v_{t, n+j} & \text{others} \end{cases} \quad (4.71)$$

using the property of $\{c_n\}$ in (4.57). Clearly, the correlation sequence is merely a periodic channel impulse response sequence contaminated by noise. Note that the training sequence carried in the frequency domain will result in the same correlation sequence as here in (4.71), because of the properties given in (4.57) and (4.58).

Often used approaches for symbol timing are cross-correlation algorithms, based on the cross correlation (4.69), see [99, 101, 105, 106]. Here we only give an often used approach, which has a relatively good performance with a low complexity. The strategy of this approach is to maximize the power captured by the FFT window, i.e. ideally the power carried by all the propagation paths is captured. With this strategy, a sliding window with the length L_{ST} can be applied to collect the power of $\mathcal{X}(j)$ such that the symbol timing is determined according to

$$\hat{p} = \arg \max_p \sum_{n=0}^{L_{ST}} |\mathcal{X}(p+n)|^2. \quad (4.72)$$

Ideally, the window length can be set to be the same as the channel length, i.e. $L_{ST} = L$. In practice, the complexity can be reduced by choosing the window length to be shorter than the channel length without causing a significant performance loss.

From (4.72) and (4.71), we see that for the window length shorter than the channel length, i.e. $L_{ST} < L$, an imperfect symbol timing estimate yields ISI from neighboring data blocks. The resulting system performance is strongly related to the channel

properties for a fixed window length. For 60-GHz applications, the channels are in general Rician fading channels following exponentially decaying power delay profile (PDP), as addressed in Chapter 2. Fig. 4.12(a), (b) and (c) show the influence of imperfect symbol timing on the constellations of 16-QAM for OFDM, SC-FDE and MC-CDMA after MMSE channel equalization in the frequency domain. The considered channel is a noiseless Rician fading channel with $K = 1$ and the channel length $L = 128$. The sliding window length for the symbol timing is $L_{ST} = 60$. From these figures, we observe that the disturbance samples of decision variables in OFDM are more scattered than those in SC-FDE and MC-CDMA. This can be explained by the fact that the disturbance levels in OFDM are strongly dependent on the channel frequency selectivity at the corresponding subcarriers, whereas the disturbance levels in SC-FDE and MC-CDMA are the same for each decision variable.

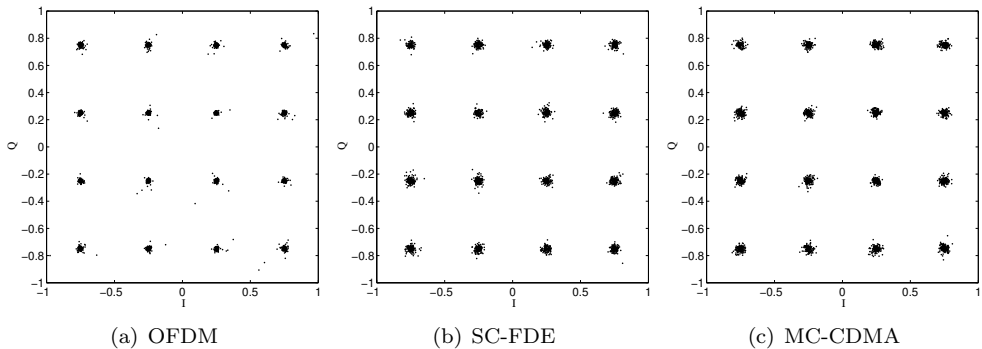


Fig. 4.12: The influence of the symbol timing on the constellation of 16-QAM in a noiseless Rician fading channel with $K = 1$. Here the channel length $L = 128$ and the sliding window length $L_{ST} = 60$.

Simulations were performed to evaluate the BER performance under the influence of imperfect symbol timing. Fig. 4.13 depicts the simulated BER performance of QPSK-modulated OFDM and SC-FDE, after the MMSE channel equalization, for sliding window lengths $L_{ST} = 128, 90, 60, 40$, where $L_{ST} = 128$ coincides with the channel length. The simulated channel is Rician fading with $K = 1$. MC-CDMA is not shown, for its performance is similar to SC-FDE. From this figure, we see that setting the window length to be about half of the channel length, i.e. $L_{ST} = 60$, leads to a small performance loss for both schemes. For $L_{ST} < 40$, the BER performance drops dramatically because of the high disturbance level.

From above analysis, we conclude that the influence of symbol timing on BER is ignorable as long as a sufficient long sliding window is properly selected. For 60-GHz radios with narrow-beam antenna configurations, the channel length is short and therefore, a good symbol timing can be effectively achieved with a relatively low complexity.

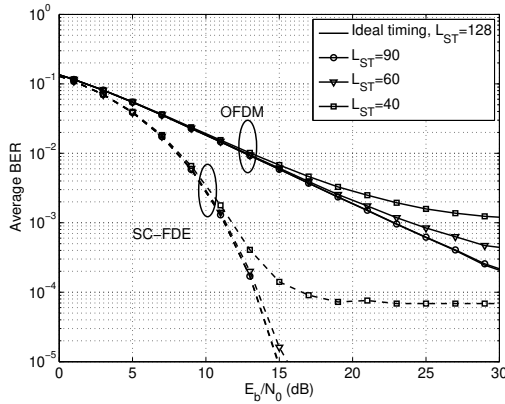


Fig. 4.13: Simulated BER for various sliding window lengths in symbol timing. The considered channel follows Rician fading with $K = 1$ and has an exponentially decaying PDP.

4.5.4 Channel estimation error

Channel estimation is an important step for the signal equalization and detection at receiver. Because of the block-by-block transmission structure, the channel estimation can be conveniently performed in the frequency domain and readily used for equalization in the frequency domain. Data-aided channel estimation can be based on either known training sequences or known pilots scatteredly inserted in data sequences. Both training sequences and pilots can be used in a practical system depending on its application and the operational environment. In this work, we focus on the training sequence based estimation techniques.

Consider that the Frank-Zadoff or Chu training sequence $\{c_k\}_{k \in [0, N-1]}$, which forms the vector \mathbf{c} , is carried in the frequency domain and transmitted. After a perfect symbol timing and Fourier transform, the resulting signal vector in the frequency domain is given by

$$\mathbf{r} = \mathbf{H}\mathbf{c} + \mathbf{v}. \quad (4.73)$$

Assuming that the channel is quasi static within a data packet and there is no frequency offset, the channel matrix \mathbf{H} is a diagonal matrix with the k th diagonal element H_k . In this case, the received signal at the k th subcarrier is given by $r_k = H_k c_k + v_k$.

1) *ZF channel estimation:* Based on the known training sequence $\{c_k\}$, the first approach for estimating the channel frequency response is to use a zero forcing (ZF) estimator in the frequency domain, which is also called least squares (LS) estimator. The ZF estimator chooses the estimate to minimize the squared error between the observed signal and the re-constructed signal, i.e. $|r_k - \hat{H}_k c_k|^2$. The resulting channel estimate is given by

$$\hat{H}_k = H_k + \epsilon_{H_k}, \quad (4.74)$$

where the estimation error $\epsilon_{H_k} = \frac{v_k}{c_k}$ with $\mathbb{E}\{|\epsilon_{H_k}|^2\} = N_0/E_s$. The advantage of the ZF estimator is its low complexity and no requirement on the knowledge of SNR.

2) *FFT-based channel estimation*: In practice, the temporal span of wireless channels in the time domain is much shorter than the FFT size. Therefore, a more accurate estimate of the channel can be obtained by setting the noise part of the ZF-estimated channel impulse response in the time domain to be zero, which involves both FFT and IFFT operations. Specifically, for the channel with a length L that is shorter than the FFT size N , one can check that the noise reduction technique applied for the original ZF channel estimation leads to the channel errors

$$\mathbb{E}\{|\epsilon_{H_k}|^2\} = \frac{LN_0}{NE_s}. \quad (4.75)$$

Compared with the regular ZF channel estimation in (4.74), the FFT-based technique leads to a significant reduction of the channel estimation errors. However, the computational complexity of the FFT-based technique is high because of the extra FFT and IFFT operations involved. A better way is to combine the channel estimation procedure with the symbol timing procedure in Section 4.5.3, where the channel response can be readily obtained from the cross correlation (4.71) after getting rid of the noise part. In this way, a comparable performance is achieved with a shared complexity with the symbol timing.

By using either one of the channel estimation techniques given above, we can obtain the channel estimate \hat{H}_k . For the obtained \hat{H}_k , the received signal of (4.25) at the k th subcarrier is re-expressed by

$$r_k = \hat{H}_k \sum_{n=0}^{N-1} C_{kn} x_n + \hat{v}_k, \quad (4.76)$$

where the disturbance $\hat{v}_k = \epsilon_{H_k} \sum_{n=0}^{N-1} C_{kn} x_n + v_k$ consists of the distortion, which is caused by the error of the estimated channel response, and the channel noise. Note that the disturbance \hat{v}_k has a zero mean and variance

$$\sigma_{\hat{v}}^2 = \mathbb{E}\{|\epsilon_{H_k}|^2\} E_s + N_0 \quad (4.77)$$

by assuming a zero-mean i.i.d. distribution of the symbol sequence $\{x_n\}$. Due to the channel estimation error, the signal-to-disturbance ratio at the k th subcarrier becomes

$$\hat{\gamma}_k = \frac{E_s}{\sigma_{\hat{v}}^2} |\hat{H}_k|^2, \quad (4.78)$$

in comparison with the SNR $\gamma_k = \frac{E_s}{N_0} |H_k|^2$ in case of perfect channel estimation.

To qualify the influence of channel errors, we define the channel SNR penalty as $\mathcal{L} = 10 \log_{10} \left(\frac{\mathbb{E}\{\gamma_k\}}{\mathbb{E}\{\hat{\gamma}_k\}} \right)$ in dB, which is further derived as

$$\mathcal{L} \text{ (dB)} = 10 \log_{10} \left(\frac{(\mathbb{E}\{|\epsilon_{H_k}|^2\} \bar{\gamma} + 1) |H_k|^2}{|\hat{H}_k|^2} \right), \quad (4.79)$$

where $\bar{\gamma} = E_s/N_0$ is the average channel SNR. For a large channel SNR $E_s/N_0 \gg 1$, we have $|H_k|^2 \approx |\hat{H}_k|^2$. For the ZF estimate (4.74), the channel SNR penalty can be well approximated by 3 dB using $\mathbb{E}\{\|\epsilon_{H_k}\|^2\} = \frac{N_0}{E_s}$. As for the FFT-based ZF estimate, the SNR penalty can be well approximated by $10 \log_{10}(L/N + 1)$ using (4.75). Obviously, the SNR penalty due to the FFT-based estimation technique is relatively smaller than the regular ZF-based techniques. For $L = 125$ and $N = 1024$, for instance, the SNR penalty is only 0.5 dB, compared to the 3 dB penalty using the regular ZF technique.

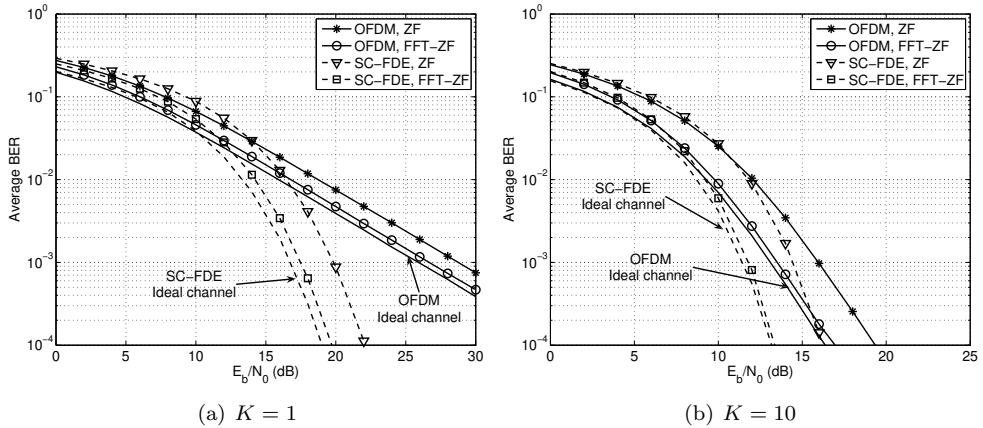


Fig. 4.14: Average BER of 16-QAM modulated OFDM and SC-FDE based on regular and FFT-based ZF channel estimation techniques in Rician fading channels with K -factor 1 and 10.

To examine the performance loss caused by the channel estimation error, we simulated 16-QAM modulated OFDM and SC-FDE without coding in Rician fading channels. The channel length $L = 125$ and the FFT size $N = 1024$, respectively. MC-CDMA has the same performance as SC-FDE and thus is not considered here. Here the MMSE weight

$$\hat{W}_k = \frac{\hat{H}_k^*}{|\hat{H}_k|^2 + \sigma_v^2/E_s} \quad (4.80)$$

is used to equalize the received signal (4.76) before code despreading and detection. Fig. 4.14(a) and (b) depict the simulated BER curves for the regular and FFT-based ZF channel estimation techniques, compared with the perfect channel estimation. From these figures, we observe that for the regular ZF technique, the SNR penalty due to the channel error is indeed about 3 dB at high channel SNR, especially for the channels with low frequency selectivity ($K = 10$). As for the FFT-based ZF technique, the SNR penalty is indeed about 0.5 dB. This confirms that the SNR penalty can be well estimated by using (4.79). It is further noted that in case of severe frequency selectivity ($K = 1$), the SNR penalty in OFDM is smaller than in SC-FDE, because the estimation error causes ignorable effect on the subcarriers with high SNRs.

4.6 Conclusions

This chapter investigated the optimal linear equalization and detection performance of wideband transmission schemes, including OFDM, SC-FDE and MC-CDMA, which are potential candidates for low-cost 60-GHz radios. Analytical BER expressions were derived under Rician fading channel conditions and have been shown to be in good agreement with the simulated BER. The comparison of the three transmission systems shows that both SC-FDE and MC-CDMA have the same uncoded BER performance and significantly outperform uncoded OFDM in frequency selective channels, due to the inherent frequency diversity gain. In combination with error correction codes and bit interleaving, the performance of coded OFDM can be significantly improved as the result of frequency diversity gain.

Frequency synchronization, symbol timing and channel estimation are crucial steps for correct demodulation at receiver for the considered wideband transmission schemes. These steps should be performed prior to channel equalization and signal detection, with the aid of training symbols in the preamble and the pilot symbols inserted in data sequences. The analysis shows that the influence of the frequency offset, symbol timing and channel error on system performance is ignorable, as long as appropriate algorithms are applied to perform these steps. In particular, the SNR penalty due to channel errors can be as low as 0.5 dB by using the FFT-based channel estimation technique.

Chapter 5

Residual ISI cancellation for code-spreading systems

5.1 Introduction

Due to the inherent frequency diversity gain, the linear detection of code-spreading schemes, such as single-carrier block transmission with FDE (SC-FDE) and multi-carrier code division multiple access (MC-CDMA), requires much less signal-to-noise ratio (SNR) than the uncoded orthogonal frequency division multiplexing (OFDM) scheme to achieve the same bit-error-rate (BER) performance in multipath propagation environments, as seen from Chapter 4. Recall that for a 60-GHz radio system configured with an omnidirectional antenna, multipath time dispersion is severe besides the relatively low power level of the received signal. In such a case, it is advantageous to apply the code-spreading schemes to relax the tight link budget design or improve the radio coverage without applying complicated error correction codes. Additionally, by the code-spreading schemes, it is possible to further improve the linear detection performance without significantly increasing the complexity, which is the main concern in this chapter.

Recall that in SC-FDE and MC-CDMA, the residual inter-symbol interference (RISI) occurs in the decision variables after the linear minimum mean square error (MMSE) equalization and the consecutive code-despreading. For the linear detection in Chapter 4, the RISI was seen as noise and therefore limits the performance capability, resulting in a channel capacity loss compared with the ideally coded OFDM, as confirmed in [107]. If the RISI information can be collected and then applied to cancel the RISI in individual decision variables before detection, then the detection performance can be improved and the channel capacity loss can be avoided.

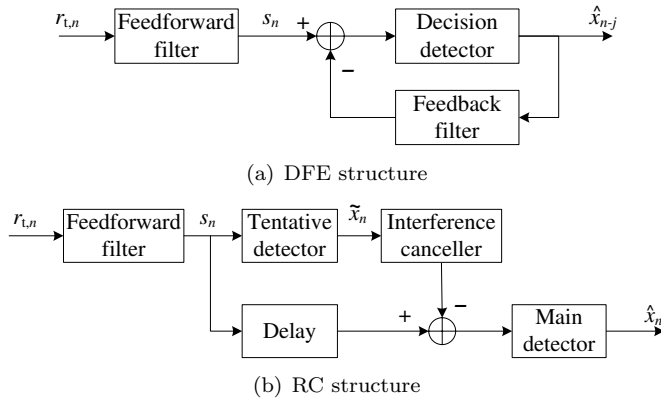


Fig. 5.1: Receiver structures of decision feedback equalizer and residual ISI canceller. The former is causal and the latter is noncausal.

One way to combat the RISI is to use the decision feedback equalizer (DFE) [87, 108, 109]. The general DFE structure is illustrated in Fig. 5.1(a). In the DFE, for the detection of the n th symbol x_n , first a feedforward (FF) filter equalizes the precursor of the ISI in the received signal $r_{t,n}$. Afterwards, a causal feedback (FB) filter is applied to suppress the residual signal error in the equalized signal s_n , based on the observation of previously detected symbols $\{\hat{x}_{n-j}\}$ for $j > 0$. Two types of DFEs are distinguished. In the first type, both the FF and FB filtering are performed in the time domain (TD) (referred to as TDFE) [87]. The second type of DFE is implemented in hybrid domains with the FF filter in the frequency domain (FD) and the FB filter in the TD (referred to as HDFE) [110, 111]. For the TDFE, the FF and FB filter orders can be any possible size, but a large number of coefficients are generally required to achieve a good performance, resulting in a high complexity. In comparison, the FF filter order in the HDFE is a fixed number that equals the fast Fourier transform (FFT) size due to its FD realization. With the aid of FFT, the FF filtering is efficiently implemented and has a relatively low complexity. The FB filter in the HDFE is causal and the filter length is generally much shorter than the FFT size, which facilitates the sequential cancellation of the residual ISI. With the channel length increased, the required number of FB filter coefficients becomes larger in order to track the RISI. As a result, the computational complexity of both the FB filtering and the filter design is increased. When the channel length is relatively large, a reduced-order FB filter is chosen in practice to leverage the complexity, but the capability of cancelling the RISI is not fully exploited.

Another approach is referred to as the RISI canceller (RC), which involves two steps, as illustrated in Fig. 5.1(b) [112, 113]. In the first step, a linearly equalized sequence s_n at the output of an FF filter is applied at the input of a tentative detector to make tentative decisions. In the second step, an interference canceller generates an estimate of the RISI in s_n and then the RISI estimate is removed from s_n before applying to the main detector for the final decision. The estimation of the RISI in

s_n is based on the tentative decisions $\{\tilde{x}_{n'}\}$ for $n' \neq n$ obtained in the first step. Since a delay is involved to make sure that all the tentative decisions are available for the estimation, the RC is essentially noncausal. The noncausal nature means that the cancellation of the RISI in an individual sample s_n is based not only on the prior decisions $\{\tilde{x}_{n'}\}$ for $n' < n$, but also on the subsequent decisions $\{\tilde{x}_{n'}\}$ for $n' > n$. Therefore, the RC is conceptually different from the DFE in that both the prediction and smoothing operations are involved for the RISI cancellation, instead of only the prediction in the DFE. In this sense, RISI cancellation is a broader concept than decision feedback equalization. Because of the noncausal nature, a memory is needed to hold the equalized signal s_n and two separate detectors are needed in the RC instead of only one in the DFE, indicating an increased complexity. On the other hand, the RC will provide a better detection performance than the DFE [112], because the RISI is more accurately cancelled.

Both the FF filter and the interference canceller in the RC can be implemented in the TD, such as applied in [112, 113]. Similar as in the DFE, the FF filter can be realized in the FD, which reduces the complexity, and the interference canceller is still realized in the TD, as applied for MC-CDMA in [114]. Also in [114], a reduced-order interference canceller is proposed to further reduce the complexity, but at the cost of performance loss.

In this chapter, we propose a low-complexity RISI canceller, which has the FF filter and the interference canceller both realized in the FD, for any code-spreading system. The low-complexity implementation in the FD owes a great deal to the explicit derivation of the optimal filter coefficients, which is not yet reported in literature. Most importantly, both the lower complexity and better performance are achieved at the same time, compared with the reduced-order DFE and RC schemes, due to the explicit derivation.

The outline of this chapter is as follows. In Section 5.2, the receiver structure configured with a RISI canceller is proposed and designed. Also addressed is its relationship with the existing reduced-order DFE and RC schemes. In Section 5.3, an alternative form of the scheme, which has a low implementation complexity, is developed. In addition, the explicit solution of filter coefficients for the interference canceller in the FD is derived and applied to clarify the design approaches for the existing reduced-order DFE and RC schemes. In Section 5.4, an upper bound on the performance of the proposed scheme is investigated. Finally, in Section 5.6, simulation results and complexity analysis will be conducted in comparison with various cancellation schemes. The analysis shows the great advantage of the proposed scheme in both performance and complexity.

5.2 Residual ISI cancellation

In this section, we consider the receiver structure of a RISI canceller, which has the FF filter realized in the FD and the interference canceller realized in the TD.

The proposed scheme will be compared with the existing DFE and RC schemes in literature. This section is the basis for developing an alternative form of the scheme, which has a low implementation complexity, as will be presented in Section 5.3.

5.2.1 Receiver structure

Consider the code-spreading systems described in Section 4.3 for the code spreading matrix $\mathbf{C} \neq \mathbf{I}$, where the spreading matrix satisfies $|C_{nn'}| = 1/\sqrt{N}$ for $n, n' \in \{0, \dots, N-1\}$. Since the received signal is processed block by block, we mainly use vectors and matrices for the description of the scheme in the following. Recall that ISI is limited inside each data block due to guard intervals, which are assumed to be longer than the channel length. Hence, only one data block will be considered for the rest of the chapter. The user symbol vector is \mathbf{x} with size $N \times 1$ and the corresponding transmit signal in the FD and TD are given by

$$\mathbf{u} = \mathbf{C}\mathbf{x} \quad \text{and} \quad \mathbf{u}_t = \mathbf{F}^H \mathbf{u}, \quad (5.1)$$

respectively, where H denotes the conjugate transpose. The received signal vector in the FD is

$$\mathbf{r} = \mathbf{H}\mathbf{C}\mathbf{x} + \mathbf{v}, \quad (5.2)$$

as given in (4.25), where \mathbf{H} and \mathbf{v} are the channel matrix and the noise vector in the FD, respectively. After the linear equalization by the weight matrix \mathbf{W} and the code despreading by \mathbf{C}^H , the resulting decision variable in a linear detection receiver is given by $\mathbf{s} = \mathbf{C}^H \mathbf{W} \mathbf{r}$ as given in (4.27). For convenience, the vector of decision variables after the linear equalization is repeated here

$$\mathbf{s} = \mathbf{x} + \underbrace{\mathbf{C}^H (\mathbf{W}\mathbf{H} - \mathbf{I}) \mathbf{C} \mathbf{x} + \mathbf{C}^H \mathbf{W} \mathbf{v}}_{\mathbf{e}}, \quad (5.3)$$

where T represents the transpose. The disturbance vector $\mathbf{e} = [e_0, \dots, e_{N-1}]^T$ consists of the RISI and the correlated noise in case of $\mathbf{W} \neq \mathbf{H}^{-1}$. As addressed in Section 4.3, the RISI occurs, because the signal and noise components at different subcarriers are combined into each decision variable by the code-despreading operation. The disturbance affects the detection performance and eventually results in a channel capacity loss, as confirmed in [107] for MC-CDMA.

To remove the RISI in (5.3), we propose a hybrid-domain RISI cancellation (HRC) scheme as illustrated in Fig. 5.2(a), where the FF filtering matrix \mathbf{W} equalizes the majority of the ISI in the FD and the cancellation matrix \mathbf{B} estimates the RISI in the TD, respectively. Both \mathbf{W} and \mathbf{B} have the same size of $N \times N$. After the linear equalization by \mathbf{W} in the FD, the equalized signal $\mathbf{y} = \mathbf{W}\mathbf{r}$ is transformed to the TD, yielding the equalized signal $\mathbf{s} = \mathbf{C}^H \mathbf{y}$ in the TD. Next, tentative decisions are made based on \mathbf{s} and denoted by $\tilde{\mathbf{x}} = [\tilde{x}_0, \dots, \tilde{x}_{N-1}]^T$. There are several ways to make tentative decisions, as will be elaborated in Section 5.4. With the tentative decisions $\tilde{\mathbf{x}}$, the tentative disturbance samples are estimated by $\tilde{\mathbf{e}} = \mathbf{s} - \tilde{\mathbf{x}}$ with $\tilde{\mathbf{e}} = [\tilde{e}_0, \dots, \tilde{e}_{N-1}]^T$

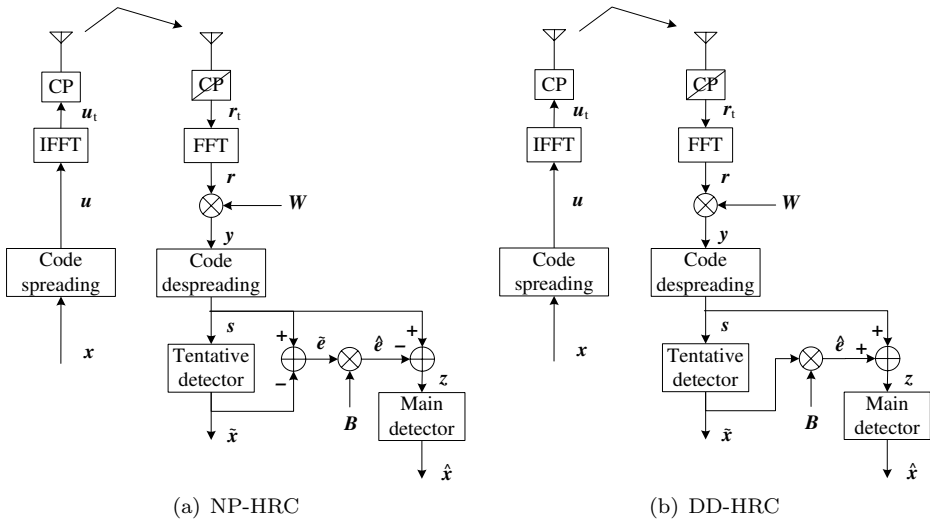


Fig. 5.2: Noise-predictive and decision-directed RISI cancellation schemes, where each scheme consists of tentative detection and RISI cancellation stages in the TD. In NP-HRC, the RISI estimate $\hat{\epsilon}$ is based on the tentative disturbance $\tilde{\epsilon}$, whereas in DD-HRC, the RISI estimate $\hat{\epsilon}$ is based on the tentative decision $\tilde{\mathbf{x}}$.

and used as the input to the cancellation matrix \mathbf{B} to generate the estimate of the RISI in \mathbf{s} . The resulting RISI estimate, denoted by $\hat{\epsilon} = [\hat{\epsilon}_0, \dots, \hat{\epsilon}_{N-1}]^T$, is given by

$$\hat{\epsilon} = \mathbf{B}\tilde{\epsilon}. \quad (5.4)$$

Next, the estimated RISI is subtracted from \mathbf{s} in the TD to produce the vector of decision variables, $\mathbf{z} = [z_0, \dots, z_{N-1}]^T$, given by

$$\mathbf{z} = \mathbf{s} - \hat{\epsilon} = \mathbf{s} - \mathbf{B}(\mathbf{s} - \tilde{\mathbf{x}}), \quad (5.5)$$

which is ideally free from the RISI. Based on \mathbf{z} , the main detector produces the final decision vector $\hat{\mathbf{x}}$. To make this scheme work, the signal vector \mathbf{s} has to be held in a memory until the RISI is cancelled. In the following, the FF filtering matrix \mathbf{W} and the cancellation matrix \mathbf{B} will be optimized under the MMSE criterion. As will be shown later, the RISI cancellation can be equivalently realized in the FD which has the advantage of low complexity.

The structure of the proposed cancellation scheme in Fig. 5.2(a) resembles the hybrid-domain noise-predictive DFE (NP-HDFE) in [111] applied in SC-FDE. In the NP-HDFE, the FB filtering is based on an estimated disturbance as well, and the FF and FB filters are implemented in the FD and the TD, respectively. For this reason, we give the name “hybrid-domain noise-predictive RISI canceller (NP-HRC)” to the proposed scheme in Fig. 5.2(a). As suggested by the block processing procedure, the NP-HRC is different from the NP-HDFE in that for the n th linearly equalized sample

s_n , the RISI cancellation is conducted based on both the past and future tentative decisions $\tilde{x}_{n'}$ for $n' \neq n$, instead of only past decisions in the NP-HDFE.

The RISI cancellation can be also based on tentative decisions directly, instead of based on the tentative disturbance, as illustrated in Fig. 5.2(b), yielding the hybrid-domain decision-directed RISI canceller (DD-HRC), which resembles the decision-directed HDFE (DD-HDFE) for SC-FDE in [110]. Here we still use \mathbf{W} and \mathbf{B} to represent the filter matrices in the DD-HRC for equalizing the majority of the ISI and cancelling the residual ISI, respectively. The linear equalization of the received signal \mathbf{r} by \mathbf{W} yields the equalized signal $\mathbf{s} = \mathbf{C}^H \mathbf{W} \mathbf{r}$, which is applied for the tentative detection. The RISI in \mathbf{s} is estimated directly based on the tentative decisions $\tilde{\mathbf{x}}$ by using $\hat{\mathbf{e}} = \mathbf{B} \tilde{\mathbf{x}}$. The compensation of $\hat{\mathbf{e}}$ results in the final decision variables

$$\mathbf{z} = \mathbf{s} + \mathbf{B} \tilde{\mathbf{x}}, \quad (5.6)$$

which is the input to the main detector.

In the following, we derive the filter matrices \mathbf{W} and \mathbf{B} , which jointly minimize the mean square error (MSE) of the main detector input \mathbf{z} , for both the NP-HRC and the DD-HRC, and clarify the difference between the two schemes.

5.2.2 Derivation of noise-predictive RISI canceller

Now we concentrate on the equalizer design for the NP-HRC scheme in Fig. 5.2(a). The error vector of the main detector input \mathbf{z} is given by

$$\boldsymbol{\epsilon}_z = \mathbf{z} - \mathbf{x} = (\mathbf{I} - \mathbf{B})(\mathbf{s} - \mathbf{x}) + \mathbf{B} \boldsymbol{\epsilon}_{\tilde{\mathbf{x}}}, \quad (5.7)$$

where $\boldsymbol{\epsilon}_{\tilde{\mathbf{x}}} = \tilde{\mathbf{x}} - \mathbf{x}$ with $\boldsymbol{\epsilon}_{\tilde{\mathbf{x}}} = [\epsilon_{\tilde{x}_0}, \dots, \epsilon_{\tilde{x}_{N-1}}]^T$ is the error vector of tentative decisions. To design the filters, we assume that the tentative decisions are perfect, i.e. $\tilde{\mathbf{x}} = \mathbf{x}$, resulting in the error vector $\boldsymbol{\epsilon}_{\tilde{\mathbf{x}}} = \mathbf{0}$. As a result, the autocorrelation matrix of $\boldsymbol{\epsilon}_z$ becomes

$$\begin{aligned} \mathbb{E}\{\boldsymbol{\epsilon}_z \boldsymbol{\epsilon}_z^H\} &= (\mathbf{I} - \mathbf{B}) \mathbb{E}\{(\mathbf{s} - \mathbf{x})(\mathbf{s} - \mathbf{x})^H\} (\mathbf{I} - \mathbf{B})^H \\ &= \frac{E_s}{N_0} (\mathbf{I} - \mathbf{B}) \mathbf{C}^H (\mathbf{W} \mathbf{T} \mathbf{W}^H - \mathbf{W} \mathbf{H} - \mathbf{H}^H \mathbf{W}^H + \mathbf{I}) \mathbf{C} (\mathbf{I} - \mathbf{B})^H. \end{aligned} \quad (5.8)$$

Here the matrix \mathbf{T} is given by

$$\mathbf{T} = \mathbf{H} \mathbf{H}^H + \frac{N_0}{E_s} \mathbf{I}, \quad (5.9)$$

where $E_s = \mathbb{E}\{|x_n|^2\}$ and $N_0 = \mathbb{E}\{|v_n|^2\}$. Now the filter matrices \mathbf{W} and \mathbf{B} can be derived by minimizing the MSE that is the trace of (5.8).

First, by setting the derivative of the trace of (5.8), with respect to \mathbf{W} , to be zero, we obtain the optimal equalization matrix

$$\mathbf{W} = \mathbf{H}^H \mathbf{T}^{-1}. \quad (5.10)$$

The rules for the differentiation over the trace of a matrix can be found in Appendix C. Note that the solution (5.10) is exactly the same as the linear MMSE equalizer given in (4.30). Substituting (5.10) back to (5.8), we have the autocorrelation matrix

$$\mathbb{E}\{\epsilon_z \epsilon_z^{\mathcal{H}}\} = (\mathbf{I} - \mathbf{B})\mathbf{C}^{\mathcal{H}}\mathbf{Q}\mathbf{C}(\mathbf{I} - \mathbf{B})^{\mathcal{H}}, \quad (5.11)$$

where \mathbf{Q} is a diagonal matrix given by

$$\mathbf{Q} = \frac{E_s}{N_0} (\mathbf{I} - \mathbf{H}^{\mathcal{H}}\mathbf{T}^{-1}\mathbf{H}) \quad (5.12)$$

with the k th diagonal element $Q_k = \frac{1}{|H_k|^2 + \frac{N_0}{E_s}}$, which is determined by the channel condition.

We next derive the optimal cancellation matrix \mathbf{B} . If the matrix \mathbf{B} is assumed to be a full rank matrix, the solution to minimize the trace of (5.11) is the identity matrix $\mathbf{B} = \mathbf{I}$. Then, the inputs to the decision device are merely the tentative decisions, i.e., $\mathbf{z} = \tilde{\mathbf{x}}$. This means that, from the point of view of information theory, the intrinsic information is fed back via the non-zero diagonal elements of \mathbf{B} , which results in no performance improvement at all. Therefore, similar to the strategy of turbo decoding [115], only extrinsic information should be used to gain the improvement by restricting the diagonal elements of \mathbf{B} to be zero.

With the diagonal elements of \mathbf{B} restricted to be zeros, the n th entry of $\hat{\mathbf{e}}$, \hat{e}_n , is the estimate of the RISI in s_n based on the observed tentative disturbance samples $\{\tilde{e}_{n'}\}$ for $n' \neq n$. The n th estimate \hat{e}_n is given by

$$\hat{e}_n = \sum_{\substack{n'=0 \\ n' \neq n}}^{N-1} B_{nn'} \tilde{e}_{n'} \quad (5.13)$$

for $0 \leq n \leq N - 1$. It is clear from (5.13) that the n th estimate is a linearly weighted combination of the prior and subsequent tentative disturbance samples. For ideally recovered tentative decisions, the tentative disturbance sample $\tilde{e}_{n'}$ is the exact disturbance $e_{n'}$ in $s_{n'}$, i.e. $\tilde{e}_{n'} = e_{n'}$.

According to the orthogonality principle for Wiener filter design, the optimal filter coefficients $B_{nn'}$ can be derived from the equation

$$\mathbb{E}\{e_n e_{n'}^*\} = \mathbb{E}\{\hat{e}_n e_{n'}^*\}, \quad (n \neq n') \quad (5.14)$$

for $n, n' \in [0, N - 1]$, where $*$ denotes conjugate. The solution to $B_{nn'}$ derived from (5.14) minimizes the trace of (5.11). Note that the left and right sides of (5.14) are the (n, n') th entries of the auto- and cross-correlation matrices, $\mathbb{E}\{\mathbf{e}\mathbf{e}^{\mathcal{H}}\}$ and $\mathbb{E}\{\hat{\mathbf{e}}\mathbf{e}^{\mathcal{H}}\}$, respectively. Combining (5.3) and (5.10), $\mathbf{e} = \mathbf{s} - \mathbf{x}$ and $\hat{\mathbf{e}} = \mathbf{B}\mathbf{e}$, we have $\mathbb{E}\{\mathbf{e}\mathbf{e}^{\mathcal{H}}\} = \mathbf{C}^{\mathcal{H}}\mathbf{Q}\mathbf{C}$ and $\mathbb{E}\{\hat{\mathbf{e}}\mathbf{e}^{\mathcal{H}}\} = \mathbf{B}\mathbf{C}^{\mathcal{H}}\mathbf{Q}\mathbf{C}$. The (n, n') th entries of the auto- and cross-correlation matrices are given by

$$\mathbb{E}\{e_n e_{n'}^*\} = q_{nn'}, \quad (5.15)$$

$$\mathbb{E}\{\hat{e}_n e_{n'}^*\} = \sum_{m=0}^{N-1} B_{nm} q_{mn'}, \quad (5.16)$$

respectively, where the autocorrelation sequence

$$q_{nn'} = \sum_{k=0}^{N-1} Q_k C_{kn}^* C_{kn'} \quad (5.17)$$

is the function of Q_k given in (5.12). Substituting (5.15) and (5.16) into (5.14), we can solve the n th row of the matrix \mathbf{B} from the $(N-1)$ equations

$$\sum_{\substack{m=0 \\ m \neq n}}^{N-1} B_{nm} q_{mn'} = q_{nn'} \quad (n' \neq n) \quad (5.18)$$

with $n' = 0, \dots, n-1, n+1, \dots, N-1$.

When the linear systems composed by (5.18) are non-singular, the solution to \mathbf{B} is unique and the off-diagonal entries of \mathbf{B} are linear functions of the autocorrelation sequence $\{q_{nn'}\}$, which is determined by the channel condition. However, obtaining the explicit solution is not a trivial task and has not been reported in literature. Therefore, online computation of \mathbf{B} from (5.18) is often needed. The full number of filter coefficients from (5.18) can be obtained by doing matrix inversion, which has a complexity of $\mathcal{O}(N(N-1)^3)$. For the two special cases when the code-spreading matrix \mathbf{C} is a Fourier matrix for SC-FDE or a Walsh-Hadamard (WH) matrix for MC-CDMA, the cancellation matrix \mathbf{B} is merely a circulant matrix or a dyadic matrix, respectively [110, 111, 114]. In such cases, the first column or the first row of \mathbf{B} can determine the whole matrix. Although the special structure can be used to reduce the complexity, obtaining the first column or the first row of \mathbf{B} is still not a trivial matter.

5.2.3 Derivation of decision-directed RISI canceller

After the derivation of the equalization matrices for the noise-predictive RISI canceller, it is interesting to derive the equalization matrices for the decision-directed canceller in Fig. 5.2(b) as well, which might have different features. The equalization matrices \mathbf{W} and \mathbf{B} of the DD-HRC scheme can be designed following a similar procedure as for the NP-HRC, by assuming ideal tentative decisions and minimizing the MSE of the equalized signal \mathbf{z} . For brevity, the detailed derivation is not repeated here. In the DD-HRC scheme, it can be proved that the cancellation matrix \mathbf{B} is exactly the same as in NP-HRC and can be computed from (5.18). However, the linear equalization matrix \mathbf{W} is different and given by

$$\mathbf{W} = \mathbf{C}(\mathbf{I} - \mathbf{B})\mathbf{C}^H \mathbf{H}^H \mathbf{T}^{-1}, \quad (5.19)$$

where \mathbf{T} has the same definition as in (5.9). Clearly, the FF filter matrix \mathbf{W} is coupled with the cancellation matrix \mathbf{B} and is different from the linear MMSE matrix (5.10) for $\mathbf{B} \neq \mathbf{0}$. Consequently, the linear detection of tentative decisions are not optimal in the DD-HRC and results in a relatively severer error propagation than in the NP-HRC. Furthermore, it can be observed from Fig. 5.2(b) that the DD-HRC does not

have a lower complexity than the NP-HRC. Therefore, only the NP-HRC will be considered in the rest of the chapter.

5.2.4 RISI cancellation with reduced-order filtering

As addressed earlier, the explicit solution to \mathbf{B} is so far unknown and obtaining the full size \mathbf{B} has a significantly high computational complexity. In addition, the full-order filtering for the RISI cancellation in (5.13) requires a number of multiplications. Therefore, the reduced-order filtering is often concerned in literature [110, 111]. The reduced-order design is to take advantage of the special structure of the cancellation matrix \mathbf{B} and restrict many elements to be zero, except a few of them, depending on the used spreading code, such that the filtering complexity can be reduced. The reasoning behind this is that the channel length L is generally much shorter than the block size N and as a result, the matrix \mathbf{B} has a number of elements with relatively small values. Here we give a short introduction about the reduced-order design, particularly for SC-FDE and MC-CDMA, which appeared in [111, 114]. The intention is to compare the existing cancellation schemes with the proposed NP-HRC.

5.2.4.1 Hybrid-domain noise-predictive DFE in SC-FDE

The receiver structure of the NP-HDFE is illustrated in Fig. 5.3 according to [111], where the FF filter is implemented in the FD and the FB filter is in the TD. A reduced-order design of the FB filter yields the Wiener estimate of the RISI in s_n given by

$$\hat{e}_n = \sum_{m=1}^{N_{\text{RC}}} b_m \tilde{e}_{n-m} \quad (5.20)$$

for the filter order $N_{\text{RC}} < N$, which predicts the RISI in the current sample s_n based on the past observations of \tilde{e}_{n-m} by using the filter coefficients $\{b_1, \dots, b_{N_{\text{RC}}}\}$. The FB filter coefficients $\{b_m\}$ are solved from the N_{RC} equations

$$\sum_{m=1}^{N_{\text{RC}}} b_m q_{m-n} = q_n, \quad (n = 1, \dots, N_{\text{RC}}), \quad (5.21)$$

where $q_n = \frac{1}{\sqrt{N}} \sum_{k=0}^{N-1} Q_k \exp\{i2\pi kn/N\}$ is the IFFT of Q_k scaled by $1/\sqrt{N}$ and Q_k is given in (5.12).

This scheme is equivalent to the NP-HRC in Fig. 5.2(a), by restricting the cancellation matrix \mathbf{B} to be a circulant matrix that is fully determined by its first column

$$\mathbf{b} = [0, b_1, \dots, b_{N_{\text{RC}}}, 0, \dots, 0]^T \quad (5.22)$$

with length N and its first row $[0, \dots, 0, b_{N_{\text{RC}}}, \dots, b_1]$. The non-zero coefficients are chosen by reasoning that the RISI in the current sample is mainly caused by

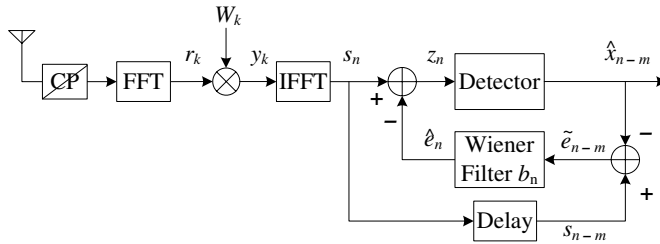


Fig. 5.3: The receiver structure of the NP-HDFE in SC-FDE.

the past samples [110, 111]. However, this reasoning is not completely correct, as will be justified in Section 5.3.3. Because of the causal feature, user symbols can be sequentially detected in the NP-HDFE and only one detector is needed, yielding a low computational complexity and a low requirement on the memory length for $N_{\text{RC}} \ll N$ [109, 111], but at the cost of performance as will be shown later.

5.2.4.2 Hybrid-domain RISI canceller in MC-CDMA

A reduced-order RISI canceller was proposed for MC-CDMA in [114], where a reduced-order cancellation filter is implemented in the TD to estimate the RISI after the FF filtering in the FD. The Wiener estimate of the RISI in the sample s_n is given by

$$\hat{\epsilon}_n = \sum_{m=1}^{N_{\text{RC}}} b_m \tilde{\epsilon}_{n \oplus m} \quad (5.23)$$

for the filter order $N_{\text{RC}} < N$, where \oplus denotes the modulo-2 addition and $\{b_m\}$ are filter coefficients. Here the modulo-2 addition performs an “exclusive OR (XOR)” operation digit by digit on the corresponding binary representations of the two decimal operands, and $n \oplus m$ is the decimal representation of the operation result¹ (e.g. $5 \oplus 7 = 2$) [116]. The FB coefficients $\{b_m\}$ is solved from the linear equations

$$\sum_{m=1}^{N_{\text{RC}}} q_{m \oplus n} b_m = q_n, \quad (n = 1, \dots, N_{\text{RC}}), \quad (5.24)$$

where $q_n = \frac{1}{\sqrt{N}} \sum_{k=0}^{N-1} Q_k C_{kn}^*$ is the inverse Walsh-Hadamard transform (IWHT) of Q_k scaled by $1/\sqrt{N}$ and Q_k is give in (5.12).

¹Modulo-2 addition is both a commutative and an associative operation, i.e.,

$$\begin{aligned} \text{commutativity:} & \quad m \oplus n = n \oplus m \\ \text{associativity:} & \quad (m \oplus n) \oplus s = m \oplus (n \oplus s) = m \oplus n \oplus s \end{aligned}$$

for non-negative integers m, n, s . Another important property of modulo-2 addition is that if $m \oplus n = s$, then $m = n \oplus s$ is valid.

This scheme is equivalent to the NP-HRC in Fig. 5.2(a), by restricting the cancellation matrix \mathbf{B} to be a dyadic matrix², which is fully determined by its first column

$$\mathbf{b} = [0, b_1, \dots, b_{RC}, \dots, 0]^T \quad (5.25)$$

with length N . As observed from simulations in [114], the non-zero coefficients $\{b_m\}$ are usually the most significant entries in the first column of the optimal \mathbf{B} , for a sequency WH matrix \mathbf{C} . This will be justified in Section 5.3.3.

The Wiener filtering (5.23) for MC-CDMA is conducted by a linear non-causal dyadic filter, instead of a regular linear causal filter as applied in (5.20) for SC-FDE. Such a filter structure arises because of the mechanism of causing the RISI in MC-CDMA, as seen from (5.3), where the WH matrix \mathbf{C} is involved for code spreading instead of the FFT matrix \mathbf{F} . For the same reason, it is impossible to design a causal cancellation filter for MC-CDMA, such that the RISI can be effectively cancelled in the TD in a sequential way.

5.2.5 Summary and discussion

The hybrid-domain RISI canceller was derived in this section for a class of code spreading systems, with the FF filter efficiently realized in the FD and the interference canceller realized in the TD. The relationship between the proposed scheme and the existing DFE and RC schemes was clarified. Since the explicit solution to the cancellation matrix \mathbf{B} is not available, solving linear equations is needed to update the canceller, once the channel condition has changed, and has high computational complexity. In addition, the interference cancellation using the full-size matrix, i.e. $\hat{\mathbf{e}} = \mathbf{B}\tilde{\mathbf{e}}$, needs a large number of multiplications as well. Reduced-order cancellation schemes have been proposed in literature to reduce the complexity, but the capability of cancelling the RISI is not fully exploited. In the next section, we develop an alternative form of the proposed NP-HRC scheme with the FF filter and the interference canceller both realized in the FD, based on the explicit derivation of the cancellation matrix. The alternative form has a low implementation complexity, in case that fast algorithms are available for the code spreading and despreading, without sacrificing the cancellation performance.

²For a $N \times N$ -size dyadic matrix \mathbf{B} , the (n, n') th entry $B_{nn'}$ has the same value of $B_{(n \oplus n')0}$ in the 0th column and $B_{0(n \oplus n')}$ in the 0th row for $0 \leq n, n' \leq N - 1$. As an example, the following matrix is a 8×8 -size dyadic matrix:

$$\mathbf{B} = \begin{bmatrix} b_0 & b_1 & b_2 & b_3 & b_4 & b_5 & b_6 & b_7 \\ b_1 & b_0 & b_3 & b_2 & b_5 & b_4 & b_7 & b_6 \\ b_2 & b_3 & b_0 & b_1 & b_6 & b_7 & b_4 & b_5 \\ b_3 & b_2 & b_1 & b_0 & b_7 & b_6 & b_5 & b_4 \\ b_4 & b_5 & b_6 & b_7 & b_0 & b_1 & b_2 & b_3 \\ b_5 & b_4 & b_7 & b_6 & b_1 & b_0 & b_3 & b_2 \\ b_6 & b_7 & b_4 & b_5 & b_2 & b_3 & b_0 & b_1 \\ b_7 & b_6 & b_5 & b_4 & b_3 & b_2 & b_1 & b_0 \end{bmatrix}.$$

5.3 Alternative implementation of the NP-HRC

5.3.1 RISI canceller in the FD

To develop an alternative form of the proposed NP-HRC in the FD, we first investigate the structure of the RISI cancellation matrix \mathbf{B} . As suggested by (5.14), the auto-correlation matrix $\mathbb{E}\{\mathbf{e}\mathbf{e}^H\} = \mathbf{C}^H\mathbf{Q}\mathbf{C}$ and the cross-correlation matrix $\mathbb{E}\{\hat{\mathbf{e}}\mathbf{e}^H\} = \mathbf{B}\mathbf{C}^H\mathbf{Q}\mathbf{C}$ have the same entries except the diagonal elements. Therefore, the cancellation matrix \mathbf{B} is the solution to the equation

$$\mathbf{C}^H\mathbf{Q}\mathbf{C} - \text{diag}\{\mathbf{C}^H\mathbf{Q}\mathbf{C}\} = \mathbf{B}\mathbf{C}^H\mathbf{Q}\mathbf{C} - \text{diag}\{\mathbf{B}\mathbf{C}^H\mathbf{Q}\mathbf{C}\}, \quad (5.26)$$

where $\text{diag}\{\mathbf{X}\}$ represents a square diagonal matrix with entries given by the diagonal entries of \mathbf{X} . The equation (5.26) is further simplified as

$$(\mathbf{B} - \mathbf{I})\mathbf{C}^H\mathbf{Q}\mathbf{C} = \text{diag}\{(\mathbf{B} - \mathbf{I})\mathbf{C}^H\mathbf{Q}\mathbf{C}\}. \quad (5.27)$$

Recall that the diagonal elements of \mathbf{B} are restricted to be zeros and the solution to \mathbf{B} is unique, we can deduce from (5.27) that the diagonal elements of $(\mathbf{B} - \mathbf{I})\mathbf{C}^H\mathbf{Q}\mathbf{C}$ have the same values and \mathbf{B} has the eigendecomposition given by

$$\mathbf{B} = \mathbf{C}^H\mathbf{D}\mathbf{C}. \quad (5.28)$$

The eigenvectors are the columns of the code-spreading matrix \mathbf{C} and the eigenvalues $\{D_k\}$ for $k = 0, \dots, N - 1$ are the entries of the diagonal matrix \mathbf{D} . The eigenvalues $\{D_k\}$ uniquely determines the cancellation matrix \mathbf{B} together with the eigenvectors. Since it is not a trivial task to derive the solution to \mathbf{D} based on (5.27), a different approach is applied in Section 5.3.2 to find the solution.

The eigendecomposition of \mathbf{B} in (5.28) reveals that the RISI estimation shown in Fig. 5.2(a), i.e. $\hat{\mathbf{e}} = \mathbf{B}\tilde{\mathbf{e}}$, can be conducted in the FD with the aid of the code-spreading and despreading operations. This yields an alternative implementation of the NP-HRC, as shown in Fig. 5.4. In the alternative form, the vector of tentative errors $\tilde{\mathbf{e}}$ is first transformed to the FD. Then the k th frequency component of $\tilde{\mathbf{e}} = \mathbf{s} - \tilde{\mathbf{x}}$ is equalized by the weight D_k to estimate the k th frequency component of the RISI, which is afterwards transformed back to the TD. Estimating the RISI in the FD is a more natural way than in the TD, in the sense that the RISI originates from the channel frequency selectivity and the FF filtering in the FD. After cancelling the RISI in the TD, the equalized signal vector is given by

$$\mathbf{z} = \mathbf{s} - \mathbf{C}^H\mathbf{D}\mathbf{C}(\mathbf{s} - \tilde{\mathbf{x}}), \quad (5.29)$$

where \mathbf{s} is the FF filtered signal by \mathbf{W} and given in (5.3).

Suppose that a fast algorithm can be implemented for code spreading/despreading, e.g. the fast Walsh-Hadamard transform in MC-CDMA and the FFT in SC-FDE, respectively, the alternative form of the NP-HRC is computationally more efficient than its original form.

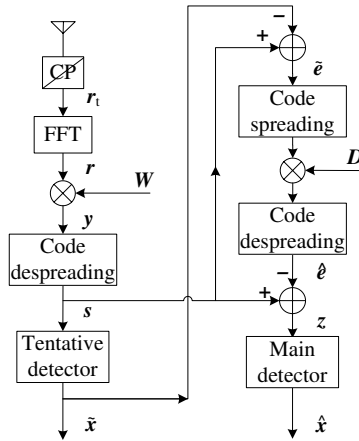


Fig. 5.4: Alternative implementation of the NP-HRC in Fig. 5.2(a). Both filtering operations by \mathbf{W} and \mathbf{D} are implemented in the FD.

5.3.2 Derivation of the FD filter coefficients D_k

In the following, we derive the explicit solution to the RISI cancellation matrix \mathbf{D} in the FD. Define $\tilde{\mathbf{B}} = \mathbf{C}^H \tilde{\mathbf{W}} \mathbf{C}$, where the diagonal matrix $\tilde{\mathbf{W}}$ is given by

$$\tilde{\mathbf{W}} = (\mathbf{I} - \mathbf{D}) \mathbf{W} \mathbf{H} \quad (5.30)$$

with the k th diagonal entry $\tilde{W}_k = W_k H_k (1 - D_k)$, and W_k is the k th diagonal entry of the diagonal weight matrix \mathbf{W} derived in (5.10). Now \tilde{W}_k and the (n, n') th entry of $\tilde{\mathbf{B}}$, $\beta_{nn'}$, are related by

$$\beta_{nn'} = \sum_{k=0}^{N-1} C_{kn}^* \tilde{W}_k C_{kn'}, \quad (5.31)$$

$$\tilde{W}_k = \sum_{n=0}^{N-1} \sum_{n'=0}^{N-1} C_{kn} \beta_{nn'} C_{kn'}^*. \quad (5.32)$$

Assuming that the tentative decisions are ideal, i.e. $\tilde{\mathbf{x}} = \mathbf{x}$, and by using $\tilde{\mathbf{B}} = \mathbf{C}^H \tilde{\mathbf{W}} \mathbf{C}$ and $\mathbf{B} = \mathbf{C}^H \mathbf{D} \mathbf{C}$, the vector of decision variables (5.5) and the MSE matrix (5.11) is re-arranged into

$$\mathbf{z} = \text{diag}\{\tilde{\mathbf{B}}\} \mathbf{x} + \left(\tilde{\mathbf{B}} + \mathbf{B} - \text{diag}\{\tilde{\mathbf{B}}\} \right) \mathbf{x} + \tilde{\mathbf{v}} \quad (5.33)$$

$$\mathbb{E}\{\boldsymbol{\epsilon}_z \boldsymbol{\epsilon}_z^H\} = (\mathbf{I} - \mathbf{B})(\mathbf{I} - \mathbf{B})^H - \tilde{\mathbf{B}}(\mathbf{I} - \mathbf{B}^H), \quad (5.34)$$

respectively, where $\boldsymbol{\epsilon}_z = \mathbf{z} - \mathbf{x}$ is the error vector of \mathbf{z} and $\tilde{\mathbf{v}} = (\mathbf{I} - \mathbf{B}) \mathbf{C}^H \mathbf{W} \mathbf{v}$ is the noise vector with the n th entry \tilde{v}_n . Note that the noise vector $\tilde{\mathbf{v}}$ has a zero mean and is independent of the desired signal \mathbf{x} .

Expanding the entries of the vectors (5.33) and (5.34) leads to the n th decision variable and its MSE

$$z_n = \beta_{nn}x_n + \sum_{\substack{n'=0 \\ n' \neq n}}^{N-1} (B_{nn'} + \beta_{nn'})x_{n'} + \tilde{v}_n \quad (5.35)$$

$$\mathbb{E} \{|z_n - x_n|^2\} = E_s \left(\sum_{\substack{n'=0 \\ n' \neq n}}^{N-1} B_{nn'}^* (B_{nn'} + \beta_{nn'}) - \beta_{nn} + 1 \right), \quad (5.36)$$

respectively, where the noise

$$\tilde{v}_n = \sum_{n'=0}^{N-1} \frac{C_{n'n}^* \widetilde{W}_{n'} v_{n'}}{H_{n'}}. \quad (5.37)$$

It is readily seen from (5.35) that the decision variable consists of a scaled desired signal, the residual ISI and a noise term.

Since $\mathbf{D} = \mathbf{C}\mathbf{B}\mathbf{C}^H$, the k th diagonal element D_k is a linear function of $B_{nn'}$, i.e.

$$D_k = \sum_{n=0}^{N-1} \sum_{\substack{n'=0 \\ n' \neq n}}^{N-1} C_{kn} C_{kn'}^* B_{nn'}. \quad (5.38)$$

Therefore, deriving the optimal $\{D_k\}$ is equivalent to derive $B_{nn'}$ by minimizing the MSE in (5.36), i.e. by solving $\frac{\partial \mathbb{E}\{|z_n - x_n|^2\}}{\partial B_{nn'}^*} = 0$ for $n' \neq n$, which results in

$$B_{nn'} = -\beta_{nn'} \quad (n' \neq n). \quad (5.39)$$

Substituting (5.39) into (5.38) and using (5.31)-(5.32), we obtain

$$D_k = -\widetilde{W}_k + \frac{1}{N} \sum_{k'=0}^{N-1} \widetilde{W}_{k'}. \quad (5.40)$$

From (5.40) and using $\widetilde{W}_k = W_k H_k (1 - D_k)$, the solution to D_k is finally derived after some manipulations and is given by

$$D_k = -\frac{|H_k|^2 - E_{|H|^2}}{\frac{N_0}{E_s} + E_{|H|^2}} \quad (5.41)$$

for $k = 0, \dots, N-1$. Here

$$E_{|H|^2} = \frac{1}{N} \sum_{k=0}^{N-1} |H_k|^2 = \sum_{l=0}^L |h_l|^2 \quad (5.42)$$

denotes the mean channel energy per subcarrier and the second equality in (5.42) is verified by using $H_k = \sum_{l=0}^L h_l e^{-j2\pi kl/N}$, where h_l is the l th channel path.

It is immediately seen from (5.41) that D_k is simply a scaled version of $|H_k|^2$ with its mean removed, which reflects the fact that the intrinsic information has been removed. Therefore, computing $\{D_k\}$ is remarkably simple, since only N multiplications of computing $\{|H_k|^2\}$ and N additions are involved, which allows a fast acquisition of $\{D_k\}$ in varying channel conditions. Actually $\{|H_k|^2\}$ are already available during the computation of the MMSE weight in (5.10).

5.3.3 Significance of RISI filtering taps in the TD

With $\{D_k\}$ obtained, the cancellation matrix \mathbf{B} in the TD is also determined. For SC-FDE and MC-CDMA, for instance, the matrices of \mathbf{B} are circulant and dyadic matrices, respectively, and can be fully determined by the first column \mathbf{b} of the matrix, with the entries

$$b_m = B_{m,0} = \frac{1}{\sqrt{N}} \sum_{k=0}^{N-1} D_k C_{km}^* \quad (5.43)$$

for $m = 1, \dots, N-1$. One can see that the first column of \mathbf{B} is merely the IFFT and IWHT of the sequence $\{D_k\}$ scaled by $1/\sqrt{N}$ for SC-FDE and MC-CDMA, respectively.

At this point, it is possible to check the significance of the entries in \mathbf{b} in terms of their amplitude, based on (5.43) with the explicit expression of D_k given in (5.41). The sequence of the significance is relevant with the reduced-order design of the RISI canceller in Section 5.2.4, about how to restrict part of entries in \mathbf{b} to be zero. For a sequency-ordered WH matrix in MC-CDMA³, the coefficients $\{b_m\}$ are real and the amplitudes of $\{b_m\}$ tend to decrease with m , due to the increasing zero crossing rates of the rows of \mathbf{C}^H . This justifies the way of designing a reduced-order filter for the RISI estimation in (5.23) for MC-CDMA.

As for SC-FDE, we first notice that the sequence $\{b_m\}$ is conjugate symmetrical over the center at $m = \frac{N}{2}$ (keep in mind that $b_0 = 0$), as the result of the Fourier transform of the real sequence $\{D_k\}$. In addition, the harmonic numbers (number of zero crossings divided by two) increase for the rows of the first half of the inverse Fourier matrix \mathbf{F}^H . For this reason, the first half part of the sequence $\{b_m\}$ tends to have the amplitudes decreasing. During the design of the FB equalizer with a reduced order in (5.22) for the NP-HDFE, only the most significant coefficients within the first half of $\{b_m\}$ were taken into account. Or in other words, half of the most significant taps were forced to be zero. This explains why RC schemes outperform DFE schemes, as will be seen in Section 5.5.

³For sequency-ordered WH spreading matrix \mathbf{C} , the rows are arranged in the ascending order of zero crossings [117]. This is analog to the concept of frequency in Fourier transform, where Fourier components are also arranged in increasing harmonic numbers. The use of the sequency-ordered WH matrix allows suitable comparisons to be made in this section for the significance of the filter coefficients in \mathbf{B} .

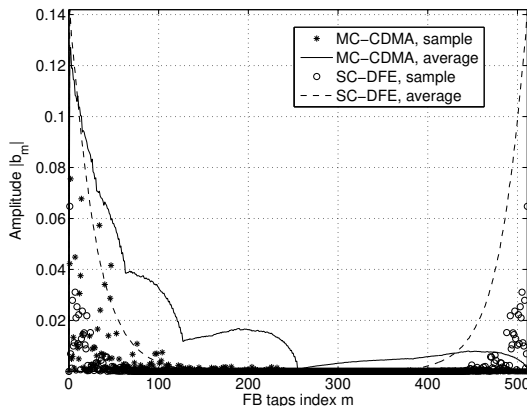


Fig. 5.5: Significance of the filter coefficients $\{b_m\}$ for the RISI estimation in MC-CDMA and SC-FDE for typical Rayleigh fading channels, where the block length $N = 512$ and the channel length $L = 125$.

To confirm the arguments made about the significance distribution of the filter coefficients, we simulated Rayleigh fading channels with an exponentially decaying delay profile to obtain the sequences of $\{b_m\}$. Fig. 5.5 shows the sample and average sequences of $\{|b_m|\}$, respectively, for MC-CDMA and SC-FDE. The simulation confirms that $\{|b_m|\}$ indeed has a decreasing tendency in MC-CDMA, but has a symmetrical “U” shape in SC-FDE. The “U” shape of $\{|b_m|\}$ in SC-FDE implies that a reduced-order filtering of the RISI can be better designed by choosing the most significant entries along the two edges of the “U” shape, instead of those within the first half of the sequence $\{b_m\}$. By doing so, the estimation of the RISI will be based not only on the previously observed samples, but also on the “future” observed samples. However, the filtering becomes non-causal and the receiver cannot do a sequential detection.

5.4 Tentative detection and upper bound performance

For the proposed noise-predictive RISI canceller, an extra decision device is needed to provide tentative decisions. In this section, we introduce several approaches for tentative detections and explore the upper bound performance. More comprehensive performance analysis for RISI cancellers using tentative decisions can be found in [112, 113].

5.4.1 Tentative detections

There are often three options for a decision device: a hard slicer, a soft decision device or a combination of a decoder and an encoder. Among the three choices, the symbols recovered from the hard slicer provides the most inaccurate information for the RISI cancellation. For the decoder/encoder, the re-generated symbols are relatively accurate with the aid of error correction codes, at the cost of bandwidth efficiency due to the redundant information added in the data sequence. In case of convolutional codes, the tentative detector is replaced by the combination of a Viterbi decoder and a symbol regenerator.

As for the second option, an optimum soft decision device can be designed, by using the maximum *a posteriori* probability (MAP) algorithm, to minimize the MSE between the transmitted symbols $\{x_n\}$ and the soft decisions $\{\tilde{x}_n\}$. The resulting optimum soft decision is given by

$$\tilde{x}_n = \mathbb{E}\{\alpha_j|\mathbf{s}\} = \sum_{\alpha_j \in \mathcal{A}} P(\alpha_j|\mathbf{s}), \quad (5.44)$$

where \mathcal{A} is the constellation alphabet and $P(\alpha_j|\mathbf{s})$ is the *a posteriori* probability of α_j for an observed equalized sequence $\{s_n\}$. The error performance of the MAP algorithm is not much different from the Viterbi algorithm at high SNR. However, the MAP algorithm is considerably more complex than the Viterbi algorithm, because the calculation of *a posteriori* probabilities for all possible state transitions involves multiplications and exponentiations, and more memory is required [118]. Therefore, the optimal MAP algorithm is not a practical solution for tentative decisions in terms of complexity and performance.

Here we introduce a simplified version of the MAP algorithm proposed in [118], where it is assumed that the soft decision \tilde{x}_n is a function only of the current observation s_n and in addition, the error disturbance in s_n is Gaussian distributed. In this case, the soft decision is given by

$$\tilde{x}_n = \mathbb{E}\{\alpha_j|s_n\} = \frac{\sum_{\alpha_j \in \mathcal{A}} \alpha_j e^{-\eta(|\alpha_j|^2 - s_n^* \alpha_j - s_n \alpha_j^*)}}{\sum_{\alpha_j \in \mathcal{A}} e^{-\eta(|\alpha_j|^2 - s_n^* \alpha_j - s_n \alpha_j^*)}}, \quad (5.45)$$

where η is the SNR of the linearly equalized signal s_n in (5.3). Assuming $\mathcal{A} = \left\{ \pm \frac{1}{\sqrt{2}}(1 \pm \iota) \right\}$ for QPSK, for instance, we have the following soft decision

$$\tilde{x}_n = \frac{1}{\sqrt{2}} \left(\tanh \left[\sqrt{2}\eta \operatorname{Re}\{s_n\} \right] + \iota \tanh \left[\sqrt{2}\eta \operatorname{Im}\{s_n\} \right] \right). \quad (5.46)$$

Here the hyperbolic tangent function $\tanh[\cdot]$ can be implemented, in practice, in the form of a lookup table.

5.4.2 Ideal tentative decisions

Assuming that the tentative decisions are perfect, i.e. $\tilde{\mathbf{x}} = \mathbf{x}$, such that the excitation of the RISI cancellation matrix is exactly the disturbance that appeared in the linearly equalized signal, i.e. $\tilde{\mathbf{e}} = \mathbf{e}$. Substituting (5.39) into (5.35) and (5.36), we obtain the decision variable after the RISI cancellation and its MSE

$$z_n = \beta_{nn}x_n + \tilde{v}_n \quad (5.47)$$

$$\mathbb{E}\{|z_n - x_n|^2\} = E_s(1 - \beta_{nn}). \quad (5.48)$$

It is readily seen from (5.47) that when the tentative decisions are ideal, the RISI appearing in the linearly equalized signal is completely eliminated after cancellation and the MSE (5.48) is minimized.

Combining (5.47) and (5.48), we obtain the noise variance $\mathbb{E}\{|\tilde{v}_n|^2\} = E_s\beta_{nn}(1 - \beta_{nn})$. Since the scaling factor

$$\beta_{nn} = \frac{1}{N} \sum_{k=0}^{N-1} \tilde{W}_k = \frac{E_{|H|^2}}{E_{|H|^2} + \frac{N_0}{E_s}} \quad (5.49)$$

is independent of n , each decision variable within a data block has the same SNR given by

$$\text{SNR}_{\text{ideal}} = \frac{\beta_{nn}^2}{\beta_{nn}(1 - \beta_{nn})} = \frac{E_s}{N_0} E_{|H|^2} = \frac{E_s}{N_0} \sum_{l=0}^L |h_l|^2. \quad (5.50)$$

The SNR of each decision variable in (5.50) reveals that the useful signal power contributed by all the propagation paths has been integrated for the recovery of user symbols and there is no remaining RISI in decision variables. This shows that channel capacity loss, caused by the RISI after linear equalization in code-spreading schemes, for instance in MC-CDMA as pointed out in [107], is prevented in the NP-HRC scheme. This feature makes the proposed NP-HRC particularly suitable for 60-GHz radios in multipath environments, e.g. in NLOS channel environment, where a sufficient signal power is needed at receiver for a reliable reception.

For a linearly modulated NP-HRC scheme, the uncoded BER for the channel realization $\{h_l\}$ with $l = 0, \dots, L$ is given by

$$\text{BER} \left(\frac{E_s}{N_0} \sum_{l=0}^L |h_l|^2 \right) \approx A \cdot \text{erfc} \left[B \sqrt{\frac{E_s}{N_0} \sum_{l=0}^L |h_l|^2} \right], \quad (5.51)$$

where $\text{BER}(\gamma) \approx A \cdot \text{erfc} [B\sqrt{\gamma}]$ as defined in (4.40), the parameters $A = 2(1 - 1/\sqrt{\mathcal{M}})/\log_2 \mathcal{M}$, $B = \sqrt{\frac{3}{2(\mathcal{M}-1)}}$ for a square \mathcal{M} -QAM and $A = 1/\log_2 \mathcal{M}$, $B = \sin \frac{\pi}{\mathcal{M}}$ for \mathcal{M} -PSK. For a Rician fading channel with taps $\{h_l\}$ and $\mathbb{E} \left\{ \sum_{l=0}^L |h_l|^2 \right\} =$

1, the average BER is given by

$$\overline{\text{BER}} = \mathbb{E} \left\{ \text{BER} \left(\frac{E_s}{N_0} \sum_{l=0}^L |h_l|^2 \right) \right\} \geq \text{BER} \left(\frac{E_s}{N_0} \right), \quad (5.52)$$

where $\text{BER} \left(\frac{E_s}{N_0} \right)$ represents the matched filter performance in an additive white Gaussian noise (AWGN) channel [87]. Since $\text{erfc}[x]$ is a convex function for $x \geq 0$, the inequality in (5.52) can be verified using Jensen's inequality. The equality is valid only in case that the channel has a constant power $\sum_{l=0}^L |h_l|^2 = 1$. Clearly, the NP-HRC scheme with the ideal tentative decisions has the performance lower bounded by the matched filter bound (MFB), which benchmarks the best performance that can be achieved, after the residual ISI is completely cancelled.

5.4.3 Non-ideal tentative decisions

In practical systems, the tentative decisions are not perfectly recovered. Otherwise, the RISI canceller is not needed anymore. For the tentative decisions $\{\tilde{x}_n\}$, which forms the vector $\tilde{\mathbf{x}}$, the n th decision variable after the RISI cancellation is given by

$$z_n = \beta_{nn}x_n - \underbrace{\sum_{\substack{m=0 \\ m \neq n}}^{N-1} \beta_{nm}\epsilon_{\tilde{x}_m}}_{\epsilon_{z_n}} + \tilde{v}_n, \quad (5.53)$$

where ϵ_{z_n} is the disturbance in z_n and $\epsilon_{\tilde{x}_m} = \tilde{x}_m - x_m$ is the error of \tilde{x}_m , the items β_{nm} and \tilde{v}_n are defined in (5.31) and (5.37), respectively.

The errors $\{\epsilon_{\tilde{x}_m}\}$ in a data block $\tilde{\mathbf{x}}$ can be assumed to be statistically independent of the symbols $\{x_n\}$ and the noise samples $\{\tilde{v}_n\}$ for $n \neq m$. Based on the assumption, the average power of the disturbance in z_n , $P_{\epsilon_{z_n}} = \mathbb{E}\{|\epsilon_{z_n}|^2\}$, is given by

$$P_{\epsilon_z} = E_s\beta_{nn}(1 - \beta_{nn}) + \mathbb{E} \left\{ \left| \sum_{\substack{m=0 \\ m \neq n}}^{N-1} \beta_{nm}\epsilon_{\tilde{x}_m} \right|^2 \right\}. \quad (5.54)$$

Now the SNR of the decision variable z_n is derived as

$$\text{SNR}_{z_n} = \frac{E_s\beta_{nn}^2}{P_{\epsilon_z}} < \text{SNR}_{\text{ideal}}, \quad (5.55)$$

where $\text{SNR}_{\text{ideal}}$ is the SNR in case of ideal tentative decisions as given in (5.50). The inequality is valid due to $P_{\epsilon_{z_n}} > E_s\beta_{nn}(1 - \beta_{nn})$. Obviously, the performance of the NP-HRC scheme with the non-ideal tentative decisions has degraded, compared with the case when the ideal tentative decisions are provided, due to the error propagation.

5.5 Simulation results

Baseband equivalent simulations are conducted in this section to evaluate the performance of the proposed noise-predictive RISI canceller. Besides the simulated performance, the complexity of the scheme will be investigated and compared with various cancellation schemes. A quasi-static Rayleigh fading channel, with the channel length $L = 125$, is simulated. The number of the simulated channel taps is 100 and the average power delay profile is exponentially decaying. The channel is perfectly known at receiver and the received signal is perfectly synchronized in time and frequency. We considered a QPSK transmission with Gray bit-mapping and the size of the spreading code is set to be $N = 512$. The cyclic prefix is set to be $1/4$ of the symbol duration and is large enough to absorb the ISI between data blocks.

5.5.1 BER performance for ideal tentative decisions

The simulated uncoded BER performance of the proposed scheme is depicted in Fig.5.6(a) and (b) for SC-FDE and MC-CDMA, respectively. Here ideally recovered tentative decisions are applied to estimate the RISI appeared in the linearly equalized signal. For comparison, the two cancellation schemes with reduced-order filtering, i.e. the NP-HDFE for SC-FDE and the NP-HRC for MC-CDMA, respectively, as presented in Section 5.2.4, are also given. The considered filtering orders are $N_{RC} = 3, 15$ and 63 . In addition, the BER performance of linear MMSE-equalized systems are also depicted. As a reference, the uncoded OFDM performance and the MFB performance are shown in the figures as well.

Let us first have a look at the two cancellation schemes with reduced-order filtering in Fig. 5.6(a) and (b), respectively. One can see that both the NP-HDFE and the NP-HRC with various filter orders always show performance improvement against the linear MMSE detection. In addition, for the same filter order, the NP-HRC in MC-CDMA shows a much better performance than the NP-HDFE in SC-FDE, especially for large filtering orders. This is consistent with the design approach of reduced-order filters given in Section 5.2.4, where only half of the most significant FB coefficients in SC-FDE were used for filtering. At the target BER 1×10^{-3} , for instance, the NP-HRC in MC-CDMA has the advantage of about 1.2 dB gain, for $N_{RC} = 63$, compared with the NP-HDFE in SC-FDE. This performance gap can be narrowed down by using the approach as suggested in Section 5.3.3.

As for the proposed NP-HRC scheme, the same performance is achieved for both SC-FDE and MC-CDMA and is superb compared with the reduced-order cancellation schemes. This is because the full number of filter coefficients are taken into account and as a result, the RISI is more accurately estimated and cancelled. At the target BER, the proposed NP-HRC has gained about 5 dB over the linear MMSE detection and is only 0.9 dB away from the theoretical MFB. The HDFE for SC-FDE requires a large number of FB coefficients, e.g. the filter order N_{RC} larger than the channel length $L = 125$ in our case, to approach the MFB, which means a significantly higher

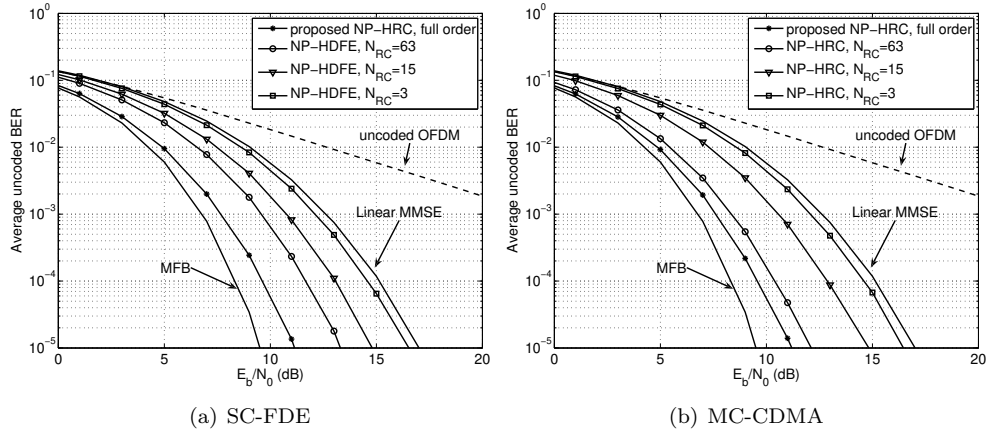


Fig. 5.6: Average BER of the proposed NP-HRC in SC-FDE and MC-CDMA, compared with the NP-HDFE with a reduced-order filtering, for ideal tentative decisions ($N = 512$ and $L = 125$).

complexity compared with the proposed scheme, as will be elaborated in Section 5.5.3.

5.5.2 BER performance for non-ideal tentative decisions

Here we simulate the detection performance in case only non-ideal tentative decisions are available. The simulated uncoded BER performance of the proposed NP-HRC in SC-FDE is shown in Fig. 5.7. Here the tentative decisions are hard decided (HD) symbols, soft decided (SD) symbols or the regenerated symbols after decoding and re-encoding (De/En) at the output of the tentative detector. The considered error correction code for the third type of the tentative detectors is a convolutional code, punctured by the rate $1/2$ code, with a constraint length of three. Two code rates, $3/4$ and $5/6$, are considered and have the minimum distances of three and two, respectively. A soft Viterbi decoder is used for decoding at receiver. This code represents a low complexity and low processing delay code often used in industry [119]. Note that the NP-HRC in MC-CDMA has about the same performance as in SC-FDE and thus it is not shown here.

From Fig. 5.7, one can see that the NP-HRC with HD and SD tentative decisions has about 2.0 dB and 2.7 dB gain, respectively, over the linear MMSE detection at the target BER. In comparison, the NP-HRC with the De/En tentative decisions exhibits about 3.4 and 4.0 dB gains for the $5/6$ and $3/4$ code rates, respectively. It is also noted that the BER performance of the NP-HRC-De/En scheme, with the $3/4$ rate, is 1 dB away from the NP-HRC with the ideal tentative decisions and 1.9 dB away from the MFB. Even better performance can be achieved by using a lower code rate. The NP-HRC-De/En scheme shows the best BER performance among the three types of

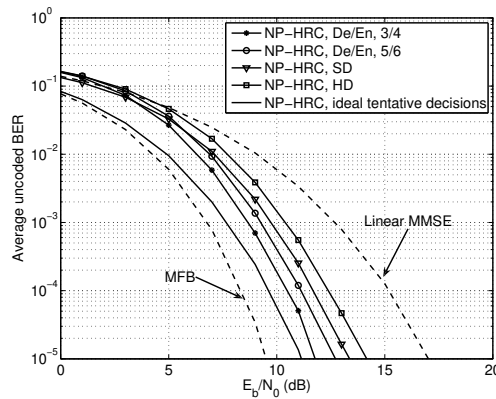


Fig. 5.7: Average BER of the proposed NP-HRC scheme for SC-FDE when using various tentative detectors.

tentative detectors, because of the highly reliable decisions from the decoder, but at the cost of bandwidth efficiency.

The BER performance of the reduced-order schemes with non-ideal tentative decisions is not shown here, but will be definitely worse than the proposed NP-HRC shown in Fig. 5.6, because of the severer error propagation.

5.5.3 Comparison of implementation complexity

Here we examine the computational complexity of the proposed NP-HRC scheme for SC-FDE, in comparison with the NP-HDFE with reduced filtering order. The alternative form of the proposed NP-HRC scheme given in Fig. 5.4 is considered for its low complexity. The complexity will be compared in terms of the number of complex multiplications, for both the filtering and the filter design. As for MC-CDMA, the receiver complexity is not given here, but will be lower than SC-FDE in that the fast WHT or the fast IWHT involve only $N \log_2 N$ real additions and subtractions [117]. We consider that a N -size FFT requires $\frac{N}{2} \log_2 N$ complex multiplications.

Table 5.1 shows the number of complex multiplications needed per subcarrier for the filtering in various schemes. In the proposed NP-HRC, both the FF filtering and the RISI cancellation operations require the same complexity of two FFTs and N multiplications. For the NP-HDFE, we consider the number of FB filter coefficients $N_{RC} = 15, 63$ and 125 . It is expected that the FB filtering with the order N_{RC} larger than the channel length $L = 125$ in the NP-HDFE could achieve a comparable performance as in the proposed NP-HRC. In addition, the decoding and re-encoding have been roughly accounted for as one FFT for the codes used in the simulation. One can see from the table that the NP-HDFE has an increasing complexity, proportional to the FB filter order, and requires at least six times the complexity to achieve a comparable performance, compared with the proposed NP-HRC for the considered channel.

Table 5.1: Equalization complexity of the proposed NP-HRC and the NP-HDFE with reduced orders in SC-FDE, in terms of complex multiplications per subcarrier. For the NP-HDFE, the filter order $N_{\text{RC}} = 15, 63, 125$. (Note that the complexity of SD here is only for QPSK.)

Cancellation schemes	Number of complex multiplications	Complexity for $N = 512$	
Linear MMSE	$\log_2 N + 1$	10	
proposed NP-HRC with HD or SD	$2 \log_2 N + 2$	20.0	
proposed NP-HRC with De/En	$2.5 \log_2 N + 2$	24.5	
NP-HDFE with HD or SD	$\log_2 N + 1 + N_{\text{RC}}$	$N_{\text{RC}} = 15$	25
		$N_{\text{RC}} = 63$	73
		$N_{\text{RC}} = 125$	135
NP-HDFE with De/En	$1.5 \log_2 N + 1 + N_{\text{RC}}$	$N_{\text{RC}} = 15$	30
		$N_{\text{RC}} = 63$	78
		$N_{\text{RC}} = 125$	140

Table 5.2: Filter design complexity in SC-FDE for various cancellatin schemes, in terms of complex multiplications. For the reduced-order NP-HDFE, the considered filter orders are $N_{\text{RC}} = 15, 63, 125$.

RISI canceller Schemes	Number of complex multiplications	Complexity for $N = 512$	
Linear MMSE	$2N$	1024	
proposed NP-HRC	$2N$	1024	
NP-HDFE: $\{D_k\}$	$\frac{N}{2} \log_2 N + 2N$	3328	
NP-HDFE: L-D	$\mathcal{O}(N_{\text{RC}}^2 + \frac{N}{2} \log_2 N + 2N)$	$N_{\text{RC}} = 15$	$\mathcal{O}(3553)$
		$N_{\text{RC}} = 63$	$\mathcal{O}(7297)$
		$N_{\text{RC}} = 125$	$\mathcal{O}(18953)$

In contrast, the proposed NP-HRC only requires a fixed amount of complexity for a certain data block size. The reduced-order design of the NP-HDFE decreases the number of multiplications, but the complexity is still relatively higher than that of the proposed NP-HRC.

In addition, Table 5.2 lists the complexity of designing the filter coefficients, which needs to be updated once the channel condition has changed. Suppose that the channel is quasi-static during the transmission of one data packet, the filter coefficients only need to be re-designed once within the duration of each packet. For the proposed NP-HRC, the equalizer design of $\{W_k\}$ and $\{D_k\}$ requires $2N$ multiplications in total, where the computation of $|H_k|^2$ is computed once and the scaling in $\{D_k\}$ is not counted. In other words, there is no complexity increase for the filter design of the NP-HRC, compared with the linear MMSE scheme. For the NP-HDFE, we consider two approaches to obtain the FB filter coefficients. The first approach is to solve N_{RC} linear equations of (5.21) using the Levinson-Durbin (L-D) algorithm, which has a complexity of $\mathcal{O}(N_{\text{RC}}^2)$ [87], in addition to one FFT needed to obtain q_n . The second

approach is to obtain the FB coefficients $\{b_n\}$ by applying IFFT on the coefficients $\{D_k\}$. It is readily seen that by the second approach the complexity of the filter design for the NP-HDFE has been significantly reduced to be a fixed amount by doing IFFT of $\{D_k\}$. However, it still requires three times the complexity of the proposed NP-HRC, because of the extra IFFT.

5.6 Conclusions

In this chapter, we have proposed the NP-HRC scheme to cancel the RISI occurring in a class of block code-spreading systems after linear equalization. The feedforward filter and the interference canceller were designed to minimize the MSE at the main detector input. Explicit derivation of filter coefficients for the scheme allows the feedforward filter and the canceller to be fully implemented in the frequency domain, resulting in a low complexity with the aid of, for instance, the fast Fourier transform in SC-FDE and the fast Walsh-Hadamard transform in MC-CDMA. In addition, a fast configuration of the filters becomes possible, because of the explicit relationship between the filter coefficients and the channel parameters. We also clarified the approach of choosing filter coefficients for the reduced-order design for the RISI cancellation, by recognizing the significance of the coefficients. The two often used transmission schemes, MC-CDMA and SC-FDE, were particularly addressed as examples for the class of block systems. Both theoretical analysis and simulations showed that the proposed NP-HRC significantly outperforms the existing DFE and reduced-order cancellation schemes, and is eventually lower bounded by the MFB. Also, the computational complexity of the NP-HRC is significantly lower than the existing DFEs and cancellation schemes, and depends only on the length of the spreading code. The low complexity and the outstanding performance make the proposed scheme particularly suitable for 60-GHz WPAN applications in multipath environments.

Quantization and RF impairments

6.1 Introduction

In previous chapters, the transmission performance of single- and multi-carrier systems is considered without taking into account the imperfections of system hardware implementation. For low-cost implementation of radio systems, especially for high frequency applications at 60 GHz, the components and devices used in the transceiver chain often work under imperfect conditions or work ideally only in a limited range, due to the noise in circuits and devices or fabrication processes. These imperfections tend to impair the signals and thus degrade the transmission performance. In particular, for a 60-GHz transceiver system, the direct-conversion (also called zero-IF or homodyne) architecture is a promising choice for a highly integrated low-cost and low-power realization of the transmitter (TX) and the receiver (RX) RF front-ends. However, this architecture generally suffers from more serious “dirty effect” from RF front-ends, compared with the conventional superheterodyne architecture, especially at such a high radio frequency [120]. A block diagram of a direct-conversion transceiver is shown in Fig. 6.1. The main components included in the diagram are digital-to-analog (D/A) converters (DAC), analog-to-digital (A/D) converters (ADC), power amplifier (PA), low noise amplifier (LNA), local oscillators (LO) and mixers.

The major challenging design issues for the direct-conversion architecture are DC offset, IQ mismatch and phase noise [121,122]. DC offset voltages occur due to “local oscillation (LO) leakage”, which can corrupt the signal. In wideband systems DC offset can be cancelled by employing AC coupling in combination with a DC-free modulation scheme [120]. In addition, the gain and phase mismatches between the I and Q signals corrupt the down-converted signal constellation. Flicker phase noise is another problem in direct-conversion architecture, especially for CMOS devices.

In addition, PAs and LNAs used at the TX and RX RF front-ends, respectively, do

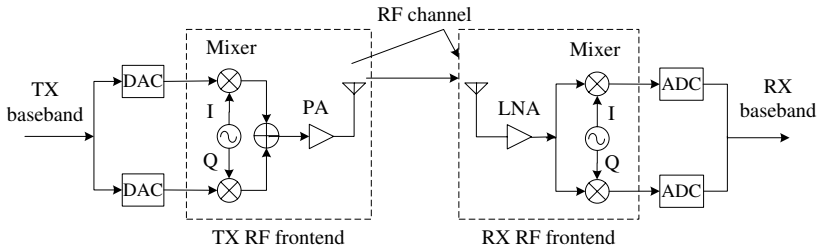


Fig. 6.1: A block diagram of a wireless zero-IF transceiver system.

not often work linearly in the whole range of signal levels, especially for signals with relatively high peak-to-average power ratios (PAPR), resulting in nonlinear distortions of the signals. The RF nonlinearities result in out-of-band spectrum regrowth, which interferes the neighboring channels. The problem may be overcome by designing highly linear amplifiers or applying a large backoff to the input signals of the amplifiers. However, the former solution increases the RF front-end cost and the latter one reduces the power efficiency. Another solution is to use baseband compensation techniques at receiver to cancel the nonlinear distortion [123,124], which tends to increase the processing power and the processing latency especially for a gigabit data throughput. A more power- and cost-effective solution is to use transmission schemes that have low PAPR levels, which are also favored for reducing the influence from other nonlinear distortions, such as the quantization addressed in the next paragraph.

The quantization processes in the DAC and ADC devices introduce an irreversible distortion, which is caused by limited bit resolutions and operating ranges of the devices. The DAC and ADC are some of the most power consuming components, where the power dissipation is related to the specific DAC/ADC architecture, the sampling rate and the bit resolution [20–22]. In spite of the steady progress in sampling rate and power reduction in recent years, the bit resolution falls off by about 1 bit for every doubling of the sampling rate [20, 22]. For the first generation deployment of 60-GHz systems, it would allow a throughput of 2 – 5 Gbps over 1 – 2 GHz bandwidth. Even higher throughput is theoretically possible for future applications. To realize the resulting high sampling rate while keeping the power consumption low, it is expected that relatively low bit resolution DACs and ADCs will be applied. With the reduced resolution, the signal distortion becomes even worse.

The RF imperfections and quantization degrade the transmission performance with the degradation level related to the transmission schemes. For 60-GHz applications, wideband transmission schemes, such as orthogonal frequency division multiplexing (OFDM), multi-carrier code division multiple access (MC-CDMA) and single-carrier with frequency-domain equalization (SC-FDE), are potential candidates for multi-gigabit-per-second transmission. In literature, single- and multi-carrier schemes are often compared under the influences of nonlinear impairments introduced at the transmitter side [125], mostly for power amplifier. The ADC effect on OFDM transmission

has been considered in [126–128]. The influences of DAC and ADC on the three wide-band schemes have been rarely addressed within the same framework. In addition, analytical comparison is rarely seen in literature.

The purpose of this chapter is to evaluate the performance of OFDM, SC-FDE and MC-CDMA under the influences of DAC, ADC and RF impairments in Rician fading channels. The coexistence of multiple nonlinear devices in a transceiver system introduces a mutual coupling of the resulting nonlinearities in the received signal, which makes it highly complicated to analyze the joint influences of these devices. For simplicity, the influences of these devices will be separately concerned in this chapter. The outline of the chapter is as follows. In Section 6.2, the general bit error rate (BER) expressions are derived for the cases of memoryless nonlinearities at the TX and RX sides, respectively, based on statistical modelling of the nonlinearities. In Section 6.3, the quantization and clipping effects due to DAC/ADC are modelled and analyzed, and the BER performance is simulated and compared with the analytical BER. In Section 6.4, the influence of a nonlinear PA on BER performance is studied. Next, the BER under the influences of phase noise and IQ imbalance is simulated and analyzed in Section 6.5 and 6.6, respectively, with and without applying digital compensation. Lastly, conclusions are summarized in Section 6.7.

6.2 Influence of memoryless nonlinearity

In this section, we derive the BER performance of OFDM, MC-CDMA and SC-FDE under the influence of memoryless nonlinearities in Rician fading channel conditions, based on the statistical modelling of nonlinearities.

6.2.1 Statistical model of nonlinearity

In wireless transceiver systems, amplifiers, ADC and DAC are the main nonlinear devices, which make it particularly difficult for statistical analysis of the systems. The nonlinearities are often approximated using linear models, for which statistical theories are well established and relatively easy to apply. Consider a time-invariant memoryless nonlinear device described by

$$\tilde{z}(t) = \mathbb{Q}(z(t)), \quad (6.1)$$

where the signals $z(t)$ and $\tilde{z}(t)$ over time t are the input and output of the device $\mathbb{Q}(\cdot)$, respectively. “*Memoryless*” here means that at a given time $t = t_1$, the output $\tilde{z}(t_1)$ depends only on $z(t_1)$, and not on any other past or future values of $z(t)$ [129].

Taking the input and output of \mathbb{Q} as stochastic processes, Bussgang showed in 1952 that for a Gaussian input $z(t)$, the output can be modelled as the addition of an attenuated input signal and an uncorrelated distortion [130]. Later, it was found by Nuttall that this model is suitable for a more general class of stochastic processes [131, 132], which is referred to as the generalized Bussgang’s theorem in this thesis.

By this theorem, the model is valid for a memoryless nonlinear device, if and only if the input signal is a *separable* stochastic process. *Separability* of a process means that the conditional expectation of a zero mean input signal $z(t)$ should satisfy [131, 132]

$$\mathbb{E}\{z(t-\tau)|z(t)\} = \frac{\mathbb{E}\{z(t)z(t-\tau)\}}{\mathbb{E}\{z^2(t)\}} \cdot z(t) \quad (6.2)$$

for all $z(t)$ and τ . Adding a non-zero constant to a separable process does not change the separability. The separability is valid for a number of signals, for instance for Gaussian processes and phase modulated processes which are useful for our interest.

Without losing generality, we consider the separable process $z(t)$, which has a zero mean and variance σ_z^2 . The generalized Bussgang's theorem leads to the decomposition of the output $\tilde{z}(t)$ of the nonlinear device \mathbb{Q} given by

$$\tilde{z}(t) = \alpha z(t) + d(t), \quad (6.3)$$

where α is a scaling factor and $d(t)$ is a distortion term which is uncorrelated with $z(t)$, i.e. $\mathbb{E}\{z(t)d^*(t)\} = 0$. The scaling factor α can be found by relating the cross-correlation of $\tilde{z}(t)$ and $z(t)$ to the autocorrelation of $z(t)$ by $\mathbb{E}\{z^*(t)\tilde{z}(t)\} = \alpha\mathbb{E}\{z^*(t)z(t)\}$. Based on this relationship, the scaling factor is found to be

$$\alpha = \frac{1}{\sigma_z^2} \int_{-\infty}^{\infty} z\mathbb{Q}(z)p_z(z)dz, \quad (6.4)$$

where $p_z(z)$ is the probability density function (pdf) of $z(t)$. From (6.3), it follows that the distortion $d(t)$ caused by the nonlinearity is generally non-Gaussian and has the variance

$$\sigma_d^2 = \sigma_{\tilde{z}}^2 - \alpha^2\sigma_z^2, \quad (6.5)$$

where $\sigma_{\tilde{z}}^2$ is the variance of the output signal. The signal-to-distortion ratio (SDR) of the output is consequently given by

$$\text{SDR} = \frac{\alpha^2\sigma_z^2}{\sigma_d^2}. \quad (6.6)$$

To examine the validity of the statistical model (6.3) for wideband transmission schemes, we check the separability of single- and multi-carrier signals according to the condition (6.2). Random values of a linearly modulated sequence at different time instants can be seen as zero-mean independently and identically distributed (i.i.d.) random variables [84]. Such a data sequence is a separable process satisfying the separability condition (6.2). Therefore, the baseband modulated signals in single- and multi-carrier block transmission systems are also separable processes, since any linear combination of independent separable processes with identical power density spectra is separable [131]. Similarly, the received signal after a multipath channel is also a separable process. The addition of the received signal and additive white Gaussian noise (AWGN) is generally non-separable, but one exception is when the received

signal is also Gaussian distributed. Fortunately, the received signal is approximately Gaussian distributed in a rich multipath channel, according to the central limit theorem. Besides, the receiver noise level is generally much lower than the signal level in order to have a reliable detection. Therefore, the statistical model (6.3) is still be, on approximation, a good model for the nonlinear distortion of the received signal contaminated by the AWGN noise.

The signal decomposition based on the generalized Busgang's theorem will be frequently applied in the later sections to investigate the influence of nonlinearities on the transmission performance of various schemes. Before proceeding, we should keep in mind that the scaling factor and the distortion term in the decomposition are merely the stochastic characterization of the influence caused by the nonlinearities. The deterministic influence of nonlinearities on the individual signal points are different. For instance, for a single-carrier signal at the input of a memoryless PA, the scaling and the distortion reflect the statistical influence of the nonlinearity. But deterministically, the constellation points with smaller magnitudes experience little or no scaling and distortion by the nonlinearity, compared with the points with larger magnitudes, as will be seen later.

6.2.2 Influence on transmission performance

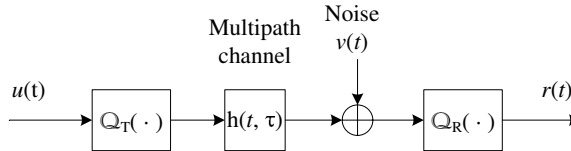


Fig. 6.2: Nonlinearity at transmitter and receiver side.

Consider the memoryless nonlinear devices $\mathbb{Q}_T(\cdot)$ and $\mathbb{Q}_R(\cdot)$ appearing in the TX and the RX, respectively, see Fig. 6.2. The multipath channel $h(t, \tau)$ is defined in (2.7) and is repeated here for convenience

$$h(t, \tau) = \sum_{l=0}^L h_l(t) \delta(\tau - \tau_l). \quad (6.7)$$

It is assumed that the channel power is normalized, i.e. $\mathbb{E} \left\{ \sum_{l=0}^L |h_l(t)|^2 \right\} = 1$. In addition, the channel is assumed to be invariant over time during the transmission of one data packet and the time dependency (t) will be omitted. For the transmit signal $u(t)$ with $\mathbb{E}\{|u(t)|^2\} = E_s$ and the receiver noise $v(t)$ with $\mathbb{E}\{|v(t)|^2\} = N_0$, the

received signal in the time domain (TD) can be decomposed into

$$\begin{aligned} r(t) &= \mathbb{Q}_R \left(\sum_{l=0}^L h_l \mathbb{Q}_T \left(u(t - \tau_l) \right) + v(t) \right), \\ &= \alpha_R \left(\sum_{l=0}^L h_l \left(\alpha_T u(t - \tau_l) + d_T(t - \tau_l) \right) + v(t) \right) + d_R(t), \end{aligned} \quad (6.8)$$

using (6.3), where the input of $\mathbb{Q}_R(\cdot)$ consists of the distorted transmit signal after experiencing the multipath channel and the channel noise. Here $\{\alpha_T, d_T(t)\}$ and $\{\alpha_R, d_R(t)\}$ are the scaling factors and the distortions caused by the nonlinear devices at the TX and the RX side, respectively. At the outputs of \mathbb{Q}_T and \mathbb{Q}_R , the power ratios between the attenuated input signal and its distortion are given by

$$\text{SDR}_T = \frac{\alpha_T^2 E_s}{\sigma_{d_T}^2} \quad (6.9)$$

$$\text{SDR}_R = \frac{\alpha_R^2 (\alpha_T^2 E_s + \sigma_{d_T}^2 + N_0)}{\sigma_{d_R}^2} \quad (6.10)$$

respectively.

Consider wideband transmission schemes with cyclic prefixes inserted in the data sequence, as described in Chapter 4. Similarly, here we assume that the inter-block symbol interference is prevented by the cyclic prefixes and only one data block with length N is considered here. Suppose that the frequency offset is zero and the symbol timing is perfect after the sampling of the received signal (6.8). After the removal of the cyclic prefix, the received signal vector in the TD is given by

$$\mathbf{r}_t = \alpha_R \left(\text{cir}\{\mathbf{h}\} (\alpha_T \mathbf{u}_t + \mathbf{d}_{t,T}) + \mathbf{v}_t \right) + \mathbf{d}_{t,R}, \quad (6.11)$$

for the transmit signal vector $\mathbf{u}_t = \mathbf{F}^H \mathbf{C} \mathbf{x}$ in the TD and the receiver noise vector \mathbf{v}_t in the TD. Here $\text{cir}\{\mathbf{h}\}$ is a $N \times N$ circulant matrix with the first column given by the channel vector $\mathbf{h} = [h_0, \dots, h_L, 0, \dots, 0]^T$. In addition, the vectors $\mathbf{d}_{t,T}$ and $\mathbf{d}_{t,R}$ are formed by the samples of distortions at the TX and RX sides, respectively. The N -point FFT of \mathbf{r}_t yields the signal vector in the frequency domain (FD), $\mathbf{r} = [r_0, \dots, r_{N-1}]^T$, given by

$$\mathbf{r} = \alpha_R \left(\mathbf{H} (\alpha_T \mathbf{u} + \mathbf{d}_T) + \mathbf{v} \right) + \mathbf{d}_R, \quad (6.12)$$

where $\mathbf{H} = \mathbf{F} \text{cir}\{\mathbf{h}\} \mathbf{F}^H$ is the channel matrix in the frequency domain (FD) and $\mathbf{u} = \mathbf{C} \mathbf{x}$ is the transmit signal vector in the FD. The three schemes OFDM, MC-CDMA or SC-FDE can be implemented by choosing the matrix \mathbf{C} to be the identity matrix, Walsh-Hadamard matrix or Fourier matrix, respectively. Here $\mathbf{v} = [v_0, \dots, v_{N-1}]^T$ is the vector of the zero mean i.i.d. noise samples in the FD with the variance N_0 . The vectors $\mathbf{d}_T = [d_{T,0}, \dots, d_{T,N-1}]^T$ and $\mathbf{d}_R = [d_{R,0}, \dots, d_{R,N-1}]^T$ are the

Fourier transform of the distortion sequences in the TD with $\mathbb{E}\{|d_{T,k}|^2\} = \sigma_{d_T}^2$ and $\mathbb{E}\{|d_{R,k}|^2\} = \sigma_{d_R}^2$, respectively. Note that both the distortion sequences are uncorrelated with the data and noise sequences.

Rewriting the vector of the received signal (6.12) into a scalar form yields

$$r_k = \underbrace{\alpha_R \alpha_T H_k}_{\hat{H}_k} u_k + \underbrace{\alpha_R (H_k d_{T,k} + v_k) + d_{R,k}}_{\hat{v}_k}, \quad (6.13)$$

where $u_k = \sum_{k'=0}^{N-1} C_{kk'} x_{k'}$, $\hat{H}_k = \alpha_R \alpha_T H_k$ and the disturbance \hat{v}_k at the k th subcarrier consists of the channel noise and distortions. The variance of the disturbance samples at the k th subcarrier, $\sigma_{\hat{v}_k}^2 = \mathbb{E}\{\hat{v}_k^2\}$, is given by

$$\sigma_{\hat{v}_k}^2 = \alpha_R^2 (|H_k|^2 \sigma_{d_T}^2 + N_0) + \sigma_{d_R}^2. \quad (6.14)$$

Note that the disturbance variance depends not only on the noise and distortion levels, but also on the channel at the k th subcarrier, due to the nonlinearity occurring at the TX side. Taking the distortions in (6.13) as noise, we have the SNR of the k th subcarrier signal

$$\gamma_k = \frac{E_s |\hat{H}_k|^2}{\sigma_{\hat{v}_k}^2} \quad (6.15)$$

given the channel $H_k = \sum_{l=0}^L h_l e^{-i2\pi kl/N}$. One can check that in case of no nonlinearities at both TX and RX sides, the received signal (6.13) at the k th subcarrier and its SNR (6.15) are the same as in (4.25) and (4.33), respectively.

For the received signal (6.13) under the influence of TX and RX nonlinearities, after equalization by the weight W_k in the FD, the resulting decision variables for OFDM in the FD and decision variables for SC-FDE and MC-CDMA in the TD before detection are given by

$$s_k = W_k \hat{H}_k x_k + W_k \hat{v}_k \quad (6.16)$$

$$s_n = \sum_{k=0}^{N-1} C_{kn}^* W_k \hat{H}_k u_k + \sum_{k=0}^{N-1} C_{kn}^* W_k \hat{v}_k, \quad (6.17)$$

respectively.

Suppose that the scaled channel \hat{H}_k and the disturbance variance $\sigma_{\hat{v}_k}^2$ are known at receiver¹. Based on the known information, the linear minimum mean square error (MMSE) weight, which minimizes the MSE $\mathbb{E}\{|s_n - x_n|^2\}$, can be found to be

$$W_k = \frac{\hat{H}_k^*}{|\hat{H}_k|^2 + \frac{\sigma_{\hat{v}_k}^2}{E_s}}. \quad (6.18)$$

¹The information is assumed to be perfectly known at receiver in order to explore the optimal linear detection performance.

For OFDM, the SNR of the k th decision variable is given in (6.15) given the channel H_k , while for SC-FDE and MC-CDMA, the SNRs are the same for each decision variable and given by

$$\eta = \frac{1}{\frac{1}{N} \sum_{k=0}^{N-1} \frac{\sigma_{\hat{v}_k}^2}{E_s |H_k|^2 + \sigma_{\hat{v}_k}^2}} - 1. \quad (6.19)$$

Note that \hat{H}_k and $\sigma_{\hat{v}_k}^2$ are different for SC-FDE and MC-CDMA, because they do not have the same values for scaling factors and distortions that are dependent on the signal distributions.

Compare the SNR of decision variables (6.15) for OFDM and (6.19) for SC-FDE and MC-CDMA, we have the following observations:

- For the three schemes, the SNRs of decision variables are never larger than the SDR at the TX side, i.e.

$$\gamma_k, \eta \leq \text{SDR}_T, \quad (6.20)$$

where the upper boundary can be approached by increasing the channel SNR $\bar{\gamma}$ and reducing the nonlinear distortion level at the RX side.

- In a frequency flat channel with $|H_k| = 1$ for $k = 0, \dots, N - 1$, i.e. in an AWGN channel, the nonlinearities give rise to the same SNR expression of decision variables given by

$$\gamma_k = \eta = \frac{\alpha_T^2 \alpha_R^2 E_s}{\alpha_R^2 (\sigma_{d_T}^2 + N_0) + \sigma_{d_R}^2}, \quad (6.21)$$

for the three schemes, where each subcarrier signal has the same SNR as decision variables. However, the influence of the nonlinearities are still different for the three schemes, because of the different scaling factors and distortion levels.

- In Rician fading channels, the nonlinearities cause different SNR reduction at each subcarriers, due to the frequency selectivity of the multipath channel. In OFDM, the SNR reduction directly influences each decision variable, while in SC-FDE and MC-CDMA, the influence is indirectly imposed on decision variables because of the averaging effect reflected in (6.19).

The first observation implies that for a cascade of nonlinear devices in a transceiver system, the nonlinearities appearing in the earlier stages have more serious influences on the system performance than the later stages. Therefore, the nonlinearity at the TX side should be as small as possible such that the SDR before transmission is still large, in order to provide a sufficiently large SNR at receiver for a reliable detection.

6.2.3 BER computation

In this section, we derive the BER expressions when the nonlinearity occurs only at the TX or the RX side, respectively, for OFDM, SC-FDE and MC-CDMA. The SNRs

of decision variables in the following are obtained based on the general expressions (6.15) and (6.19). For convenience, these SNRs will be listed in Table 6.1 for different nonlinearity scenarios.

6.2.3.1 Only TX Nonlinearity

In case of nonlinearity only at the TX side, i.e. $\alpha_R = 1$ and $\sigma_{d_R}^2 = 0$, we have the SNR of decision variables for OFDM and the SNR for SC-FDE and MC-CDMA given by

$$\gamma_k = \frac{\alpha_T^2 \bar{\gamma} |H_k|^2}{\frac{\alpha_T^2}{\text{SDR}_T} \bar{\gamma} |H_k|^2 + 1} \quad (6.22)$$

$$\eta = \frac{1}{\frac{1}{N} \sum_{k=0}^{N-1} \frac{\alpha_T^2 \bar{\gamma} |H_k|^2 + \text{SDR}_T}{\alpha_T^2 (1 + \text{SDR}_T) \bar{\gamma} |H_k|^2 + \text{SDR}_T}} - 1, \quad (6.23)$$

respectively. Both the SNRs γ_k and η change over the channel conditions of H_k for $k = 0, \dots, N - 1$.

1) *OFDM*: To compute the BER under the influence of the nonlinearity at the TX side, we assume that the addition of the distortion and the noise in decision variables (6.12) are zero mean Gaussian distributed. Although the distortion is generally non-Gaussian, the pdf of the distortion has tails, which are analog to the Gaussian pdf tails and have a relative large impact on BER performance compared with other parts of the distribution. It will be justified that the derived BER expression based on this assumption is relatively accurate to predict the actual BER performance in Section 6.3.2. Similar to the BER derivation for linear channels as described in Section 4.4.2, the average BER of OFDM under the influence of TX nonlinearity is found to be

$$\overline{\text{BER}}(K, \bar{\gamma}) = \int_0^\infty A \cdot \text{erfc} \left[B \sqrt{\frac{x}{\frac{1}{\text{SDR}_T} x + \frac{1}{\alpha_T^2}}} \right] p_x(x) dx \quad (6.24)$$

$$= \int_0^{\text{SDR}_T} \frac{A \cdot \text{erfc}[B\sqrt{t}]}{\alpha_T^2 \left(1 - \frac{t}{\text{SDR}_T}\right)^2} p_x \left(\frac{t}{\alpha_T^2 \left(1 - \frac{t}{\text{SDR}_T}\right)} \right) dt, \quad (6.25)$$

where $A = 2(1 - 1/\sqrt{M})/\log_2 M$, $B = \sqrt{\frac{3}{2(M-1)}}$ for a square M -QAM and $A = 1/\log_2 M$, $B = \sin \frac{\pi}{M}$ for M -PSK, respectively, for the constellation size M of the data symbols. The pdf $p_x(x)$ is the distribution of $x = \bar{\gamma} |H_k|^2$ for Rician fading channels given in (4.41). The type of integral in (6.24) involves the term $x \left(\frac{x}{\text{SDR}_T} + \frac{1}{\alpha_T^2} \right)^{-1}$ and a closed form solution is unknown. By using t to replace this term, the integration over t in (6.25) can be conducted within a limited range, which facilitates a numerical computation applied for the prediction of BER performance.

2) *SC-FDE and MC-CDMA*: When the number of subcarriers goes to infinity, i.e. $N \rightarrow \infty$, the SNR η of decision variables approaches a constant value η_∞ for a

certain pdf of the subcarrier SNR γ_k . For Rician fading channels under the influence of nonlinearities, we can obtain the expression of η_∞ given by

$$\eta_\infty = \frac{1}{\mathbb{E} \left\{ \frac{\alpha_T^2 \bar{\gamma} |H_k|^2 + \text{SDR}_T}{\alpha_T^2 (1 + \text{SDR}_T) \bar{\gamma} |H_k|^2 + \text{SDR}_T} \right\}} - 1 = \frac{1 - \varepsilon[K, \bar{\gamma}_T]}{\varepsilon[K, \bar{\gamma}_T] + \frac{1}{\text{SDR}_T}}, \quad (6.26)$$

which is similar to the derivation of η_∞ in (4.48) without nonlinearity influence. Here the function $\varepsilon[K, \bar{\gamma}_T]$ is defined in (4.49) and the parameter

$$\bar{\gamma}_T = \frac{\alpha_T^2 E_s + \sigma_{d_T}^2}{N_0} = \frac{\alpha_T^2 (1 + \text{SDR}_T)}{\text{SDR}_T} \cdot \bar{\gamma} \quad (6.27)$$

describes the power ratio between the average received signal (including distorted and non-distorted signals) and the receiver noise. By using (6.26), the BER expression when $N \rightarrow \infty$ is given by

$$\overline{\text{BER}}(K, \bar{\gamma}) = A \cdot \text{erfc} \left[B \sqrt{\frac{1 - \varepsilon[K, \bar{\gamma}_T]}{\varepsilon[K, \bar{\gamma}_T] + \frac{1}{\text{SDR}_T}}} \right], \quad (N \rightarrow \infty). \quad (6.28)$$

For a limited number of subcarriers N , the BER can still be computed approximately by using (6.28) for the similar reason as explained in detail in Section 4.4.2.

3) *Observations:* In case of no nonlinearity occurring at all, we have $\text{SDR}_T \rightarrow \infty$ and as a result, the BER expressions (6.25) and (6.28) are exactly the same as (4.44) and (4.51), respectively. In addition, one can check that for the three transmission schemes, the BER performance under the influence of TX nonlinearity is lower bounded by

$$\overline{\text{BER}}(K, \bar{\gamma}) \geq A \cdot \text{erfc} \left[B \sqrt{\text{SDR}_T} \right], \quad (6.29)$$

due to $\gamma_k, \eta \leq \text{SDR}_T$ given in (6.20), which is independent of the channel condition.

6.2.3.2 Only RX Nonlinearity

When nonlinearity occurs only at receiver side, the transmit signal is undistorted, i.e. $\alpha_T = 1$ and $\sigma_{d_T} = 0$. The SNR of the decision variables for OFDM and the SNR for SC-FDE and MC-CDMA are found to be

$$\gamma_k = \bar{\gamma}_R |H_k|^2 \quad (6.30)$$

$$\eta = \frac{1}{\frac{1}{N} \sum_{k=0}^{N-1} \frac{1}{\bar{\gamma}_R |H_k|^2 + 1}} - 1, \quad (6.31)$$

where $\bar{\gamma}_R$ is the average SNR of the received signal at the output of the nonlinear device $\mathbb{Q}_R(\cdot)$ and defined as

$$\bar{\gamma}_R = \frac{\alpha_R^2 E_s}{\alpha_R^2 N_0 + \sigma_{d_R}^2} = \frac{\bar{\gamma}}{1 + \frac{\bar{\gamma} + 1}{\text{SDR}_R}} \quad (6.32)$$

Table 6.1: SNR of decision variables in OFDM, SC-FDE and MC-CDMA under the effect of nonlinearities in Rician fading channels with the Rician factor K . Here the notations $\bar{\gamma} = \frac{E_s}{N_0}$, $\bar{\gamma}_T = \frac{\alpha_T^2(1+\text{SDR}_T)}{\text{SDR}_T}\bar{\gamma}$ and $\bar{\gamma}_R = \frac{\bar{\gamma}}{1+\text{SDR}_R}$.

Channel	OFDM	SC-FDE & MC-CDMA
Linear	$\gamma_k = \bar{\gamma} H_k ^2$	$\eta = \left(\frac{1}{N} \sum_{k=0}^{N-1} \frac{1}{\bar{\gamma} H_k ^2 + 1} \right)^{-1} - 1$ $\approx \frac{1}{\varepsilon[K, \bar{\gamma}]} - 1$
Nonlinear TX	$\gamma_k = \frac{\alpha_T^2 \bar{\gamma} H_k ^2}{\frac{\alpha_T^2}{\text{SDR}_T} \bar{\gamma} H_k ^2 + 1}$	$\eta = \left(\frac{1}{N} \sum_{k=0}^{N-1} \frac{\frac{\alpha_T^2 \bar{\gamma} H_k ^2}{\text{SDR}_T} + 1}{\bar{\gamma}_T H_k ^2 + 1} \right)^{-1} - 1$ $\approx \frac{1 - \varepsilon[K, \bar{\gamma}_T]}{\varepsilon[K, \bar{\gamma}_T] + \frac{1}{\text{SDR}_T}}$
Nonlinear RX	$\gamma_k = \bar{\gamma}_R H_k ^2$	$\eta = \left(\frac{1}{N} \sum_{k=0}^{N-1} \frac{1}{\bar{\gamma}_R H_k ^2 + 1} \right)^{-1} - 1$ $\approx \frac{1}{\varepsilon[K, \bar{\gamma}_R]} - 1$

with $\text{SDR}_R = \frac{\alpha_R^2(E_s + N_0)}{\sigma_{dR}^2}$. Comparing the SNR (6.22) for TX nonlinearities and the SNR (6.30) for RX nonlinearities of the k th subcarrier signal, we see that the former is mainly constrained by the scaling factor α_T in case of large SDR_T , whereas the latter is mainly constrained by both the scaling factor α_R and the distortion variance σ_{dR}^2 in case of large channel SNR E_s/N_0 . This observation is helpful to understand the influence difference on the BER performance by DAC and ADC, as will be seen in Section 6.3.2.

1) *OFDM*: Assuming a Gaussian distribution for the distortion plus the channel noise, the BER performance under the influence of nonlinearity at the RX side can also be computed. Similar to (4.44) as in a linear channel, the average uncoded BER of OFDM can be obtained by merely replacing $\bar{\gamma}$ by $\bar{\gamma}_R$ and is given by

$$\overline{\text{BER}}(K, \bar{\gamma}) = \frac{2A(1+K)}{\pi} \int_0^{\frac{\pi}{2}} \frac{\sin^2 \theta}{f(\theta)} e^{-\frac{KB^2 \bar{\gamma}_R}{f(\theta)}} d\theta, \quad (6.33)$$

where the function $f(\theta) = B^2 \bar{\gamma}_R + (1+K) \sin^2 \theta$.

2) *SC-FDE and MC-CDMA*: For the number of subcarriers $N \rightarrow \infty$, the SNR of decision variables in (6.31) approaches η_∞ , which is given by

$$\eta_\infty = \frac{1}{\varepsilon[K, \bar{\gamma}_R]} - 1. \quad (6.34)$$

By using (6.34), the BER expression for SC-FDE and MC-CDMA is given by

$$\overline{\text{BER}}(K, \bar{\gamma}) = A \cdot \text{erfc} \left[B \sqrt{\frac{1}{\varepsilon[K, \bar{\gamma}_R - 1]}} \right], \quad (N \rightarrow \infty). \quad (6.35)$$

For a limited number of subcarriers N , the BER can still be computed approximately by using (6.35) for the similar reason as explained in detail in Section 4.4.2.

6.3 D/A and A/D conversions

In wireless transceivers, DAC and ADC of I and Q branches, as shown in Fig. 6.1, are the links between the analog world of transducers and the digital world of base-band signal processing. The block diagrams of D/A and A/D conversion systems are elaborated in Fig. 6.3 (a) and (b), respectively. To convert a digital signal into an

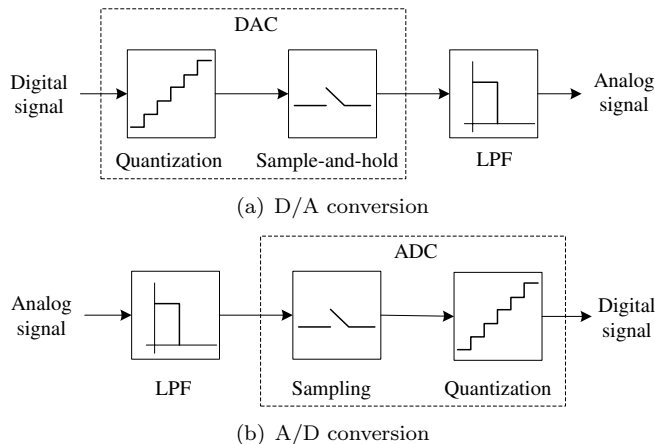


Fig. 6.3: D/A and A/D conversion systems.

analog signal by a DAC, the digital signal undergoes the quantization and sample-and-hold operations, which are followed by low-pass filtering in order to reject the high-frequency components in the DAC output signal. During A/D conversion, the analog input signal first passes through a low-pass filter (LPF) to remove all frequencies above one-half the sampling rate, then the output signal is sampled and quantized. Mathematically, the operations of quantization and sample-and-hold in the DAC and the ADC are the same [133]. Without losing generality, only uniform quantizers are considered here, since any nonuniform quantization can be decomposed into two steps: nonlinear transformation and uniform quantization.

The quantization process in the DAC or the ADC introduces an irreversible distortion, which consists of both quantization noise and clipping error, as will be elaborated later. This type of distortion is caused by a limited bit resolution and a limited

operating range, and its influences on transmission schemes are the major concern in this section. In physical DAC and ADC devices, additional distortions are introduced by physical imperfections, such as aliasing, aperture jitter, differential and integral nonlinearities, which are not considered here [133].

6.3.1 Modelling of the quantization process in DAC or ADC

6.3.1.1 Uniform quantization

For an R bits resolution quantizer with $Q = 2^R$ quantization levels, the real output sequence $\{\tilde{z}_n\}$ and the real input sequence $\{z_n\}$ of a uniform quantizer are related by the quantization function \mathbb{Q} , defined as

$$\tilde{z}_n = \mathbb{Q}(z_n) = \sum_{j=-\frac{Q}{2}+1}^{j=\frac{Q}{2}} q_j \cdot U(z_n, \hat{z}_{j-1}, \hat{z}_j), \quad (6.36)$$

where \hat{z}_j represents the j th quantization threshold value. The quantizer output $\tilde{z}_n \in \{q_j\}$ for $-\frac{Q}{2} + 1 \leq j \leq \frac{Q}{2}$, where q_j is the output amplitude of the j th quantization interval. The rectangular function $U(z_n, a, b)$ is defined by

$$U(z_n, a, b) = \begin{cases} 1, & a \leq z_n < b \\ 0, & \text{otherwise.} \end{cases} \quad (6.37)$$

Clearly, the output sequence of the quantizer follows a Q -level discrete distribution. Also, the quantizer is a time invariant and memoryless nonlinear device.

In the case of the commonly used mid-raiser uniform quantization with the step size Δ , we have the quantization threshold and the output amplitude given by

$$\hat{z}_j = \begin{cases} j\Delta & |j| < \frac{Q}{2} \\ -\infty & j = -\frac{Q}{2} \\ +\infty & j = \frac{Q}{2} \end{cases}, \quad (6.38)$$

$$q_j = j\Delta - \frac{\Delta}{2}, \quad (6.39)$$

respectively. Fig. 6.4 (left) illustrates the uniform quantization for the example of $R = 2$ bit resolution. For the input sequence z_n which follows any pdf, the output has a uniformly spaced discrete pdf, as seen from Fig. 6.4 (right). The signal distortion at the quantizer output consists of the quantization noise and the clipping error², which occur when the input signal amplitude is inside or outside the range of $\left[-\frac{Q\Delta}{2}, \frac{Q\Delta}{2}\right]$, respectively.

²Here the quantization noise and the clipping error are referred to as the granular noise and overloading distortion, respectively, in literature [134].

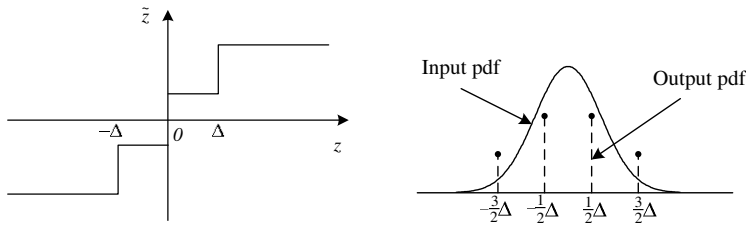


Fig. 6.4: Mid-raiser uniform quantization (left) and the pdfs before and after quantization (right) for the example of $R = 2$ bit resolution.

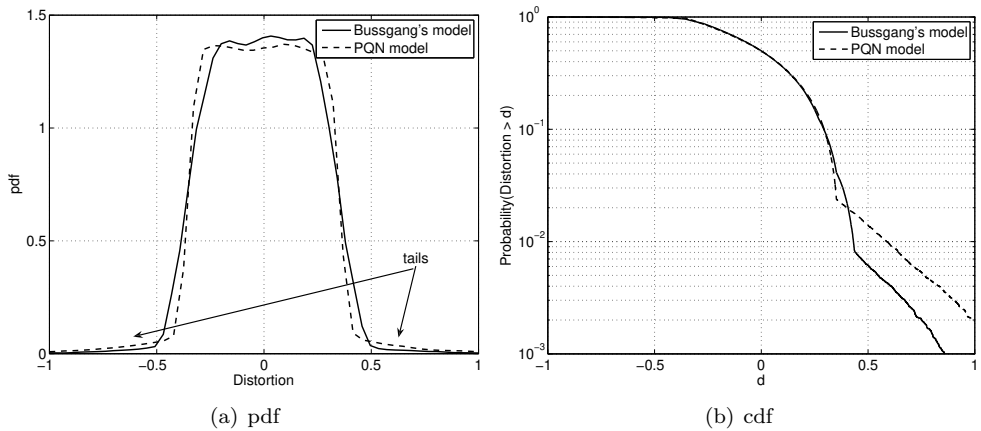


Fig. 6.5: For the quantizer $R = 2$ bits and for a Gaussian input, the simulated pdf and cdf of the distortion noise d_n at the quantizer output using the model (6.40) and (6.41).

The signal distortion introduced by a quantizer has been widely analyzed in literature by modelling the quantizer output as the addition of the input signal and the distortion noise given by [134, 135]

$$\tilde{z}_n = z_n + d_n. \quad (6.40)$$

The model (6.40) is referred to as the pseudo quantization noise (PQN) model [135]. For a high bit quantizer, the distortion noise can be assumed to be uniformly distributed and uncorrelated with the input signal. For a low bit ADC, however, clipping errors become dominant in d_n , which results in large tails in the pdf of the distortion noise. As a result, the correlation between the input signal and the distortion noise becomes large. Therefore, instead of the PQN model (6.40), we use the generalized Bussgang's model (6.3) which is repeated here

$$\tilde{z}_n = \alpha z_n + d_n. \quad (6.41)$$

As an example, Fig. 6.5 depicts a simulated pdf and cumulative distribution function (cdf) of the distortion d_n in the models (6.40) and (6.41), respectively, for a zero-mean Gaussian input with a unit variance. Here the resolution $R = 2$ bits and the

quantization interval $\Delta = 1$. It is observed from the figures that the tails caused by the clipping errors based on (6.41) are indeed smaller than those based on (6.40).

6.3.1.2 Optimal quantization interval design

For a random input signal of a quantizer following a certain pdf, the optimal quantization interval Δ can be chosen such as to maximize the SDR at the quantizer output. Optimizing the interval is closely related to the automatic gain control (AGC) for the quantizer input. For the AGC, the input signal level is adjusted to maximize the output SDR for a fixed quantization interval.

For the special case of a zero-mean Gaussian distribution, the optimal quantization interval can be designed by maximizing the SDR level at the quantizer output by using either the PQN model (6.40) or the generalized Bussgang's model (6.41). Based on the two models, the SDR expressions as function of the normalized quantizer interval Δ/σ_z are derived in Appendix D and depicted in Fig. 6.6, where σ_z^2 is the variance of the input signal. The peak SDRs are marked in Fig. 6.6 and represent the optimal SDR that can be achieved. It is shown in Appendix D and can be read from Fig. 6.6

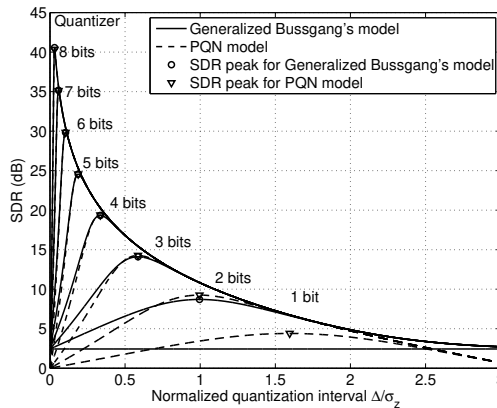


Fig. 6.6: The SDR of the quantizer output versus the normalized quantization interval based on the models (6.41) and (6.40) for a Gaussian input.

as well that the optimal quantization intervals based on both models are exactly the same for $R \geq 2$ bits. For instance, the optimal quantization intervals for $R = 2$ to 8 bits can be read from Fig. 6.6 for a Gaussian input signal and given by

$$\Delta_G \approx \sigma_z [0.9957, 0.5860, 0.3352, 0.1881, 0.1041, 0.0569, 0.0308], \quad (6.42)$$

respectively, which are the same as given in [128]. Note that the subscript G is used to denote Gaussian distributions. In addition, the optimal SDRs based on the two models are slightly different at low bit resolutions, as seen from Fig. 6.6. Here we only give the maximum SDRs and the corresponding scaling factors $R = 2$ to 8 bits

based on the generalized Bussgang's theorem:

$$\text{SDR}_G \approx [8.70, 14.10, 19.33, 24.55, 29.83, 35.17, 40.57] \text{ dB}, \quad (6.43)$$

$$\alpha_G \approx [0.8812, 0.9626, 0.9885, 0.9965, 0.9990, 0.9997, 0.9999]. \quad (6.44)$$

The SDRs based on the generalized Bussgang's model (6.41) are more accurate than based on the PQN model (6.40), in the sense that the distortion is uncorrelated with the input signal.

As for $R = 1$ bit, the quantizer is merely a hard slicer and the optimal interval based on the PQN model is given by $\Delta_G = \sqrt{\frac{8}{\pi}}$ and the optimal SDR is 4.40 dB. In comparison, the output SDR based on the generalized Bussgang's model is constant at 2.44 dB, which is independent of the quantization interval, and the scaling factor $\alpha = \frac{\Delta}{\sqrt{2\pi}\sigma_z}$ and the distortion variance $\sigma_d^2 = \frac{(\pi-2)\Delta^2}{4\pi}$ (see Appendix D).

6.3.1.3 Optimal interval for a noisy input

For an ADC device, the quantizer input is contaminated by the receiver noise. Consider that both the signal sequence $\{z_n\}$ and the noise sequence $\{v_n\}$ are zero-mean i.i.d. Gaussian distributed and they are independent from each other. In addition, only the generalized Bussgang's model (6.3) will be considered in the following. Since $\{z_n + v_n\}$ is a separable process, the output of the quantizer can be statistically modelled by

$$\tilde{z}_n = \alpha(z_n + v_n) + d_n. \quad (6.45)$$

Now the optimal quantization interval should be chosen such that the signal-to-noise-and-distortion ratio (SNDR) is maximized and the SNDR is given by

$$\text{SNDR} = \frac{\alpha^2 \sigma_z^2}{\alpha^2 \sigma_v^2 + \sigma_d^2} = \frac{\text{SNR}_{\text{in}}}{1 + \frac{\text{SNR}_{\text{in}} + 1}{\text{SDR}}} < \text{SDR}, \quad (6.46)$$

where $\text{SNR}_{\text{in}} = \frac{\sigma_z^2}{\sigma_v^2}$ is the SNR of the ADC input and $\text{SDR} = \alpha^2(\sigma_x^2 + \sigma_v^2)/\sigma_d^2$. Observe (6.46) we found that maximizing the SNDR is equivalent to maximizing the SDR (note that this is also suitable for the PQN model). Therefore, the optimal intervals and the scaling factors are the same as (6.42) and (6.44), respectively. In addition, we see from (6.46) that the output SNDR is upper bounded by the SDR. With the quantizer intervals (6.42) optimally configured for the ADC $R = 1$ bit to 8 bits, the output SNDR versus the input SNR is depicted in Fig. 6.7. Taking the distortion as noise, one can see from the figure that the SNR degrades significantly for a low resolution ADC.

6.3.2 BER performance

In this section, we first examine the distributions of the transmitted and receive signals in single- and multi-carrier transmission schemes and then investigate the

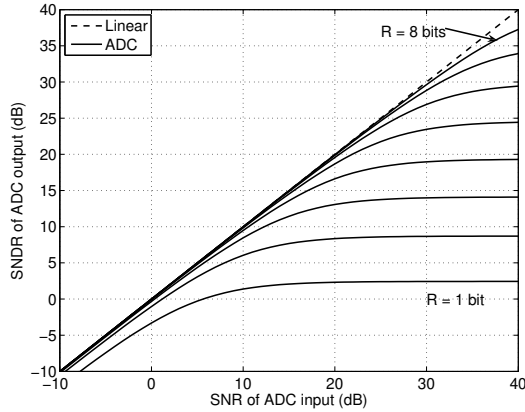


Fig. 6.7: For the optimally designed quantization interval for Gaussian inputs, the output SNDR versus the input SNR of the ADC $R = 1$ to 8 bits.

BER performance under the influence of DAC and ADC.

6.3.2.1 Signal distributions

Distribution of DAC input signals: Let us examine the distributions of the I and Q signals at the DAC inputs in OFDM, MC-CDMA and SC-FDE. The transmitted signal distributions are relevant for the determination of the optimal quantization interval of the DACs.

For a single-carrier transmission system, the baseband linearly modulated signal can be considered as a quantized signal, thanks to the discretely distributed constellations of \mathcal{M} -PSK or \mathcal{M} -QAM with a limited alphabet size. For instance, the I and Q signals of a square 16-QAM constellation are discrete signals with four levels. For this reason, the quantization step during D/A conversion, as shown in Fig. 6.3(a), for a single-carrier signal may be bypassed and there is no quantization loss caused by the conversion.

As for multi-carrier transmission schemes, the baseband modulated signal in the TD is a linear combination of user symbols, which are zero mean complex i.i.d. random variables with variance E_s , due to the linear transformations such as the IFFT and the code spreading operation in case of MC-CDMA. The I and Q signals can be well approximated by a Gaussian distribution with zero mean and variance $\frac{E_s}{2}$, when the subcarrier number is sufficiently large, according to the central-limit theorem [129]. Therefore, it is reasonable to set the DAC quantization interval to be the optimal interval (6.42) designed for a Gaussian input.

Because of its Gaussian distribution, the transmit signals in OFDM and MC-CDMA have much larger PAPR than the signal in SC-FDE. The empirical cdfs of the PAPRs are shown in Fig. 6.8 for the three transmission schemes, where an ideal LPF, i.e.

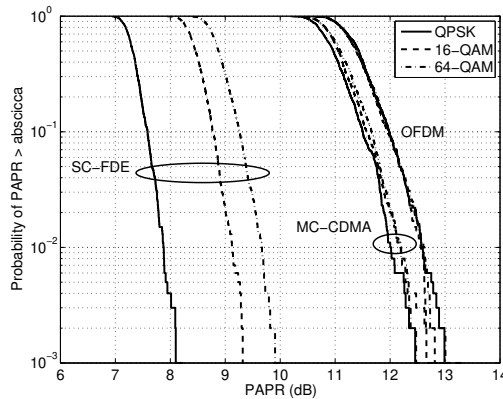


Fig. 6.8: PAPR of transmit signals in OFDM, MC-CDMA and SC-FDE.

the filter in (4.7) with the roll-off factor $\alpha = 0$, is used as the transmit filter. Here the oversampling factor is 5. Observe that the PAPR levels of OFDM and MC-CDMA are relatively insensitive to constellations, while SC-FDE has reduced PAPRs with low-order constellations. The average PAPRs of MC-CDMA and OFDM are 11.1 and 11.4 dB, respectively. The average PAPRs of SC-FDE are 7.3, 8.5 and 8.9 dB for QPSK, 16-QAM and 64-QAM, respectively.

In case that a pulse shaping filter (roll-off $\alpha > 0$) is used, the PAPRs of single-carrier signals reduce with the increasing roll-off factor, whereas the PAPRs of multi-carrier signals are insensitive to the roll-off factor [136]. Since ideal LPFs are always used in the chapter, the simulated BER of SC-FDE under the influence of nonlinearities represents the worse performance than using pulse shaping filters, as the result of the larger PAPRs.

Distribution of ADC input signals: Let us subsequently examine the signal distributions of the received I and Q branches just before the ADC, which are relevant for the design of the ADC quantization interval. As mentioned earlier, the wireless received signal consists of a linear combination of the transmit signal because of the multipath propagation channel. According to the central-limit theorem, the multi-carrier received I and Q signals in OFDM and MC-CDMA will follow Gaussian distributions.

For SC-FDE, the I and Q signals can be also approximated by Gaussian distributions, as long as the number of propagation paths are relatively large. But in a channel with a few paths, the distributions are dependent not only on the channel but also on the order of the constellation, and will have relatively smaller tails compared with a Gaussian distribution. These claims can be confirmed from the empirical distributions of the received I and Q signals as shown in Fig. 6.9(a) and (b) for the sample omnidirectional and narrow-beam channels, respectively. As described in Section 4.4.3, the path numbers are 25 and 7, respectively, for the two channels. The sample channel responses are also shown in the figures.

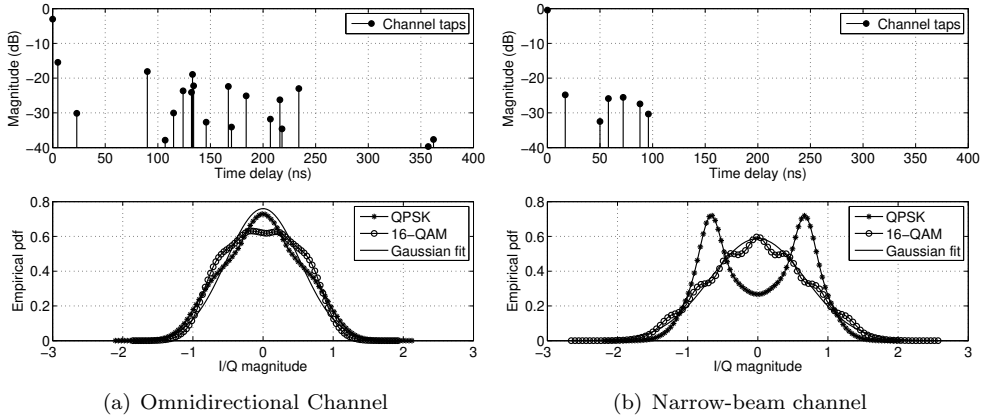


Fig. 6.9: Distributions of received I and Q signals in SC-FDE in case of two sample channel realizations.

Based on the signal models (6.41) and (6.45), the BER performance of linear MMSE detection under the effect of DAC and ADC can be computed respectively by using (6.25) (by numerical computation) and (6.33) for OFDM, (6.28) and (6.35) for SC-FDE and MC-CDMA. In the following, the BER performance is simulated and compared with the analytically computed BER. Here the quantization intervals are set to be the optimal interval given in (6.42), which is designed for Gaussian inputs. Also, the scaling factor α_G in (6.44) and the SDR_G in (6.43) for Gaussian distributions will be used for BER computation. Since the transmit and received IQ signals are only approximately Gaussian distributed, it is expected that the distribution mismatch will result in a discrepancy between the simulated and analytical BERs, as shown later. In addition, the two Rician fading channels with $K = 1$ and 10, as described in Section 4.4.3, are considered to represent high and low level frequency selectivity of the channels. The configuration of the transmission systems are also the same as in Section 4.4.3.

6.3.2.2 BER under the effect of DAC

The simulated BER performance of OFDM and MC-CDMA under the effect of DAC with various resolutions is shown in Fig. 6.10(a) and (b) (dashed line), respectively, for QPSK with Gray-bit mapping. The performance of SC-FDE is not shown here, since it is not affected by the DAC, as discussed earlier. Also shown in the figures is the analytical performance by solid line. The BER curves are depicted as a function of the average SNR per bit, i.e. $\frac{E_s}{N_0 \log_2 \mathcal{M}}$, for the case that no nonlinearity is experienced, where \mathcal{M} is the constellation size and E_s is the symbol energy. Note that the effective SNRs of decision variables, i.e. γ_k in (6.22) for OFDM and η in (6.23) for MC-CDMA, are applied in (6.25) and (6.28), respectively to find the theoretical results.

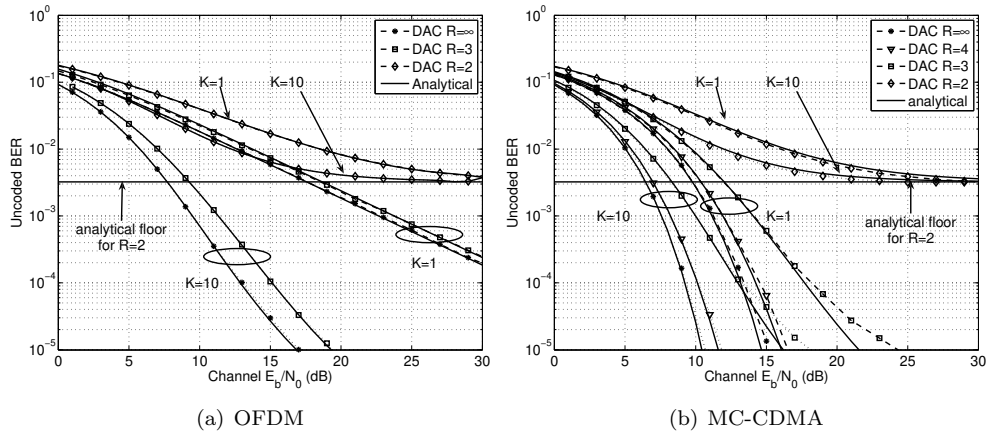


Fig. 6.10: Average BER performance of OFDM and MC-CDMA for various DAC resolution bits in Rician fading channels $K = 1$ and 10 .

It can be seen that the analytically derived BER curves are very close to the simulated ones, especially for OFDM. For MC-CDMA, the analytical curves deviates from the simulated ones, especially at higher SNR, since the analytical computation (6.28) is not exact and the approximation of η is worse at high SNR, as also noticed in Section 4.4.3. It is also observed that both OFDM and MC-CDMA indeed have the common performance floor given by (6.29), independent of the channel fading conditions.

For the DAC resolution $R \geq 3$ bits, OFDM has a minor performance loss. For instance, when $R = 3$ bits, the required channel bit SNRs, E_b/N_0 , at the target BER 1×10^{-3} are only about 1.8 and 0.9 dB more than for the case without DAC effect, in Rician fading channels with $K = 10$ and 1 , respectively. As for MC-CDMA, the E_b/N_0 penalties are larger than in OFDM for the same DAC resolution bits. This difference originates from the fact that all the symbols within a data block in MC-CDMA are equally affected by the DAC in MC-CDMA, whereas only part of them are severely affected in OFDM. For instance, the channel E_b/N_0 penalties in MC-CDMA are about 2.4 dB for $K = 1$ and 2.8 dB for $K = 10$, respectively, when $R = 3$. However, MC-CDMA still has a better BER performance than OFDM, because of the inherent frequency diversity gain.

6.3.2.3 BER under the effect of ADC

Next, the average BER performances of OFDM, MC-CDMA and SC-FDE under the influence of ADC are presented in Fig. 6.11(a), (b) and (c). The BER curves are depicted as a function of the average SNR per bit for the case that no nonlinearity is experienced. Note that the effective SNRs of decision variables, i.e. γ_k in (6.30) for OFDM and η in (6.31) for MC-CDMA and SC-FDE, are applied in (6.33) and (6.35), respectively to find the theoretical results.

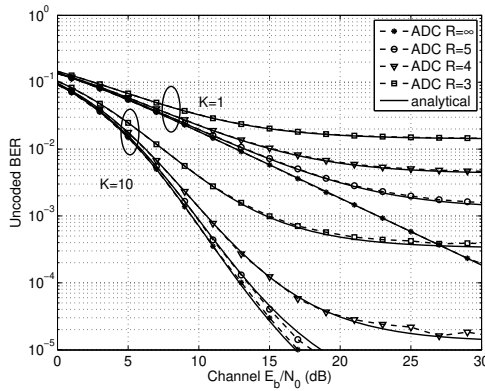
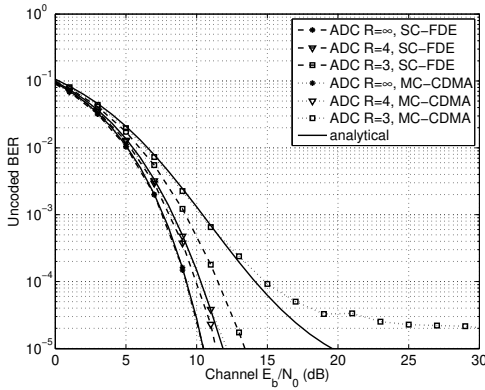
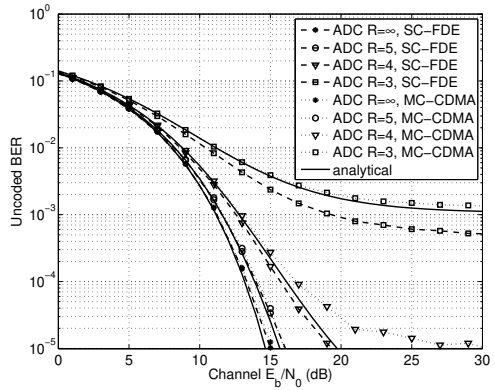
(a) OFDM ($K = 1, 10$)(b) SC-FDE, MC-CDMA ($K = 10$)(c) SC-FDE, MC-CDMA ($K = 1$)

Fig. 6.11: Average BER performance of SC-FDE and MC-CDMA for various ADC resolution bits in Rician fading channels $K = 1$ and 10 .

From Fig. 6.11(a), we see that the simulated OFDM performance can be well predicted by the analytical computation given in (6.33). This justifies the Gaussian assumption for the distortion, which has tails in its distribution due to the clipping error caused by the ADC, in decision variables during the derivation of (6.33). From Fig. 6.11(b) and (c), we see that the simulated performance of SC-FDE is usually better than the predicted, especially for lower ADC resolution bits in fading channels with higher Rician K -factors. Recall that the input signals of ADC devices are assumed to be Gaussian distributed and thus the scaling factors α_G in (6.44) and the signal-to-distortion ratio SDR_G in (6.43) for Gaussian signals are used for BER computation. Since the actual signal distribution has small tails, the actual α and SDR are larger than α_G and SDR_G , respectively, especially for the channels with low frequency selectivity, yielding a better performance than predicted. As for MC-CDMA, the simulated performance is worse than predicted, especially at higher SNR due to

Table 6.2: The channel SNR penalty in dB for QPSK modulated signals at the target BER 1×10^{-3} caused by DAC/ADC nonlinearities in fading channels with Rician factors $K = 10$ and 1. The considered DAC/ADC resolutions $R = 5, 4, 3$ bits.

Cases		Rician factor $K = 10$			Rician factor $K = 1$		
		$R = 5$	$R = 4$	$R = 3$	$R = 5$	$R = 4$	$R = 3$
DAC	OFDM	0.2	0.3	1.9	0	0.2	1.0
	MC-CDMA	0.2	0.7	2.4	0.2	0.7	2.8
	SC-FDE	0	0	0	0	0	0
ADC	OFDM	0.3	1.1	5.5	-	-	-
	MC-CDMA	0.2	0.7	2.8	0.4	1.7	-
	SC-FDE	0.2	0.5	1.7	0.4	1.5	8.0

the BER approximation by using (6.35).

In addition, for a high resolution ADC ($R \geq 4$ bits), the three schemes have about the same performance in near-flat channels ($K = 10$), although MC-CDMA and SC-FDE are slightly better. But in a near-Rayleigh fading channel ($K = 1$), MC-CDMA and SC-FDE show much better performance than OFDM, due to the inherently exploited frequency diversity, and this difference becomes larger with reducing ADC resolution ($R = 3$ bits).

Finally, from simulations we can obtain the channel SNR penalty caused by the effect of DAC and ADC, compared to the case of without DAC/ADC effect. Table 6.2 lists the penalty at the target BER 1×10^{-3} . From the table, one can clearly see that for the same bit resolution, the performance losses caused by the ADCs are more significant than those caused by the DACs. Recall the observation in Section 6.2.2 that the SNR reduction of each subcarrier caused by the TX nonlinearity is mainly related to the scaling factor and is generally less severe than the SNR reduction that is related to both the scaling factor and the distortion variance due to the RX nonlinearity. Moreover, we can also conclude from Table 6.2 that SC-FDE is the most robust one, among the three schemes, to the DAC/ADC nonlinearities.

6.3.3 Summary and discussions

Based on the statistical modelling of the quantization processes, optimal quantization intervals were designed and the influence of the DAC/ADC nonlinearities on BER performance were investigated in this section. Concerning the linear MMSE detection, there is a good agreement between the simulated and analytical BER performance, at least within the operational range of channel SNR. Particularly for SC-FDE and MC-CDMA, the closed-form BER generally provides an upper bound and a lower bound, respectively, due to the assumptions and approximations applied during the derivations.

In addition, the results show that in both high and low frequency selective channels,

the DACs cause about 0.5 dB SNR penalty for moderate resolutions ($R = 5, 4$ bits) and about less than 3 dB loss for the low resolution $R = 3$ bits for multi-carrier transmissions, while the loss in single-carrier transmission is ignorable. When $R \leq 2$ bits, the performance floor is significantly raised, due to the dramatic drop of SDR at the TX side. Therefore, the DAC resolution of $R = 4$ bit is a good compromise between the system performance and the implementation cost.

In comparison, the effect of the ADCs on the three transmission schemes is rather more severe than that of the DACs and more sensitive to the channel conditions. Recall that under TX nonlinearity, the SNR of each subcarrier is mainly constrained by the scaling factor, which is less influential than the constraint factor of SDR under RX nonlinearity, by comparing (6.22) and (6.30). This explains the BER difference caused by DACs and ADCs.

In case of moderate ADC resolutions ($R = 5, 4$ bits), SC-FDE and MC-CDMA achieve about the same performance and the channel penalties are less than 2 dB depending on the channel condition. But the performance of OFDM only approaches that of SC-FDE and MC-CDMA in near-flat channels. In severe frequency selective channels, either error correction codes or adaptive modulations are necessary for OFDM to improve the performance. This leads to the conclusion that exploiting frequency diversity is effective to combat the ADC effect for moderate ADC resolutions. However, for the lower ADC resolutions ($R \leq 3$ bits), the resulting significant performance loss for all the schemes indicates that we must seek for other solutions to combat the ADC effect. Moreover, the results suggest that concerning the reasonable SNR penalty, the ADC resolution of $R = 4$ bit is a good option for the low-power low-cost applications of the three schemes in near-AWGN channels, while $R = 5$ bit is a good option in near-Rayleigh fading channels. Concerning the absolute BER performance, OFDM needs to take advantage of frequency diversity by using, for instance, error correction codes to achieve a comparable performance as of SC-FDE and MC-CDMA.

6.4 Nonlinear power amplification

A power amplifier exhibits nonlinear transfer behavior, when the PA works in the range up to its saturation point. One way to eliminate the nonlinearity is to apply an input power backoff (IBO) such that the amplifier works in a more linear region, which reduces the power efficiency of the RF front-end but is needed in practical situations. In this section, we investigate the influence of the PA on single- and multi-carrier transmission schemes for various IBOs. Since a LNA is generally driven by the input signal at a relatively low level, the nonlinearity of the LNA causes no significant signal distortion as by the PA and will not be addressed in this thesis.

6.4.1 Modelling of PA

In general, it is complicated to model a nonlinear PA. The often used model is Rapp's model, which is suitable for solid-state power amplifiers [137]. In this model, the AM/AM nonlinearity (amplitude distortion) is described by a transfer function, while the AM/PM (phase distortion) is assumed to be negligibly small. A modified Rapp model also takes the phase distortion into account [138]. A more general nonlinear model is the polynomial model, which models both AM/AM and AM/PM distortions. It is pointed out in [123] that the Rapp's model and the polynomial models are equivalent. Both the models have assumed that the nonlinearity of the PA is *frequency independent* over the bandwidth of the communication signal, i.e. the PA is assumed to be a *memoryless* device. A more accurate and complete description of PAs can be based on Volterra series expansion [139,140], which can characterize the *frequency-dependent* nonlinear behavior for wideband input signals. However, the modelling approach of Volterra series is far too complicated for simulations. For our purpose, the Rapp model is sufficient to investigate the influence of nonlinear AM/AM distortion, which is more dominant than the AM/PM distortion in case of the quite linear class AB amplifiers [138], on single- and multi-carrier transmission schemes.

For the input signal $z(t)$ and the output signal $\tilde{z}(t)$ of a PA, the Rapp's model describes the input and output relationship given by

$$\tilde{z}(t) = \mathbb{Q}(z(t)) = e^{i\phi_z(t)} \frac{g_0 |z(t)|}{\left(1 + \left(\frac{|z(t)|}{V_{\text{sat}}}\right)^{2p}\right)^{\frac{1}{2p}}}, \quad (6.47)$$

where $\phi_z(t)$ is the phase of the input signal $z(t)$, g_0 is the small signal amplification gain, V_{sat} is the output saturation level and p controls the AM/AM sharpness of the saturation region. The AM/AM transfer function of the Rapp model is depicted in Fig. 6.12 for different sharpness factors with the saturation levels $V_{\text{sat}} = 1.6$ and 2.5. From this figure, we see that the nonlinearity becomes more severe when reducing the value of p and the saturation level V_{sat} . To reduce nonlinear distortion in the amplified signal, the operation point of the amplifier is backed off from the saturation level to the more linear region of the amplifier. The IBO is defined as the ratio between the saturation levels and the average input power, i.e.

$$\text{IBO} = \frac{V_{\text{sat}}^2}{\sigma_z^2}, \quad (6.48)$$

where $\sigma_z^2 = \mathbb{E}\{|z(t)|^2\}$ is the average power of the input signal.

Note that the PA described by the Rapp's model in (6.47) is memoryless, and the single- and multi-carrier signals can be considered to be separable processes. Therefore, the output of the nonlinear PA can be modelled by using the generalized Bussgang's theorem given in (6.3). For multi-carrier transmission of OFDM and MC-CDMA, the input I and Q signals of the PA are zero mean Gaussian distributed for a large FFT size N . As a result, the input magnitude follows the Rayleigh distribution

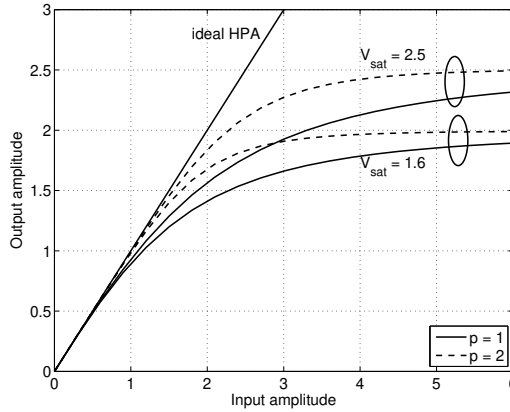


Fig. 6.12: AM/AM transfer function of Rapp's model for different sharpness factors p and for saturation levels $V_{\text{sat}} = 1.6$ and 2.5 .

given by $P_{|z(t)|} = \frac{2|z(t)|}{\sigma_z^2} \exp\left\{-\frac{|z(t)|^2}{\sigma_z^2}\right\}$. Accordingly, the scaling factor and the distortion variance can be determined according to the Generalized Bussnag's theorem. Here we consider the amplifier gain $g_0 = 1$ and the sharpness factor $p = 1$, the scaling factor and the distortion variance are obtained as [123]

$$\alpha_T = \lambda^2 + \frac{\sqrt{\pi}}{2} \lambda (1 - 2\lambda^2) e^{\lambda^2} \operatorname{erfc}[\lambda] \quad (6.49)$$

$$\sigma_{d_T}^2 = E_s \left(\lambda^2 - \lambda^4 e^{\lambda^2} \Gamma[0, \lambda^2] - |\alpha|^2 \right), \quad (6.50)$$

using (6.4) and (6.5), respectively, where $\lambda = \frac{V_{\text{sat}}}{\sqrt{E_s}} = \sqrt{\overline{\text{IBO}}}$ and $\Gamma[n, x] = \int_x^\infty t^{n-1} e^{-t} dt$ is the incomplete Gamma function.

As for the single-carrier signal in SC-FDE, the user data symbols are carried in the TD and thus the distribution of the transmit signal is dependent on the constellation size. Consider the discrete baseband equivalent transmission as described in Chapter 4, in which Nyquist filters are used and the sampling of the received signal is perfect in timing. Therefore, the magnitude of the PA input follows a discrete distribution, which is merely the distribution of the symbols magnitudes. Since there are no tails in the distribution, the PAPR level of the transmit signal in SC-FDE is much lower than that in OFDM and MC-CDMA. Assuming that every symbol within the symbol alphabet has the same probability to be transmitted³, the scaling factor and the

³For QPSK, the signal magnitude is constant. For 16-QAM, the signal magnitude follows the distribution given by

$$P_{|z(t)|} = \begin{cases} 1/4 & |z(t)| = \frac{\sqrt{5}}{5} \sqrt{E_s} \\ 1/2 & |z(t)| = \sqrt{E_s} \\ 1/4 & |z(t)| = \frac{3\sqrt{5}}{5} \sqrt{E_s}. \end{cases}$$

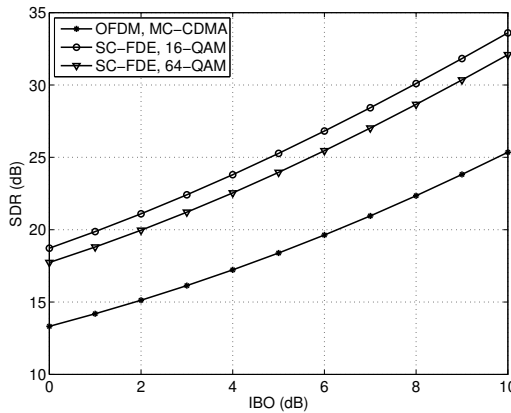


Fig. 6.13: The signal-to-distortion ratio at the output of the PA versus the input backoff for single- and multi-carrier signals.

distortion variance can be also determined and given by

$$\text{QPSK:} \quad \alpha_T = f_1(\lambda) \quad \text{and} \quad \sigma_{d_T}^2 = 0, \quad (6.51)$$

$$\text{16-QAM:} \quad \alpha_T = \frac{f_1\left(\frac{\lambda}{\sqrt{5}}\right)}{4} + \frac{f_1(\lambda)}{2} + \frac{f_1\left(\frac{3\lambda}{\sqrt{5}}\right)}{4}, \quad (6.52)$$

$$\frac{\sigma_{d_T}^2}{E_s} = \frac{f_2\left(\frac{\lambda}{\sqrt{5}}\right)}{4} + \frac{f_2(\lambda)}{2} + \frac{f_2\left(\frac{3\lambda}{\sqrt{5}}\right)}{4} - \alpha_T^2, \quad (6.53)$$

for $g_0 = 1$ and $p = 1$, where the functions $f_1(a\lambda) = \frac{a^2}{\sqrt{1+a^2}}$ and $f_2(a\lambda) = \frac{a^2}{1+a^2}$. Note that for QPSK, the distortion is zero, since the PA input has a constant magnitude.

The calculated values of α_T and σ_d^2 in (6.49)-(6.53) can be used to calculate the signal-to-distortion ratio as $\text{SDR}_T = \frac{\alpha_T^2 \sigma_z^2}{\sigma_{d_T}^2}$ for OFDM, MC-CDMA and SC-FDE, which will be used in Section 6.4.2 for analytical BER computations. The average SDRs at the output of the PA are depicted in Fig. 6.13 for the single- and multi-carrier signals. Clearly, the SDRs of single-carrier signals are dependent on the constellation orders and are much higher than multi-carrier signals.

To illustrate the influence of the PA nonlinearity on 16-QAM modulated signals, we depict the received signal points (scattered points) in Fig. 6.14(a)-(c) without adding the multipath fading channel and the receiver noise. The circular dots in the figures are the constellation points. From these figures, it is evident that the constellation diagrams of the multi-carrier signals indeed experience the effect of scaling and additive distortion due to the nonlinearity, as suggested by the generalized Bussgang's theorem (6.3). As for the single-carrier signal, the individual constellation points are scaled at different levels, depending on the magnitudes, without additive distortion, since the user symbols are transmitted in the TD. Therefore, the scaling factor and

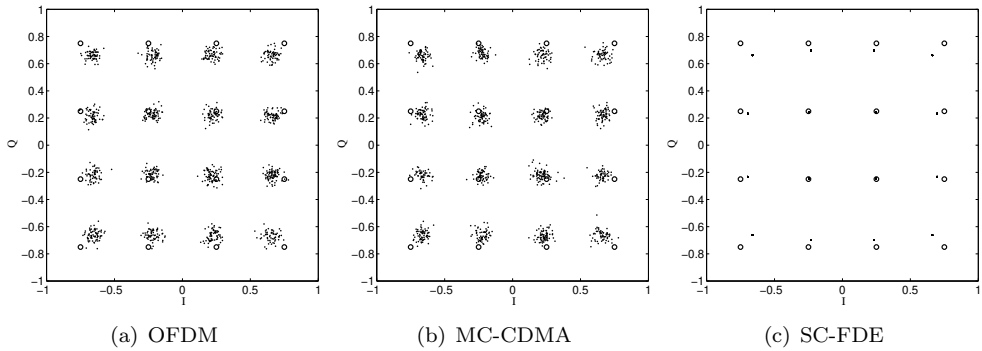


Fig. 6.14: The influence of the PA nonlinearity on the constellation of 16-QAM in a noiseless frequency flat channel.

the distortion level suggested by the theorem only describes the statistical influence of the nonlinearity on a sequence of randomly transmitted symbols, instead of the influence on individual symbols.

6.4.2 BER performance

The BER performance under the influence of the PA can be computed by using (6.25) (by numerical computation) for OFDM and (6.28) for SC-FDE and MC-CDMA. Here we consider $g_0 = 1$ and $p = 1$ for the configuration of the PA in (6.47). In the following, the BER performance is also simulated and compared with the analytical BER for various IBO values, as shown in Fig. 6.15 for the three QPSK-modulated transmission schemes. Rician channels are considered with the Rician factors $K = 1$ and 10, respectively. Here the infinite IBO corresponds to a linearly operated PA. The BER curves are depicted as a function of the average SNR per bit for the case that no nonlinearity is experienced. Note that the effective SNRs of decision variables, i.e. γ_k in (6.22) for OFDM and η in (6.23) for MC-CDMA and SC-FDE, are applied in (6.25) and (6.28), respectively, to find the theoretical results.

From the figures, we also obtained the SNR penalties, due to the nonlinearity, at the target BER 1×10^{-3} , which are listed in Table 6.3 for both QPSK and 16-QAM modulated transmission schemes. From the figures and the table, we have the following observations and explanations.

- There is a good agreement between the simulated and the computed BERs. The discrepancy at high SNR in SC-FDE and MC-CDMA is mainly due to the BER approximation by using (6.35), as explained in Section 4.4.2.
- The SNR penalties of the three schemes are relatively independent of the channel conditions, especially for a low constellation order (e.g. QPSK). This can be explained by the fact that the SDR is relatively high and the SNR loss of

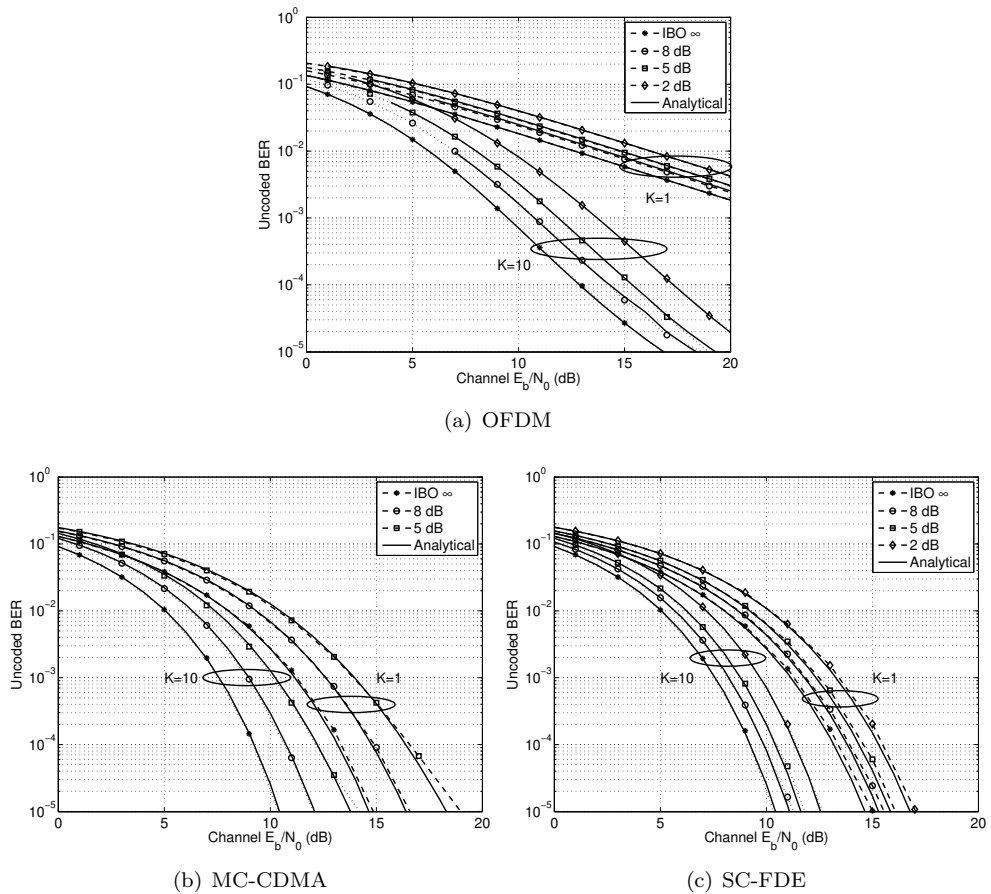


Fig. 6.15: Average BER of QPSK-modulated transmissions in Rician fading channels $K = 1$ and 10, under the influence of nonlinear PA for $\text{IBO} = 8, 5$ and 2 dB.

each subcarrier is strongly dependent on the scaling factor α_T caused by the nonlinearity, by observing the subcarrier SNR γ_k in Table 6.1 for the case of the nonlinearity at the TX side. In particular for SC-FDE and OFDM, it is checked that for QPSK, the SNR penalties can be well estimated by using $-20 \log_{10} \alpha_T$.

- Although the SNR penalties are larger than for OFDM, the absolute BERs of SC-FDE and MC-CDMA still outperform uncoded OFDM due to their inherent exploited frequency diversity. In particular, SC-FDE is the most robust solution to the nonlinearity, not only due to the frequency diversity but also due to the low PAPR of the transmit signal.

Table 6.3: SNR penalties at BER = 1×10^{-3} due to the PA nonlinearity for various IBOs.

Cases		Rician factor $K = 10$			Rician factor $K = 1$		
		IBO = 8 dB	5	2	8	5	2
QPSK	OFDM	1.3	2.3	4.2	1.1	2.1	3.5
	MC-CDMA	1.4	2.7	5.0	1.5	2.6	4.7
	SC-FDE	0.6	1.2	2.1	0.6	1.2	2.1
16-QAM	OFDM	2.1	5.8	-	1.6	3.9	-
	MC-CDMA	2.7	8.7	-	3.0	10.0	-
	SC-FDE	0.7	1.3	2.2	0.7	1.3	2.2

6.5 Phase noise

So far, we have assumed that the radio frequency oscillator is perfectly locked at a certain frequency. In practical systems, the amplitude and phase of the oscillator are randomly disturbed by the circuit and device noise. Since the amplitude fluctuations can be generally controlled to be at a limited level, the frequency fluctuations dominate the influence of the oscillator imperfection on the systems [141]. These random frequency fluctuations are often modelled as random phase fluctuations, which is referred to as *phase noise* (PN). In this section, we investigate the influence of PN on the performance of single- and multi-carrier transmission systems.

6.5.1 Modelling of phase noise

Consider a local oscillator affected by a phase noise process $\theta(t)$, the carrier signal becomes $e^{i(2\pi f_c t + \theta(t))}$. For a free running oscillator, the phase noise is usually modelled as a Wiener process, which has a zero mean and the variance

$$\mathbb{E}\{\theta^2(t)\} = at. \quad (6.54)$$

Here the parameter a depends on the quality of the oscillator. Being a Wiener process, the phase noise is also a Gaussian process and has the pdf given by

$$p_{\theta(t)} = \frac{1}{\sqrt{2\pi at}} \exp\left\{-\frac{\theta^2(t)}{2at}\right\}. \quad (6.55)$$

The multiplicative noise, $e^{i\theta(t)}$, on the ideal carrier signal $e^{i2\pi f_c t}$ has the first and second order statistics given by

$$\mathbb{E}\{e^{i\theta(t)}\} = \exp\left\{-\frac{at}{2}\right\} \quad (6.56)$$

$$\mathbb{E}\{e^{i\theta(t_1)} e^{-i\theta(t_2)}\} = \exp\left\{-\frac{a|\tau|}{2}\right\}, \quad (6.57)$$

respectively, where $\tau = t_1 - t_2$. Although $\theta(t)$ is non-stationary, the resulting multiplicative noise $e^{i\theta(t)}$ is a stationary process, since its autocorrelation is only a function

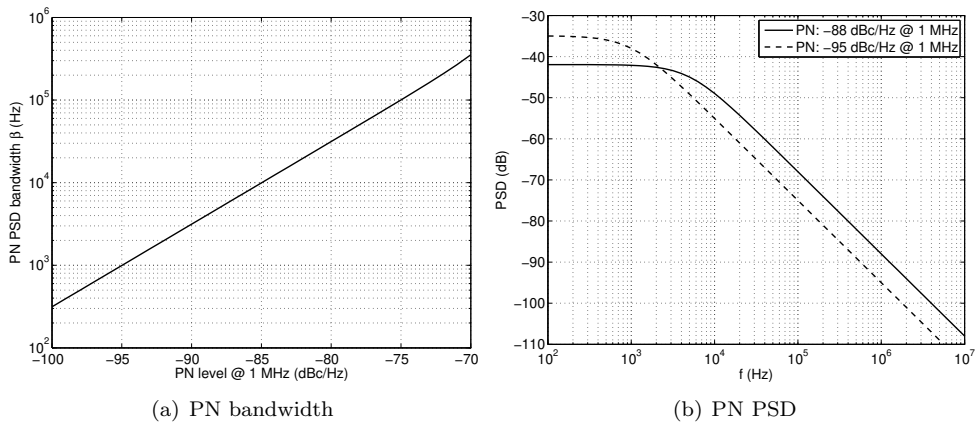


Fig. 6.16: (a) The PN PSD bandwidth β versus the PN level at 1 MHz using the PN model (6.58); (b) PSD of phase noise with the levels -85 and -95 dBc/Hz at 1 MHz.

of τ . The Fourier transform of the autocorrelation function (6.57) yields the double-sided power spectrum density (PSD) of $e^{j\theta(t)}$. Here we only give the often used single-sided PSD given by

$$S(f) = \frac{a}{4\pi^2 f^2 + a^2/4}, \quad (6.58)$$

which is the well known Lorentzian spectrum [142].

A commonly used measure for the characterization of a PSD is the single sideband -3 dB bandwidth. It can be found that the -3 dB bandwidth of the Lorentzian spectrum is given by $\beta = \frac{a}{4\pi}$ [123]. In addition, the phase noise level of an oscillator reported in literature is typically expressed in units of dBc/Hz at a certain offset from the carrier frequency for a measured PSD. Given the PN level $S(f_{\text{pn}})$ dBc/Hz at the offset f_{pn} Hz reference to the carrier frequency, the -3 dB bandwidth β of the spectrum (6.58) can be determined by

$$\beta = \frac{1 - \sqrt{1 - 4\pi^2 S^2(f_{\text{pn}}) f_{\text{pn}}^2}}{2\pi S(f_{\text{pn}})}. \quad (6.59)$$

The -3 dB bandwidth β versus the PN level at 1 MHz is depicted in Fig. 6.16(a). Clearly, the PN PSD bandwidth approximately linearly increases over the PN level in a logarithmic scale.

Concerning the oscillators applied in 60-GHz transceivers, the reported PN levels in literature are from -88 to -95 dBc/Hz at 1 MHz reference to the carrier frequency based on the 130-nm CMOS technologies [143–145]. If the PSD (6.58) is applied to fit the reported PN levels, we have the corresponding -3 dB bandwidths given by $\beta = 5.0$ kHz and 1.0 kHz, respectively, and the PSDs are depicted in Fig. 6.16(b).

6.5.2 Influence on transmission performance

Consider the wideband transmission systems as described in Chapter 4, which have phase noise at both the TX and RX side and experience a time invariant fading channel. Assume that the frequency offset is zero and the symbol timing is perfect at receiver. After the removal of the cyclic prefix, the received signals in the TD and the FD are given by

$$\mathbf{r}_t = \mathbf{E}_R \text{cir}\{\mathbf{h}\} \mathbf{E}_T \mathbf{u}_t + \mathbf{v}_t \quad (6.60)$$

$$\mathbf{r} = \mathbf{\Xi}_R \mathbf{H} \mathbf{\Xi}_T \mathbf{C} \mathbf{x} + \mathbf{v}, \quad (6.61)$$

respectively. Here $\mathbf{u}_t = \mathbf{F}^H \mathbf{C} \mathbf{x}$ is the transmit signal vector in the TD and the diagonal matrix \mathbf{E}_x for $x \in \{T, R\}$ is the phase rotation matrix due to the phase noise at the TX or RX sides. The n th diagonal element of \mathbf{E}_x is given by $e^{i\theta_{x,n}}$, where $\theta_{x,n}$ is the n th phase sample in the data block. The matrix $\mathbf{\Xi}_x = \mathbf{F} \mathbf{E}_x \mathbf{F}^H$ models the influence of the phase noise in the FD and is given by

$$\mathbf{\Xi}_x = \begin{pmatrix} \xi_{x,0} & \xi_{x,-1} & \cdots & \xi_{x,-N+1} \\ \xi_{x,1} & \xi_{x,0} & \cdots & \xi_{x,-N+2} \\ \vdots & \vdots & \ddots & \vdots \\ \xi_{x,N-1} & \xi_{x,N-2} & \cdots & \xi_{x,0} \end{pmatrix}, \quad (6.62)$$

where the element

$$\xi_{x,k} = \frac{1}{N} \sum_{n=0}^{N-1} e^{i\theta_{x,n}} e^{-i\frac{2\pi kn}{N}} \quad (6.63)$$

for $k \in (-N, N)$. The average power of $\xi_{x,k}$ can be derived by

$$\begin{aligned} \mathbb{E}\{|\xi_{x,k}|^2\} &= \frac{1}{N^2} \sum_{n=0}^{N-1} \sum_{n'=0}^{N-1} \mathbb{E}\left\{e^{i(\theta_{x,n} - \theta_{x,n'})}\right\} e^{-i\frac{2\pi k(n-n')}{N}} \\ &= \frac{1}{N^2} \left(N + 2 \sum_{n=1}^{N-1} (N-n) e^{-2\pi n \beta T_s} \cos\left(\frac{2\pi kn}{N}\right) \right) \end{aligned} \quad (6.64)$$

using the autocorrelation function $\mathbb{E}\left\{e^{i(\theta_{x,n} - \theta_{x,n'})}\right\} = e^{-2\pi\beta|n-n'|T_s}$ based on (6.57) for the sampling rate $1/T_s$, where T_s is the sampling interval. From (6.64), we see that the average level of $|\xi_k|^2$ is strongly related to the normalized PN PSD bandwidth βNT_s , which represents the ratio between the PN bandwidth and the subcarrier spacing. Fig. 6.17 depicts $\mathbb{E}\{|\xi_{x,k}|^2\}$ for $\beta NT_s = 0.01, 0.1$ and 1 . The considered data block sizes are $N = 256$ and 1024 . According to the figure, we have the following observations for the received signal (6.61):

- Since $\mathbb{E}\{|\xi_{x,k}|^2\} \neq 0$ for $k \neq 0$, which indicates a non-diagonal matrix of $\mathbf{\Xi}_x$, the interference among subcarriers occurs and is often referred to as the inter-carrier interference (ICI). The ICI levels contributed by individual subcarriers decrease with increasing subcarrier distance.

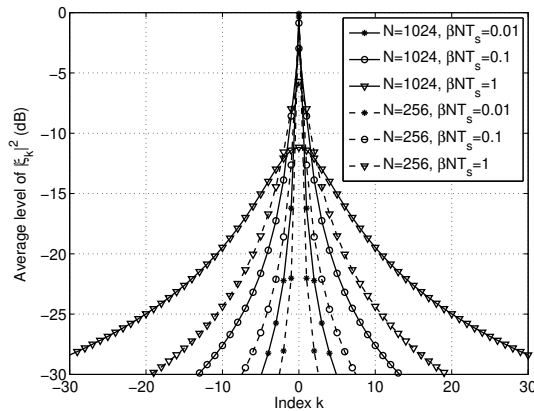


Fig. 6.17: The magnitude of ξ_k in dB for the normalized PN PSD bandwidth $\beta NT_s = 0.001, 0.1, 1$.

- If $\beta NT_s \ll 1$ for both TX and RX PN, i.e. when the PN bandwidth is much narrower than the subcarrier spacing, we have $\mathbb{E}\{|\xi_{x,k}|^2\} \approx \delta(k)$, which implies $\Xi_x \approx \mathbf{I}$ for $x \in \{\text{T}, \text{R}\}$. Consequently, the resulting ICI is ignorable and the received signal can be well approximated by

$$\mathbf{r} \approx \xi_0 \mathbf{H} \mathbf{C} \mathbf{x} + \mathbf{v}. \quad (6.65)$$

Here $\xi_0 = \xi_{\text{T},0} \xi_{\text{R},0}$ is common to all the subcarriers and is often referred to as the common phase error (CPE), since it has an approximately unity amplitude.

- If βNT_s tends to be one or even larger, i.e. when the PN bandwidth tends to be equal or larger than the subcarrier spacing, the desired signal is significantly attenuated, due to $|\xi_{x,0}|^2 \ll 1$, and meanwhile the severe ICI occurs, due to the rising level of $|\xi_{x,k}|^2$ for $k > 0$.
- For the same level of βNT_s , the larger the data block size of N , the severe is the ICI level.

Phase noise has different influence on OFDM, SC-FDE and MC-CDMA. In the following, we closely look at the influence of phase noise on them.

Frequency flat channel: First consider the case of a frequency flat channel, i.e. $|H_k| = 1$ for $0 \leq k \leq N - 1$. Since the channel is flat, the phase disturbances at the TX and RX sides can be added together. For the purpose of illustration, the received symbols are depicted in Fig. 6.18 under the influence of PN with $\beta NT_s = 0.01$ without adding the channel noise. From this figure, we see that the whole constellation diagrams are rotated independent of the type of the transmission scheme, due to the CPE ξ_0 for the whole frequency spectrum. However, the noise patterns on the constellations are different for the three schemes. In SC-FDE, the PN is directly imposed on the user symbols, resulting in random phase rotations on the constellation

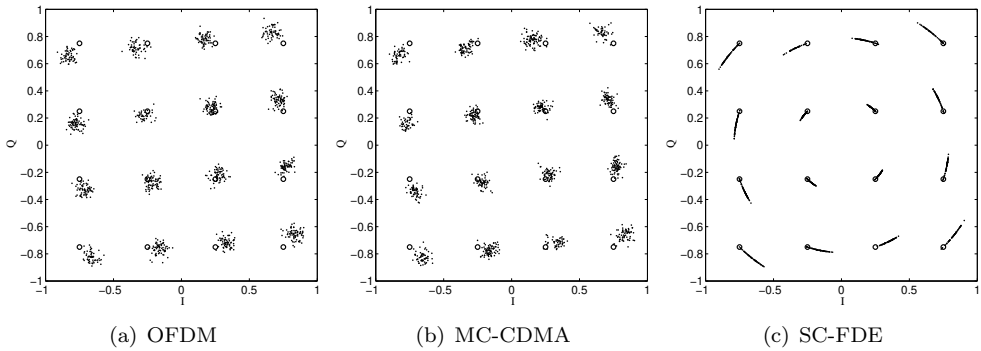


Fig. 6.18: The PN influence on the constellation of 16-QAM in a noiseless frequency flat channel (the PN level $\beta NT_s = 0.01$).

points, as suggested by (6.60). In comparison, the PN in OFDM and MC-CDMA results in AWGN-alike disturbances around the constellations, in addition to the CPE, due to the combination of interferences from other symbols inside the data block.

Frequency selective channel: In case of a frequency selective channel, the phase disturbance at the TX and RX sides can not be simply added together. To distinguish the individual influences, we consider the TX and RX PNs separately. When PN only occurs at the TX or the RX side, the k th subcarrier signal is given by

$$\text{TX PN:} \quad r_k = \xi_0 H_k \sum_{n=0}^{N-1} C_{kn} x_n + H_k \underbrace{\sum_{\substack{k'=0 \\ k' \neq k}}^{N-1} \xi_{k-k'} \sum_{n=0}^{N-1} C_{k'n} x_n}_{v_{\text{ICI},k}} + v_k, \quad (6.66)$$

$$\text{RX PN:} \quad r_k = \xi_0 H_k \sum_{n=0}^{N-1} C_{kn} x_n + \underbrace{\sum_{\substack{k'=0 \\ k' \neq k}}^{N-1} \xi_{k-k'} H_{k'} \sum_{n=0}^{N-1} C_{k'n} x_n}_{v_{\text{ICI},k}} + v_k, \quad (6.67)$$

with the corresponding ICI levels, $\sigma_{\text{ICI},k}^2 = \mathbb{E}\{|v_{\text{ICI},k}|^2\}$, given by

$$\text{TX PN:} \quad \sigma_{\text{ICI},k}^2 = E_s |H_k|^2 \sum_{\substack{k'=0 \\ k' \neq k}}^{N-1} \mathbb{E}\{|\xi_{k-k'}|^2\}, \quad (6.68)$$

$$\text{RX PN:} \quad \sigma_{\text{ICI},k}^2 = E_s \sum_{\substack{k'=0 \\ k' \neq k}}^{N-1} |H_{k'}|^2 \mathbb{E}\{|\xi_{k-k'}|^2\}, \quad (6.69)$$

respectively. Note that in case of the TX PN, the ICI level of the k th subcarrier is linearly dependent on $|H_k|^2$, indicating a larger ICI for the subcarrier signal which has

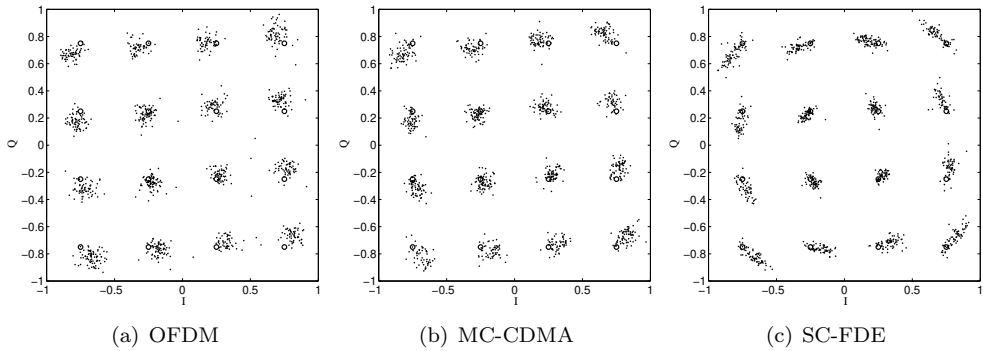


Fig. 6.19: The influence of the TX PN on the constellation of 16-QAM after equalization in a noiseless frequency selective channel (the PN level $\beta N T_s = 0.01$).

a larger SNR. In comparison, the RX PN causes an ICI level relatively independent of the subcarrier channel, since the ICI is a linear combination of $|H_{k'}|^2$ for all the subcarriers $k' \neq k$.

For a moderate PN which has a much narrower bandwidth than the subcarrier spacing, the ICI level is relatively low and is ignorable. However, the CPE results in a phase rotation for each subcarrier signal, which can be destructive for the signal detection. Therefore, it is often necessary to estimate and compensate the CPE for each data block, which can be realized by inserting pilots in data sequences. After the removal of the CPE ξ_0 , the resulting signal r_k/ξ_0 needs to be equalized by the weight W_k to remove the channel effect before detection. The symbols in OFDM will be detected based on the equalized signal $W_k r_k/\xi_0$, where W_k is the weight of the k th subcarrier. For both SC-FDE and MC-CDMA, the decision variables are obtained by doing the code despreading on the equalized signal $W_k r_k/\xi_0$. For a relatively low level of the PN, the MMSE weight $W_k = \frac{H_k^*}{|H_k|^2 + 1/\gamma}$, which is applied when there is no phase noise, can be applied for the equalization.

To illustrate the influence of PN in case of frequency selectivity, we depict the received symbols after channel equalization in Fig. 6.19 when the TX PN occurs. Here the channel noise is not added and the CPE is not corrected at receiver. In addition, the phase noise samples used here are the same as in Fig. 6.18 for the purpose of comparison. It is observed from the figure that the same CPE still exists compared with in the case of frequency flat channel. In addition, the constellation points in SC-FDE are contaminated not only by the random phase rotations, but also by the amplitude fluctuations, which is generated by the linear combination of the neighboring symbols due to the multipath propagation, as suggested by (6.60).

BER performance: To investigate the influence of PN on the transmission performance, we simulated the single- and multi-carrier schemes with the MMSE equalization performed at receiver. The considered FFT size is 1024, which indicates a relatively high ICI level compared to the case of using a shorter FFT size according

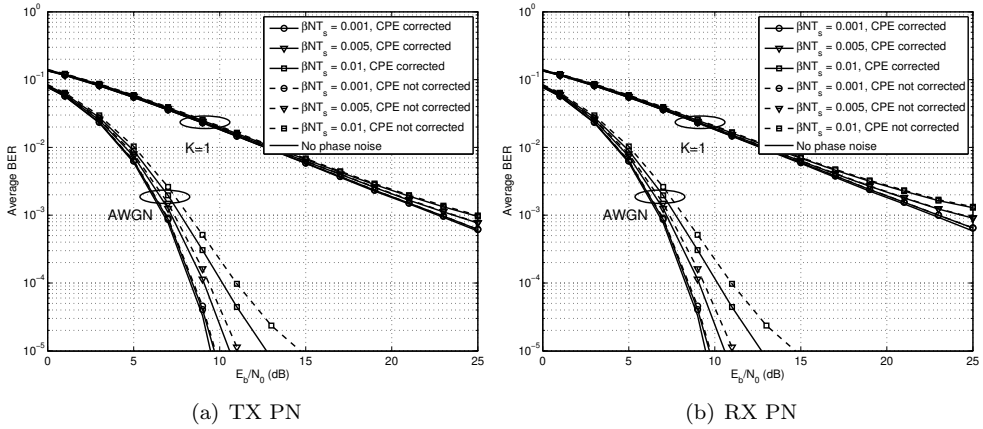


Fig. 6.20: Simulated BER of OFDM in case of TX PN and RX PN for various βNT_s (solid line: CPE corrected; dash line: CPE not corrected).

to Fig. 6.17. The BER performance is depicted in Fig. 6.20, Fig. 6.21 and Fig. 6.22 for QPSK-modulated OFDM, MC-CDMA and SC-FDE, respectively. Here the TX PN and the RX PN are applied separately, and the considered PN levels are $\beta NT_s = 0.001, 0.005, 0.01$, which correspondent to $-93, -86$ and -83 dBc/Hz at 1 MHz, respectively (see Fig. 6.16(a)). In addition, both the frequency flat channel, i.e. the AWGN channel, and the frequency selective channel with the Rician factor $K = 1$ are considered. The CPE is either corrected or not corrected, as shown in the figures by the solid or dash lines, respectively. From the figures, we have the following observations and analysis:

- In OFDM, the TX PN causes slightly less performance loss than the RX PN in frequency selective channels. This can be explained by the fact that the ICI levels vary over subcarriers in case of the TX PN, which tends to result in a relatively low error probability on average, compared with the same ICI level for all the subcarriers in case of the RX PN.
- In MC-CDMA and SC-FDE, the TX PN and the RX PN result in the same performance, since the error disturbances in all the decision variables have the same variance.
- In AWGN channels, SC-FDE and OFDM have a comparable performance for both TX PN and RX PN. In comparison, MC-CDMA shows a slightly worse performance, since the error disturbances are after code despreading of the ICI and have relatively longer tails in the error distribution than in SC-FDE and OFDM.
- In frequency selective channels, SC-FDE and MC-CDMA have about the same performance, because the noise patterns on the constellation points become similar, as seen from Fig. 6.19. OFDM is relatively more robust to the PN,

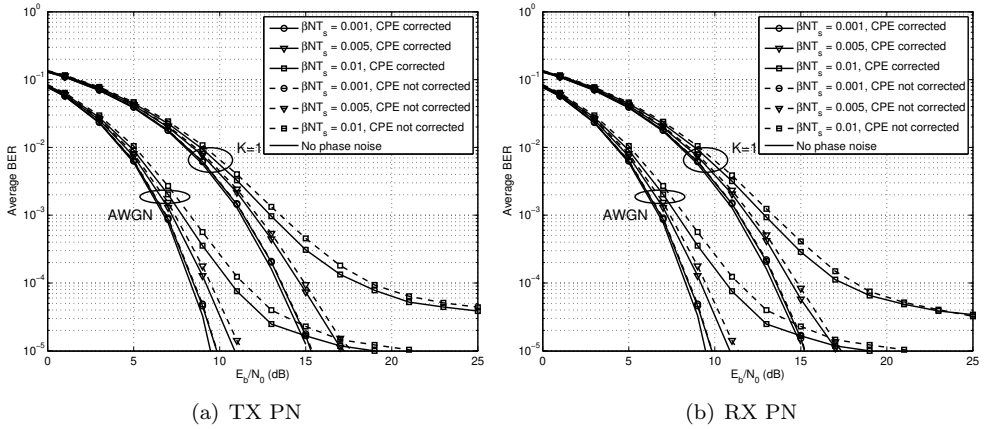


Fig. 6.21: Simulated BER of MC-CDMA in case of TX PN and RX PN for various βNT_s (solid line: CPE corrected; dash line: CPE not corrected).

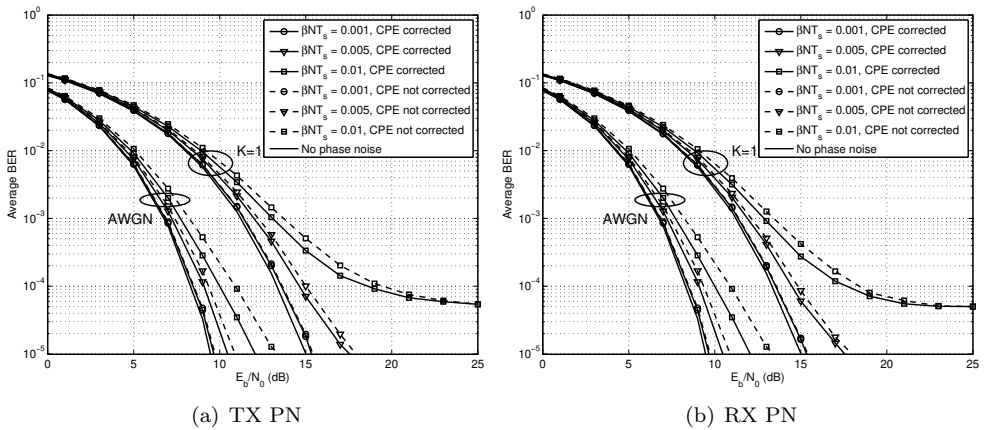


Fig. 6.22: Simulated BER of SC-FDE in case of TX PN and RX PN for various βNT_s (solid line: CPE corrected; dash line: CPE not corrected).

since only part of the symbols in a data block are severely affected by the ICI due to the frequency selectivity.

- In case the PN level $\beta NT_s < 0.001$, the performance loss caused by the PN is ignorable for all the transmission schemes in any channel conditions, due to the relatively low ICI level.
- In case the PN level $\beta NT_s > 0.005$, the performance loss becomes significant, especially in SC-FDE and MC-CDMA. In such a case, the CPE correction leads to the performance improvement up to 0.5 dB at the target BER 1×10^{-3} . The CPE correction tends to be more effective on improving the performance in

the frequency flat channels than in the frequency selective channels. To further improve the performance, the ICI cancellation is needed, but can largely increase the receiver complexity.

Concerning the PN influence on 60 GHz transmission, we consider a possible configuration with a receiver bandwidth 1.75 GHz and the data block size 1024, yielding the subcarrier spacing at 1.7 MHz. For the typical 0.13- μm CMOS based 60-GHz oscillators with the phase noise levels from -88 to -95 dBc/Hz at 1 MHz, we can examine that the PN levels are in the range of 0.003 to 0.0006, which results in an ignorable performance loss for the considered schemes here.

6.6 IQ imbalance

Due to its simplicity, the direct-conversion transceiver architecture is a promising solution for the highly integrated low-power implementation of 60-GHz RF front-ends. For a transmission scheme which involves both amplitude and phase modulations, quadrature mixing is conducted to generate the I and Q branches for the RF front-end. Ideally, the LO signals for the I and Q branches should have equal amplitudes and a phase difference of 90° . In practice, however, the amplitudes and phases of the IQ branches are often imbalanced, resulting in a mixture of the desired signal and its image components, especially for a direct-conversion structured RF front-end. The purpose of this section is to investigate the influence of the IQ imbalance on the transmission performance for OFDM, SC-FDE and MC-CDMA.

6.6.1 Amplitude and phase mismatch

Consider the imbalanced I and Q branches in the direct-conversion structured transmitter and receiver, as illustrated in Fig. 6.23. At the TX side, the baseband signal $u(t)$ after the D/A conversion is filtered and up-converted to the RF frequency f_c by doing quadrature mixing, yielding the RF signal $u_{\text{RF}}(t)$. The local oscillator (LO) generates the signals $\cos(\omega_c t)$ and $\mu_T \sin(\omega_c t + \phi_T)$ used for the mixing of the I and Q branch signals, respectively. Similarly, the received RF signal $r_{\text{RF}}(t)$ is down-converted by doing quadrature mixing at receiver. After the low-passing filtering and the A/D conversion, the baseband signal $r(t)$ is obtained. Here the LO signals are $\cos(\omega_c t)$ and $-\mu_R \sin(\omega_c t + \phi_R)$.

Here the TX and RX IQ imbalances are characterized respectively by the amplitude imbalances, defined by μ_T and μ_R , and the phase imbalances, defined by ϕ_T and ϕ_R . Often the amplitude imbalances are defined by the power ratio between the I and Q branches in dB, i.e. $20 \log_{10} |\mu|$ (dB), and the phase imbalances are defined by the phase difference between them in degree. In case of perfect matching between the I and Q branches, the LO signals for the two branches have the same amplitude and have a 90° phase difference, i.e. $\mu_T = \mu_R = 1$ (0 dB) and $\phi_T = \phi_R = 0^\circ$. Note that here the IQ imbalances are modelled in an asymmetrical way, but can be equivalently

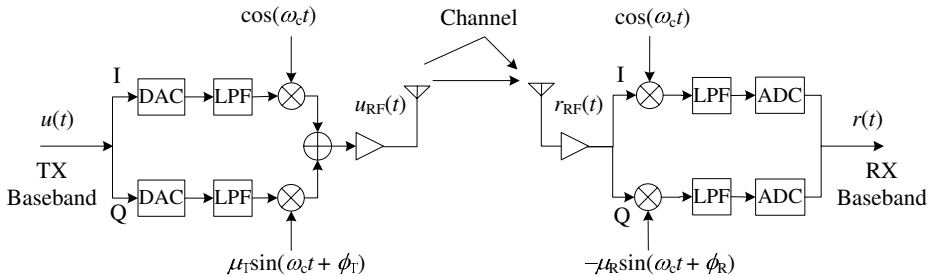


Fig. 6.23: IQ imbalances in the direct-conversion architecture transmitter and receiver.

modelled in a symmetrical way such that each branch experiences half of the phase and amplitude errors [123, 146].

Although imperfect mixing is the main source for IQ imbalances, other components in the transceiver could cause imbalances as well. For instance, the mismatch between the frequency responses of two analog low-pass filters in I and Q branches results in frequency dependent IQ imbalances [147], instead of the frequency independent imbalances caused by the quadrature mixing. In the following, we only consider the IQ imbalances caused by the quadrature mixing.

For the transmit RF signal $u_{\text{RF}}(t)$ with the I and Q imbalanced due to the imperfect quadrature mixing, the baseband equivalent signal in the TD is given by [123, 148, 149]

$$\tilde{u}(t) = \kappa_{\text{T}}u(t) + (1 - \kappa_{\text{T}})u^*(t), \quad (6.70)$$

where the coefficient κ_{T} characterizes the TX imbalances and is given by

$$\kappa_{\text{T}} = (1 + \mu_{\text{T}}e^{j\phi_{\text{T}}})/2. \quad (6.71)$$

From (6.70), we see that the IQ imbalance at the TX side results in the mirrored spectrum, which is the Fourier transform of $u^*(t)$, of the desired signal $u(t)$.

In the receiver, the baseband received signal $r(t)$ in the TD is given by

$$r(t) = \kappa_{\text{R}}\left(h(t) * \tilde{u}(t) + v(t)\right) + (1 - \kappa_{\text{R}}^*)\left(h^*(t) * \tilde{u}^*(t) + v^*(t)\right), \quad (6.72)$$

where the coefficient κ_{R} characterizes the RX imbalances and is given by

$$\kappa_{\text{R}} = (1 + \mu_{\text{R}}e^{-j\phi_{\text{R}}})/2. \quad (6.73)$$

Note that “*” in (6.72) denotes convolution and should be distinguished from the superscript “*” as the conjugate. The influence of the IQ imbalance on the signal spectrum is schematically shown in Fig. 6.24, where we assume an ideal up-conversion and a frequency selective channel. This figure clearly shows that the IQ imbalance at the RX side causes the mirroring of the signal spectrum, after experiencing the multipath channel. It is also seen from (6.72) that the receiver noise spectrum is mirrored as well in case of the RX imbalance.

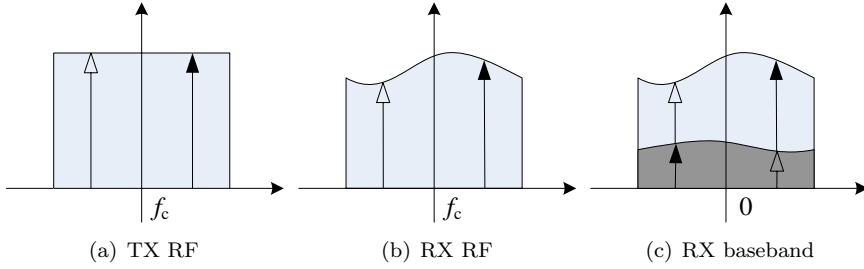


Fig. 6.24: Influence of RX IQ imbalance on the signal spectrum.

6.6.2 Influence on transmission performance

Consider the wideband transmission systems, as described in Section 4.3, which experience both the IQ imbalances at the TX and RX sides. The baseband transmit signal vector in the TD before up-conversion is given by $\mathbf{u}_t = \mathbf{F}^H \mathbf{C} \mathbf{x}$ with the size $N \times 1$, which corresponds to the FD representation $\mathbf{u} = \mathbf{C} \mathbf{x}$. In the receiver, after the removal of the cyclic prefix, the signal vector in the TD is given by

$$\mathbf{r}_t = \kappa_R \left(\text{cir}\{\mathbf{h}\} \tilde{\mathbf{u}}_t + \mathbf{v}_t \right) + (1 - \kappa_R^*) \left(\text{cir}\{\mathbf{h}^*\} \tilde{\mathbf{u}}_t^* + \mathbf{v}_t^* \right), \quad (6.74)$$

where $\tilde{\mathbf{u}}_t = [\tilde{u}_{t,0}, \dots, \tilde{u}_{t,N-1}]^T$ is the baseband equivalent transmit signal vector in the TD with the influence of the TX IQ imbalance included, and is given by

$$\tilde{\mathbf{u}}_t = \kappa_T \mathbf{u}_t + (1 - \kappa_T) \mathbf{u}_t^*. \quad (6.75)$$

The entries of $\tilde{\mathbf{u}}_t$ are the samples of $\tilde{u}(t)$ in (6.70). The N -size FFT yields $\mathbf{r} = \mathbf{F} \mathbf{r}_t$ given by

$$\mathbf{r} = \kappa_R \mathbf{H} \tilde{\mathbf{u}} + (1 - \kappa_R^*) \mathbf{H}_m^* \tilde{\mathbf{u}}_m^* + \kappa_R \mathbf{v} + (1 - \kappa_R^*) \mathbf{v}_m^*, \quad (6.76)$$

where the FD vectors $\tilde{\mathbf{u}} = \mathbf{F} \tilde{\mathbf{u}}_t$, $\mathbf{v} = \mathbf{F} \mathbf{v}_t$, and their *mirror signals* $\tilde{\mathbf{u}}_m^* = \mathbf{F} \tilde{\mathbf{u}}_t^*$ and $\tilde{\mathbf{v}}_m^* = \mathbf{F} \mathbf{v}_t^*$, respectively. The mirrored spectrum implies the relationship $\tilde{u}_{m,k} = \tilde{u}_{\text{mod}(N-k,N)}$ for the subcarrier index $0 \leq k \leq N-1$.

Note from (6.76) that each subcarrier experiences the same IQ imbalances described by κ_T and κ_R . In addition, the received signal spectrum is a linear combination of the transmit signal spectrum and its mirrored spectrum. Therefore, it is convenient for the purpose of signal processing at receiver to construct the vector composed by the k th subcarrier signal r_k and its mirror subcarrier $r_{m,k}^*$ given by

$$\begin{bmatrix} r_k \\ r_{m,k}^* \end{bmatrix} = \kappa_R \left(\begin{bmatrix} H_k & 0 \\ 0 & H_{m,k}^* \end{bmatrix} \kappa_T \begin{bmatrix} u_k \\ u_{m,k}^* \end{bmatrix} + \begin{bmatrix} v_k \\ v_{m,k}^* \end{bmatrix} \right). \quad (6.77)$$

Here $u_{m,k}^*$ is the mirror signal of u_k , the 2×2 matrices κ_T and κ_R characterize the TX and RX IQ imbalances, respectively, and are given by

$$\kappa_T = \begin{bmatrix} \kappa_T & 1 - \kappa_T \\ 1 - \kappa_T^* & \kappa_T^* \end{bmatrix}, \quad \kappa_R = \begin{bmatrix} \kappa_R & 1 - \kappa_R^* \\ 1 - \kappa_R & \kappa_R^* \end{bmatrix}. \quad (6.78)$$

It should be pointed out that the matrices κ_T and κ_R only characterize the IQ imbalances caused by imperfect mixing at TX and RX sides, respectively, and thus are frequency independent. In case of mismatch between LPFs occurring in I and Q branches, the two matrices can be still used to characterize the IQ imbalances, but vary over subcarrier index k . The expression (6.77) is insightful to understand the structural influence of the TX IQ imbalance, the multipath channel and the RX IQ imbalance, and is useful for the IQ compensation and the channel equalization at receiver, as will be discussed later.

In a frequency flat channel, i.e. $\text{cir}\{\mathbf{h}\} = \mathbf{I}$ and $\mathbf{H} = \mathbf{I}$, the IQ imbalances have different influences on the transmission schemes of OFDM, MC-CDMA and SC-FDE. For the purpose of illustration, the received symbols are depicted in Fig. 6.25 for the 16-QAM modulated schemes in a frequency flat and noiseless channel. In such a case, both the TX and RX IQ imbalances have the same influence on the signal. Here we only consider the imbalance at one side, and the amplitude imbalance is 2 dB and the phase imbalance is 10° . From the figure, we see that in SC-FDE, signal points are directly transmitted in the TD, and the I and Q branches of each

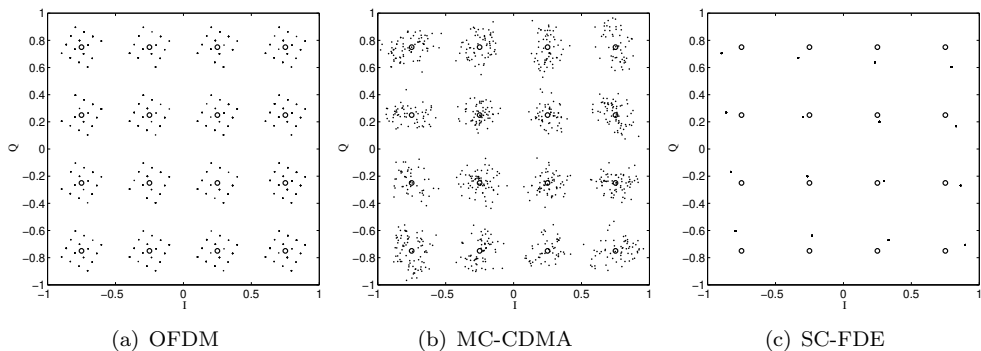


Fig. 6.25: The influence of IQ imbalance on the constellation of 16-QAM in a frequency flat and noiseless channel.

signal point experience different amplifications caused by the IQ imbalance, yielding the distortion of the constellation diagram in both the phase and the magnitude, as suggested by (6.77). In comparison, each signal point at a subcarrier in OFDM is disturbed by another signal point at its mirror subcarrier which is scaled and rotated, as suggested by (6.76). In MC-CDMA, the code-despreading operation at receiver results in additive-noise alike disturbance.

In a frequency selective channel, we have $\text{cir}\{\mathbf{h}\} \neq \mathbf{I}$ and $\mathbf{H} \neq \mathbf{I}$ and the channel selectivity occurs in between the TX and RX IQ imbalances. As a result, the TX and RX IQ imbalances are somehow twisted by the frequency selective channel, as suggested by (6.77), and the constellation diagrams can be seriously distorted for a large level of imbalances.

In case of small IQ imbalances, only the channel equalization is needed to cancel the

influence of the channel before detection. In case of large IQ influence, the compensation of the IQ imbalances is needed besides the channel equalization. Given the knowledge of the channel response H_k , and the IQ influence matrices κ_T and κ_R , three steps can be followed to apply the IQ compensation and the channel equalization based on the signal structure (6.77). First, the RX IQ imbalance is compensated by applying κ_R^{-1} on $[r_k \ r_{m,k}^*]^T$. Second, the resulting signal is equalized to cancel the channel attenuation. Third, the equalized signal is multiplied by κ_T^{-1} to compensate the TX IQ imbalance. In realistic systems, the knowledge of H_k , κ_T and κ_R can be obtained by using known training sequence before the IQ compensation and channel equalization [123, 146]. In the following, we develop the equalization algorithms with and without including the IQ compensation, concerning the IQ imbalances occurring only at the TX or RX side, respectively. These algorithms will be applied in the later simulations to investigate the separate influence of the TX and RX IQ imbalances.

TX IQ imbalance: Concerning the IQ imbalance occurring only at the TX side, we have $\kappa_R = \mathbf{0}$ and the k th subcarrier signal is given by

$$r_k = \kappa_T H_k u_k + (1 - \kappa_T) H_k u_{m,k}^* + v_k. \quad (6.79)$$

In case of no IQ compensation, the mirror signal is taken as noise and the linear MMSE weight for the equalization of r_k is given by

$$W_k = \frac{\kappa_T^* H_k^*}{(|\kappa_T|^2 + |1 - \kappa_T|^2) |H_k|^2 + \frac{N_0}{E_s}}. \quad (6.80)$$

In case that it is needed to compensate the IQ imbalance, the signal $[r_k \ r_{m,k}^*]^T$ in (6.77) can be equalized by the linear MMSE weight $[W_k \ W_{m,k}^*]^T$, where W_k is given by

$$W_k = \frac{H_k^*}{|H_k|^2 + \frac{N_0}{E_s}}. \quad (6.81)$$

Both the weights (6.80) and (6.81) are obtained by minimizing the MSE between the decision variables and desired symbols. The equalized signal is then compensated by applying κ_T^{-1} and the resulting signal at the k th subcarrier is given by

$$\begin{aligned} y_k &= \left\{ \left(|\kappa_T|^2 W_k H_k - |1 - \kappa_T|^2 W_{m,k}^* H_{m,k}^* \right) u_k \right. \\ &\quad \left. + \kappa_T^* (1 - \kappa_T) \left(W_k H_k - W_{m,k}^* H_{m,k}^* \right) u_{m,k}^* \right. \\ &\quad \left. + \kappa_T^* W_k v_k - (1 - \kappa_T) W_{m,k}^* v_{m,k}^* \right\} \cdot \frac{1}{\kappa_T + \kappa_T^* - 1} \end{aligned} \quad (6.82)$$

$$\approx u_k + \tilde{v}_k, \quad (E_s/N_0 \gg 1), \quad (6.83)$$

where the approximation is valid only in case of relatively large channel SNR, since $W_k H_k \approx 1$ for $E_s/N_0 \gg 1$, and the noise component \tilde{v}_k is given by

$$\tilde{v}_k = \frac{\kappa_T^* W_k v_k + (\kappa_T - 1) W_{m,k}^* v_{m,k}^*}{\kappa_T + \kappa_T^* - 1}. \quad (6.84)$$

As seen from (6.83) that the IQ imbalanced signal at the k th subcarrier is well compensated at a large SNR. It is also noticed that after the compensation, the remaining noise at the subcarrier is related to the noise at its mirror subcarrier, with the noise level depending on the level of the TX IQ imbalance.

RX IQ imbalance: Concerning the IQ imbalance occurring only at the RX side, we have $\kappa_T = \mathbf{0}$ and the k th subcarrier signal is given by

$$r_k = \kappa_R H_k u_k + \kappa_R v_k + (1 - \kappa_R^*) (H_{m,k}^* u_{m,k}^* + v_{m,k}^*). \quad (6.85)$$

In case of no IQ compensation, the linear MMSE weight for the equalization of r_k is given by

$$W_k = \frac{\kappa_R^* H_k^*}{(|\kappa_R|^2 + |1 - \kappa_R|^2) \left(|H_k|^2 + \frac{N_0}{E_s} \right)}, \quad (6.86)$$

which minimizes the MSE between the decision variables and the desired symbols. In case of a large RX IQ imbalance, the imbalance can be first compensated by applying κ_R^{-1} on $[r_k \ r_{m,k}^*]^T$ in (6.77). Note from (6.77) that after the compensation, the influence of the IQ imbalance is completely removed and the resulting signal can be equalized just like no IQ imbalance ever occurred. Therefore, the signal can be equalized by using the linear MMSE weight given in (4.31) and the decision variables are the same as in (4.32) and (4.34) for OFDM and code-spreading schemes, respectively.

BER performance: Simulations are conducted to study the influence of the IQ imbalances at the TX and RX sides separately on the BER performance in AWGN and Rician fading channels. Three groups of amplitude and phase imbalances are considered: $\{1 \text{ dB}, 2^\circ\}$, $\{2 \text{ dB}, 4^\circ\}$ and $\{3 \text{ dB}, 6^\circ\}$, which represent relatively low to high IQ imbalance levels. The system configuration is the same as in Section 4.4.3. The simulated BER curves for QPSK-modulated schemes are depicted in Fig. 6.26, 6.27 and 6.28 for OFDM, MC-CDMA and SC-FDE, respectively. The BER curves are depicted as a function of the average SNR per bit for the case that no IQ imbalance is experienced.

From these figures, we have the following observations and discussions:

- In frequency flat non-fading channels, i.e. in AWGN channels, the IQ imbalances have about the same influences on OFDM and SC-FDE, whereas MC-CDMA has a slight worse performance due to the AWGN-like disturbance as seen from Fig. 6.25(b). Specifically, the SNR penalties for the three groups of imbalances are about $\{0.6, 1.5, 2.6\}$ dB, due to the TX IQ imbalances, and $\{0.3, 0.6, 1.5\}$ dB, due to the RX IQ imbalances, respectively.
- In frequency selective (Rician fading) channels, the BER performance without IQ compensation is very sensitive to the RX IQ imbalance compared with the TX IQ imbalance, for relatively large imbalances (e.g. $\{2 \text{ dB}, 4^\circ\}$ and $\{3 \text{ dB}, 6^\circ\}$), since the mirroring influence is imposed not only on the transmit signal spectrum, but also on the channel spectrum. The SNR penalties caused by the RX IQ imbalances increase rapidly over the channel SNR, due to the rapidly increased power of mirror signals.

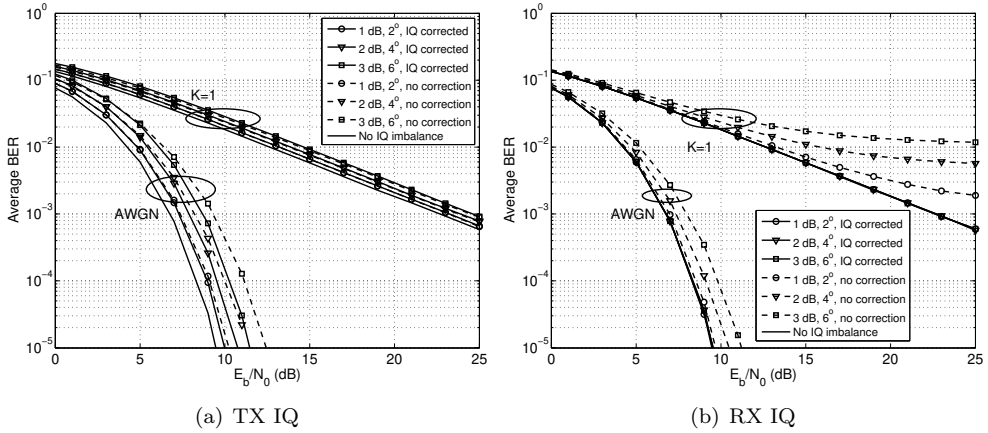


Fig. 6.26: Average BER of OFDM under the influence of TX and RX IQ imbalances.

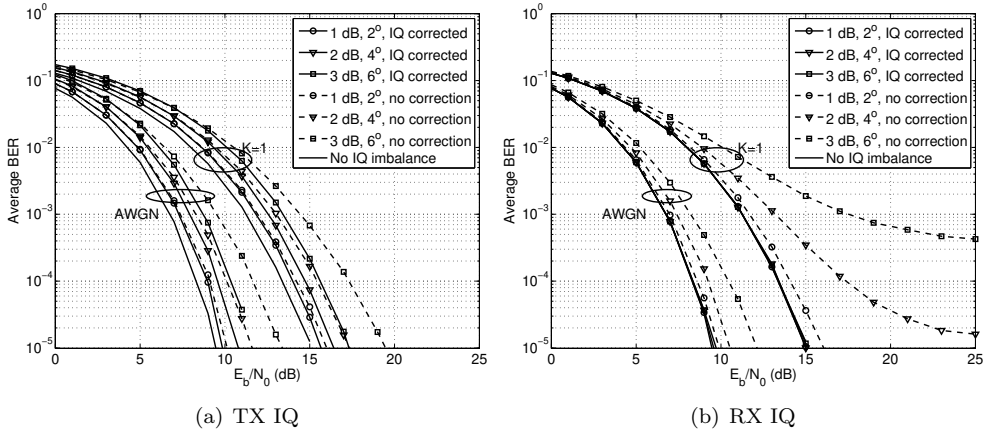


Fig. 6.27: Average BER of MC-CDMA under the influence of TX and RX IQ imbalances.

- The influences of the RX IQ imbalances can be completely compensated, as explained earlier, whereas the influences of the TX IQ imbalances are partially compensated due to the remaining influence on the noise, as seen from (6.83).
- For the TX and RX IQ imbalances with relatively small level (e.g. $\{1 \text{ dB}, 2^\circ\}$), the performance loss is minor and it is not needed to apply the IQ compensation, in both frequency flat and selective channels.
- In general, MC-CDMA and SC-FDE outperform the uncoded OFDM in frequency selective channels under the influence of IQ imbalances, due to the frequency diversity gain. It is expected that coded OFDM can achieve a comparable performance as the other two schemes.

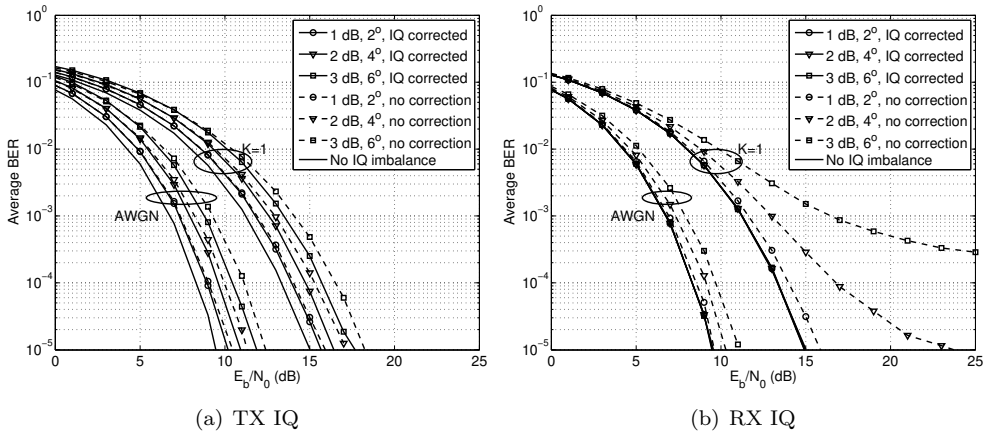


Fig. 6.28: Average BER of SC-FDE under the influence of TX and RX IQ imbalances.

The measured IQ imbalance figures for zero-IF architecture transceivers at 60 GHz have been rarely reported in literature so far. For the non-zero IF architecture, the reported imbalance figures are about $\{3 \text{ dB}, 5^\circ\}$ [150] and $\{1.1 \text{ dB}, 2.1^\circ\}$ [151], based on the CMOS 130-nm and 90-nm technologies, respectively. It is deduced from these figures that the IQ imbalances of zero-IF architecture transceivers will be much worse. Based on the results in Fig. 6.26, 6.27 and 6.28, we see that in frequency flat non-fading channels, the IQ imbalances may still be tolerable for the three transmission schemes, while in frequency selective fading channels, IQ compensation is needed to achieve a satisfactory BER performance.

6.7 Summary and conclusions

In this chapter, the individual influences of quantization, nonlinear amplification, phase noise and IQ imbalance on the transmission performance of OFDM, MC-CDMA and SC-FDE were investigated and compared in AWGN and Rician fading channels. In detail, the BER expressions of the considered schemes were derived based on the statistical modelling of the nonlinear distortions caused by the DAC, ADC and PA, and were confirmed by simulated BERs. In addition, the BER performance under the influence of phase noise and IQ imbalance is evaluated, concerning the design of 60-GHz transceiver systems, with and without compensation of the RF impairments in baseband. Moreover, three steps were proposed to apply the TX/RX IQ compensation and channel equalization in baseband. The results and conclusions obtained in this chapter are summarized as follows:

- For the considered three transmission schemes under the influence of nonlinear distortions, there is a good agreement between the simulated and analytical BER performance within the operational SNR range.

- The SNR penalties caused by nonlinear distortions in SC-FDE are generally smaller than for OFDM, due to the low PAPR level and the inherently exploited frequency diversity. MC-CDMA suffers comparable or even more SNR penalties than OFDM, since every symbol in a data block is affected in MC-CDMA, instead of part of the symbols as in OFDM. In addition, the absolute performance of both SC-FDE and MC-CDMA is better than for uncoded OFDM due to the frequency diversity gain, indicating that exploiting frequency diversity is an effective way to combat the nonlinear distortion. Therefore, it is expected that coded OFDM will have a comparable performance as SC-FDE and MC-CDMA.
- Concerning a low-power low-cost system implementation while keeping a reasonable performance, the DAC with $R = 4$ bit is a good option for OFDM and MC-CDMA, while choosing the DAC for SC-FDE depends on the order of the constellation used. In addition, the ADC with $R = 4$ and 5 bits can be chosen for the three schemes in near-AWGN channels and in near-Rayleigh fading channels, respectively.
- Under the influence of TX and RX phase noises, in AWGN channels, OFDM and SC-FDE have about the same performance, whereas MC-CDMA has a slightly worse performance. In frequency selective channels, SC-FDE and MC-CDMA have the same sensitivity to the PN, whereas OFDM is slightly more robust to the PN, in terms of SNR penalties.
- With the phase noise level $\beta NT_s < 0.001$, the resulting SNR penalties are ignorable for the three transmission schemes. For the relatively large SNR penalties in case of $\beta NT_s > 0.005$, the CPE correction gains only up to 0.5 dB and is more effective in frequency flat channels than in frequency selective channels. With a sufficiently large subcarrier spacing design, the PN influence on the system performance can be kept at a satisfactory level without applying compensation techniques in the baseband.
- In AWGN channels, both the TX and RX IQ imbalances have the same influences on OFDM and SC-FDE, whereas MC-CDMA has a slightly worse performance. In near-Rayleigh fading channels, the BER performance is significantly more sensitive to IQ imbalance at the RX side than at the TX side. The SNR penalties increase rapidly over the channel SNR.
- The influence of RX IQ imbalances can be completely compensated in the baseband, while the influence of TX IQ imbalances remains in noise samples after the compensation. In case of small IQ imbalances (e.g. $\{1 \text{ dB}, 2^\circ\}$), the performance loss is ignorable for the three schemes and thus no IQ compensation is needed. For larger imbalances, IQ compensation is needed to achieve a satisfactory performance, especially for the IQ imbalance at the RX side.

Chapter 7

Baseline design of low-cost 60-GHz radios

As addressed in the introduction, the availability of broadband spectrum in the frequency band of 60 GHz makes it suitable for multiple gigabit-per-second (Gb/s) multimedia applications. Massive commercial production of such broadband and high throughput applications calls for low-cost, low-power and low-complexity implementations of the 60-GHz wireless systems.

The channel characteristics at 60 GHz were extensively studied in Chapter 2, based on channel measurements and simulations. Afterwards, the influences of antenna pattern and multi-antenna beamforming on channel propagation were theoretically investigated in Chapter 3. Single- and multi-carrier wideband transmission schemes and baseband processing of these schemes were discussed in Chapter 4 and 5. Moreover, the influences of quantization and RF impairments on the considered transmission schemes were analyzed in Chapter 6.

In this chapter we will apply results obtained in the previous chapters to address the basic design considerations for 60-GHz low-cost radios. Also a baseline link budget analysis will be conducted to illustrate the potential and limitations of the concept.

7.1 Propagation channel and antenna effect

Compared with the traditional frequency bands of 2 GHz and 5 GHz for WLAN applications, the characteristics of the wave propagation in the frequency bands of 60 GHz for WPAN applications are different in several aspects, as addressed in Chapter 2. Here we summarize the 60-GHz channel features as follows:

- First of all, propagation losses at 60 GHz are about 22 and 30 dB higher than those at 5 and 2 GHz, respectively, according to the free space transmission

model in Section 2.2.1. Therefore, the resulting link budget becomes tight and is one of the major concerns for the overall system design. In addition, the average path loss under NLOS conditions is about 5 dB higher than under LOS conditions for the considered room environments. In particular, the low diffraction levels cause a considerable shadowing loss as high as 10 dB, implying a low radio coverage under NLOS conditions.

- Besides the severe propagation loss, high penetration losses, as high as tens of dBs through construction materials such as walls and ceilings, limits typical 60-GHz applications within the range of 10 meters in a single room, e.g. in an open office. Due to the natural isolation properties of walls and ceilings, the 60-GHz radio will not be subject to significant interference from neighboring rooms. It allows therefore high reuse of the frequency spectrum.
- For 60-GHz wave propagation in a room environment, the multipath channel dispersion, implying channel frequency selectivity, is mainly caused by wave reflections from walls, the floor, the ceiling and the surrounding furniture. Also due to the small wavelength of about 5 mm, even small objects, such as small metallic studs, will contribute to the multipath fading. Root-mean-squared (RMS) delay spreads of 60-GHz channels are in the order of 10 ns, which are only about half of those at 2 GHz. However, concerning the target data rates of multiple Gb/s for 60-GHz radios, which are many times higher than the low-frequency WLAN systems, the multipath dispersion and frequency selectivity are relatively more severe, in the sense that more significant inter-symbol interference (ISI) will deteriorate the system performance.
- Doppler spread at 60 GHz is 30 times higher than that at 2 GHz. Fortunately, for indoor applications, indoor objects move at a relatively slow speed without rapidly changing the channel characteristic.

Based on the preliminary results presented above, we address hereby the relevant issues for designing low-cost 60-GHz radios.

Because of the limited link budget and severe multipath fading, a relatively high antenna gain is preferred, especially for point-to-point applications, to achieve a reliable Gb/s transmission at 60 GHz. Owing to the short wavelength at 60 GHz, multiple antenna elements can be integrated on a small circuit board area and antenna gain can be conveniently achieved by using narrow beam antennas, in combination with adaptive beamforming techniques. Adaptive beamforming increases the flexibility of operation of the system. With such a narrow-beam configuration, RMS delay spreads can be kept amazingly low, in the order of a few nanoseconds at maximum (see Table 2.4 and Fig. 2.26 in Chapter 2). This implies that it is possible to achieve very high data rates in the order of Gb/s by applying a simple modulation scheme without doing involved channel equalization. Another benefit of using directive antenna configurations is that the Doppler effect, mainly caused by the movements of surrounding objects, is significantly suppressed by the formed narrow antenna beams and leveraged by the large bandwidth. This favorable characteristic on itself implies that the fluctuation of signal strength is low in a local area and the available signal power at

a certain position depends solely on the large-scale properties of the environment.

On the other hand, because of the poor diffraction levels at 60 GHz, the directive configurations make the system even more vulnerable to misalignment of the antenna beams or obstruction of the pointing beams.

For the former case, it was manifested in Chapter 2 and 3 that the signal quality, in terms of the signal power level and the time dispersion level, will not have a significant drop, as long as the misaligned angle is less than half the antenna beamwidth. Concerning a RF beamformer operational in a half sphere, for instance, a 3-bit phase shifter has a beam resolution of 22.5° and the maximum beam misalignment is 11.25° . To cope with the maximum misalignment, the formed beam should have a beamwidth of at least 22.5° .

For the latter case, when the beam direction is blocked by an object, for instance by a human body, the signal could be completely lost. There are several approaches or strategies to solve the problem. First, a fast response mechanism may be built in the medium access control (MAC) layer to allow an immediate switch from the suddenly disrupted beam direction to another available beam direction. For such a case, it is needed to design an MAC architecture that is very suitable for the highly directive antenna configurations. For instance, for fixed point-to-point applications, transceiver systems can “smartly” recognize and remember several operational propagation paths, e.g. of strongly reflected waves, at the beginning of the system startup, which would allow a fast switch between the nominate and the backup beam directions. Besides, some artificial reflectors on the wall or the ceiling will be certainly helpful to enhance the communication links over the backup beam directions. In the second approach, several redundant nodes, which have the ability of beam steering, can be deployed in different positions and used to relay the signal via the indirect routes in case of obstruction of the nominal communication link. For this approach, a low-cost and low-power implementation of a relay system is necessary. For the third approach, broad-beam or omnidirectional antenna elements, instead of narrow-beam elements, can be used in order to have multiple propagation paths. By such a configuration, the system becomes less vulnerable to obstructions of objects. Although the antenna gain is reduced, advanced baseband signal processing techniques are needed at receiver. For instance, the proposed ISI cancellation technique in Chapter 5 for code-spreading systems can fully explore the power contributed by multiple channel paths. The resulting SNR advantage can be up to 5 dB for Rayleigh fading channels. By this approach, the radio coverage is largely increased.

7.2 RF front-end and system architecture

The 60-GHz RF technologies have been traditionally based on III-V compound materials, such as gallium arsenide (GaAs) and indium phosphide (InP). Despite their outstanding performance, these technologies are expensive and have a limited capability for low-cost chip-scale packaging. The recent progress in semiconductor technolo-

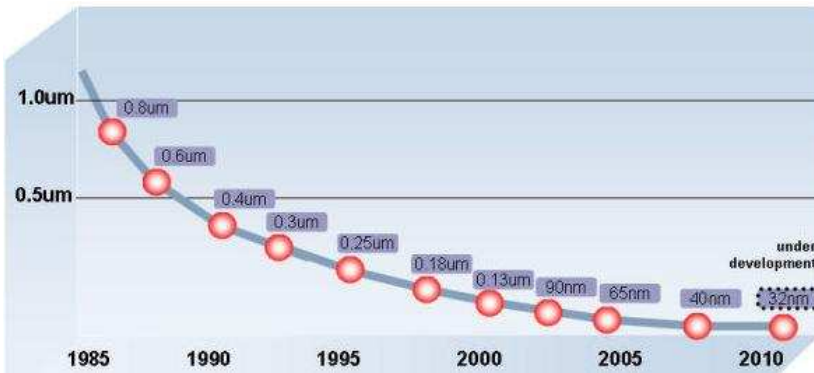


Fig. 7.1: CMOS technology roadmap (from [152]).

gies based on silicon, such as silicon germanium (SiGe) and baseline complementary metal-oxide semiconductor (CMOS) technologies, has provided new options for the low-cost 60-GHz RF front-end with considerable RF performance and remarkable integration levels [10, 11]. For instance, SiGe technology is able to provide a maximum frequency of operation (f_{\max}) up to hundreds of GHz and provides sufficient RF performance. The RF performance of CMOS is worse but increases rapidly due to the enormous world-wide effort to scale to lower gate-lengths (see the roadmap of CMOS technologies in Fig. 7.1), implying a higher f_{\max} . The speed of analog CMOS circuits increases by roughly one order of magnitude every ten years. With its rapid performance improvement due to continuous scaling, CMOS is becoming the future technology of choice to address the low-cost millimeter-wave market.

Besides the RF process technologies, antennas and RF architecture are also crucial issues for a low-cost RF front-end of 60-GHz radios.

7.2.1 Antennas and adaptive beamforming

As mentioned earlier, antenna arrays can be used to achieve a sufficient link budget, by means of adaptive beamforming, at both transmitter (TX) and receiver (RX) sides. Because the wavelengths are so short, it is possible to implement many antennas on a small area of printed circuit board (PCB). For the purpose of low-cost applications, such an antenna array should satisfy the following requirements: low fabrication cost, light weight, easy to integrate with RF front-end circuitry, high efficiency, sufficient bandwidth and sufficient antenna directivity. With these requirements in mind, an obvious option is to use microstrip patch antennas, which are inherently low cost, light weight and low volume. Microstrip patch antennas can be realized based on PCB technology. Their design is essentially a joint optimization of bandwidth and power efficiency, which may be achieved by choosing appropriate materials and structures. A good example of the design is the balanced-fed aperture-coupled patch antenna proposed in [153], which has a good performance in both bandwidth and radiation

efficiency. This design results in a radiation efficiency better than 0.8 and a pattern directivity better than 12 dBi within a scan angle of 45° . Yet, it is still a design challenge to have a good match and integration between the antennas and RF front-end circuits, including power amplifier (PA) and low noise amplifier (LNA), such that the reflection loss, caused by the balanced antenna feed, is as less as possible. Instead of a dedicated RF front-end section close to each antenna element, all the front-end electronics can be integrated on one single chip, which minimizes the total chip area, as well as differentiation in antenna branch properties [10].

With multiple antennas configured, narrowband beamforming¹ can be adaptively conducted to steer signal transmission in a particular direction. One solution is to do analog beamforming in the RF stage (also referred to as RF beamforming), i.e., after frequency up-conversion and before frequency down-conversion at TX and RX sides, respectively. The control signals for the beamforming, including variable gains and phase shifts, are calculated in the baseband and fed back to the RF stage.

It is obvious that the RF beamforming only requires one mixer and one digital-to-analog (D/A) or analog-to-digital (A/D) converter (DAC or ADC) for each I/Q branch. This is quite advantageous over digital beamforming, in which a number of the conversion devices are necessary and a significant amount of data throughput introduces a heavy burden to the baseband processor. Therefore, RF beamforming is a particularly effective way to reduce the power consumptions and fabrication costs of the whole system, since DAC/ADC and baseband processor are among the most power consuming units in a transceiver [9]. Another advantage of applying RF beamforming is that analog signals have a wider dynamic range, compared with applying digital beamforming in the baseband. This is because digital signals suffer from quantization errors, though more elaborate algorithms can be used in digital beamforming.

7.2.2 RF architecture and impairments

Direct-conversion architecture (also referred to as zero-IF or homodyne architecture) is a promising solution for the low-cost and low-power implementation of 60-GHz radios, in comparison with conventional heterodyne architectures [16, 17]. It does not require image rejection filtering, as there is no image frequency at all, but only low-pass filters (LPF) are needed. Therefore, this allows a great simplicity of the RF architecture. Also, the absence of IF filters makes it very suitable for multi-band and multi-standard operation.

Combination of a direct-conversion architecture and RF beamforming leads to a further simplification of the RF front-end. The basic architecture of such a RF transceiver is illustrated in Fig. 7.2. In this architecture, one PA and one LNA are applied per TX and RX antenna branch, respectively, and can provide sufficiently

¹From the point view of RF beamforming, the 60-GHz signal is narrowband in case the propagation time delay across an antenna array is considerably smaller than the inverse bandwidth of the signal. For instance, the time delay along a three wavelength distance is about $\tau = 5 \times 10^{-11}$ second, which is much smaller than $1/B = 5 \times 10^{-10}$ second for the bandwidth of $B = 2$ GHz.

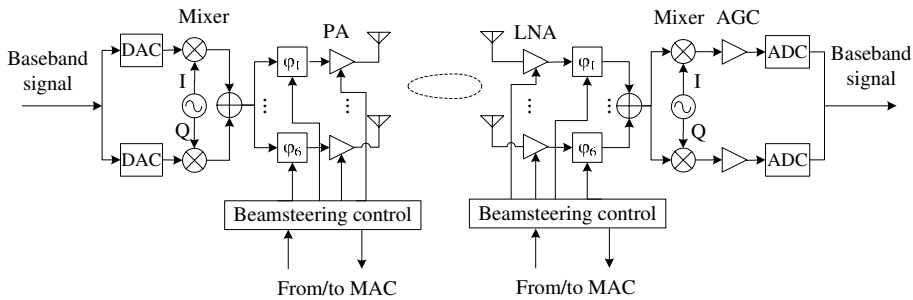


Fig. 7.2: A direct conversion transceiver architecture in combination with analog beamforming for 6 antenna elements at both TX and RX sides.

high transmit power and low noise figure. Specifically, with n parallel PAs of equal output power, the transmit power can be as high as $10 \log_{10} n$ dB, compared to one individual PA. Similarly with n parallel LNAs, about $10 \log_{10} n$ dB lower noise figure can be achieved compared with one such LNA alone. In addition, only one pair of DACs and one pair of ADCs are needed in this transceiver structure. Automatic gain control is needed at receiver before ADCs to adjust the signal range for the purpose of optimal quantization.

Adaptive beamforming can be carried out by combining controllable phase shifters and variable gain amplifiers. Phase shifters can steer the beam at a particular direction and variable-gain PAs and LNAs can adapt the antenna pattern better to the angular profiles of the radio waves at antenna front-ends. The application of variable gain amplifiers can be useful in NLOS situations, where dominant power contributions come from various directions.

Implementation of RF front-ends by CMOS technologies is particularly attractive for its potential of integration with analog devices and baseband digital signal processing (DSP) functions, enabling true systems-on-chip [12]. As CMOS circuitry continues to scale down, the analog and RF blocks suffer from large variation over process, voltage and temperature. The resulting “dirty effect” such as nonlinear distortion, phase noise and I-Q imbalance gives rise to a serious performance loss, as presented in Chapter 6. As suggested by the results presented in the chapter, the severe signal distortion and impairments caused by both the dirty RF and the limited bit resolution of DAC and ADC can be largely absorbed by the baseband section, e.g. by applying appropriate baseband modulation schemes and digital compensation techniques.

For a direct-conversion architecture, the main impairments caused by RF front-ends are phase noise (PN) and IQ imbalance, which are particularly more serious for the high frequency radios at 60 GHz, as studied in Section 6.5 and 6.6. As suggested by the results presented, both the TX PN and the RX PN have about the same influence on the single- and multi-carrier transmission systems. The influence of phase noise can be largely absorbed by properly designing the system, such as having a large subcarrier spacing, in combination with proper semiconductor processes. In

case of a relatively high phase noise level, the resulting common phase error can be compensated at receiver to improve the performance, but the compensation is more effective for narrow-beam channels than omnidirectional channels. As for IQ imbalance, the system performance is more sensitive to the RX IQ imbalance than the TX IQ imbalance in case of omnidirectional channels, and vice versa in case of highly directive channels. For the direct-conversion architecture, digital compensation is generally needed at receiver to achieve a satisfactory system performance, especially under omnidirectional channel conditions.

Other imperfections caused by circuit components include the quantization noises due to DAC and ADC devices and the nonlinear amplification by PA, which were studied in Chapter 6 (Section 6.2-6.4). As addressed in this chapter, DAC, ADC and PA cause scaling and distortion of the transmit signal. The results presented in the chapter suggest that to make a tradeoff between the performance and implementation cost, the resolutions of four to five bits are good options for the DAC and ADC devices for the considered wideband transmission schemes. As for the RF nonlinearities, it is shown in Section 6.4 that a certain backoff of the input power level is necessary to reduce the nonlinearity influence. Another effective way of combating the RF nonlinearities is to reduce the peak-to-average power ratio (PAPR) level of the transmit signal, either by appropriately choosing the transmission scheme (e.g. by using single carrier schemes) or by predistorting the transmit signal, which are beneficial for reducing the quantization noise as well. The PAPR level of the received signal can be also reduced by using directive antenna configurations. In addition, baseband compensation techniques can be used at receiver to cancel the nonlinearity influence [123, 124].

7.2.3 Channelization

Channelization of the available spectrum in the frequency band of 60 GHz would allow multiple devices simultaneously operating over a short range without causing interference among them. With multiple channels available, each device occupies one of these channels with a limited bandwidth centered at certain frequency. According to the technical requirements of IEEE Task Group 3c, at least one mandatory mode with a net bit rate of 2 Gb/s or more is required [4]. If four channels are planned in the available frequency band that ranges from 57.05 to 64 GHz, that is, the 60-GHz band as allocated in the United States and Canada, the required spectral efficiency would be $2 \text{ Gb/s} / (6.95/4 \text{ GHz}) = 1.151 \text{ b/s/Hz}$, whereas the accommodation of three channels would reduce the spectral efficiency requirement to 0.863 b/s/Hz . With a four-channel system, instead of a three-channel system, the problem of co-channel interference in a multi-user environment is alleviated and it becomes easier to route the 60-GHz channels via different transceivers to improve coverage.

For the four-channel channelization scheme, the center frequencies of individual channels can be chosen appropriately for the design of a frequency synthesizer, which generates clock and oscillator signals needed for up and down conversion in RF front-ends. A good example is the simple synthesizer architecture proposed in [4], in which all of

the center frequencies are generated by using a single phase locked loop (PLL) and the channel spacing is 1.705 GHz. In the next section, baseband modulation schemes will be designed for the receiver bandwidth of 1.705 GHz.

7.3 Transmission schemes and system design

Linear modulations in combination with the wideband transmission schemes of OFDM, SC-FDE and MC-CDMA, as studied in Chapter 4, have the advantages of high spectral efficiency and high robustness against multipath channel dispersion, in comparison with continuous phase modulations. In these wideband schemes, low-complexity channel equalization techniques can be conveniently used at receiver, which makes them particularly suitable for low-cost 60-GHz radios. In this section, we highlight the system design based on OFDM and SC-FDE, according to the four-channel channelization scheme proposed in Section 7.2.3, based on the results obtained in Chapter 4, 5 and 6. Both MC-CDMA and SC-FDE belong to the same class of code-spreading schemes and have the same performance in linear channels. But SC-FDE is a more favorable option compared with MC-CDMA, for its outstanding performance under the influence of RF nonlinearities. Therefore, MC-CDMA will not be considered here.

First we consider the design of an OFDM system. An important parameter when designing an OFDM system is the FFT size N . The FFT block takes about 20 percent of the RX digital baseband complexity, in terms of the number of logic gates, and the block size must be as small as possible [155,156]. Table 7.1 shows the trade-off of three options for the four-channel system that supports 2 Gb/s net data rate over one such RF channel, with the determined channel spacing of 1.705 GHz. In all options, all subcarriers are modulated using quadrature phase-shift keying (QPSK).

For option I, the FFT size $N = 512$, whereas the guard time T_g amounts to one-fourth of the FFT integration time T_u . The problem with this option is that the required number of data subcarriers is 501 so that there are only 11 subcarriers left for pilot transmission, which is an insufficient number for adequate channel estimation and correction. This problem can be solved by decreasing the guard interval to $T_u/8$ to improve the efficiency, which yields the option II. However, with this option, another problem arises: the guard time becomes too short. The guard time should be at least two to four times of the maximum encountered RMS delay spread to reduce inter-block interference (IBI) to an acceptable level. With the use of directional antennas under NLOS conditions, RMS delay spread values can reach values of 20 ns [41]. The only way to achieve a sufficiently large guard interval, as well as a sufficient number of subcarriers is to increase the FFT size to 1024, which is represented by option III. The guard time then becomes 75 ns, which implies a good robustness against channel dispersion, whereas one pilot can be accommodated per 12 subcarriers, leaving 47 subcarriers available for different purposes.

System design of SC-FDE follows the same procedure as above for OFDM. The block size and guard interval in Table 7.1 are also applicable to SC-FDE. SC-FDE has

Table 7.1: Design options for a coded OFDM with a net data rate 2 Gb/s.

	Option I	Option II	Option III
Number of RF channels	4	4	4
Channel spacing B	1.705 GHz	1.705 GHz	1.705 GHz
FFT size N	512	512	1024
Subcarrier spacing $\Delta f = \frac{B}{N}$	3.330 MHz	3.330 MHz	1.665 MHz
FFT integration time $T_u = \frac{1}{\Delta f}$	300.3 ns	300.3 ns	600.6 ns
Guard time $T_g = \frac{T_u}{4}$ or $\frac{T_u}{8}$	$\frac{T_u}{4} = 75.075$ ns	$\frac{T_u}{8} = 37.537$ ns	$\frac{T_u}{8} = 75.075$ ns
OFDM symbol time $T_{of} = T_g + T_u$	375.375 ns	337.837 ns	675.675 ns
Modulation format	QPSK	QPSK	QPSK
Gross subcarrier data rate $r_{b, \text{gross}} = \frac{2}{T_{of}}$	5.328 Mb/s	5.920 Mb/s	2.960 Mb/s
Code rate r_c	3/4	3/4	3/4
Net subcarrier data rate $r_{b, \text{net}} = r_c \cdot r_{b, \text{gross}}$	3.996 Mb/s	4.440 Mb/s	2.220 Mb/s
Required number of data carriers (2 Gb/ $r_{b, \text{net}}$)	501	451	901
Number of the rest carriers for other purpose	11	61	123

about the same implementation complexity as OFDM, though the complexity is more concentrated at receiver side. Both OFDM and SC-FDE have similar spectral efficiencies [136]. However, SC-FDE is essentially different from OFDM, in that frequency diversity is exploited in SC-FDE by spreading user symbols across the whole transmission spectrum. In contrast, user symbols in OFDM are directly carried by subchannels and the performance is sensitive to deep fades in frequency. In near-flat fading channels, OFDM and SC-FDE have similar uncoded system performance (see Fig. fig:theBERLinear). But in multipath fading channels, especially in NLOS channel conditions, SC-FDE is resistant to multipath dispersion and probably only light coding is needed, while the performance of OFDM heavily relies on error correction codes (ECC). Adaptive modulations may be also applied in OFDM to reduce performance degradation and increase the data throughput, but a feedback channel is usually needed to provide channel state information (CSI) before transmission [157]. In addition, combination of SC-FDE and the proposed residual ISI cancellation scheme in Chapter 5 can further improve the performance and reduce the required SNR by several dBs in multipath fading channels.

Because of the much lower PAPR, in combination with the inherent frequency diversity gain, SC-FDE is more robust to the RF nonlinearities compared with OFDM. With respect to phase noise and IQ imbalance, the resulting performance loss is quite dependent on the channel conditions. In near-AWGN channels, e.g. in channels with narrow-beam antenna configurations, OFDM and SC-FDE have about the same performance loss caused by the RF impairments, in terms of SNR penalties. In near-Rayleigh fading channels, e.g. in channels with omnidirectional configurations, OFDM is relatively more robust to the phase noise and TX IQ imbalance, since part of symbols in OFDM are not affected at all by the RF impairments in terms of BER performance, by taking advantage of the channel frequency selectivity. Both OFDM and SC-FDE are very sensitive to the RX IQ imbalance. With the subcarrier spacing as large as 1.7 MHz, the phase noise problem becomes insignificant for both schemes, as confirmed in Section 6.5. As for IQ imbalance, IQ compensation is generally needed at receiver, especially under NLOS conditions.

7.4 Link budget design

Examining the link budget requirement for a radio system boils down to determine the minimum required signal strength for demodulation, i.e. the receiver sensitivity, which is given by

$$P_{\text{RX}} = C/N + P_n \text{ (dB)}. \quad (7.1)$$

Here $C/N = E_s/N_0$ stands for the required SNR per symbol for demodulation and the thermal noise level P_n within the receiver bandwidth B is given by $P_n = KT_0BF$ in watt or

$$P_{n[\text{dBm}]} = -174.0_{[\text{dBm}]} + 10 \log_{10} B + F_{[\text{dB}]} \quad (7.2)$$

in dBm, where $K = 1.38 \cdot 10^{-23}$ J/K is the Boltzmann's constant, $T_0 = 290$ K is the standard Kelvin temperature (equivalent to 17° Celsius), and F is the noise figure of the receiver. Typical values for F range from 5 to 10 dB for commercial receivers. By knowing the receiver sensitivity and the received power at a distance d , one can examine the link margin figure

$$M = P_{\text{R}}(d) - P_{\text{RX}}, \quad (7.3)$$

to see whether the transmitted signal can be recovered properly, where $P_{\text{R}}(d)$ is the actual received signal level. For the separation distance d between transmitter and receiver, the wideband received power level at antenna front-end is related to the path loss, $PL(d)$, at a distance d and given by

$$P_{\text{R}}(d)_{[\text{dBm}]} = P_{\text{T}} + G_{\text{T}} + G_{\text{T, array}} + G_{\text{R}} + G_{\text{R, array}} - IL_{\text{T}} - IL_{\text{R}} - PL(d), \quad (7.4)$$

Here P_{T} is the transmit power of each antenna element, G_{T} , $G_{\text{T, array}}$, G_{R} and $G_{\text{R, array}}$ represent antenna element gain and array gain at the TX and RX sides, respectively. In addition, IL_{T} and IL_{R} are the interconnect losses between PA/LNA and TX/RX antenna elements, respectively.

Here we give some examples for the link budget calculations of uncoded OFDM and SC-FDE, under 60-GHz LOS and NLOS channel conditions. The receiver bandwidth is set to be $B = 1.705$ GHz and the noise figure $F = 8$ dB. The considered modulation format is QPSK. For the target BER at 1×10^{-3} , the required SNRs for detection after linear channel equalization are $C/N = 12.5, 25.6$ for OFDM and 10.6, 14.2 for SC-FDE, in Rician fading channels with Rician K -factors $K = 10$ and 1, respectively, without RF impairments (see from Table 4.1). Here the channels with Rician factors $K = 10$ and 1 are typical values under LOS and NLOS conditions, respectively, as seen in Table 2.4.

In all the cases, it is assumed that each transmit branch comprises a power amplifier having an output power $P_{\text{T}} = 10$ dBm, which is a peak power level at the input of one antenna element allowed in many countries [4, 6]. The interconnect losses IL_{T} and IL_{R} amount to 2 dB [10]. Furthermore, the use of the six-element antenna array,

Table 7.2: Some 60 GHz link budget examples for uncoded demodulations (in dB values).

Parameters	OFDM		SC-FDE	
	LOS	NLOS	LOS	NLOS
P_T (dBm)	10.0	10.0	10.0	10.0
IL_T (dB)	2.0	2.0	2.0	2.0
G_T (dBi)	6.0	6.0	6.0	6.0
$G_{T,array}$ (dB)	15.6	15.6	15.6	15.6
PL at 10 m (dB)	88.0	93.0	88.0	93.0
G_R (dBi)	6.0	6.0	6.0	6.0
$G_{R,array}$ (dB)	7.8	7.8	7.8	7.8
IL_R (dB)	2.0	2.0	2.0	2.0
C/N (dB) for QPSK	12.5	25.6	10.6	14.2
P_n (dBm)	-73.7	-73.7	-73.7	-73.7
P_R (dBm)	-46.6	-51.6	-46.6	-51.6
$P_{RX} = C/N + P_n$ (dBm)	-61.2	-48.2	-63.1	-59.5
$M = P_R - P_{RX}$ (dB)	14.6	-3.5	16.5	7.9

proposed in [153], at both ends of the link is assumed and each element has a gain $G_T = G_R = 6$ dBi. The transmit array gain $G_{T,array}$ is then $20 \log_{10} 6$ dB, due to the coherent addition of the signals at each receive branch. The receive array gain equals $G_{R,array} = 10 \log_{10} 6$ due to the coherent addition of signals and incoherent addition of noise contributions of the individual receive branches. Note that here we have assumed that the six antenna branches have exactly the same amplification gains by the PAs and LNAs. In doing so, the maximum array gains are achieved at both the transmitter and receiver side.

The antenna separation distance is assumed to be 10 meters in all the cases. Because of the narrow-beam configuration, the path loss for LOS channel conditions is about the same as that in free space and equals 88 dB. For the NLOS channel conditions, the path loss $PL = 93$ dB is considered, assuming 5 dB shadow loss, according to the measured results in Section 2.3.2.

Table 7.2 lists the link budget calculations. The resulting link margin can be used to obviate polarization mismatch, antenna misalignment, channel interference, additional implementation losses and RF impairments. According to the calculations in this table, both uncoded OFDM and SC-FDE have about 15 dB link margin under LOS channel conditions, and even higher constellations could be feasible. Such a high link margin can be used to obviate channel fading, polarization mismatch, antenna misalignment, channel interference and additional implementation losses caused by RF impairments and nonlinearities. Under NLOS channel conditions, SC-FDE still has 8 dB link margin, in contrast to the insufficient margin in uncoded OFDM. Furthermore, if the proposed ISI cancellation technique in Chapter 5 is applied in SC-FDE, the link margin can be further improved.

Next, we examine the sufficiency of the above link margins for combating the SNR

Table 7.3: SNR penalties (in dB) due to quantization and RF imperfections. DAC/ADC: 5 bit; PA backoff: 5 dB; PN level: -86 dBc/Hz@1 MHz; IQ mismatch: 3 dB, 6° .

Quantization and RF imperfections	OFDM		SC-FDE	
	LOS	NLOS	LOS	NLOS
D/A conversion (Table 6.2)	0.2	0.2	0.0	0.0
A/D conversion (Table 6.2)	0.3	> 7.0	0.2	0.4
Nonlinear PA (Table 6.3)	2.3	2.1	1.2	1.2
TX PN (Fig. 6.20, 6.22, $\beta NT_s = 0.005$)	0.5	1.0	0.5	1.0
RX PN (Fig. 6.20, 6.22, $\beta NT_s = 0.005$)	0.5	1.0	0.5	1.0
TX IQ mismatch (Fig. 6.26, 6.28)	2.5	2.0	2.5	2.8
RX IQ mismatch, with ideal compensation	0.0	0.0	0.0	0.0
Total SNR penalty (dB)	6.3	> 13.3	4.9	6.4

penalties caused by quantization and RF imperfections. The following scenario is considered: the DAC and ADC devices have a 5 bit resolution; the TX power amplifier input backoff is 5 dB; the phase noise level is -86 dBc/Hz@1 MHz; the TX and RX IQ mismatches are (3 dB, 6°). Here we assume that RX IQ mismatch is perfectly compensated. The resulting SNR penalties, as obtained in Chapter 6, are listed in Table 7.3. By comparing the link margins in Table 7.2 with the total SNR penalties in Table 7.3, it is confirmed that SC-FDE has sufficient link margins to combat the imperfections in both LOS and NLOS channel conditions, while uncoded OFDM has a sufficient link margin only in LOS condition.

7.5 Conclusions

The baseline design of low-cost 60-GHz radios was presented in this chapter, based on general considerations on channel characteristic, antenna effects, RF front-end and baseband modulations. It is shown that with the considered design choices, a net data rate of 2 Gb/s, according to the IEEE 802.15.3c requirement, can be achieved with an antenna separation distance of 10 meters. This is possible by using narrow-beam antennas in combination with adaptive beamforming at both ends of the link. In addition, combination of direct conversion and RF beamforming allows a simple and low-cost implementation of RF front-end. A sufficiently high transmit power, as well as a sufficiently low effective noise figure is obtained by applying one PA and one LNA per antenna element, respectively. Moreover, modulation schemes for 60-GHz radios were also discussed and two main candidates, OFDM and SC-FDE, were compared. Link-budget calculations show that both OFDM and SC-FDE are feasible schemes under LOS conditions. SC-FDE is the more preferred scheme, because it can provide sufficient link budget under NLOS conditions as well, without requiring a sophisticated coding scheme, which is a significant complexity advantage for multi-Gb/s systems. Moreover, applying the ISI cancellation technique in SC-FDE, as proposed in Chapter 5, can further improve the link margin.

Conclusions and future work

8.1 Summary and conclusions

The use of the license-free 60-GHz frequency band will allow multi-Gb/s data transmission over short distances. The work presented in this thesis is aimed at contributing to the development of low-cost multi-Gb/s radio systems at 60 GHz, as regards channel characteristics, antenna effect, RF impairment and baseband modulation.

Chapter 2 addressed the channel characteristics of 60-GHz radios based on channel sounding and ray-tracing simulations. For the channel sounding, wideband frequency responses were measured by channel sounding equipment and used to derive channel parameters and empirical models. A 3D ray tracing simulator was first verified by comparing the measured and simulated results, and then used for extensive channel simulations. Experimental characterization of the 60-GHz channels reveals that shadowing loss is up to 5.3 dB higher than for the 2-GHz channels in the considered environment. In addition, time domain dispersion of the channels at 60 GHz is about half of that at 2 GHz, but is still significant for the multi-Gb/s transmission. Narrow-beam antenna configurations can be used to boost the received power by tens of dBs, compared with omnidirectional ones. Meanwhile, they significantly reduce the channel time dispersion to be in the order of nanoseconds. Measurement results also indicate that antenna beam pointing errors do not tend to seriously reduce the channel quality, as long as the pointing errors are smaller than half the beamwidth. Ray tracing simulations for various antenna polarization schemes reveal that circularly-polarized schemes result in 2 to 6 dB losses of signal strength and give a limited improvement on reducing both large- and small-scale fading of wideband channels, compared with a linearly-polarized scheme.

In Chapter 3, the influence of antenna directivity on radio transmission, in terms of the change of channel SNR, Rician K -factor and RMS delay spread, was analytically

formulated and studied for multipath Rician channel environments. The antenna beam pointing errors were also considered in the formulation. The results presented in this chapter are suitable not only for the frequency band of 60 GHz, but also for the other frequency bands. By way of illustration, a cosine-shaped hypothetical antenna was used for each antenna element. It was found that by using a directional antenna at one side of the radio link, the Rician K -factor and SNR gain can range up to 16 dB and the RMS delay spread reduction may be more than 80%. If multi-antenna beamformers are used at both sides of the radio link, the Rician K -factor gain, SNR gain and RMS delay spread reduction will be even higher. In addition, for conventional beamforming, the 3-dB scan range can be approximated by the antenna element beamwidth. In case of misalignment between the antenna main lobe and the LOS wave, the optimal antenna beamwidth is about twice the maximum misalignment angle, otherwise the narrower beamwidth will result in a significant drop of channel quality, which confirms the measured results in Chapter 2.

Chapter 4 treated the optimal linear equalization and detection performance of wide-band transmission schemes. The considered schemes include OFDM, SC-FDE and MC-CDMA, which are potential schemes for 60-GHz radios. Analytical BER expressions were derived under Rician fading channel conditions and have a good agreement with the simulated BER. The comparison of the three transmission systems shows that both SC-FDE and MC-CDMA have the same BER performance and significantly outperform uncoded OFDM in frequency selective channels, due to the inherent frequency diversity gain. Moreover, simulation results reveal that the frequency synchronization, symbol timing and channel estimation can be performed such that their influence on BER performance can be kept at an ignorable level.

As observed in Chapter 4, residual inter-symbol interference (ISI) remains in the code-spreading systems of SC-FDE and MC-CDMA after the linear MMSE equalization, and results in a channel capacity loss. To combat the residual ISI and further improve the performance, a cancellation scheme was proposed in Chapter 5. In this scheme, a feedforward filter and an interference canceller were designed to minimize the mean square error at the main detector input. The feedforward filter equalizes the majority of the ISI and the canceller estimates and cancels the residual ISI with the aid of tentative decisions. The explicit derivation of the filter coefficients allows a fast configuration of the cancellation system. Both theoretical analysis and simulation showed that the proposed scheme significantly outperforms the existing DFE and reduced-order cancellation schemes, and is eventually lower bounded by the matched filter bound, which indicates that the channel capacity loss caused by the residual ISI is avoided. Moreover, since both the feedforward filter and the interference canceller can be implemented in the frequency domain, the computational complexity of the scheme is significantly lower than the existing cancellation schemes.

In Chapter 6, the influences of DAC and ADC, RF nonlinearities, phase noise and IQ imbalances on OFDM, SC-FDE and MC-CDMA were studied in Rician fading channel conditions. BER expressions of the considered systems were derived, reflecting the influence of the nonlinear distortions caused by DAC, ADC and power amplifier (PA), based on the statistical modelling of nonlinear devices. The analytical BER is in good

agreement with the simulated BER. In particular, the joint influence of quantization and clipping caused by the DAC/ADC was studied. It was concluded from the studies that for the same resolution, the ADC devices cause more severe performance loss than the DAC devices. Comparison shows that both SC-FDE and MC-CDMA outperform uncoded OFDM under the influence of nonlinear distortions, due to the inherent frequency diversity gain. However, MC-CDMA performs worse than SC-FDE due to the high PAPR values. Therefore, SC-FDE is the most favorable scheme under the influence of nonlinear distortions. Concerning the low-power and low-complexity implementation of 60-GHz radios in near-AWGN channel conditions, e.g. in highly directive channel conditions, the resolution of $R = 4$ bit is a good option for the DAC and ADC devices as a compromise between cost and performance. In frequency selective channels, e.g. in omnidirectional channels, a higher bit resolution is needed.

In addition to the influences of nonlinear distortions, Chapter 6 also treated the influences of phase noise (PN) and IQ imbalances occurring in the RF front-end at both the transmitter (TX) and receiver (RX) sides. Simulations were conducted to study the BER performance of OFDM, SC-FDE and MC-CDMA under various channel conditions, with and without using digital compensation techniques at receiver. Both TX PN and RX PN have about the same influence on the BER performance. It was concluded that with the subcarrier spacing properly designed together with properly chosen semiconductor processes, the phase noises causes ignorable performance loss for the considered transmission schemes, without applying compensation algorithms in the baseband. As for IQ imbalances, the amplitude and phase mismatches at the RX side cause a significantly large performance loss due to the image signals, compared with the mismatches at the TX side, but can be well compensated in baseband. For a direct-conversion RF architecture, the mismatches need to be compensated at receiver to achieve a satisfactory performance.

Finally in Chapter 7, a baseline design of low-cost 60-GHz radios was presented, based on overall considerations on the wave propagation, antenna effect, baseband modulations and RF impairments. It was shown that by using narrow beam antennas in combination with adaptive beamforming at both ends of the link, a data rate of 2 Gb/s can be achieved with an antenna separation distance of 10 meters. Combination of direct conversion and RF beamforming allows a simple and low-cost implementation of RF front-end. Link-budget calculations show that both OFDM and SC-FDE are feasible schemes under LOS conditions and link margins are sufficient to offset the influences caused by the imperfections occurring in the transmission chain of the transmitter, radio channel and receiver. In particular, SC-FDE is a more favorable scheme for its inherent frequency diversity gain and high tolerance to RF nonlinearities, which makes the 60-GHz radios operational under NLOS conditions as well. Moreover, applying the residual ISI cancellation technique for SC-FDE, as proposed in Chapter 5, can either improve the service quality or further increase the data rate.

8.2 Contributions of this thesis

This thesis contributes to the low-cost system design of 60-GHz digital radios and mainly focuses on channel characterization and baseband optimization. The main contributions of this thesis cover the following individual aspects:

1. Channel modelling and antenna effect
 - (a) Characteristics of narrow-beam and omnidirectional 60-GHz radio channels in the considered environments;
 - (b) Comparison of channel properties in the frequency bands of 2 and 60 GHz;
 - (c) Large- and small-scale fading properties of wideband channels configured with linearly- and circularly-polarized antennas;
 - (d) Multipath distribution in time and spatial domains;
 - (e) Theoretical analysis of the influence of antenna directivity on radio transmission;
 - (f) Experimental and analytical studies on the influence of beam pointing errors on radio transmission.
2. Baseband optimization
 - (a) BER expressions of OFDM, MC-CDMA and SC-FDE under Rician fading channel conditions, with and without taking into account channel nonlinearities caused by quantization processes and nonlinear amplification;
 - (b) Influence of synchronization and channel estimation on single- and multi-carrier transmission;
 - (c) Comprehensive comparisons of single- and multi-carrier transmission schemes in linear channel conditions or under the influences of quantization and RF imperfections, supported by both theoretical and simulation results;
 - (d) Development of a low-complexity and high-performance ISI cancellation technique, for a class of code-spreading systems, with the feedforward filter and the interference canceller fully realized in the frequency domain.
3. Baseline system design
 - (a) Link budget design to examine the feasibility of low-cost Gb/s 60-GHz radios in LOS and NLOS channel conditions under the influence of RF imperfections.

8.3 Future work

This thesis covers wide aspects of low-cost 60-GHz radios as regards channel characteristics, antenna effects, RF impairments and baseband processing. However, there

are still some issues that are not addressed and need to be studied in the future. In the following, we highlight these issues and point out possible research directions.

- Several assumptions were made in Section 3.6 to simplify the analytical analysis on the influence of directional radiation patterns on radio transmission. These assumptions are: the joint channel spectrum $P_S(\tau, \Omega_T, \Omega_R)$ is separable and decomposed as the product of delay spectrum and angular spectrum; the signal power is uniformly distributed in angular domain; the delay spectrum is exponentially decaying. A further study is to evaluate the difference between the analytical results and those obtained based on practical channels (i.e. directly based on the joint channel spectrum), and the influences of these assumptions on the difference.
- Throughout Chapter 4 - 6, the baseband modulation and algorithms concern only transmission schemes configured with single antenna elements at TX and RX sides. For 60-GHz radio applications, further studies on baseband optimization can be performed in combination with multi-antenna adaptive beamforming at both TX and RX sides.
- Throughout the thesis, error correction codes were not considered in single- and multi-carrier transmission schemes, except in Chapter 4, where convolutional codes were applied to investigate the performance under linear channel conditions. It is useful to study also the coded performance under the influences of quantization and RF impairments. In addition, concerning the gigabit throughput in 60-GHz radio systems, low-complexity and low-latency coding and decoding methods should be considered.
- The ISI cancellation technique proposed in Chapter 5 has the advantage of both low complexity and good performance, which makes the technique particularly suitable for 60-GHz applications. Although the technique was applied only under linear channel conditions, it could be also effective to combat the influence of nonlinear distortions, such as quantization and RF impairments, which need to be further studied.
- The influences of nonlinear distortions caused by DAC, ADC and PA were investigated in Chapter 6. As a next step, mitigation approaches should be applied to combat the nonlinear distortions.
- The influence of ideal quantization processes on data transmission was considered in the thesis. A further step is to include the influence of differential and integral non-linearities (i.e. DNL and INL) for non-ideal quantization processes.
- Baseband compensation of IQ imbalances was performed in Chapter 6 by assuming that the channel, the amplitude and phase mismatches are perfectly known at receiver. The acquisition of the channel and mismatch information is not addressed. A further step is to combine baseband compensation algorithms with the acquisition of channel responses and IQ mismatches.

Appendix A

Antennas and beamforming

A.1 Optimal antenna beamwidth

A.1.1 Uniform power angular spectrum in a sphere

Suppose that the scattered waves are uniformly distributed in a sphere for the considered scenario in Section 3.6.2. In case of the misalignment between the main lobe direction and the LOS path, the optimum HPBW, concerning the largest Rician K -factor gain, SNR gain and RMS delay spread reduction, can be achieved by solving

$$\ln \cos \frac{\sigma_{A_R[\text{opt}]}}{2} = \frac{\ln 2 \cdot \ln \cos \phi_{R,\text{ANT}}}{1 + \ln \cos \phi_{R,\text{ANT}}}, \quad (\phi_{R,\text{ANT}} \neq 0) \quad (\text{A.1})$$

which is derived by computing $\frac{\partial G_K}{\partial \sigma_{A_R}} = 0$, $\frac{\partial G_\rho}{\partial \sigma_{A_R}} = 0$ and $\frac{\partial R_{\sigma\tau}}{\partial \sigma_{A_R}} = 0$ from (3.66)-(3.68).

Using $\ln \cos \phi_{R,\text{ANT}} \sim -\frac{\phi_{R,\text{ANT}}^2}{2}$ for $|\phi_{R,\text{ANT}}| \rightarrow 0$, we have

$$\sigma_{A_R[\text{opt}]} \sim \frac{2\sqrt{2 \ln 2} \phi_{R,\text{ANT}}}{\sqrt{2 - \phi_{R,\text{ANT}}^2}} \approx 2\sqrt{\ln 2} \phi_{R,\text{ANT}} \approx 1.67 \phi_{R,\text{ANT}}. \quad (\text{A.2})$$

Fig. A.1 depicts the theoretical relationship (A.1) and its approximation (A.2) between the HPBW and the misalignment $\phi_{R,\text{ANT}}$, respectively, which indicates that (A.2) is a fairly good approximation in a large misalignment range.

A.1.2 Uniform PAS in the azimuth plane

Suppose the scattered waves are uniformly distributed in the azimuth plane for the scenario in Section 3.6.2. In case of the misalignment between the main lobe direction

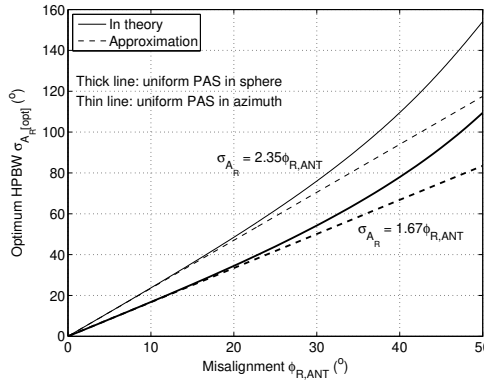


Fig. A.1: The optimum HPBW σ_{A_R} versus the misalignment $\phi_{R,ANT}$ for the cases of uniform angular spectrum in azimuth and in 3D for the scattered waves.

and the LOS path, the optimum HPBW concerning the largest Rician K -factor gain and RMS delay spread reduction can be achieved by solving

$$\psi \left[\frac{1}{2} + q_R \right] - \psi[1 + q_R] = \ln \cos^2 \phi_{R,ANT}, \quad (\phi_{R,ANT} \neq 0) \quad (\text{A.3})$$

which is derived by computing $\frac{\partial G_K}{\partial \sigma_{A_R}} = 0$ and $\frac{\partial R_{\sigma\tau}}{\partial \sigma_{A_R}} = 0$ from (3.66) and (3.68). Here $\psi[z]$ is the Digamma function, which is defined as the logarithmic derivative of the gamma function [90]. Although the closed-form solution cannot be carried out, a simple relationship between the optimum HPBW and the misalignment $\phi_{R,ANT}$ can be found for a small misalignment in an approximate way.

Since the first order derivative of the Digamma function $\psi[q_R]$ ($q_R \geq 0$) is a decreasing function and goes to zero in the infinity, the limit

$$\lim_{q_R \rightarrow +\infty} \left(\psi \left[\frac{1}{2} + q_R \right] - \psi[1 + q_R] \right) = \lim_{q_R \rightarrow +\infty} \left(\psi[q_R] - \psi \left[\frac{1}{2} + q_R \right] \right) = 0 \quad (\text{A.4})$$

is valid. It can be seen that if the misalignment $|\phi_{R,ANT}| \rightarrow 0$, the parameter q_R must be $q_R \rightarrow +\infty$ for the equality in (A.3) to be valid. Next, according to the property of Digamma function $\psi[z+1] = \psi[z] + \frac{1}{z}$, we have

$$\left(\psi \left[\frac{1}{2} + q_R \right] - \psi[1 + q_R] \right) = - \left(\psi[q_R] - \psi \left[\frac{1}{2} + q_R \right] \right) - \frac{1}{q_R}. \quad (\text{A.5})$$

Using (A.4), the relationship in (A.5) can be approximated by

$$\psi \left[\frac{1}{2} + q_R \right] - \psi[1 + q_R] \approx -\frac{1}{2q_R} \quad (\text{A.6})$$

for a sufficiently large value of q_R . Combining the relationships (3.53), (A.3) and (A.6), the following approximation is achieved

$$\cos \frac{\sigma_{A_R, \text{opt}}}{2} \approx (\cos \phi_{R,ANT})^{2 \ln 2}. \quad (\text{A.7})$$

Lastly, using $\cos^n \phi_{R,ANT} \sim \left(1 - \frac{n\phi_{R,ANT}^2}{2}\right)$ for $|\phi_{R,ANT}| \rightarrow 0$, the optimum HPBW is related to a small misalignment $\phi_{R,ANT}$ by the following approximation

$$\sigma_{A_R[\text{opt}]} \approx 2\sqrt{2 \ln 2} \phi_{R,ANT} \approx 2.35 \phi_{R,ANT}. \quad (\text{A.8})$$

Fig. A.1 depicts the theoretical relationship (A.3) and its approximate (A.8) between the optimum HPBW and the misalignment $\phi_{R,ANT}$, respectively, which indicates that (A.8) is a fairly good approximation in a large misalignment range.

Note that the optimal HPBW here is derived concerning the largest Rician K -factor gain and RMS delay spread reduction, but not concerning the SNR gain. This is different from the case of scattered waves distributed in a sphere, where the optimal HPBW is also achievable for the SNR gain. To study the behavior of the SNR gain in case of misalignment, we rewrite (3.67) as

$$G_\rho = \underbrace{\frac{K}{K+1} \cdot 2(2q_R + 1)(\cos \phi_{R,ANT})^{2q_R}}_{G_{\rho_1}} + \underbrace{\frac{1}{K+1} \cdot \frac{(2q_R + 1)\Gamma\left[\frac{1}{2} + q_R\right]}{\sqrt{\pi}\Gamma[1 + q_R]}}_{G_{\rho_2}}, \quad (\text{A.9})$$

in which the two parts G_{ρ_1} and G_{ρ_2} are contributed by the LOS wave and the scattered waves, respectively. The first part G_{ρ_1} is a unimodal function of HPBW¹ and the second part G_{ρ_2} is a strictly monotonically decreasing function of HPBW. Note that in case of scattered waves in a sphere, G_{ρ_2} is a constant and the behavior of G_ρ is merely determined by the first part G_{ρ_1} , which explains the difference in SNR gain for the two types of the distributions.

Here the addition of the two parts results in the total SNR gain G_ρ that has one local minimum and one local maximum, for a sufficiently large Rician K -factor ($K > 0.13$ from numerical simulations). As an example, Fig. A.2 illustrates the behavior of G_{ρ_1} , G_{ρ_2} and their addition G_ρ as a function of HPBW for $K = 1$ and $\phi_{R,ANT} = 10^\circ$. From this figure, we see that the SNR gain G_ρ is dominated by the contribution of scattered waves when the HPBW is smaller than the local minimum, while it is dominated by the contribution from the LOS wave when the HPBW is larger than the local minimum. In addition, the local maximum of G_ρ may be achieved at a certain beamwidth, which is approximately the same as the beamwidth at which the global maximum of G_{ρ_1} is achieved, i.e. $\sigma_{A_R[\text{opt}]} \approx 1.67\phi_{R,ANT}$.

A.2 Azimuth scan range and element beamwidth

Here we only investigate the relationship between the 3-dB beam scan range in the azimuth plane and the antenna element beamwidth at the receiver side. The following results are also true for the scan range at the transmitter side. Suppose that both the formed multi-antenna beams at transmitter and receiver sides are pointed to the

¹A function is unimodal if it is monotonically increasing up to some point and then monotonically decreasing.

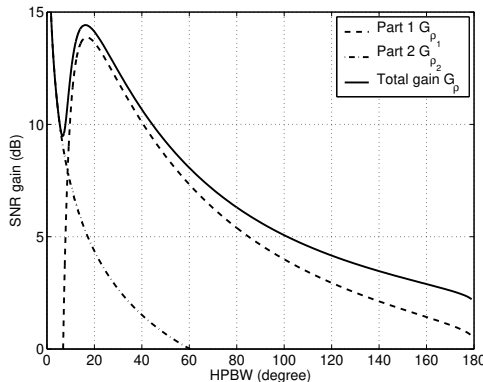


Fig. A.2: For the case of scattered waves distributed in the azimuth plane, the SNR gain is decomposed into two parts contributed by the LOS wave and the scattered waves (here $K = 1$ and $\phi_{R,ANT} = 10^\circ$).

departure and arrival directions of the LOS wave, i.e. $\Omega'_{x,0} = \Omega_{x,0}$ for $x \in \{T, R\}$, respectively. The departure direction of the LOS wave is fixed at $\Omega_{T,0}$, but the arrival direction $\Omega_{R,0} = (\frac{\pi}{2}, \phi_{R,0})$ with the steering angle $\phi'_{R,0} = \phi_{R,0}$ changing in azimuth. In addition, the main lobe directions of TX and RX elements are $\Psi_x = (\theta_{R,ANT}, \phi_{R,ANT})$ and $\Psi_x = (\frac{\pi}{2}, 0)$, respectively. For such a case, according to (3.60) and (3.61), the maximum gains of Rician K -factor and SNR may be achieved when the LOS wave arrives in the receiver at broadside $\Omega_{R,0} = (\frac{\pi}{2}, 0)$ and given by

$$\max\{G_K\} = \frac{P^2 Q^2 A_T(\Omega_{T,0}, \Psi_T) A_R(\frac{\pi}{2}, 0)}{F_{T,C} F_{R,C}} \quad (\text{A.10})$$

$$\max\{G_\rho\} = \frac{(K \cdot \max\{G_K\} + 1) F_{T,C} F_{R,C}}{PQ(K + 1)}, \quad (\text{A.11})$$

respectively, where the gains of scattered waves $F_{T,C}$ and $F_{R,C}$ are fixed values for a certain TX-RX array configuration. Now the 3-dB scan range in the azimuth plane can be derived as $\phi_{scan} = |\phi_{R,0}^U - \phi_{R,0}^L|$, where $\phi_{R,0}^U$ and $\phi_{R,0}^L$ are the solutions to $G_\rho = \frac{1}{2} \max\{G_\rho\}$. By using (3.60), (3.61) and (A.11), the equation $G_\rho = \frac{1}{2} \max\{G_\rho\}$ is simplified as

$$\frac{A_T(\frac{\pi}{2}, \phi_{R,0})}{A_R(\frac{\pi}{2}, 0)} = \frac{1}{2} - X, \quad (\text{A.12})$$

where the item $X = \frac{1}{2K \max\{G_K\}}$. It can be seen from (A.12) that the azimuth scan range is never larger than the element HPBW because of $\frac{A_R(\frac{\pi}{2}, \phi_{R,0})}{A_R(\frac{\pi}{2}, 0)} = \frac{1}{2}$ at $\phi_{R,0} = \pm \frac{\sigma_{AR}}{2}$. Fig. 3.8(a) indicates that for a fairly large number of antenna elements, a large Rician K -factor gain can be achieved that leads to $X \ll \frac{1}{2}$ for a fairly large Rician K -factor. In this case, the RX azimuth scan range is approximated by the element beamwidth, i.e.

$$\phi_{scan} \approx \sigma_{AR}. \quad (\text{A.13})$$

Appendix B

Derivation of (4.49)

For convenience, we rewrite

$$\mathbb{E} \left\{ \frac{1}{1 + \gamma_k} \right\} = a \int_0^\infty \frac{1}{1 + \gamma_k} e^{-b\gamma_k} I_0[\sqrt{c\gamma_k}] d\gamma_k, \quad (\text{B.1})$$

where $a = \frac{1+K}{\bar{\gamma}} e^{-K}$, $b = \frac{1+K}{\bar{\gamma}}$ and $c = \frac{4K(K+1)}{\bar{\gamma}}$. By using $I_0(x) = \sum_{m=0}^\infty \frac{(\frac{x}{2})^{2m}}{(m!)^2}$ [90], we rewrite (B.1) as

$$\begin{aligned} \mathbb{E} \left\{ \frac{1}{1 + \gamma_k} \right\} &= a \sum_{m=0}^\infty \frac{(\frac{c}{4})^m}{(m!)^2} \int_0^\infty \frac{1}{\gamma_k + 1} e^{-b\gamma_k} \gamma_k^m d\gamma_k \\ &= a \sum_{m=0}^\infty \frac{(\frac{c}{4})^m}{(m!)^2} \cdot \frac{e^b m!}{b^m} \int_1^\infty \frac{e^{-bt}}{t^{m+1}} dt \\ &= \frac{1+K}{\bar{\gamma}} e^{-K + \frac{1+K}{\bar{\gamma}}} \sum_{m=0}^\infty \frac{K^m}{m!} E_{m+1} \left[\frac{1+K}{\bar{\gamma}} \right], \end{aligned} \quad (\text{B.2})$$

where the exponential integral is defined as $E_{m+1}[x] = \int_1^\infty \frac{e^{-xt}}{t^{m+1}} dt$. For the purpose of numerical computation, the following recurrent relation may be used [90]

$$E_{m+1}[x] = \frac{1}{m} (e^{-x} - x E_m[x]) \quad (\text{B.3})$$

for an integer m .

Differentiation involving complex vectors and matrices

Derivatives of scalar functions with respect to complex matrices and vectors are frequently seen in the context of filter optimization and signal processing. The derivatives of $f(x, x^*)$ with respect to x and x^* are called formal partial derivatives of f for the complex scalar x and defined as

$$\frac{\partial f}{\partial x} \triangleq \frac{1}{2} \left(\frac{\partial f}{\partial \operatorname{Re}\{x\}} - \iota \frac{\partial f}{\partial \operatorname{Im}\{x\}} \right) \quad (\text{C.1})$$

$$\frac{\partial f}{\partial x^*} \triangleq \frac{1}{2} \left(\frac{\partial f}{\partial \operatorname{Re}\{x\}} + \iota \frac{\partial f}{\partial \operatorname{Im}\{x\}} \right), \quad (\text{C.2})$$

respectively [158, 159], where $\iota = \sqrt{-1}$ and $*$ denotes conjugate.

For scalar functions of the type $f(\mathbf{X}, \mathbf{X}^*)$, the derivative with respect to the complex matrix \mathbf{X} has the same size as \mathbf{X} and is given by $\frac{\partial f}{\partial \mathbf{X}} = \left[\frac{\partial f}{\partial x_{kl}} \right]$, where $\{x_{kl}\}$ are the entries of \mathbf{X} . In a similar way, the derivative of $f(\mathbf{x}, \mathbf{x}^*)$ with respect to the complex vector \mathbf{x} may be also defined.

Table C.1 lists some useful derivatives of the functions $f(\mathbf{x}, \mathbf{x}^*)$ and $f(\mathbf{X}, \mathbf{X}^*)$. The scalar function of scalar variable $f(x, x^*)$ can be considered as a special case. In the table, the superscripts T and \mathcal{H} represent transpose and complex transpose, respectively. In addition, $\operatorname{tr}\{\mathbf{X}\}$ and $\det\{\mathbf{X}\}$ represent the trace and the determinant of the matrix \mathbf{X} , respectively.

Table C.1: Derivatives of the scalar functions $f(\mathbf{x}, \mathbf{x}^*)$ and $f(\mathbf{X}, \mathbf{X}^*)$.

$f(\mathbf{x}, \mathbf{x}^*)$	$\frac{\partial f}{\partial \mathbf{x}}$	$\frac{\partial f}{\partial \mathbf{x}^*}$
$\mathbf{a}^T \mathbf{x}$	\mathbf{a}^T	$\mathbf{0}_{1 \times N}$
$\mathbf{a}^T \mathbf{x}^*$	$\mathbf{0}_{1 \times N}$	\mathbf{a}^T
$\mathbf{x}^T \mathbf{A} \mathbf{x}$	$\mathbf{x}^T (\mathbf{A} + \mathbf{A}^T)$	$\mathbf{0}_{1 \times N}$
$\mathbf{x}^H \mathbf{A} \mathbf{x}$	$\mathbf{z}^H \mathbf{A}$	$\mathbf{z}^T \mathbf{A}^T$
$\mathbf{x}^H \mathbf{A} \mathbf{x}^*$	$\mathbf{0}_{1 \times N}$	$\mathbf{x}^H (\mathbf{A} + \mathbf{A}^T)$
$f(\mathbf{X}, \mathbf{X}^*)$	$\frac{\partial f}{\partial \mathbf{X}}$	$\frac{\partial f}{\partial \mathbf{X}^*}$
$\text{tr}\{\mathbf{X}\}$	\mathbf{I}_N	$\mathbf{0}_{N \times N}$
$\text{tr}\{\mathbf{X}^*\}$	$\mathbf{0}_{N \times N}$	\mathbf{I}_N
$\text{tr}\{\mathbf{A} \mathbf{X}\}$	\mathbf{A}^T	$\mathbf{0}_{N \times M}$
$\text{tr}\{\mathbf{X}^H \mathbf{A}\}$	$\mathbf{0}_{N \times M}$	\mathbf{A}
$\text{tr}\{\mathbf{X} \mathbf{A}_0 \mathbf{X}^T \mathbf{A}_1\}$	$\mathbf{A}_1^T \mathbf{X} \mathbf{A}_0^T + \mathbf{A}_1 \mathbf{X} \mathbf{A}_0$	$\mathbf{0}_{N \times M}$
$\text{tr}\{\mathbf{X} \mathbf{A}_0 \mathbf{X} \mathbf{A}_1\}$	$\mathbf{A}_1^T \mathbf{X}^T \mathbf{A}_0^T + \mathbf{A}_0^T \mathbf{X}^T \mathbf{A}_1^T$	$\mathbf{0}_{N \times M}$
$\text{tr}\{\mathbf{X} \mathbf{A}_0 \mathbf{X}^H \mathbf{A}_1\}$	$\mathbf{A}_1^T \mathbf{X}^* \mathbf{A}_0^T$	$\mathbf{A}_1 \mathbf{X} \mathbf{A}_0$
$\text{tr}\{\mathbf{X} \mathbf{A}_0 \mathbf{X}^* \mathbf{A}_1\}$	$\mathbf{A}_1^T \mathbf{X}^H \mathbf{A}_0^T$	$\mathbf{A}_0^T \mathbf{X}^T \mathbf{A}_1^T$
$\text{tr}\{\mathbf{A} \mathbf{X}^{-1}\}$	$-(\mathbf{X}^T)^{-1} \mathbf{A}^T (\mathbf{X}^T)^{-1}$	$\mathbf{0}_{N \times N}$
$\text{tr}\{\mathbf{X}^p\}$	$p (\mathbf{X}^T)^{p-1}$	$\mathbf{0}_{N \times N}$
$\det\{\mathbf{A}_0 \mathbf{X} \mathbf{A}_1\}$	$\det\{\mathbf{A}_0 \mathbf{X} \mathbf{A}_1\} (\mathbf{A}_1^T \mathbf{X}^T \mathbf{A}_0^T)^{-1} \mathbf{A}_1^T$	$\mathbf{0}_{N \times M}$
$\det\{\mathbf{X} \mathbf{X}^T\}$	$2 \det\{\mathbf{X} \mathbf{X}^T\} (\mathbf{X} \mathbf{X}^T)^{-1} \mathbf{X}$	$\mathbf{0}_{N \times M}$
$\det\{\mathbf{X} \mathbf{X}^*\}$	$\det\{\mathbf{X} \mathbf{X}^*\} (\mathbf{X}^H \mathbf{X}^T)^{-1} \mathbf{X}^H$	$\det\{\mathbf{X} \mathbf{X}^*\} \mathbf{X}^T (\mathbf{X}^H \mathbf{X}^T)^{-1}$
$\det\{\mathbf{X} \mathbf{X}^H\}$	$\det\{\mathbf{X} \mathbf{X}^H\} (\mathbf{X}^* \mathbf{X}^T)^{-1} \mathbf{X}^*$	$\det\{\mathbf{X} \mathbf{X}^H\} (\mathbf{X} \mathbf{X}^H)^{-1} \mathbf{X}$
$\det\{\mathbf{X}^p\}$	$p \det^p\{\mathbf{X}\} (\mathbf{X}^T)^{-1}$	$\mathbf{0}_{N \times N}$

Appendix D

Signal-to-distortion ratio at quantizer output

Consider the quantized signal $\tilde{z}_n = \mathbb{Q}(z_n)$, which is modelled by $\tilde{z}_n = \alpha z_n + d_n$ using the generalized Bussgang's theorem, yielding the signal to distortion ratio $\text{SDR} = \frac{\alpha^2 \sigma_z^2}{\sigma_{\tilde{z}}^2 - \alpha^2 \sigma_z^2}$. For the Gaussian input z_n , the scaling factor, $\alpha = \frac{\mathbb{E}\{z\mathbb{Q}(z)\}}{\sigma_z^2}$, can be found to be

$$\alpha = \frac{1}{\sigma_z^2} \sum_{j=-\frac{Q}{2}+1}^{j=\frac{Q}{2}} q_j \int_{-\infty}^{\infty} z U(z, \hat{z}_{j-1}, \hat{z}_j) p_z(z) dz \quad (\text{D.1})$$

$$= \frac{\Delta}{\sqrt{2\pi}\sigma_z} \sum_{j=-\frac{Q}{2}+1}^{j=\frac{Q}{2}} j \left(e^{-\frac{\hat{z}_{j-1}}{2\sigma_z^2}} - e^{-\frac{\hat{z}_j}{2\sigma_z^2}} \right) \quad (\text{D.2})$$

$$= \frac{\Delta}{\sqrt{2\pi}\sigma_z} \left(1 + 2 \sum_{j=1}^{\frac{Q}{2}-1} e^{-\frac{j^2}{2} \left(\frac{\Delta}{\sigma_z}\right)^2} \right). \quad (\text{D.3})$$

In addition, the total output power, $\sigma_{\tilde{z}}^2 = \mathbb{E}\{\mathbb{Q}^2(\tilde{z})\}$, is found to be

$$\sigma_{\tilde{z}}^2 = \sum_{j=-\frac{Q}{2}+1}^{j=\frac{Q}{2}} q_j^2 \int_{-\infty}^{\infty} p_z(z) dz \quad (\text{D.4})$$

$$= \frac{\Delta^2}{4} + 2\Delta^2 \sum_{j=1}^{\frac{Q}{2}-1} j \text{erfc} \left[\frac{j\Delta}{\sqrt{2}\sigma_z} \right]. \quad (\text{D.5})$$

For $R = 1$ bit, we have $\alpha = \frac{\Delta}{\sqrt{2\pi}\sigma_z}$ and $\sigma_{\tilde{z}}^2 = \frac{\Delta^2}{4}$, yielding the output SDR, $\text{SDR} = \frac{2}{\pi-2}$ (2.44 dB), which is independent of the quantization interval Δ . In other words, for the Gaussian input z_n of the quantizer $R = 1$ bit, the output SDR is fixed for whatever the interval is chosen. For $R > 1$ bits, the normalized optimal interval $\frac{\Delta_G}{\sigma_z}$ can be obtained by maximizing the SDR given by

$$\text{SDR} = \frac{\left(1 + 2 \sum_{j=1}^{\frac{Q}{2}-1} e^{-\frac{j^2}{2} \cdot \left(\frac{\Delta}{\sigma_z}\right)^2}\right)^2}{\frac{\pi}{2} + 4\pi \sum_{j=1}^{\frac{Q}{2}-1} \text{jerfc} \left[\frac{j\Delta}{\sqrt{2}\sigma_z} \right] - \left(1 + 2 \sum_{j=1}^{\frac{Q}{2}-1} e^{-\frac{j^2}{2} \cdot \left(\frac{\Delta}{\sigma_z}\right)^2}\right)^2}. \quad (\text{D.6})$$

By doing so, we found that the optimal interval $\frac{\Delta_G}{\sigma_z}$ is the solution to

$$\frac{\Delta_G}{\sigma_z} = \sqrt{\frac{8}{\pi}} \cdot \frac{1 + 2 \sum_{j=1}^{\frac{Q}{2}-1} \frac{Q}{2} \exp \left\{ -\frac{j^2 \Delta_G^2}{2\sigma_z^2} \right\}}{1 + 8 \sum_{j=1}^{\frac{Q}{2}-1} \text{jerfc} \left[\frac{j\Delta_G}{\sqrt{2}\sigma_z} \right]} \quad (R > 1 \text{ bits}). \quad (\text{D.7})$$

For the PQN model $\tilde{z}_n = z_n + d_n$, the output SDR, defined as $\text{SDR} = \frac{\sigma_z^2}{\sigma_d^2}$ with $\sigma_d^2 = \mathbb{E}\{(\tilde{z} - z)^2\}$, are derived as

$$\text{SDR} = \frac{\sigma_z^2}{\sigma_{\tilde{z}}^2 - 2\alpha\sigma_z^2 + \sigma_z^2}. \quad (\text{D.8})$$

It is found that the optimal quantization interval, which maximizes the SDR, has the same solution as of (D.7) for any $R \geq 1$ bits.

Glossary

Notation

*	the superscript denotes conjugate
\top	the superscript denotes transpose
\mathcal{H}	the superscript denotes complex Transpose
i	imaginary unit, i.e. $i = \sqrt{-1}$
x	scalar
\mathbf{x}	vector with the m th entry x_m
\mathbf{X}	matrix with the (m, n) th entry X_{mn}
\mathbf{I}	identity matrix
$\mathbf{0}$	full zero matrix or vector
$\lceil x \rceil$	the ceiling function returns the smallest integer not less than x
$\text{cir}\{\mathbf{x}\}$	circulant matrix with the first column formed by the vector \mathbf{x}
$\text{diag}\{\mathbf{X}\}$	diagonal matrix with entries formed by the diagonal entries of \mathbf{X}
$\det\{\mathbf{X}\}$	determinant of the matrix \mathbf{X}
$\text{tr}\{\mathbf{X}\}$	trace of the matrix \mathbf{X}
$\delta(x)$	Dirac function
$E_m[x]$	exponential integral function
$\text{erfc}[x]$	complementary error function
$\Gamma[x]$	Gamma function
$\Gamma[n, x]$	incomplete Gamma function
$I_0[x]$	zero-order modified Bessel function of the first kind
$\psi[x]$	Digamma function
$\tanh[x]$	hyperbolic tangent function
$\text{mod}(m, n)$	modulo operation
$\mathbb{E}\{x\}$	expectation of x
$\text{Re}\{x\}$	real part of x

$\text{Im}\{x\}$	imaginary part of x
$\mathcal{R}(\Delta t)$	Autocorrelation function of $x(t)$
$\mathcal{X}(\Delta t)$	Cross correlation function of $x(t)$ and $y(t + \Delta t)$
$x(t) * y(t)$	convolution between $x(t)$ and $y(t)$
$\frac{\partial f}{\partial x}$	partial derivative of $f(x)$
\otimes	Kronecker product
\odot	element-wise product
\oplus	modulo-2 addition

Abbreviations and acronyms

3D	three dimension
3G	the third-generation
4G	the fourth-generation
A/D	analogue-to-digital
ADC	analogue-to-digital converter
AGC	automatic gain control
AOA	angle of arrival
AOD	angle of departure
AWGN	additive white Gaussian noise
BER	bit-error rate
BPSK	binary phase shift keying
CFO	carrier frequency offset
CIR	channel impulse response
CMOS	Complementary metaloxidesemiconductor
CP	cyclic prefix
CPE	common phase error
CPM	continuous phase modulations
CSI	channel state information
DAC	digital-to-analogue converter
dB	decibel
dBi	decibel relative to isotropic
D/A	digital-to-analogue
DFE	decision feedback equalization
DFT	discrete Fourier transform
DOA	direction of arrival
DOD	direction of departure
DSP	digital signal processing
ECC	error correction code
cdf	cumulative distribution function
EIRP	equivalent isotropic radiated power
ETSI	European Telecommunications Standards Institute
FCC	Federal Communications Commission
FD	frequency domain

FDE	frequency-domain equalization
FET	field effect transistor
FFT	fast Fourier transform
GaAs	gallium arsenide
Gb/s	gigabit per second
GMSK	Gaussian minimum-shift keying
GI	guard interval
GSM	global system for mobile
HDTV	high-definition television
HPBW	half-power beamwidth
HRC	hybrid-domain RISI cancellation
IBI	inter-block interference
IBO	input backoff
IF	intermediate frequency
i.i.d.	independent and identically distributed
I/Q	in-phase and quadrature
IDFT	inverse discrete Fourier transform
IEEE	institute of electrical and electronics engineers
IFFT	inverse fast Fourier transform
ISI	inter-symbol interference
ISM	industrial, scientific and medical
LNA	low noise amplifier
LO	local oscillator
LOS	line-of-sight
LPF	low-pass filter
LTE	long-term evolution
MAC	medium access control
MAP	maximum <i>a posteriori</i> probability
MC	multi-carrier
MC-CDMA	multi-carrier code division multiple access
MIMO	multiple-input multiple-output
ML	maximum-likelihood
MMIC	millimeter wave integrated circuit
MMSE	minimum mean-square error
MRC	maximum ratio combining
MSE	mean square error
NLOS	non-line-of-sight
NRP	normalized received power
OFDM	orthogonal frequency division multiplexing
PA	power amplifier
QAM	quadrature amplitude modulations
PAPR	peak-to-average power ratio
PAS	power angular spectrum
PCB	printed circuit board
pdf	probability density function

PDP	power delay profile
PDS	power delay spectrum
PLL	phase-locked loop
PN	phase noise
PQN	Pseudo quantization noise
PSD	power spectrum density
PSK	phase shift keying
QAM	quadrature amplitude modulation
QPSK	quadrature phase shift keying
RF	radio frequency
RMS	root-mean-square
RDS	RMS delay spread
RISI	residual ISI
RoF	radio-over-fiber
RPS	Radio Propagation Simulator
RX	receiver
SC	single carrier
SDR	signal-to-distortion ratio
SER	symbol-error rate
SC-FDE	single-carrier frequency domain equalization
SiGe	silicon germanium
SNR	signal-to-noise ratio
TD	time domain
TOA	time of arrival
TX	transmitter
ULA	uniform linear array
US	uncorrelated scattering
UWB	ultra wideband
VCO	voltage-controlled oscillator
WHT	Walsh-Hadamard transform
WLAN	wireless local area network
WMAN	wireless metropolitan area networks
WPAN	wireless personal area network
WSS	wide-sense stationary
WSSUS	WSS and US
WWAN	wireless wide-area networks
ZF	zero-forcing

References

- [1] WirelessHD, “WirelessHD Specification Version 1.0 Overview,” Res. Lab. Electron., M.I.T., Cambridge, MA, Tech. Rep., October 9, 2007.
- [2] P. Smulders, “Exploiting the 60 GHz band for local wireless multimedia access: prospects and future directions,” *IEEE Commun. Mag.*, vol. 40, pp. 140–147, Jan. 2002.
- [3] T. Kuri, K. Kitayama, A. Stöhr, and Y. Ogawa, “Fiber-Optic Millimeter-Wave Downlink System Using 60 GHz-Band External Modulation,” *J. Lightw. Technol.*, vol. 17, no. 5, pp. 799–806, May 1999.
- [4] IEEE 802.15 WPAN Millimeter Wave Alternative PHY Task Group 3c (TG3c). [Online]. Available: <http://www.ieee802.org/15/pub/TG3c.html>.
- [5] ETSI TR 102 555, “Electromagnetic compatibility and Radio spectrum Matters (ERM); System Reference Document; Technical Characteristics of Multiple Gigabit Wireless Systems in the 60 GHz Range,” Tech. Rep., February 2007.
- [6] “About Short-range Wireless Applications in the Frequency Band of 60 GHz,” by Ministry of Information Industry of the People’s Republic of China. [Online]. Available: http://www.miit.gov.cn/art/2007/10/23/art_4413_41260.html.
- [7] ECMA International, “Ecma TC48 draft standard for high rate 60 GHz WPANs,” Tech. Rep., Mar. 2008, White paper, Ecma/TC48/2008/024.
- [8] A. Sadri, “802.15.3c Usage Model Document (UMD), Draft,” Tech. Rep., Jan. 2006, iEEE 802.15 TG3c document: 15-06-0055-14-003c.
- [9] A.K. Salkintzis and N. Hong and P.T. Mathiopoulos, “ADC and DSP Challenges in the Development of Software Radio Base Stations,” *IEEE Personal Commun. Mag.*, vol. 6, no. 4, pp. 47–55, Aug. 1999.
- [10] U.R. Pfeiffer and et al., “A Chip-Scale Packaging Technology for 60-GHz Wireless Chipsets,” *IEEE Trans. Microw. Theory Tech.*, vol. 54, no. 8, pp. 3387–3397, Aug. 2006.

-
- [11] S. Sarkar and J. Laskar, "A Single-Chip 25pJ/bit Multi-Gigabit 60 GHz Receiver Module," in *IEEE/MTT-S IMS'07*, 2007, pp. 475–478.
- [12] T. Yao, M. Gordon, K. Tang, K. Yau, M. Yang, P. Schvan, and S. Voinigescu, "Algorithmic Design of CMOS LNAs and PAs for 60-GHz Radio," *IEEE J. Solid-State Circuits*, vol. 42, no. 5, pp. 1044–1057, May 2007.
- [13] L. Franca-Neto, R. Bishop, and B. Bloechel, "64-GHz and 100-GHz VCO's in 90-nm CMOS using optimum pumping method," in *IEEE ISSCC Dig. Tech. Papers*, Feb. 2004, pp. 444–445.
- [14] C. Doan, S. Emami, A. Niknejad, and R. Brodersen, "Millimeter-wave CMOS design," *IEEE J. Solid-State Circuits*, vol. 40, pp. 144–155, Jan. 2005.
- [15] T. Mitomo and etc., "A 60-GHz CMOS Receiver Front-End With Frequency Synthesizer," *IEEE J. Solid-State Circuits*, vol. 43, no. 4, pp. 1030–1037, Apr. 2008.
- [16] B. Razavi, "A 60-GHz direct-conversion CMOS receiver," in *IEEE ISSCC Dig. Tech. Papers*, Feb. 2005, pp. 400–401.
- [17] P. Chen, M. Chen, and C. Wu, "An Integrated 60-GHz Front-end Receiver with a Frequency Tripler Using 0.13- μm CMOS Technology," in *IEEE ICECS*, Dec. 2007, pp. 829–832.
- [18] B. Razavi, "A Millimeter-Wave CMOS Heterodyne Receiver With On-Chip LO and Divider," *IEEE J. Solid-State Circuits*, vol. 43, no. 2, pp. 477–485, Feb. 2008.
- [19] G. Fettweis and etc., "Dirty RF: A New Paradigm," in *IEEE PIMRC'05*, Berlin, Germany, Sep. 2005.
- [20] R. Walden, "Analog-to-Digital Converter Survey and Analysis," *IEEE J. Sel. Areas Commun.*, vol. 17, no. 4, pp. 539–550, Apr. 1999.
- [21] P. Kenington and L. Astier, "Power consumption of A/D converters for software radio applications," *IEEE Trans. Veh. Technol.*, vol. 49, no. 2, pp. 643–650, Mar. 2000.
- [22] B. Le, T. Rondeau, J. Reed, and C. Bostian, "Analog-to-Digital Converters," *IEEE Signal Process. Mag.*, vol. 22, no. 6, pp. 69–77, Nov. 2005.
- [23] G. V. der Plas, S. Decoutere, and S. Donnay, "A 2.5 mW 1.25 GS/s 4b ADC in a 90 nm Digital CMOS process achieving 0.16 pJ/conversion step," in *IEEE ISSCC'06*, Feb. 2006.
- [24] J.R. Long and J.N. Burghartz, "Foundations of Wireless Communication (WiComm): Project plan," Freeband Communication, Tech. Rep., Nov. 2004.
- [25] M. Steinbauer, A. Molisch, and E. Bonek, "The Double-Directional Radio Channel," *IEEE Antennas Propag. Mag.*, vol. 43, no. 4, pp. 51–63, Aug. 2001.

- [26] T. S. Rappaport, *Wireless Communication Principle and Practice*. Prentice Hall PTR, 1996.
- [27] A. Molisch, *Wireless Communications*. John Wiley & Sons, 2005.
- [28] G. Durgin, “Theory of stochastic local area channel modeling for wireless communications,” Ph.D. dissertation, Virginia Tech, Blacksburg, VA, Dec. 2000.
- [29] D. Hogg, “Fun with the Friis free-space transmission formula,” *IEEE Antennas Propag. Mag.*, vol. 35, pp. 33–35, Aug. 1993.
- [30] J. B. Andersen, T. S. Rappaport, and S. Yoshida, “Propagation measurements and models for wireless communications channels,” *IEEE Commun. Mag.*, vol. 33, pp. 42–49, Jan. 1995.
- [31] P. A. Bello, “Characterization of randomly time-variant linear channels,” *IEEE Trans. Commun. Sys.*, vol. CS-11, pp. 360–393, Dec. 1963.
- [32] L. Dossi, G. Tartara, and F. Tallone, “Statistical analysis of measured impulse response functions of 2.0 GHz indoor radio channels,” *IEEE J. Sel. Areas Commun.*, vol. 14, pp. 405–410, Apr. 1996.
- [33] J. Medbo, H. Hallenberg, and J. E. Berg, “Propagation Characteristics at 5 GHz in Typical RadioLAN Scenarios,” in *Proc. Of VTC’ 99 Spring (Houston)*, 1999, pp. 185–189.
- [34] H. Hashemi, “The Indoor Radio Propagation Channel,” *Proceedings of IEEE*, vol. 81, no. 7, pp. 943–968, Jul. 1993.
- [35] P. Marinier, G. Y. Delisle, and C. L. Despins, “Temporal variations of the indoor wireless millimeter-wave channel,” *IEEE Trans. Antennas Propag.*, vol. 46, pp. 928–934, Jun. 1998.
- [36] N. Moraitis and P. Constantinou, “Indoor Channel Measurements and Characterization at 60 GHz for Wireless Local Area Network Applications,” *IEEE Trans. Antennas Propag.*, vol. 52, no. 12, pp. 3180–3189, Dec. 2004.
- [37] A. A. M. Saleh and R. A. Valenzuela, “A Statistical Model for Indoor Multipath Propagation,” *IEEE J. Sel. Areas Commun.*, vol. 5, no. 2, pp. 128–137, Feb. 1987.
- [38] Q. H. Spencer, B. D. Jeffs, M. A. Jensen, and A. L. Swindlehurst, “Modeling the Statistical Time and Angle of Arrival Characteristics of an Indoor Multipath Channel,” *IEEE J. Sel. Areas Commun.*, vol. 18, no. 3, pp. 347–360, Mar. 2000.
- [39] C.-C. Chong, C.-M. Tan, D. I. Laurenson, S. McLaughlin, M. A. Beach, and A. R. Nix, “A new Statistical wideband spatio-temporal channel model for 5-GHz band WLAN systems,” *IEEE J. Sel. Areas Commun.*, vol. 21, no. 2, pp. 139–150, Feb. 2003.
- [40] H. Takai, “In-room transmission BER performance of anti-multipath modulation PSK-VP,” *IEEE Trans. Veh. Technol.*, vol. 42, pp. 177–185, May 1993.

-
- [41] P. F. M. Smulders, "Broadband Wireless LANs: A Feasibility Study," Ph.D. dissertation, Eindhoven University of Technology, Eindhoven, The Netherlands, Dec. 1995.
- [42] K. Witrisal, G. Landman, and A. Bohdanowicz, "Practical Application of a Novel Method for Estimating the RMS Delay Spread from Power Measurements," in *Proc. EPMCC 2001*, Vienna, Austria, Feb. 2001.
- [43] D. Cox and R. Leck, "Correlation Bandwidth and Delay Spread Multipath Propagation Statistics for 910-MHz Urban Mobile Radio Channels," *IEEE Trans. Wireless Commun.*, vol. 23, pp. 1271–1280, Nov. 1975.
- [44] A. Molisch and M. Steinbauer, "Condensed Parameters for Characterizing Wideband Mobile Radio Channels," *International Journal of Wireless Information Networks*, vol. 6, no. 3, pp. 133–154, 1999.
- [45] M. Al-Nuaimi and A. Siamarou, "Coherence bandwidth characterisation and estimation for indoor Rician multipath wireless channels using measurements at 62.4 GHz," *IEE Proceedings: Microwaves, Antennas and Propagation*, vol. 149, no. 3, pp. 181–187, Jun. 2002.
- [46] K. Witrisal, "OFDM Air-Interface Design for Multimedia Communications," Ph.D. dissertation, Delft University of Technology, International Research Centre for Telecommunications-transmission and Radar, Oct. 2001.
- [47] R. Clarke, "A Statistical Theory of Mobile-Radio Reception," *Bell System Technical Journal*, vol. 47, pp. 957–1000, Jul. 1968.
- [48] C. Jakes, *Microwave mobile communications*. J. Wiley and Sons Inc., 1974.
- [49] S. Thoen, L. V. Perre, and M. Engels, "Modeling the Channel Time-Variance for Fixed Wireless Communications," *IEEE Commun. Lett.*, vol. 6, no. 8, pp. 331–333, Aug. 2002.
- [50] R. J. C. Bultitude, R. F. Hahn, and R. J. Davies, "Propagation considerations for the design of an indoor broad-band communications system at EHF," *IEEE Trans. Veh. Technol.*, vol. 47, pp. 235–245, Feb. 1998.
- [51] K. J. Harris, "On the use of windows for harmonic analysis with the discrete Fourier transform," *Proceedings IEEE*, vol. 66, pp. 51–83, Jan. 1978.
- [52] G.A.J. van Dooren, "A deterministic approach to the modelling of electromagnetic wave propagation in urban environments," Ph.D. dissertation, Eindhoven University of Technology, Eindhoven, The Netherlands, Mar. 1994.
- [53] G. Dolmans and L. Leyten, "Effect of delay-spread and fading on the performance of an adaptive dual-antenna handset," in *Proc. IEEE 50th Vehicular Technology Conference (VTC'99)*, Sep. 1999, pp. 77–81.
- [54] R. Davies, M. Bensebti, M. A. Beach, and J. P. McGeehan, "Wireless Propagation Measurements in Indoor Multipath Environments at 1.7GHz and 60GHz

- for Small Cell Systems,” in *Proc. IEEE 41st Vehicular Technology Conference (VTC'91)*, St Louis, Missouri, May 1991, pp. 589–593.
- [55] K. Kobayashi and K. Miura, “Diffraction of a plane wave by a thick strip grating,” *IEEE Trans. Antennas Propag.*, vol. 37, pp. 459–470, Apr. 1989.
- [56] M. Fiacco, M. Parks, H. Radi, and S. R. Saunders, “Final report — Indoor Propagation Factors at 17 and 60GHz,” Tech. Rep., Aug. 1998, study carried out on behalf of the Radiocommunications Agency, University of Surrey.
- [57] H. Xu, V. Kukshya, and T. Rappaport, “Spatial and temporal characteristics of 60-GHz indoor channels,” *IEEE J. Sel. Areas Commun.*, vol. 20, pp. 620–630, Apr. 2002.
- [58] R. A. Valenzuela, “A ray tracing approach to predicting indoor wireless transmission,” in *Proc. of VTC'93 spring*, 1993, pp. 214–218.
- [59] M. Williamson, G. Athanasiadou, and A. Nix, “Investigating the effects of antenna directivity on wireless indoor communication at 60 GHz.”
- [60] “WP1-Study: Functional System Parameters description,” Tech. Rep., 2002, iST-2001-32686 BROADWAY.
- [61] J. Deibner and J. Hübner and D. Hunold and J. Voigt, *RPS Radiowave Propagation Simulator User manual*. Dresden: Radioplan GmbH, 2003.
- [62] E. Sousa, V. Jovanovic, and C. Daigneault, “Delay spread measurements for the digital cellular channel in Toronto,” *IEEE Trans. Veh. Technol.*, vol. 43, pp. 837–847, Nov. 1994.
- [63] R. Ertel, P. Cardieri, K. Sowerby, T. Rappaport, and J. Reed, “Overview of the Spatial Channel Models for Antenna Array Communication Systems,” *IEEE Personal Communications*, pp. 10–22, Feb. 1998.
- [64] T. Taga and T. Tanaka, “Delay spread reduction effect of beam antenna and adaptively controlled beam facing access system in urban line-of-sight street microcells,” *IEEE Trans. Veh. Technol.*, vol. 52, pp. 761–771, Jul. 2003.
- [65] T. Manabe, Y. Miura, and T. Ihara, “Effects of antenna directivity and polarization on indoor multipath propagation characteristics at 60 GHz,” *IEEE J. Sel. Areas Commun.*, vol. 14, pp. 441–448, Apr. 1996.
- [66] Y. Sun, P. Hafezi, A. Nix, and M. Beach, “Indoor channel characterisation measurements with directional antennas for future high frequency ATM wireless access systems,” in *In Proc. Personal Indoor and Mobile Radio Communications 1997 (PIMRC'97)*, Helsinki, Finland, 1997, pp. 184–188.
- [67] J. Dabin, N. Ni, A. Haimovich, E. Niver, and H. Grebel, “The effects of antenna directivity on path loss and multipath propagation in UWB indoor wireless channels,” in *IEEE Conference on Ultra Wideband Systems and Technologies*, Nov. 2003, pp. 305–309.

- [68] H. Yang, M. H. A. J. Herben, and P. F. M. Smulders, "Frequency Selectivity of 60-GHz LOS and NLOS Indoor Radio Channels," in *Proc. of IEEE Vehicular Technology Conference Spring in 2006 (VTC'06 spring)*, Melbourne, Australia, 2006, pp. 2727–2731.
- [69] T. Taga, "Analysis for mean effective gain of mobile antennas in land mobile radio environments," *IEEE Trans. Veh. Technol.*, vol. 39, pp. 117–131, May 1990.
- [70] A. Glazunov, "Theoretical analysis of mean effective gain of mobile terminal antennas in Ricean channels," in *Proc. IEEE VTC'02 fall*, 2002, pp. 1796–1800.
- [71] —, "Mean effective gain of user equipment antennas in double directional channels," in *In Proc. Personal Indoor and Mobile Radio Communications 1994 (PIMRC'04)*, vol. 1, 2004, pp. 432–436.
- [72] S. Silver, *Microwave antenna theory and design*. London: Peregrinus, 1984.
- [73] C. A. Balanis, *Antenna Theory: Analysis and Design, 2nd Edition*. John Wiley & Sons, Inc, 1997.
- [74] E. Bonek and M. Steinbauer, "double-directional channel measurements," in *11th International Conference on Antennas and Propagation (IEE 2001)*, vol. 1, Apr. 2001, pp. 226–230.
- [75] B. H. Fleury, "First- and Second-Order Characterization of Direction Dispersion and Space Selectivity in the Radio Channel," *IEEE Trans. Inf. Theory*, vol. 46, no. 6, pp. 2027–2044, Sep. 2000.
- [76] R. Heddergott and P. Truffer, "Results of indoor wideband delay-azimuth-elevation measurements for stochastic radio channel modeling," AT&T Bell Laboratories, Tech. Rep., Sep. 1999, tech. Rep. COST 259 TD (99) 083, COST 259.
- [77] K. Pedersen, P. E. Mogensen, and B. H. Fleury, "A Stochastic Model of the Temporal and Azimuthal Dispersion Seen at the Base Station in Outdoor Propagation Environments," *IEEE Trans. Veh. Technol.*, vol. 49, pp. 437–447, Mar. 2000.
- [78] A. Kuchar, J.-P. Rossi, and E. Bonek, "Directional macro-cell channel characterization from urban measurements," *IEEE Trans. Antennas Propag.*, vol. 48, pp. 137–146, Feb. 2000.
- [79] J. Laurila, K. Kalliola, M. Toeltsch, K. Hugl, P. Vainikainen, and E. Bonek, "Wide-Band 3-D Characterization of Mobile Radio Channels in Urban Environment," *IEEE Trans. Antennas Propag.*, vol. 50, no. 2, pp. 233–243, Feb. 2002.
- [80] H. J. Visser, *Array and phased array antenna basics*. Chichester : Wiley, 2005, 2005.

- [81] K. Kalliola, K. Sulonen, H. Laitinen, O. Kivekas, J. Krogerus, and P. Vainikainen, "Angular power distribution and mean effective gain of mobile antenna in different propagation environments," *IEEE Trans. Veh. Technol.*, vol. 51, no. 5, pp. 823–838, Sep. 2002.
- [82] N. Blaunstein and et. al., "Signal Power Distribution in the Azimuth, Elevation and Time Delay Domains in Urban Environments for Various Elevations of Base Station Antenna," *IEEE Trans. Antennas Propag.*, vol. 54, pp. 2902–2916, Oct. 2006.
- [83] H. Meyr, M. Moeneclaey, and S. Fechtel, *Digital Communication Receivers: Synchronization, Channel Estimation and Signal Processing*. New York: J. Wiley and Sons, 1998.
- [84] S. Benedetto and E. Biglieri, *Principles of Digital Transmission With Wireless Applications*. Kluwer Academic/Plenum Publishers, 1999.
- [85] A. Bury and J. Egle and J. Lindner, "Diversity comparison of spreading transforms for multicarrier spread spectrum transmission," *IEEE Trans. Commun.*, vol. 51, no. 5, pp. 774–781, May 2003.
- [86] J.M. Cioffi and G.P. Dudevoir and M.V. Eyuboglu and G.D. Forney, Jr., "MMSE decision-feedback equalizers and coding. I. Equalization Results," *IEEE Trans. Commun.*, vol. 43, pp. 2582–2594, Oct. 1995.
- [87] J. Proakis, *Digital communications*. McGraw-Hill, 2001.
- [88] M. Simon and M. Alouini, *Digital Communication over Fading Channels*. John Wiley & Sons, Inc, 2000.
- [89] I.S. Gradshteyn and I.M. Ryzhik, *Table of Integrals, Series, and Products*. Academic Press, New York, 1994.
- [90] M. Abramowitz and I. A. Stegun, *Handbook of mathematical functions with formulas, graphs, and mathematical tables*. New York: John Wiley & Sons Inc., 1984.
- [91] D. Falconer, S. Ariyavisitakul, A. Benyamin-Seeyar, and B. Eidson, "Frequency domain equalization for single-carrier broadband wireless systems," *IEEE Commun. Mag.*, vol. 40, no. 4, pp. 58–66, Apr. 2002.
- [92] A. Milewski, "Periodic sequences with optimal properties for channel estimation and fast start-up equalization," *IBM J. Res. Develop.*, vol. 27, pp. 426–431, 1983.
- [93] J.C.L. Ng and K. Letaief and R. Murch, "Complex optimal sequences with constant magnitude for fast channel estimation initialization," *IEEE Trans. Commun.*, vol. 46, no. 3, pp. 305–308, Mar. 1983.
- [94] J. Siew and et al, "A channel estimation algorithm for MIMO-SCFDE," *IEEE Commun. Lett.*, vol. 8, no. 9, pp. 555–557, Sep. 2004.

- [95] R.L. Frank and S.A. Zadoff, "Phase Shift Codes with Good Periodic Correlation Properties," *IRE Trans. Info. Theory*, pp. 381–382, Oct. 1962.
- [96] D.C. Chu, "Polyphase Codes with Good Periodic Correlation Properties," *IEEE Trans. Inf. Theory*, pp. 531–532, Jul. 1972.
- [97] P.H. Moose, "A technique for orthogonal frequency division multiplexing frequency offset correction," *IEEE Trans. Commun.*, vol. 42, no. 10, pp. 2908–2914, Oct. 1994.
- [98] M. V. B. T. Pollet and M. Moeneclaey, "BER sensitivity of OFDM systems to carrier frequency offset and Wiener phase noise," *IEEE Trans. Commun.*, vol. 43, no. 2/3/4, pp. 191–193, apr/feb/mar 1995.
- [99] T. Schmidl and D. Cox, "Robust Frequency and Timing Synchronization for OFDM," *IEEE Trans. Commun.*, vol. 45, no. 12, Dec. 1997.
- [100] M. Hsieh and C. Wei, "A low-complexity frame synchronization and frequency offset compensation scheme for OFDM systems over fading channels," *IEEE Trans. Veh. Technol.*, vol. 48, no. 5, pp. 1596–1609, Sep. 1999.
- [101] T. Keller, L. Piazzo, P. Mandarini, and L. Hanzo, "Orthogonal frequency division multiplex synchronization techniques for frequency-selective fading channels," *IEEE J. Sel. Areas Commun.*, vol. 19, no. 6, Jun. 2001.
- [102] IEEE Standard 802.11a-1999, "Part 11: wireless LAN medium access control (MAC) and physical layer (PHY) specifications – amendment 1: high-speed physical layer in the 5 GHz band," Sep. 1999.
- [103] M. Speth, F. Classen, and H. Meyr, "Frame synchronization of OFDM systems in frequency selective fading channels," in *IEEE VTC'97*, May 1997, pp. 1807–1811.
- [104] D. Lee and K. Cheun, "Coarse symbol synchronization algorithms for OFDM systems in multipath channels," *IEEE Commun. Lett.*, vol. 6, no. 10, p. 446448, Oct. 2002.
- [105] A. Fort, J.-W. Weijers, V. Derudder, W. Eberle, and A. Bourdoux, "A performance and complexity comparison of auto-correlation and cross-correlation for OFDM burst synchronization," in *Proc. ICASSP'03*, vol. 2, 2003.
- [106] Y.-C. Wu, K.-W. Yip, T.-S. Ng, and E. Serpedin, "Maximum-likelihood symbol synchronization for IEEE 802.11a WLANs in unknown frequency-selective fading channels," *IEEE Trans. Wireless Commun.*, vol. 4, no. 6, Nov. 2005.
- [107] J. P. M. G. Linnartz, "Performance Analysis of Synchronous MC-CDMA in Mobile Rayleigh channel with both Delay and Doppler Spreads," *IEEE Trans. Veh. Technol.*, vol. 50, no. 6, pp. 1375–1387, Nov. 2001.
- [108] C. Belfiore and J. Park, "Decision feedback equalization," *Proc. IEEE*, vol. 67, pp. 1143–1156, Aug. 1979.

- [109] K. Zhou, J. Proakis, and F. Ling, "Decision-Feedback Equalization of Time-Dispersive Channels with Coded Modulation," *IEEE Trans. Commun.*, vol. 38, no. 1, pp. 18–24, Jan. 1990.
- [110] N. Benvenuto and S. Tomasin, "On the comparison between OFDM and single carrier with a DFE using a frequency domain feedforward filter," *IEEE Trans. Commun.*, vol. 50, no. 6, pp. 947–955, 2002.
- [111] Y. Zhu and K. B. Letaief, "Single carrier frequency domain equalization with noise prediction for broadband wireless systems," in *IEEE Globecom'04*, Dec. 2004, pp. 3098–3102.
- [112] O.E. Agazzi and N. Seshradsi, "On the use of tentative decisions to cancel intersymbol interference and nonlinear distortion (with application to magnetic recording channels)," *IEEE Trans. Inf. Theory*, vol. 43, no. 2, pp. 394–408, Mar. 1997.
- [113] S. Benedetto and J. Riani and J.W.M. Bergmans and A.H.J. Imminck, "Cancellation of Linear Intersymbol Interference for Two-Dimensional Storage Systems," *IEEE Trans. Magn.*, vol. 42, no. 8, pp. 2096–2106, Aug. 2006.
- [114] H. Yang and J.P.M.G. Linnartz, "Wiener Feedback Filtering for Suppression of Residual ISI and Correlated Noise in MC-CDMA," in *the 14th IEEE Symposium on Communications and Vehicular Technology in the Benelux in 2007 (SCVT'07)*, Delft, The Netherlands, Nov. 2007, pp. 144–148.
- [115] J. Hagenauer, "The Turbo Principle: Tutorial Introduction and State of the Art," in *Proc. of Int. Symposium on Turbo-Codes*, Sep. 1997, pp. 1–11.
- [116] A. Tanenbaum, *Computer Networks*. Prentice Hall, 1996.
- [117] K. Beauchamp, *Applications of Walsh and Related Functions: With an Introduction to Sequency Theory*. London : Academic Press, 1984.
- [118] S. Ariyavisitakul and Y. Li, "Joint coding and decision feedback equalization for broadband wireless channels," *IEEE J. Sel. Areas Commun.*, vol. 16, no. 9, pp. 1670–1678, Dec. 1998.
- [119] Xilinx, "Convolution encoder v6.1," May 2007, Product Specification.
- [120] B. Razavi, *RF Microelectronics*. Prentice Hall PTR, 1998.
- [121] —, "Design Considerations for Direct-Conversion Receivers," *IEEE Trans. Circuits Syst.*, vol. 44, no. 6, pp. 428–435, Jun. 1997.
- [122] A. Loke and F. Ali, "Complex-Valued Matrix Differentiation: Techniques and Key Results," *IEEE Trans. Microw. Theory Tech.*, vol. 50, no. 11, pp. 2422–2435, Nov. 2002.
- [123] T. Schenk, "RF Impairments in Multiple Antenna OFDM," Ph.D. dissertation, Eindhoven Universiteit of Technische, Nov. 2006.

- [124] C. Dehos and T.C.W. Schenk, "Digital Compensation Amplifier Nonlinearities in the Receiver of a Wireless System," in *The 14th IEEE Symposium on communications and Vehicular Technology in the Benelux (SCVT'07)*, Delft, The Netherlands, Nov. 2007.
- [125] J. Tubbax, B. Come, L. Van der Perre, L. Deneire, S. Donnay, , and M. Engels, "OFDM versus single carrier with cyclic prefix: A system-based comparison," in *Proc. IEEE VTC'01*, Oct. 2001, pp. 1115–1119.
- [126] A. Moschitta and D. Petri, "Wideband Communication System Sensitivity to Overloading Quantization Noise," *IEEE Trans. Instrum. Meas.*, vol. 52, no. 4, pp. 1302–1307, Aug. 2003.
- [127] M. Sawada, H. Okada, T. Yamazato, and M. Katayama, "Influence of ADC Nonlinearity on the Performance of an OFDM Receiver," *IEICE Trans. Commun.*, vol. E89-B, no. 12, pp. 3250–3256, Dec. 2006.
- [128] D. Dardari, "Joint Clip and Quantization Effects Characterization in OFDM Receivers," *IEEE Trans. Circuits Syst.*, vol. 53, no. 8, pp. 1741–1748, Aug. 2006.
- [129] A. Papoulis, *Probability, Random Variables and Stochastic Processes*. McGraw-hill book company, 1965.
- [130] J.J. Bussgang, "Crosscorrelation functions of amplitude-distorted Gaussian signals," Technical Report 215, Research Laboratory of Electronics, M. I. T., Tech. Rep., March 1952.
- [131] A. Nuttall, "Theory and application of the separable class of random processes," Res. Lab. Electron., M.I.T., Cambridge, MA, Tech. Rep., 1958, tech. Rep. 343.
- [132] M. Enqvist and L. Ljung, "Linear approximations of nonlinear FIR systems for separable input processes," *Automatica*, vol. 41, pp. 459–473, 2005.
- [133] R. van de Plassche, *CMOS Integrated Analog-to-Digital and Digital-to-Analog Converters*. Kluwer Academic Publishers, 2003.
- [134] N. Jayant and P. Noll, *Digital coding of waveforms: principles and applications to speech and video*. Prentice-Hall, Inc., 1984.
- [135] B. Widrow and I. Kollár and M. Liu, "Statistical Theory of Quantization," *IEEE Trans. Instrum. Meas.*, vol. 45, no. 2, pp. 353–361, Apr. 1996.
- [136] A. Bourdoux, J. Nsenga, W. V. Thillo, P. Wambacq, and L. V. der Perre, "Gbit/s Radios @ 60GHz: To OFDM or Not to OFDM?" in *IEEE ISSSTA'08*, Aug. 2008, pp. 560–565.
- [137] C. Rapp, "Effects of HPA-Nonlinearity on a 4-DPSK/OFDM-Signal for a Digital Sound Broadcasting System," in *Second European Conference on Satellite Communications, Liege, Belgium*, Oct. 1991, pp. 179–184.

- [138] M. Honkanen and S.-G. Haffman, "New Aspects on Nonlinear Power Amplifier Modeling in Radio Communication System Simulations," in *In Proc. Personal Indoor and Mobile Radio Communications 1997 (PIMRC'97)*, Sep. 1997, pp. 844–848.
- [139] M.C. Jeruchim and P. Balaban and K.S. Shanmugan, *Simulation of Communication Systems*. New York: Plenum Press, 1992.
- [140] I. Santamaria, J. Ibanez, M. Lazaro, C. Pantaleon, , and L. Vielva, "Modeling nonlinear power amplifiers in OFDM systems from subsampled data: A comparative study using real measurements," in *EURASIP Journal on Applied Signal Processing*, no. 12, pp. 1219–1228, Jun. 2003.
- [141] T. Lee and A. Hajimiri, "Oscillator Phase Noise: A Tutorial," *IEEE J. Solid-State Circuits*, vol. 35, no. 3, pp. 326–336, Mar. 2000.
- [142] A. Demir, A. Mehrotra, and J. Roychowdhury, "Phase Noise in Oscillators: A Unifying Theory and Numerical Methods for Characterization," *IEEE Trans. Circuits Syst. I*, vol. 47, no. 5, pp. 655–674, May 2000.
- [143] M. Sanduleanu, W.-L. Chan, H. Cheema, and J. Long, "WP2 Broadband WLAN Report on Architectures (Deliverable D2.4)," Tech. Rep., 2005, WiComm Project, The Netherlands.
- [144] S. Reynolds and etc., "A Silicon 60-GHz Receiver and Transmitter Chipset for Broadband Communications," *IEEE J. Solid-State Circuits*, vol. 41, no. 12, pp. 2820–2831, Dec. 2006.
- [145] C. Cao and K. Kenneth, "Millimeter-Wave voltage-Controlled Oscillators in 0.13- μm CMOS Technology," *IEEE J. Solid-State Circuits*, vol. 41, no. 6, pp. 1297–1304, Jun. 2006.
- [146] J. Tubbax, B. Come, L. van der Perre, L. Deneire, S. Donnay, and M. Engels, "Compensation of IQ imbalance in OFDM systems," in *Proc. IEEE International Conf. on Commun. 2003*, vol. 5, May 2003, pp. 3403–3407.
- [147] P. Kiss and V. Prodanov, "One-Tap Wideband I/Q Compensation for Zero-IF Filters," *IEEE Trans. Circuits Syst.*, vol. 51, no. 6, pp. 1062–1074, Jun. 2004.
- [148] M. Valkama, M. Renfors, and V. Koivunen, "Advanced methods for I/Q imbalance compensation in communication receivers," *IEEE Trans. Signal Process.*, vol. 49, pp. 2335–2344, Oct. 2001.
- [149] M. Windisch and G. Fettweis, "Standard-independent I/Q imbalance compensation in OFDM direct-conversion receivers," in *In Proc. 9th International OFDM Workshop*, Sep. 2004, pp. 57–61.
- [150] G. Felic and E. Skafidas, "An Integrated Transformer Balun for 60 GHz Silicon RF IC Design," in *International Symposium on Signal, Systems and Electronics, 2007 (ISSSE'07)*, Jul. 2007, pp. 541–542.

-
- [151] A. Parsa and B. Razavi, "A 60GHz CMOS Receiver Using a 30GHz LO," in *International Symposium on Signal, Systems and Electronics, 2008 (ISSSE'08)*, Feb. 2008, pp. 190–192.
- [152] "Toshiba CMOS Technology Roadmap for ASIC," [Online]. Available: <http://www.toshiba-components.com/ASIC/Technology.html>.
- [153] J.A.G. Akkermans and M.H.A.J. Herben, "Planar Beam-Forming Array for Broadband Communication in the 60-GHz Band," in *Proc. EuCAP'07, Nov.*, Edinburgh, UK, 2007, pp. 1–6.
- [154] P. Smulders and H. Yang and I. Akkermans, "On the Design of Low-cost 60 GHz Radios for Multi-Gbps Transmission over Short Distances," *IEEE Commun. Mag.*, pp. 44–51, Dec. 2007.
- [155] D. Lacroix and D. Castelain, "A Study of OFDM Parameters for High Data Rate Radio LANs," in *Proc. IEEE VTC'00*, May 2000.
- [156] J. Heiskala and J. Terry, *OFDM Wireless LANs: A Theoretical and Practical Guide*. Sams Publishing, 2001.
- [157] A. Czylik, "Comparison between adaptive OFDM and single carrier modulation with frequency domain equalization," in *IEEE VTC'05*, vol. 2, May 1997, pp. 865–869.
- [158] D.H. Brandwood, "A complex gradient operator and its application in adaptive array theory," *IEE Proc.*, vol. 130, no. 1, pp. 11–16, Feb. 1983.
- [159] A. Hjørungnes and D. Gesbert, "Complex-Valued Matrix Differentiation: Techniques and Key Results," *IEEE Trans. Signal Process.*, vol. 55, no. 6, pp. 2740–2746, Jun. 2007.

Author's publications

Journal papers

- [1] H. Yang and J.P. Linnartz and J.W.M. Bergmans, "Cancellation of Residual ISI for A Class of Code-Spreading Systems," *To be submitted*, 2008.
- [2] H. Yang and T.C.W. Schenk and P.F.M. Smulders and E.R. Fledderus, "Impact of Low-Resolution DAC/ADC on the Performance of Block Transmission Systems," *to be submitted*, 2008
- [3] H. Yang and M.H.A.J. Herben and I.J.A.G. Akkermans and P.F.M. Smulders, "Impact analysis of directional antennas and multi-antenna beamformers on radio transmission," *IEEE Trans. Veh. Technol.*, vol. 57, No. 3, pp. 1695–1707, May 2008.
- [4] P.F.M. Smulders and H. Yang and I.J.A.G. Akkermans, "On the Design of Low-cost 60 GHz Radios for Multi-Gbps Transmission over Short Distances," *IEEE Commun. Mag.*, vol. 45, No. 12, pp. 44–51, Dec. 2007.
- [5] H. Yang and P.F.M. Smulders and M.H.A.J. Herben, "Channel Characteristics and Transmission Performance for Various Channel Configurations at 60 GHz," *EURASIP Journal on Wireless Communications and Networking*, Article ID 19613, 15 pages, 2007.
- [6] H. Yang, M.H.A.J. Herben, and P.F.M. Smulders, "Impact of Antenna Pattern and Reflective Environment on 60 GHz Indoor Radio Channel Characteristics," *IEEE Antennas Wireless Propag. Lett.*, vol. 4, pp. 300–303, 2005.

Conference papers

- [7] H. Yang and T.C.W. Schenk and P.F.M. Smulders and E.R. Fledderus, "Joint Impact of Quantization and Clipping on Single- and Multi-carrier Block Transmission Systems," in *Proc. of IEEE Wireless Communications & Networking Conference in 2008 (WCNC08)*, Las Vegas, USA, Apr. 2008.

- [8] H. Yang and J.P.M.G. Linnartz, "Wiener Feedback Filtering for Suppression of Residual ISI and Correlated Noise in MC-CDMA," in *The 14th IEEE Symposium on communications and Vehicular Technology in the Benelux (SCVT'07)*, Delft, The Netherlands, Nov. 2007.
- [9] H. Yang and P.F.M. Smulders and E.R. Fledderus, "Comparison of Single- and Multi-carrier Block Transmissions under the Effect of Nonlinear HPA," in *The 14th IEEE Symposium on communications and Vehicular Technology in the Benelux (SCVT'07)*, Delft, The Netherlands, Nov. 2007.
- [10] H. Yang and P.F.M. Smulders and M.H.A.J. Herben, "Frequency Selectivity of 60-GHz LOS and NLOS Indoor Radio Channels," in *Proc. of IEEE Vehicular Technology Conference Spring in 2006 (VTC'06 spring)*, Melbourne, Australia, 2006, pp. 2727–2731.
- [11] H. Yang and M.H.A.J. Herben and P.F.M. Smulders, "Indoor Radio Channel Fading Analysis via Deterministic Simulations at 60 GHz," in *Proc. of Int. Symposium on Wireless Communications Systems in 2006 (ISWCS'06)*, Valencia, Sep. 2006, pp. 144–148.
- [12] H. Yang and P.F.M. Smulders and M.H.A.J. Herben, "Indoor Channel Measurements and Analysis in the Frequency bands 2 GHz and 60 GHz," in *Proc. of IEEE 16th International Symposium on Personal, Indoor and Mobile Radio Communications (PIMRC'05)*, Berlin, Germany, Sep. 2005, pp. 579–583.
- [13] H. Yang and M.H.A.J. Herben and P.F.M. Smulders, "Channel Measurement and Analysis for the 60 GHz Radio in a Reflective Environment," in *Proc. 8th IEEE International Symposium on Wireless Personal Multimedia Communications (WPMC'05)*, Aalborg, Denmark, Sep. 2005, pp. 475–478.
- [14] H. Yang and M. Herben, "Spatial dispersion and performance evaluation of indoor MIMO channels at 2.25 GHz," in *Proc. The 11th IEEE Symposium on communications and Vehicular Technology in the Benelux chapter (SCVT'04)*, Gent, Belgium, Nov. 2004.
- [15] P.F.M Smulders and C.F. Li and H. Yang and E.F.T. Martijn and M.H.A.J. Herben, "60 GHz Indoor Radio Propagation - Comparison of Simulation and Measurement Results," in *The 11th IEEE Symposium on communications and Vehicular Technology in the Benelux (SCVT'04)*, Gent, Belgium, Nov. 2004.

Contributions to individual chapters

The contributions of the publications to chapters.

Chapter 2	Chapter 3	Chapter 4	Chapter 5	Chapter 6	Chapter 7
[6], [10]-[15]	[3]	[2][5]	[1][8]	[2][7][9]	[4][5]

Samenvatting

De wereldwijde beschikbaarheid van de enorme hoeveelheid vergunningsvrije spectrale ruimte in de 60 GHz band geeft ruime mogelijkheden voor gigabit-per-seconde (Gb/s) draadloze toepassingen. Een commerciële (lees: low-cost) 60 GHz transceiver zal echter een beperkte performance leveren vanwege het stringente linkbudget en de substantiële imperfecties die op zullen treden in de RF circuits. Het werk dat gepresenteerd wordt in dit proefschrift is bedoeld ter ondersteuning van het ontwerp van low-cost 60 GHz transceivers voor Gb/s transmissie over korte afstanden (enkele meters). Typische toepassingen zijn de overdacht van high-definition streaming video en high-speed download. Het gepresenteerde werk omvat onderzoek naar de karakteristieken van typische 60 GHz kanalen, de evaluatie van de transmissiekwaliteit alsmede de ontwikkeling van geschikte basisbandalgoritmen. Dit kan als volgt worden samengevat:

In het eerste deel worden de karakteristieken van de golfvoorplanting op 60 GHz in kaart gebracht door middel van kanaalmetingen en ray-tracing simulaties voor zowel gebundelde als omnidirectionele antennestralingspatronen. Zowel situaties met line-of-sight (LOS) als non-line-of-sight (NLOS) worden daartoe beschouwd. Dit onderzoek maakt duidelijk dat antennes die een smalle bundel produceren gebruikt kunnen worden om het ontvangen vermogen met tientallen dB's op te voeren in vergelijking met omnidirectionele configuraties. Tevens wordt daarbij de tijd-domein dispersie van het kanaal aanzienlijk beperkt tot in de orde van nanoseconden, hetgeen Gb/s datatransmissie over 60 GHz kanalen aanzienlijk vereenvoudigd. Naast het uitvoeren van metingen en simulaties wordt de invloed van antennestralingspatronen ook theoretisch geanalyseerd. Een indicatie wordt gegeven van de mate waarin de signaal-ruisverhouding, Rician- K factor en kanaaldispersie worden verbeterd door het toepassen van antennes met een smalle antennebundel en in welke mate deze parameters worden beïnvloed door uitrichtfouten. Uit zowel het experimentele- als analytische werk kan worden geconcludeerd dat het probleem van het stringente linkbudget effectief kan worden opgelost door het toepassen van bundelsturing.

Het tweede deel behandelt breedbandige transmissiemethoden en daarvoor relevante

basisbandalgoritmen. Aan de orde komen orthogonal frequency division multiplexing (OFDM), multi-carrier code division multiple access (MC-CDMA) en single-carrier met frequency domain equalization (SC-FDE), welke veelbelovende kandidaten zijn voor Gb/s draadloze transmissie. In het bijzonder wordt de optimale lineaire egalisatie in het frequentie domein en daarmee geassocieerde implementatieproblematiek zoals synchronisatie en kanaalschatting onderzocht. Ter evaluatie van de transmissiekwaliteit worden uitdrukkingen voor de bit error rate (BER) afgeleid. Naast lineaire egalisatietechnieken wordt een nieuwe techniek voor het opheffen van inter-symbool interferentie (ISI) voorgesteld ter verkrijging van een veel betere performance van code-spreiding systemen zoals MC-CDMA en SC-FDE. Zowel theoretische analyse als simulaties tonen aan dat de voorgestelde methode grote voordelen biedt voor wat betreft complexiteit en performance. Dit maakt het speciaal geschikt voor low-cost 60 GHz toepassingen.

Het derde deel behandelt de invloed van kwantisatie en RF imperfecties op de beschouwde transmissiemethoden in de context van 60 GHz radio. Eerst worden uitdrukkingen voor de BER afgeleid en wordt de invloed van niet-lineaire vervormingen welke worden veroorzaakt door digitaal-naar-analoog omzeters, analoog-naar-digitaal omzeters en vermogensversterkers op de BER-performance van deze methoden onderzocht. Vervolgens wordt de BER die optreedt door faseruis en IQ onbalans geëvalueerd voor het geval dat digitale compensatietechnieken in de ontvanger worden toegepast alsmede voor het geval dat deze niet worden toegepast.

Ten slotte wordt een baseline ontwerp van een low-cost Gb/s 60 GHz transceiver gepresenteerd. Er wordt aangetoond dat, door toepassing van bundelsturing in combinatie met SC-FDE zonder kanaalcodering, een datasnelheid in de orde van 2 Gb/s kan worden bereikt over een afstand van 10 meter in een typisch NLOS inhuis-scenario.

Acknowledgements

This thesis summarizes the research work I have performed within the Radiocommunications group (ECR) of Eindhoven University of Technology. By this opportunity, I would like to express my sincere gratitude to the following people, without whom the completion of this thesis would not have been possible.

First of all, I owe a great deal to dr. Matti Herben and dr. Peter Smulders for offering me the opportunity to join the projects of B4 Broadband Radio@Hand and WiComm and for being my copromotoren. As daily supervisors, they have provided me invaluable guidance, support and freedom to my research. I am indebted to my promotor prof. Erik Fledderus for the inspiring and enjoyable discussions about my research work and for critical comments and constructive suggestions on the manuscript of my thesis.

Sjoerd Ypma, Ewart Martijn and Jaap Swijghuisen Reigersberg provided technical assistance on configuring channel sounding equipment during the first year, for which I am grateful. Sjoerd is also appreciated for introducing me to the ECR group. Ewart Martijn and Chaofeng Li also helped me get familiar with the RPS ray tracing simulator.

I would like to thank my roommate Iwan Akkermans for interesting discussions and nice cooperations on the topic of antenna directivity and its influence on wave propagation. I am grateful to my ex-colleague dr. Tim Schenk for useful discussions and cooperations on the topic of nonlinearities. I am indebted to prof. Jean-Paul Linnartz for motivational and inspiring discussions on DFE and its application in code-spreading systems, which are reflected in Chapter 5. Thanks go to prof. Jan Bergmans for useful discussions and comments on DFE and cancellation techniques, and for his enthusiasm on coauthoring a paper based on Chapter 5. As well, I thank dr. Stefano Tomasin from University of Padova for his comments and suggestions on the initial ideas of using DFE in MC-CDMA.

Also, I would like to thank all the other colleagues, ex-colleagues and students from the ECR group and other groups, for good cooperation, useful discussions, excellent

atmosphere, nice lunch talks, coffee breaks, etc. over the past five years. I especially would like to mention, without the intention to forget someone: Yvonne Broers, Hammad Cheema, Archi Delphinanto, Rainier van Dommele, Rian van Gaalen, Els Gerritsen, Marija Jevrosimivić, Imran Kazim, Maurice Kwakkernaat, Jeffrey Lee, Susan de Leeuw, Thijs van Lieshout, Yong Liu, Harald van den Meerendonk, Akogo Moses, Christopher Nambale, Dries Neiryck, Robbert van Poppel, Andrei Sazonov, Erwin Verdurmen and Yikun Yu.

It is now a good opportunity for me to thank all the researchers and PhD students I met during the Broadband Radio@Hand project meetings and the WiComm project meetings for valuable discussions and wonderful time we have shared together. They are from Delft University, Twente University, Eindhoven University, TNO ICT, TNO D&V and Philips Research, and their names could not be printed in this limited space. Many of them have different backgrounds and work on different topics. The useful interactions and discussions with them during the regular meetings have broadened my horizons on various aspects of wireless technologies, for which I am very thankful. Next to people from the two projects, I also want to acknowledge the discussions with many of the participants of the project SiGi-Spot.

Thanks go to dr. Gerard Janssen, prof. Arthur van Roermund, prof. Liesbet van der Perre and prof. Jean-Paul Linnartz for being part of my doctorate committee. Their views and comments on the thesis work were insightful and very helpful.

I am deeply indebted to my parents, my parents-in-law and my sisters for understanding and supporting me throughout these years.

I would like to thank my wife Jieheng for her continuous support, love and encouragement, as well as for reading part of my thesis while travelling between home and office. She always believes in me and stands firmly together with me, no matter what challenges we've faced in our life. And finally, I welcome our baby daughter, Anjali, who is kicking inside mummy's womb while I am writing, to the wonderful world!

Curriculum vitae

Haibing Yang was born in Hebei province, China, on March 16, 1974. He received his B.Eng in detection and instrumentation and M.Eng degree in electrical engineering from Xidian University, Xi'an, China, in 1997 and 2000, respectively. He performed his graduation project on Neural Network for Signal Processing in the National Key Laboratory for Radar Signal Processing, Xian, China. In 2002, he received his Professional Doctorate in engineering (PDEng) in Eindhoven University of Technology, Eindhoven, The Netherlands. During the period 2001-2002, he worked on Doppler cancellation algorithm development for mobile DVB-T reception in Philips Research Laboratories, Eindhoven.

Since 2003, he was with the Radiocommunications (ECR) as a wireless researcher and joined several projects. During the period 2003-2005, he was involved in the project "B4 Broadband Radio@hand" working on radio channel measurement and modelling. During the period 2005-2008, he was involved in the project "Foundations of Wireless Communication" (WiComm) and meanwhile worked towards his PhD degree. Within the WiComm project, he mainly focused on baseband modulation and algorithm development for low-cost gigabit wireless systems at 60 GHz, taking into account the particular properties of the 60-GHz channels, antennas and RF front-ends.

Index

- A posteriori* probability, 119
- A/D conversion, 128, 138
- Amplitude mismatch, 163
- Analog beamforming, *see* RF beamforming
- Antenna polarization, 39
- Antenna radiation pattern, 33, 36, 62, 63
- Array gain, 182
- Array pattern, 59, 63
- Autocorrelation matrix, 108
- Automatic gain control, 141
- AWGN channel, 75, 84

- Bandwidth-limited system, 74
- Baseband, 74, 180
- Baseband equivalent signal, 74
- Beam pattern, 58, 63
- Beam scanning range, 68
- Beam steering, 58, 174, 177
- Beam-pointing error, 20, 23, 25, 27, 32, 54, 58, 66, 175
- Beamwidth, *see* Half-power beamwidth
- Biased detection, 83
- Bit error rate
 - AWGN channel, 84
 - DAC/ADC, 145
 - IQ mismatch, 168
 - nonlinearities, 134
 - PA, 153
 - phase noise, 160
 - Rician fading channel, 84, 87
 - RISI cancellation, 120, 122
- Busgang's theorem, 129

- Carrier frequency offset, 75, 76, 92
- Channel estimation, 91
 - FFT-based, 100
 - ZF, 99
- Channel fading, 12
- Channel measurement, 20
- Channel modelling, 13, 25
- Channelization, 179
- Chu sequence, 92
- Circulant matrix, 81, 110
- Clarke's model, 20
- Clipping error, 138
- CMOS, 175
- Code spreading, 78, 103
- Coherence bandwidth, 19, 27
- Common phase error, 158
- Complementary error function, 84
- Complex permittivities, 38
- Continuous phase modulations (CPM), 73
- Cosine-shaped antenna pattern, 63
- Cross-correlation matrix, 108
- Cyclic convolution, 80
- Cyclic prefix, 80

- D/A conversion, 128, 138
- Decision feedback equalization, 103, 111
- Digital beamforming, 177
- Digital compensation
 - CPE correction, 160
 - IQ compensation, 166
- Direct conversion, 127, 163, 177
- Direct path, 15, 50
- Direction of arrival, 44, 51, 52, 63

- Direction of departure, 44, 51, 52, 63
- Directional, 20, 44, 52, 66
- Directivity, 21, 62, 176
- Dirty RF, 127
- Doppler effect, 20, 174
- Doppler spread, 20
- Double-directional channel, 11, 44, 52
- Down-conversion, 75, 163, 177
- Dyadic convolution, 112
- Dyadic matrix, 112
- ECMA, 2
- Effective isotropic radiated powers, 2
- Fast fading, 12
- Fast Fourier transform, 79
- Fourier matrix, 79
- Frank-Zadoff sequence, 92
- Free space transmission, 13, 182
- Frequency diversity, 74, 78, 84, 146, 148, 154, 180
- Frequency domain equalization, 114
- Frequency flat channel, 76, 83, 121, 134, 158, 166
- Frequency offset, *see* Carrier frequency offset
- Frequency selective channel, 13, 19, 25, 75, 84, 159, 174
- Frequency selectivity, 13, 19, 25
- Frequency synchronization, 91, 92
- Frequency-domain equalization, 81, 134
- Gaussian minimum shift keying (GMSK), 73
- Generalized Bussgang's theorem, 129
- Gigabit wireless, 1
- Guard interval, 80
- Half-power beamwidth, 64
- Half-power beamwidth, 21, 62, 68, 176
- IEEE 802.15.3 TG3c, 2
- Input power backoff, 127, 149
- Inter-block interference, 78, 180
- Inter-carrier interference, 76, 92, 157
- Inter-symbol interference, 76, 81
- Interconnect loss, 182
- IQ imbalance, 163
- IQ mismatch, *see* IQ imbalance
- ISI cancellation, 104, 112, 114
- Isotropic antenna, 52, 66
- Jensen's inequality, 83, 121
- Large-scale fading, 12, 23, 42
- Levinson-Durbin algorithm, 126
- Line-of-sight, 13, 15, 25, 52, 182
- Linear equalization, 81
- Linear modulation, 73
 - \mathcal{M} -PSK, 84, 120, 135
 - \mathcal{M} -QAM, 84, 120, 135
- Link budget design, 182
- Link margin, 182
- Local oscillator, 127, 155, 163
- Log-distance model, 15, 23, 34, 43
- Low pass filtering, 76
- Main detector, 104, 106, 119
- Matched filter bound, 120
- Maximum excess delay, 29
- MC-CDMA, 78, 84, 103, 131
- medium access control, 175
- Memoryless nonlinearity, 129, 138, 149
- mid-raiser uniform quantization, 139
- Mirror signal, 164, 165
- mm-wave, 2, 11
- MMSE equalization, 81, 134, 167
- Modulo-2 addition, 112
- Multi-carrier transmission, 78, 134, 179, 180
- Multi-cluster channel model, 17
- Multipath channel, 15, 25, 75, 84, 103, 174
- Multiple-input multiple-output, 57, 178
- Narrow-beam, 20, 44
- Narrowband beamforming, 177
- Narrowband channel, 12
- Noise figure, 182
- Non-line-of-sight, 16, 25, 183
- Nonlinear amplification, 127, 149
- Nonlinear distortion, 127, 128, 130, 131, 138, 149

- Normalized received power, 34
 Nyquist criterion, 76
 Nyquist filtering, 76
- OFDM, 78, 131, 180
 Omnidirectional, 20, 66
 Orthogonality principle, 109, 114
- Path loss, 14, 23, 42, 182
 Path loss exponent, 15
 Peak-to-average power ratio, 143, 179
 Perfect sequence, 91
 Phase mismatch, 163
 Phase noise, 155
 Phase rotation, 92, 157
 Phase shifter, 178
 Pilot sequence, 96
 Power angular spectrum, 44, 59
 Power delay profile, 16, 17, 25, 32, 62
 Power delay spectrum, *see* Power delay profile
 Power delay-DOD-DOA spectrum, 52
 Propagation channel, 11, 37, 52, 59
 Pseudo quantization noise (PQN) model, 140
 Pulse shaping, 76
- Quantization interval, 141
 Quantization noise, 138
 Quantization process, 128, 138
- Radio channel, 11, 20, 33
 Raised-cosine filter, 76
 Rapp's model, 150
 Ray tracing, 37
 Rayleigh fading, 16, 84
 Reduced-order filtering, 111
 Residual ISI, 82, 103, 106
 RF beamforming, 175, 177
 RF front-end, 127, 175, 177
 RF impairment, *see* RF front-end
 Rician K -factor, 16, 27, 53
 Rician K -factor gain, 56, 59, 65
 Rician fading, 16, 53, 84, 134
 RMS delay spread, 16, 27, 44, 54
 RMS delay spread reduction, 56, 59, 65
- Saleh-Valenzuela channel model, 17
 Sample timing, 77
 SC-FDE, *see* Single-carrier transmission
 Scattered waves, 15, 50
 Separable stochastic process, 129
 Shadowing effect, 13, 15, 23, 34, 39
 Signal model, 74
 Single-carrier transmission, 78, 134, 179, 180
 Single-cluster channel model, 17
 Single-input single-output, 50, 66
 Slow fading, 12
 Small-scale fading, 12, 44
 SNR gain, 56, 59, 65
 Soft feedback, 119
 Spatial selectivity, 13, 44
 Specular path, 15, 50
 Subcarrier, 78, 180
 Symbol timing, 91, 96
 Symbol-by-symbol decision, 82
 System model, 78, 131
 System performance, *see* BER
- Tentative detector, 104, 106, 119
 Time dispersion, 15
 Time invariant channel, 15
 Time selectivity, 13, 20
 Training sequence, 92
- Unbiased detection, 83
 Uniform linear array, 58, 68
 Uniform power distribution, 61
 Uniform quantization, 139
 Unitary matrix, 79
 Up-conversion, 75, 163, 177
- Viterbi detection, 89, 119
- Walsh-Hadamard matrix, 79
 Wide-sense stationary uncorrelated scattering, 16, 52
 Wideband channel, 12, 15, 75
 Wideband systems, 78
 Wiener filtering, 109
 Wireless LAN, 1
 Wireless PAN, 1, 182
 WirelessHD, 2

